

Review Article

Electronic Structure of Strongly Correlated Systems

V. N. Antonov,^{1,2} L. V. Bekenov,² and A. N. Yaresko¹

¹Andersen Department, Max-Planck-Institut für Festkörperforschung, Heisenberg Straße 1, 70569 Stuttgart, Germany

²Computational Physics Department, Institute of Metal Physics, 36 Vernadskii street, 03142 Kiev, Ukraine

Correspondence should be addressed to V. N. Antonov, v.antonov@fkf.mpg.de

Received 23 March 2011; Accepted 12 July 2011

Academic Editor: P. Guptasarma

Copyright © 2011 V. N. Antonov et al. This is an open access article distributed under the Creative Commons Attribution License, which permits unrestricted use, distribution, and reproduction in any medium, provided the original work is properly cited.

The article reviews the rich phenomena of metal-insulator transitions, anomalous metallicity, taking as examples iron and titanium oxides. The diverse phenomena include strong spin and orbital fluctuations, incoherence of charge dynamics, and phase transitions under control of key parameters such as band filling, bandwidth, and dimensionality. Another important phenomena presented in the article is a valence fluctuation which occur often in rare-earth compounds. We consider some Ce, Sm, Eu, Tm, and Yb compounds such as Ce, Sm and Tm monochalcogenides, Sm and Yb borides, mixed-valent and charge-ordered Sm, Eu and Yb pnictides and chalcogenides R_4X_3 and R_3X_4 ($R = \text{Sm, Eu, Yb}$; $X = \text{As, Sb, Bi}$), intermediate-valence YbInCu_4 and heavy-fermion compounds YbMCu_4 ($M = \text{Cu, Ag, Au, Pd}$). Issues addressed include the nature of the electronic ground states, the metal-insulator transition, the electronic and magnetic structures. The discussion includes key experiments, such as optical and magneto-optical spectroscopic measurements, x-ray photoemission and x-ray absorption, bremsstrahlung isochromat spectroscopy measurements as well as x-ray magnetic circular dichroism.

1. Introduction

Determination of the energy band structure of solids is a many-body problem. Band theory, a mean-field theory to treat this problem, in the framework of the local spin density approximation (LSDA), has been successful for many kinds of materials and has become the *de facto* tool of first-principles calculations in solid-state physics. It has contributed significantly to the understanding of material properties at the microscopic level. However, there are some systematic errors which have been observed when using the LSDA. In particular, the LSDA fails to describe the electronic structure and properties of the electron systems in which the interaction among the electrons is strong. These are now called strongly correlated electron systems, and many new concepts to address these phenomena have been constructed. However, the understanding of these systems is not complete. A wide variety of physical properties arise from the correlations among $3d$ and $4f$ electrons: metal-insulator transitions, valence fluctuations in the Kondo effect, heavy-fermion behavior, superconductivity, and so on.

The investigation of this class of systems goes back to the early 1960s. The main motivations at the time came

from experiments on transition metal oxides, from the Mott metal-insulator transition, and from the problem of itinerant ferromagnetism. Theoretical progress in the field has been impeded however by the extreme difficulty of dealing with even the simplest model Hamiltonians appropriate for these systems, such as the Hubbard model and the Kondo lattice model [1]. Only in the one-dimensional case do we have a variety of theoretical tools at our disposal to study these models in a systematic manner. For two- and three-dimensional models, one is often unable to assess confidently whether a given physical phenomenon is indeed captured by the idealized Hamiltonian under consideration or whether a theoretical prediction reflects a true feature of this Hamiltonian, rather than an artifact of the approximation used in its solution. These difficulties originate in the nonperturbative nature of the problem and reflect the presence of several competing physical mechanisms for even the simplest models. The interplay of localization and lattice coherence, that of quantum and spatial fluctuations and that of various competing types of long-range order are important examples.

With the aim of undertaking a systematic investigation of the trends in some mixed-valent and charge- and orbital-ordering compounds, we present the theoretically calculated

electronic structure, optical, magneto-optical, and photo-emission spectra for some $3d$ and $4f$ compounds. The main idea of the paper is to show how the modern band structure methods which take into account strong electron-electron interaction can properly describe the electronic structure and physical properties of strongly correlated electron systems.

In the first part of the article we concentrate on the description of the methods and the results for the $3d$ transition metal oxides which possess different fascinating physical properties including charge and orbital ordering as well as metal-insulator transition (MIT). Metal-insulator transitions are accompanied by huge resistivity changes, even over tens of orders of magnitude, and are widely observed in condensed-matter systems [2]. Especially important are the transitions driven by correlation effects associated with the electron-electron interaction. The insulating phase caused by the correlation effects is categorized as the Mott Insulator. Near the transition point the metallic state shows fluctuations and orderings in the spin, charge, and orbital degrees of freedom. The properties of these metals are frequently quite different from those of ordinary metals, as measured by transport, optical, and magnetic probes. We consider the Fe_3O_4 , Fe_2O_3 , Ti_4O_7 , and α' - NaV_2O_5 .

The second part of the paper is devoted to the strongly correlated $4f$ systems such as CeFe_2 , Ce , Sm , and Tm monochalcogenides RX ($\text{R} = \text{Ce}, \text{Sm}, \text{Tm}$; $\text{X} = \text{S}, \text{Se}, \text{Te}$), Sm and Yb borides SmB_6 , YbB_{12} , mixed-valent and charge-ordered Sm , Eu and Yb pnictides and chalcogenides R_4X_3 and R_3X_4 ($\text{R} = \text{Sm}, \text{Eu}, \text{Yb}$; $\text{X} = \text{As}, \text{Sb}, \text{Bi}$), intermediate-valence YbInCu_4 and heavy-fermion compounds YbMCu_4 ($\text{M} = \text{Cu}, \text{Ag}, \text{Au}, \text{Pd}$).

In rare-earth compounds, where $4f$ levels are relatively close to the Fermi energy, various anomalous phenomena frequently appear. Most of them can be attributed to the hybridization between the $4f$ states and conduction bands. A mixed-valence (MV) state is one of these phenomena. The MV phenomenon has attracted a great deal of interest during the last several decades in connection with valence fluctuations [3–7]. In the gas phase most rare earths are divalent, but in the solid state most are trivalent, due to the large cohesive energy gained by promoting a $4f$ electron into an extended bonding state. The rare-earth compounds based on Sm , Eu , Tm , and Yb ions frequently exhibit a mixed-valence state consisting of divalent and trivalent valences. In the mixed-valence compounds, therefore, one must also consider the charge degrees of freedom of the $4f$ ions in addition to the spin and orbital degrees of freedom.

It is necessary to distinguish between *homogeneously* mixed-valence compounds and *inhomogeneously* mixed-valence compounds. In the former, all the rare-earth ions occupy crystallographically equivalent sites, and, therefore, this is essentially a single ion property where the magnetic ion hybridizes with the sea of the conduction electrons, causing an exchange of the inner $4f$ electron with the conduction band at the Fermi level. Such effects are expected to arise in systems where two electron configurations corresponding to $4f$ occupation numbers n and $n - 1$ have nearly degenerate energies. So the ground state of a homogeneously mixed-valence compound is a quantum mechanical mixture of both

the $4f^n$ and the $4f^{n-1}d$ configuration on each rare-earth ion. Typical compounds exhibiting homogeneously mixed-valence phenomena are rare-earth materials TmSe , SmS (high-pressure golden phase), SmB_6 , YbB_{12} , and YbInCu_4 .

In the case of inhomogeneously or static mixed-valence compounds, rare-earth ions with different valency occupy clearly different sites. However, at high temperatures they become homogeneously mixed-valence semimetals or valence-fluctuating insulators. Their $4f$ electrons are strongly correlated and close to localization, that is, having a low effective kinetic energy. The $4f$ electrons can hop between the magnetic ions with different valences due to thermal activation (a thermal valence-fluctuating state). If the intersite Coulomb repulsion is large enough, it may dominate the kinetic energy and, once the charge-disorder entropy due to hopping is low enough, lead to a charge-ordered transition at a critical temperature T_{co} below which the valence fluctuation is suppressed. The resulting inhomogeneously mixed-valence state consists of two species of ions with the $4f^n$ and the $4f^{n-1}d$ configurations. This transition may be compared to a Wigner crystallization on a lattice [8], and its earliest example is the Verwey transition in magnetite Fe_3O_4 [9], although this picture turned out to be too simplified for this compound [10, 11]. There are several charge-fluctuating inhomogeneous mixed-valence compounds containing rare-earth ions. They are the rare-earth pnictides Yb_4As_3 , Sm_4Bi_3 , and Eu_4As_3 with the cubic anti- Th_3P_4 structure and rare earth chalcogenides Sm_3X_4 ($\text{X} = \text{S}, \text{Se}$ or Te) and Eu_3S_4 with the Th_3P_4 structure.

2. Theoretical Framework

It is well known that the LSDA fails to describe the electronic structure and properties of the systems in which the interaction among the electrons is strong. In recent years more advanced methods of electronic structure determination such as LSDA plus self-interaction corrections (SIC-LSDA) [12], the LSDA+ U [13] method, the GW approximation [14], and dynamical mean-field theory (DMFT) [1, 15, 16] have sought to remedy this problem and have met with considerable success. The LSDA+ U method is the simplest among them and most frequently used in the literature therefore; we describe the method in detail.

2.1. LSDA+ U Method. A rigorous formulation for the quasiparticle properties of solids is the Green function approach. The self-energy $\Sigma = G_0^{-1} - G^{-1}$ of the single-particle Green function G is energy dependent and yields the correlation corrections to the single-particle (mean-field) approximation to the quasiparticle excitation spectrum described by G_0 . With a number of plausible assumptions, the LSDA+ U approach has been related to the so-called GW approximation to Σ in [17]. Already the simplest random phase approximation applied to Σ for the Hubbard model yields a jump of $\Sigma(\epsilon)$ at the Fermi level ϵ_F by the Hubbard U . The more elaborate analysis of [17] results in a correlation correction to the mean-field approximation of the self-energy, which is $U_{\text{eff}}/2$ downward below the Fermi level and

$U_{\text{eff}}/2$ upward above the Fermi level. As mean-field theory in a crystal describes always a delocalized situation and the LSDA Kohn-Sham potential is a well-proved approximation to the self-energy of weakly correlated situations [18], the suggestion is

$$\begin{aligned} \Sigma(\vec{r}, \vec{r}'; \epsilon) &\approx \delta(\vec{r} - \vec{r}') v_{\text{LSDA}}(\vec{r}) \\ &+ P_m \frac{U_{\text{eff}}}{2} (\theta(\epsilon - \epsilon_F) - \theta(\epsilon_F - \epsilon)) P_m, \end{aligned} \quad (1)$$

where P_m is the projector onto a strongly correlated m state.

The LSDA+ U approach simply uses (1) to replace the LSDA Kohn-Sham potential in the self-consistency loop. This can be considered as a rough approximation to Σ . Since the potential shift is taken to be constant in space, it does not deform the Kohn-Sham orbital ϕ_m . However, it shifts the levels of strongly correlated motion away from the Fermi level and thus removes incorrect hybridization with conduction states, which would spoil the calculated ground-state spin density. On the other hand, being also understood as an approximation to Σ , it hopefully yields for the Kohn-Sham band structure the same quality of a working approximation to the quasiparticle excitation spectrum as it does in the case of weakly correlated metals.

The main idea of the LSDA+ U is the same as in the Anderson impurity model [19]: the separate treatment of localized f -electrons for which the Coulomb f - f interaction is taken into account by a Hubbard-type term in the Hamiltonian $(1/2)U \sum_{i \neq j} n_i n_j$ (n_i are f orbital occupancies) and delocalized s, p, d electrons for which the local density approximation for the Coulomb interaction is regarded as sufficient.

The spectrum of excitations for the shell of an f electron system is a set of many-body levels describing processes of removing and adding electrons. In the simplified case, when every f electron has roughly the same kinetic energy ϵ_f and Coulomb repulsion energy U , the total energy of the shell with n electrons is given by $E_n = \epsilon_f n + Un(n-1)/2$ and the excitation spectrum is given by $\epsilon_n = E_{n+1} - E_n = \epsilon_f + Un$.

Let us consider f ion as an open system with a fluctuating number of f electrons. The correct formula for the Coulomb energy of f - f interactions as a function of the number of f electrons N given by the LDA should be $E = UN(N-1)/2$ [20]. If we subtract this expression from the LDA total energy functional and add a Hubbard-like term (neglecting for a while exchange and nonsphericity), we will have the following functional:

$$E = E^{\text{LDA}} - \frac{UN(N-1)}{2} + \frac{1}{2}U \sum_{i \neq j} n_i n_j. \quad (2)$$

The orbital energies ϵ_i are derivatives of (2):

$$\epsilon_i = \frac{\partial E}{\partial n_i} = \epsilon^{\text{LDA}} + U \left(\frac{1}{2} - n_i \right). \quad (3)$$

This simple formula gives the shift of the LDA orbital energy $-U/2$ for occupied orbitals ($n_i = 1$) and $+U/2$ for unoccupied orbitals ($n_i = 0$). A similar formula is found

for the orbital-dependent potential $V_i(\vec{r}) = \delta E / \delta n_i(\vec{r})$ where variation is taken not on the total charge density $\rho(\vec{r})$ but on the charge density of a particular i th orbital $n_i(\vec{r})$:

$$V_i(\vec{r}) = V^{\text{LDA}}(\vec{r}) + U \left(\frac{1}{2} - n_i \right). \quad (4)$$

Expression (4) restores the discontinuous behavior of the one-electron potential of the exact density-functional theory.

The functional (2) neglects exchange and nonsphericity of the Coulomb interaction. In the most general rotationally invariant form the LDA+ U functional is defined as [21, 22]

$$E^{\text{LDA}+U}[\rho(\vec{r}), \hat{n}] = E^{\text{L(S)DA}}[\rho(\vec{r})] + E^U(\hat{n}) - E^{\text{dc}}(\hat{n}), \quad (5)$$

where $E^{\text{L(S)DA}}[\rho(\vec{r})]$ is the LSDA (or LDA as in [20]) functional of the total electron spin densities, $E^U(\hat{n})$ is the electron-electron interaction energy of the localized electrons, and $E^{\text{dc}}(\hat{n})$ is the so-called ‘‘double counting’’ term which cancels approximately the part of an electron-electron energy which is already included in E^{LDA} . The last two terms are functions of the occupation matrix \hat{n} defined using the local orbitals $\{\phi_{lm\sigma}\}$.

The matrix $\hat{n} = \|n_{\sigma m, \sigma' m'}\|$ generally consists of both spin-diagonal and spin-nondiagonal terms. The latter can appear due to the spin-orbit interaction or a noncollinear magnetic order. Then, the second term in (5) can be written as [21–23]

$$\begin{aligned} E^U = \frac{1}{2} \sum_{\sigma, \sigma', \{lm\}} &(n_{\sigma m_1, \sigma m_2} U_{m_1 m_2 m_3 m_4} n_{\sigma' m_3, \sigma' m_4} \\ &- n_{\sigma m_1, \sigma' m_2} U_{m_1 m_4 m_3 m_2} n_{\sigma' m_3, \sigma m_4}), \end{aligned} \quad (6)$$

where $U_{m_1 m_2 m_3 m_4}$ are the matrix elements of the on-site Coulomb interaction which are given by

$$U_{m_1 m_2 m_3 m_4} = \sum_{k=0}^{2l} a_{m_1 m_2 m_3 m_4}^k F^k, \quad (7)$$

with F^k being screened Slater integrals for a given l and

$$a_{m_1 m_2 m_3 m_4}^k = \frac{4\pi}{2k+1} \sum_{q=-k}^k \langle lm_1 | Y_{kq} | lm_2 \rangle \langle lm_3 | Y_{kq}^* | lm_4 \rangle. \quad (8)$$

The $\langle lm_1 | Y_{kq} | lm_2 \rangle$ angular integrals of a product of three spherical harmonics Y_{lm} can be expressed in terms of Clebsch-Gordan coefficients, and (8) becomes

$$\begin{aligned} a_{m_1 m_2 m_3 m_4}^k &= \delta_{m_1 - m_2 + m_3, m_4} \left(C_{k0, l0}^{l0} \right)^2 \\ &\times C_{km_1 - m_2, lm_2}^{lm_1} C_{km_1 - m_2, lm_3}^{lm_4}. \end{aligned} \quad (9)$$

The matrix elements $U_{mmmm'}$ and $U_{mm'm'm}$ which enter those terms in the sum in (6) which contain a product of the diagonal elements of the occupation matrix can be identified as pair Coulomb and exchange integrals

$$\begin{aligned} U_{mmmm'} &= U_{mm'}, \\ U_{mm'm'm} &= J_{mm'}. \end{aligned} \quad (10)$$

The averaging of the matrices $U_{mm'}$ and $U_{mm'} - J_{mm'}$ over all possible pairs of m, m' defines the averaged Coulomb U and exchange J integrals which enter the expression for E^{dc} . Using the properties of Clebsch-Gordan coefficients, one can show that

$$\begin{aligned} U &= \frac{1}{(2l+1)^2} \sum_{mm'} U_{mm'} = F^0, \\ U - J &= \frac{1}{2l(2l+1)} \sum'_{mm'} (U_{mm'} - J_{mm'}) \\ &= F^0 - \frac{1}{2l} \sum_{k=2}^{2l} \left(C_{n0,l0}^{l0} \right)^2 F^k, \end{aligned} \quad (11)$$

where the primed sum is over $m' \neq m$. Equation (11) allows us to establish the following relation between the average exchange integral J and Slater integrals:

$$J = \frac{1}{2l} \sum_{k=2}^{2l} \left(C_{n0,l0}^{l0} \right)^2 F^k, \quad (12)$$

or explicitly

$$\begin{aligned} J &= \frac{1}{14} (F^2 + F^4) \quad \text{for } l = 2, \\ J &= \frac{1}{6435} (286F^2 + 195F^4 + 250F^6) \quad \text{for } l = 3. \end{aligned} \quad (13)$$

The meaning of U has been carefully discussed by Herring [24]. In, for example, an f electron system with nf electrons per atom, U is defined as the energy cost for the reaction

$$2(f^n) \longrightarrow f^{n+1} + f^{n-1}, \quad (14)$$

that is, the energy cost for moving an f electron between two atoms where both initially had nf electrons. It should be emphasized that U is a renormalized quantity which contains the effects of screening by fast s and p electrons. The number of these delocalized electrons on an atom with $n+1f$ electrons decreases, whereas their number on an atom with $n-1f$ electrons increases. The screening reduces the energy cost for the reaction given by (14). It is worth noting that because of the screening the value of U in L(S)DA+ U calculations is significantly smaller than the bare U used in the Hubbard model [25, 26].

Some aspects of currently used LDA+ U formulation and, in particular, of the determination of the parameters entering the model have been so far tied to the LMTO approach. The reformulation of the method for different basis sets has been made recently [27–29]. Pickett et al. [27] present a reformulation of the LDA+ U method based on a local-orbital expansion (linear combination of atomic orbitals). The implementation of the LDA+ U method by Bengone et al. [28] is based on the projector augmented wave (PAW) method [30], an efficient all-electron method without shape approximations on the potential or electron density. Based on a Car-Parrinello-like formalism [31], the PAW method

allows complex relaxations and dynamical properties in strongly correlated systems. Cococcioni and De Gironcoli [29] reexamine the LDA+ U method in the framework of a plane-wave pseudopotential approach (PWPP). A simplified rotational-invariant formulation was adopted. They demonstrate the accuracy of the method, computing structural, and electronic properties of a few systems including transition and rare-earth correlated metals, transition metal monoxides, and iron silicate [29], transition metal centers $\text{Fe}_2, \text{Fe}_2^-, \text{FeO}^-$ [32], and iron heme complexes [33].

In principle, the screened Coulomb U and exchange J integrals can be determined from supercell LSDA calculations using Slater's transition-state technique [34] or from constrained LSDA calculations [27, 35, 36].

To obtain Hubbard U and exchange parameter J , Anisimov and coworkers [34, 36] propose to perform LMTO calculations in supercells in which the occupation of the localized orbitals of one atom is constrained. The localized orbitals of all atoms in the supercell are decoupled from the remainder of the basis set. This makes the treatment of the local orbitals an atomic-like problem making it easy to fix their occupation numbers and allows them to use Janak's theorem [37] to identify the shift in the corresponding eigenvalue with the second-order derivative of the LDA total energy with respect to orbital occupation. It has, however, the effect of leaving a rather artificial system to perform the screening, in particular when it is not completely intra-atomic. In elemental metallic iron, for instance, only half of the screening charge is contained in the Wigner-Seitz cell [34]. This fact, in addition to a sizable error due to the atomic sphere approximation used, could be at the origin of the severe overestimation of the computed on-site Coulomb interaction. For example, Anisimov and Gunnarsson computed the effective on-site Coulomb interaction in metallic Fe and Ce. For Ce the calculated Coulomb interaction was found to be about 6 eV in good agreement with empirical and experimental estimates ranging from 5 to 7 eV [38], while the result for Fe (also about 6 eV) was surprisingly high since U was expected to be in the range of 1-2 eV for elemental transition metals, with the exception of Ni [39, 40].

Cococcioni and De Gironcoli [29] provide an internally consistent, basis-set-independent, method based on a linear response approach for the calculation of the effective interaction parameters in the LDA+ U method. They estimate the Hubbard U in elemental iron at the experimental lattice parameter to be equal to 2.2 ± 0.2 eV in good agreement with the experimental data [39, 40].

Alternatively, the value of U estimated from the photoemission spectroscopy (PES) and X-ray Bremsstrahlung isochromat spectroscopy (BIS) experiments can be used. Because of the difficulties with unambiguous determination of U , it can be considered as a parameter of the model. Then its value can be adjusted to achieve the best agreement of the results of LDA+ U calculations with PES or optical spectra [28]. While the use of an adjustable parameter is generally considered an anathema among first principles practitioners, the LDA+ U approach does offer a plausible and practical method to approximately treat strongly correlated orbitals in solids.

2.2. Magneto-Optical Effects. Magneto-optical (MO) effects refer to various changes in the polarization state of light upon interaction with materials possessing a net magnetic moment, including rotation of the plane of linearly polarized light (Faraday, Kerr rotation) and the complementary differential absorption of left and right circularly polarized light (circular dichroism). In the near visible spectral range these effects result from excitation of electrons in the conduction band. Near X-ray absorption edges, or resonances, magneto-optical effects can be enhanced by transitions from well-defined atomic core levels to transition symmetry selected valence states.

For a crystal of cubic symmetry, where the magnetization \mathbf{M} is parallel to the z -axis, the dielectric tensor is composed of the diagonal ϵ_{xx} and ϵ_{zz} and the off-diagonal ϵ_{xy} components in the form

$$\epsilon = \begin{pmatrix} \epsilon_{xx} & \epsilon_{xy} & 0 \\ -\epsilon_{xy} & \epsilon_{xx} & 0 \\ 0 & 0 & \epsilon_{zz} \end{pmatrix}. \quad (15)$$

A complete description of the MO effects is given by the four nonzero elements of the dielectric tensor or, equivalently, by the complex refractive index $n(\omega)$

$$n(\omega) \equiv \sqrt{\epsilon(\omega)} = 1 - \delta(\omega) + i\beta(\omega) \quad (16)$$

for several normal modes corresponding to the propagation of pure polarization states along specific directions in the sample, which can be obtained by solving Maxwell's equations [41]. Two of these modes are for circular components of opposite (\pm) helicity with the wave vector $\mathbf{h} \parallel \mathbf{M}$ and have indices

$$n_{\pm} = 1 - \delta_{\pm} + i\beta_{\pm} = \sqrt{\epsilon_{xx} \pm i\epsilon_{xy}}. \quad (17)$$

The other two modes are for linear polarizations with $\mathbf{h} \perp \mathbf{M}$ [42]. One has the electric vector $\mathbf{E} \parallel \mathbf{M}$ and index $n_{\parallel} = 1 - \delta_{\parallel} + i\beta_{\parallel} = \sqrt{\epsilon_{zz}}$. The other has $\mathbf{E} \perp \mathbf{M}$ and $n_{\perp} = 1 - \delta_{\perp} + i\beta_{\perp} = \sqrt{(\epsilon_{xx}^2 + \epsilon_{xy}^2)/\epsilon_{xx}}$.

At normal light incidence the relation between the polar complex Kerr angle and the dielectric tensor components is given by the expression [43]

$$\theta + i\eta \approx \frac{-\epsilon_{xy}}{(\epsilon_{xx} - 1)\sqrt{\epsilon_{xx}}}. \quad (18)$$

X-ray magnetic circular dichroism is given by $\beta_{+} - \beta_{-}$ and is first-order in \mathbf{M} . Magnetic linear dichroism $n_{\perp} - n_{\parallel}$ (also known as the Voigt effect) is quadratic in \mathbf{M} . The Voigt effect is present in both ferromagnets and antiferromagnets, while the first order MO effects in the forward scattering beam are absent with the net magnetization in antiferromagnets.

Within the one-particle approximation, the absorption coefficient $\mu_{\lambda}^j(\omega)$ for incident X-ray of polarization λ and photon energy $\hbar\omega$ can be determined as the probability of

electronic transitions from initial core states with the total angular momentum j to final unoccupied Bloch states

$$\mu_{\lambda}^j(\omega) = \sum_{mj} \sum_{nk} \left| \langle \Psi_{nk} | \Pi_{\lambda} | \Psi_{jm_j} \rangle \right|^2 \delta(E_{nk} - E_{jm_j} - \hbar\omega) \times \theta(E_{nk} - E_F), \quad (19)$$

where Ψ_{jm_j} and E_{jm_j} are the wave function and the energy of a core state with the projection of the total angular momentum m_j ; Ψ_{nk} and E_{nk} are the wave function and the energy of a valence state in the n th band with the wave vector \mathbf{k} ; E_F is the Fermi energy.

Π_{λ} is the electron-photon interaction operator in the dipole approximation

$$\Pi_{\lambda} = -e\alpha\mathbf{a}_{\lambda}, \quad (20)$$

where α are the Dirac matrices, \mathbf{a}_{λ} is the λ polarization unit vector of the photon vector potential, with $a_{\pm} = 1/\sqrt{2}(1, \pm i, 0)$, $a_{\parallel} = (0, 0, 1)$. Here, + and - denote, respectively, left and right circular photon polarizations with respect to the magnetization direction in the solid. Then, X-ray magnetic circular and linear dichroisms are given by $\mu_{+} - \mu_{-}$ and $\mu_{\parallel} - (\mu_{+} + \mu_{-})/2$, respectively.

The Kerr effect has now been known for more than a century, but it was only in recent times that it became the subject of intensive investigations. The reason for this recent development is twofold: first, the Kerr effect gained considerable interest due to modern data storage technology, because it can be used to "read" suitably stored magnetic information in an optical manner [44], and, second, the Kerr effect has rapidly developed into an appealing spectroscopic tool in materials research. The technological research on the Kerr effect was initially motivated by the search for good magneto-optical materials that could be used as information storage medium. In the sequence of this research, the Kerr spectra of many ferromagnetic materials were investigated. An overview of the experimental data collected on the Kerr effect can be found in the review articles by Buschow [45], Reim and Schoenes [46], and Schoenes [43].

The quantum mechanical understanding of the Kerr effect began as early as 1932 when Hulme [47] proposed that the Kerr effect could be attributed to spin-orbit (SO) coupling (see also Kittel [48]). The symmetry between left- and right-hand circularly polarized light is broken due to the SO coupling in a magnetic solid. This leads to different refractive indices for the two kinds of circularly polarized light, so that incident linearly polarized light is reflected with elliptical polarization, and the major elliptical axis is rotated by the so-called Kerr angle from the original axis of linear polarization. The first systematic study of the frequency-dependent Kerr and Faraday effects was developed by Argyres [49] and later Cooper presented a more general theory using some simplifying assumptions [50]. The very powerful linear response techniques of Kubo [51] gave general formulas for the conductivity tensor which are being widely used now. A general theory of frequency dependent conductivity of ferromagnetic (FM) metals over a wide range of frequencies and

temperatures was developed in 1968 by Kondorsky and Vediaev [52].

The main problem afterward was the evaluation of the complicated formulas involving MO matrix elements using electronic states of the real FM system. With the tremendous increases in computational power and the concomitant progress in electronic structure methods, the calculation of such matrix elements became possible, if not routine. Subsequently much earlier, simplified calculations have been shown to be inadequate, and only calculations from “first principles” have provided, on the whole, a satisfactory description of the experimental results [53]. The existing difficulties stem either from problems using the local spin density approximation (LDA) to describe the electronic structure of FM materials containing highly correlated electrons or simply from the difficulty of dealing with very complex crystal structures. For 15 years after the work of Wang and Callaway [53] there was a lull in MO calculations until MO effects were found to be important for magnetic recording and the computational resources had advanced. Different reliable numerical schemes for the calculation of optical matrix elements and the integration over the Brillouin zone have been implemented, giving essentially identical results [54]. Prototype studies have been performed using modern methods of band theory for Fe, Co, and Ni [55–59]. Following the calculations for the elemental $3d$ ferromagnets, a number of groups have evaluated the MO and XMCD spectra for more interesting compounds [10, 60–88] and multilayers [89–102].

3. Iron Oxides

3.1. Cubic Fe_3O_4 . The problem of a theoretical description of metal-insulator transitions has a challenging history of almost 70 years. It was first addressed by Verwey, de Boer, and Peierls in the late 1930s; they pointed out the extremely important role of electron-electron correlations in a partially filled d electron band in transition metal oxides [103, 104], for example, nickel oxide (NiO) and magnetite (Fe_3O_4). In both systems the metal-insulator transition occurs, violating the Bloch-Wilson band-insulator concept, the only one known at that time [105–108]. These earlier observations launched the long and continuing history of the field of strongly correlated electrons. In the past 80 years, much progress has been achieved from both theoretical and experimental sides in understanding strongly correlated electrons and metal-insulator transitions [2]. However, the charge ordering proposed by Verwey behind the metal-insulator transition [9, 109, 110] in Fe_3O_4 remains at the focus of active debate [111, 112].

Historically, magnetite, discovered before 1500 B.C., is the first known magnet and is extensively used for industrial applications, notably in magnetic recording. Most of the properties of magnetite have been thoroughly studied and are well documented [113, 114]. However, the electronic structure of Fe_3O_4 as well as that of many other MIT compounds is still a subject of debate [115–119].

Fe_3O_4 is a strongly correlated $3d$ compound which is ferrimagnetically ordered below a high transition temper-

ature (~ 850 K). The valence of various atoms is described by the formal chemical formula, $Fe_A^{3+}[Fe^{2+}Fe^{3+}]_B(O^{2-})_4$. The tetrahedral lattice sites (A sites) in the inverse spinel structure are occupied by Fe^{3+} ions, whereas the octahedral lattice sites (B sites) are occupied alternately by equal numbers of Fe^{2+} and Fe^{3+} . At $T_V = 120$ K Fe_3O_4 undergoes a first-order phase transition (Verwey transition) [9]. This is a particular MIT that has been studied for quite some time [120]. The Verwey transition is characterized by an abrupt increase in the electrical conductivity by two orders of magnitude on heating through T_V [121–123]. Verwey and co-workers [9, 110] were the first to point out that this transition is associated with an electron localization-delocalization transition. The Fe^{2+} ion can be regarded as an “extra” electron plus an Fe^{3+} ion. When all B sites are equivalent, the “extra” electron is moving between Fe_B^{3+} ions and the system is a mixed-valent metal, with average Fe_B -valence, $Z = 2.5$. The Verwey phase transition below T_V is accompanied by long-range charge ordering (LRCO) of Fe^{3+} and Fe^{2+} ions on $B1$ and $B2$ sites of the B sublattice. Indeed, studies by electron and neutron diffraction and nuclear magnetic resonance [124–126] show that below T_V the $B1$ and $B2$ sites are structurally distinguishable with the crystal structure slightly distorted because of the charge ordering. Just how these charges arrange themselves has been the subject of debate [120] since Verwey first proposed that, below T_V , all Fe_B^{3+} and Fe_B^{2+} sit on different chains [9].

The electronic structure of Fe_3O_4 has been investigated experimentally by means of soft X-ray spectroscopy [127–129], Seebeck-effect measurements [130, 131], photoelectron spectroscopy [132–139], optical [140, 141] and MO spectroscopies [142–149], and magnetic dichroism [150, 151]. The optical data [141] indicate a gap of 0.14 eV between occupied and empty electronic states and also show a strong temperature dependence of the optical conductivity in the energy region of 0 to 1 eV.

The interpretation of the optical and MO spectra of Fe_3O_4 is very difficult due to the existence of three kinds of iron atoms, that is, Fe_B^{2+} , Fe_B^{3+} , and Fe_A^{3+} . The substitution for one of the types of iron ions by nonmagnetic ions provides a possibility for distinguishing transitions from various sites. There are several such experimental studies in the literature. Simsa and coworkers reported the polar Kerr rotation and ellipticity of Fe_3O_4 as well as the influence of a systematic substitution of Fe^{2+} by Mn^{2+} in the 0.5–3.0 eV energy range [144, 145]. Zhang and coworkers reported the polar Kerr spectra and the off-diagonal element of the dielectric tensor of Fe_3O_4 between 0.5 and 4.3 eV. They also reported spectra of $Li_{0.5}Fe_{2.5}O_4$ and $MgFe_2O_4$ between 0.5 and 5.0 eV [142]. Finally, recent investigation of the optical and MO spectra of Fe_3O_4 and Al^{3+} and Mg^{2+} substitution has been carried out in [143].

Energy band structure calculations for Fe_3O_4 in the high-temperature cubic phase have been presented in [152] using the self-consistent spin-polarized augmented plane wave method with the local spin-density approximation. The calculations show that Fe_3O_4 is a half-metallic ferrimagnet. The Fermi level crosses only the minority-spin energy bands consisting of t_{2g} orbitals on the $Fe(B)$ sublattice. There is an

energy gap for the majority-spin bands at the Fermi level. A similar energy band structure of Fe_3O_4 was obtained in [153] using the LMTO method. The energy band structure for charge ordering in the low-temperature phase of Fe_3O_4 has been calculated in [10, 11, 154, 155] using the LMTO method in the LSDA+ U approximation.

3.1.1. Crystal Structure and Charge Ordering. Fe_3O_4 crystallizes in the face-centered cubic (FCC) inverse spinel structure (Figure 1) with two formula units (14 atoms) per primitive cell. The space group is $Fd\bar{3}m$ (no. 227). The oxygen atoms form a close-packed face-centered cubic structure with the iron atoms occupying the interstitial positions. There are two types of interstitial sites both occupied by the iron atoms. One site is called the *A* or $8a$ site, tetrahedrally coordinated by four O^{2-} ions composing a diamond lattice. The interstices of these coordination tetrahedra are too small for larger Fe^{2+} ions, and this site is occupied only by Fe^{3+} ions. Another cation site is called the *B* or $16d$ site, and is coordinated by six O^{2-} ions forming slightly distorted octahedra, which line up along the $\langle 110 \rangle$ axes of the cubic lattice sharing edges. The point symmetry of the *B* site is $D3d$. This site forms exactly one-half of a face-centered cubic lattice. The lattice of the *B* site can be considered as a diamond lattice of cation tetrahedra, sharing corners with each other. All the tetrahedra on the same (e.g., xy) plane are isolated. In the following, we refer to b_1 axes or b_1 chains and b_2 axes or b_2 chains. The b_1 direction is $[1\bar{1}0]$, b_2 is $[110]$ and the c -axis is $[001]$. All the Fe octahedral or *B* sites lie on either b_1 or b_2 chains. It should be mentioned also that the distances $\text{Fe}_A\text{-O}_1$ and $\text{Fe}_B\text{-O}_2$ are different and equal to 1.876 and 2.066 Å, respectively.

Details concerning the mechanism of the Verwey transition and the type of LRCO are still unclear. Many elaborate theories for the Verwey transition have been proposed. Anderson [156] pointed out the essential role of short-range charge ordering (SRCO) in the thermodynamics of the transition. The observed entropy change in the transition $[(\sim 0.3 \text{ to } 0.35)R/B\text{-site mole}]$ is decisively smaller than the $R \ln 2 = 0.69R$ expected in a complete order-disorder transition. Anderson interpreted the Verwey transition as a loss of the LRCO of the “extra” electrons on the *B* sublattice at temperatures above T_V , while the short-range charge order is maintained across the transition. Using a Hartree-Fock analysis, Alben and Cullen and Callen [157–159] showed that an ordering transition could occur in Fe_3O_4 as a function of the ratio V/B , where B is the bandwidth of the “extra” electrons in the absence of disorder. The transition in this case is of second order, while experimentally a first-order transition is observed. The conduction mechanisms in Fe_3O_4 have been reviewed by Mott [160–162] (see also [120, 163]). A basic problem concerning magnetite is that both the localization of the valence states and the mixing of the oxygen p states and iron d states are considerable.

In the disordered high-temperature phase the *B* sites are occupied by equal numbers of Fe^{2+} and Fe^{3+} ions randomly distributed between B_1 and B_2 sites. Below T_V the system undergoes a first-order transition accompanied by long-range charge ordering of Fe^{3+} and Fe^{2+} ions on the *B* sites.

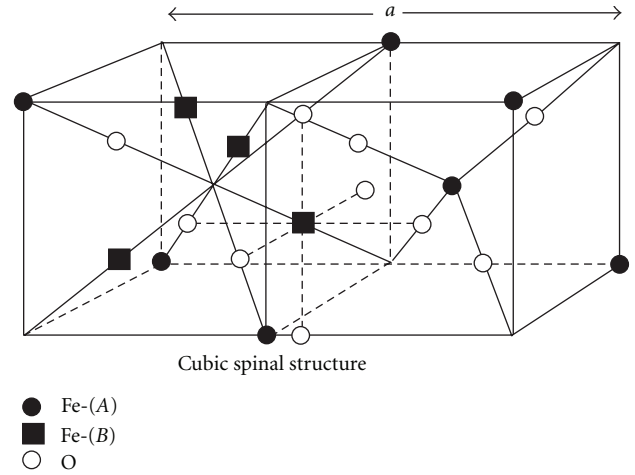


FIGURE 1: Crystal structure of Fe_3O_4 .

Verwey from the very beginning proposed a rather simple charge separation: b_1 chains occupied only by Fe^{2+} ions and b_2 chains by Fe^{3+} ions (or vice versa) [9]. Since that time the type of charge ordering has been the subject of debate [120]. As an example, in Mizoguchi’s model [164, 165] ions run in pairs of Fe^{2+} followed by Fe^{3+} along each b chain. Another charge ordering considers three Fe^{2+} alternating with one Fe^{3+} on one half of the chains, and a sequence of three Fe^{3+} alternating with one Fe^{2+} on the other half and so on [120]. Despite the wealth of effort devoted to investigating the low-temperature phase of magnetite, there is still no completely satisfactory description of the ordering of the Fe atoms on the octahedral or *B* sites in this spinel structure. In addition some experimental measurements disproved the orthorhombic Verwey CO model. These experiments have clearly established the rhombohedral distortions of the cubic unit cell first detected by Rooksby et al. from X-ray powder diffraction [166, 167]. Furthermore, observations of superstructure reflections revealed half-integer satellite reflections, indexed as $(h, k, l + 1/2)$ on the cubic unit cell, which points to a doubling of the unit cell along the c -axis and shows the symmetry to be monoclinic [168, 169]. The observation of monoclinic lattice symmetry was also confirmed by a single-crystal X-ray study [170], whereas the observation of a magnetoelectric effect indicated even lower $P1$ symmetry in the low-temperature phase [171]. Although clear evidence of the monoclinic lattice symmetry below T_V was obtained, small atomic displacements have not been fully resolved so far. The absence of a definitive, experimentally determined structure gives rise to many theoretical models proposed for the low-temperature (LT) phase of magnetite [172]. In particular, purely electronic [158, 159, 164, 173] and electron-phonon [174–176] models for CO, as well as a bond-dimerized ground state without charge separation [177], have been proposed.

Recent bond-valence-sum analysis [178] of high-resolution neutron and X-ray powder diffraction data results in a small charge disproportion of only $0.2\bar{e}$ between Fe_B cations with the 2+ and 3+ formal valency [111, 179]. This

interpretation has been the subject of much controversy [112, 180]. However, the smallness of the charge-order parameter was reproduced in an electronic structure study of the refined low-temperature crystal structure using the local-spin-density approximation (LSDA)+ U method [181, 182]. In particular, a more complicated charge-ordering pattern inconsistent with the Verwey CO model was obtained. In addition to that, the t_{2g} occupancy self-consistently obtained in the LSDA+ U calculations is strongly modulated between the Fe_B^{2+} and Fe_B^{3+} cations, yielding a distinct orbital order with an order parameter that reaches 70% of the ideal value [181]. Since no direct experimental confirmation of this charge- and orbital-order pattern is so far available, the interpretation of these results is still open to debate. However, this behavior seems to be universal and has recently been found in several other charge-ordered mixed-valent systems [182–186].

In order to check the pertinence of the CO model obtained self-consistently in [181], authors of [187] carried out a detailed theoretical study of exchange coupling constants, optical conductivity, magneto-optical (MO) Kerr effect, and X-ray absorption at the O K edge of low-temperature Fe_3O_4 and compared the results of the calculations to the available experimental data.

3.1.2. LSDA Band Structure. Figure 2 shows the partial density of states of Fe_3O_4 obtained from the LSDA calculation. The occupied part of the valence band can be subdivided into several regions separated by energy gaps. The oxygen $2s$ bands, which are not shown in the figure, appear between -20.0 and -19.7 eV for both spins with the exchange splitting of about 0.2 eV. The next group of bands in the energy region -7.4 to -3.4 eV is formed mostly by oxygen $2p$ states. The Fe d energy bands are located above and below E_F at about -4.0 to 3.0 eV. As indicated from Figure 2, the exchange splitting between the spin-up and spin-down d electrons on the Fe atom is about 3.5 eV. In addition to the exchange splitting, the five d levels of the Fe atom are split due to the crystal field. At the A site (T_d point symmetry) in the spinel structure the crystal field causes the d orbitals to split into a doublet e ($3z^2 - 1$ and $x^2 - y^2$) and a triplet t_2 (xy , yz , and xz). The octahedral component of the crystal field at the B site is strong enough that the t_{2g} (xy , yz , and xz) and e_g ($3z^2 - 1$ and $x^2 - y^2$) orbitals form two separate nonoverlapping bands. At the B site the crystal field is trigonal ($D3d$), as a result the t_{2g} orbitals split into a singlet a_{1g} and a doublet e'_g . However, the $a_{1g} - e'_g$ splitting of the t_{2g} band is negligible in comparison with its width in LSDA calculations; therefore, in the following we will denote the states formed by a_{1g} and e'_g orbitals as t_{2g} states. Accordingly, we present in Figure 2 the DOS of “ t_{2g} ” orbitals as a sum of the a_{1g} and e'_g ones. The crystal-field splitting Δ_{CF} is approximately 2 eV for the Fe_B atom and 1 eV for the Fe_A atom. This difference may be attributed to the large covalent mixing of the Fe_B orbitals with its six nearest neighbors of the same kind. The spin-polarized calculations show that Fe_3O_4 in the high-temperature phase is a half-metallic ferrimagnet. The Fermi level crosses only

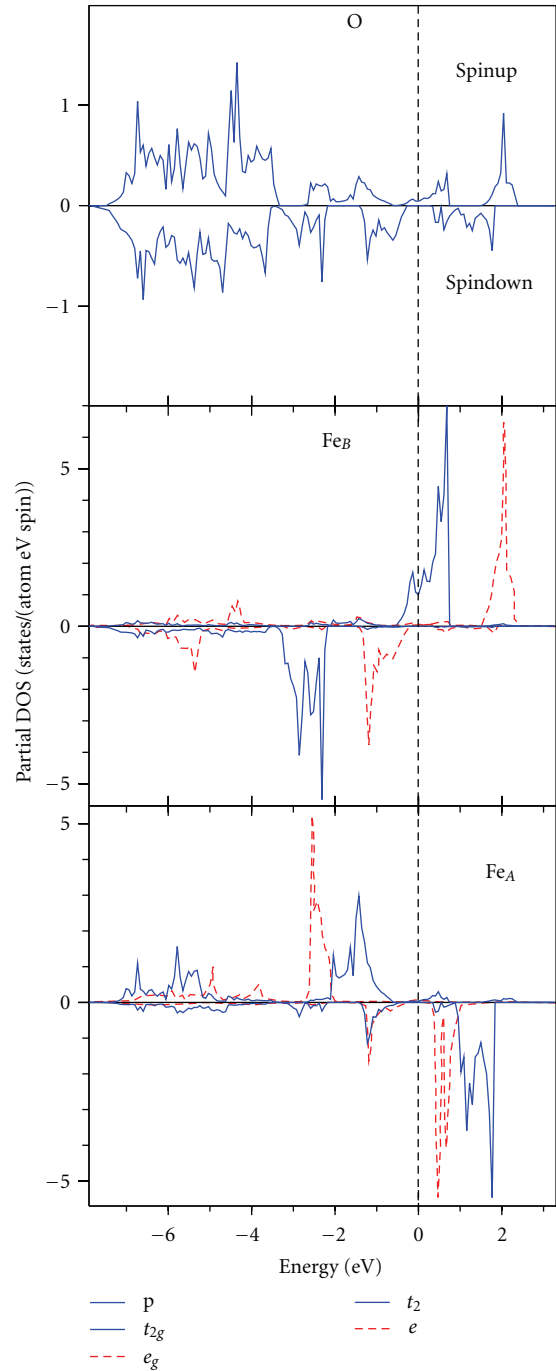


FIGURE 2: LSDA partial DOS of Fe_3O_4 [10].

the majority spin energy bands, consisting of spin-up t_{2g} orbitals on the Fe_B sublattice (Figure 2). There is an energy gap for the minority spin bands at the Fermi level. Spin-orbit splitting of the d energy band at Γ is about 0.02 eV and much smaller than the crystal-field splitting.

In Fe_3O_4 the magnetic moments within the A and the B sublattices are ferromagnetically aligned while the two sublattices are antiferromagnetic with respect to each other. This magnetic structure was first proposed by Neel [188]

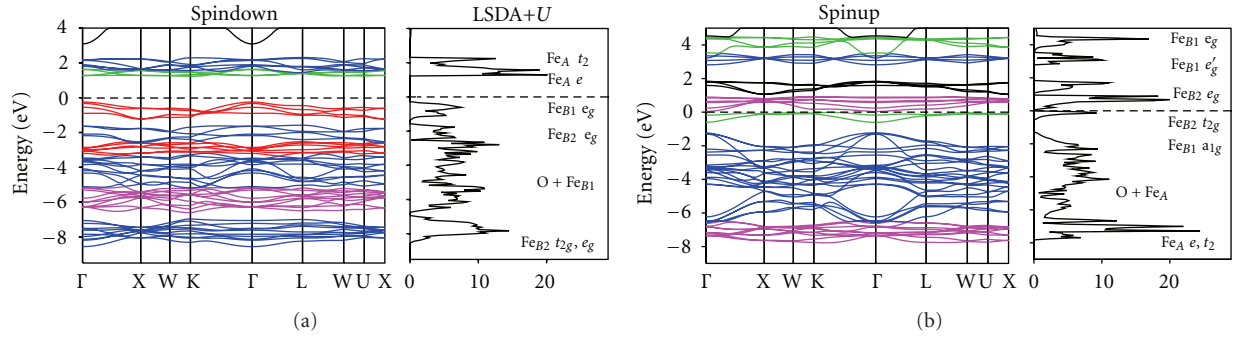


FIGURE 3: LSDA+ U energy band structure and total DOS (in states/(unit cell eV)) of Fe_3O_4 [10].

to explain the magnetization data and was later confirmed by neutron scattering measurements [189]. Measurements indicated that the magnetic moment of an iron atom on the A site is much smaller than the $5.0 \mu_B$ of a pure Fe^{3+} ion [190]. This is an indication of strong hybridization between the $3d$ orbitals of Fe_A . The orbital magnetic moment is rather small for all the atoms due to small spin-orbit coupling.

3.1.3. LSDA+ U Band Structure. The application of LSDA calculations to Fe_3O_4 is problematic, because of the correlated nature of d electrons in this compound. The intersite Coulomb correlation is well described by the LSDA. However, the on-site Coulomb interaction, which is a driving force for Mott-Hubbard localization, is not well treated within LSDA. As a result, LSDA gives only a metallic solution without charge ordering. The LSDA+ U calculations [10] started from a $d^5(t_{2g}^3, e_g^2)$ configuration for Fe_A^{3+} ions on the tetrahedral site of the sublattice A and $d^6(t_{2g}^3, e_g^2, a_{1g}^1)$ and $d^5(t_{2g}^3, e_g^2)$ for Fe_B^{2+} and Fe_B^{3+} ions on octahedral site of the sublattices B_1 and B_2 , respectively. U_{eff} was applied to all the d states, and the occupation numbers were obtained as a result of the self-consistent relaxation.

Figures 3 and 4 show the energy band structure along the symmetry lines and the total and partial density of states obtained from the LSDA+ U calculation. In contrast to LSDA, where the stable solution is a metal with a uniform distribution of the t_{2g} electrons on the B octahedral sites, the LSDA+ U gives a charge-ordered insulator with a direct energy gap value of 0.19 eV at the Γ point. The experimental optical measurements [141] gave a gap of 0.14 eV at $T = 10$ K. The energy gap occurs between the $\text{Fe}_B^{2+} a_{1g}$ (the top of valence band) and $\text{Fe}_B^{3+} t_{2g}$ (bottom of empty conduction band) states (Figure 4). Actually, the LSDA+ U band structure calculations support the key assumption that Cullen and Callen have made earlier [157–159] in proposing the one-band model Hamiltonian, where it was assumed that the “extra” electron moves in the a_{1g} band split off below the rest of the d bands of other symmetries. Two electrons at the $\text{Fe}_B^{2+} a_{1g}$ orbitals situated in the close vicinity of the Fermi level are mostly localized. Other electrons at the B_1 site are well hybridized with oxygen p -electrons (Figure 4). The screening of the Coulomb interaction in Fe_3O_4 is very effective and the system is close to the metallic state. Even a small

change in the ratio $(\text{Fe}^{2+}/\text{Fe}^{3+})_{\text{oct}}$. (which can be modeled by changing of the occupation numbers of the a_{1g} orbital at the B_1 and B_2 sites in the framework of the “virtual crystal approximation”) leads to the closing of the energy gap and a suppression of the metal-insulating transition [10].

3.1.4. Optical and MO Properties. After the consideration of the above band structure properties, we turn to the optical and MO spectra. In Figure 5 experimental optical reflectivity and the diagonal part of the dielectric function ϵ_{xx} of Fe_3O_4 are compared to the theoretical ones calculated within the LSDA and LSDA+ U approaches. Better agreement between the theory and the experiment was found when the LSDA+ U approximation was used. As was mentioned above, the LSDA theory produces the metallic solution and, therefore, gives a wrong asymptotic behavior for the optical reflectivity and the dispersive part of the dielectric function $\epsilon_{1,xx}$ as $\omega \rightarrow 0$. In Figure 6 we show the calculated and experimental absorptive part of the diagonal optical conductivity spectra $\sigma_{1,xx}$ in a wide energy range. The characteristic features of the LSDA calculation of $\sigma_{1,xx}$ is an erroneous peak at 1.9 eV which is absent in the experimental measurement. The absence of this peak in the experiment indicates that the LSDA calculations produce incorrect energy band positions. Accounting for the Coulomb repulsion U_{eff} strongly influences not only the electronic structure but also the calculated optical spectra of Fe_3O_4 . The LSDA+ U calculations make better job in describing the optical spectra of Fe_3O_4 than the LSDA approach (see Figures 5 and 6). The calculated optical conductivity spectrum (Figure 6) can be sorted into the following groups of interband transitions: (1) the interband transitions between the Fe $3d$ bands below 2.5 eV, (2) the transitions from O $2p$ to Fe $3d$ bands in the region of 2.5 to 9 eV, and (3) Fe $3d \rightarrow 4p$ and O $2p \rightarrow \text{Fe}$ $4s$ interband transitions above 9 eV. To avoid misunderstanding, we should mention that here and in the following when talking about $d \rightarrow d$ transitions we mean that the energy bands involved in the transitions have predominantly d character; however, the contribution of p or f states to these bands is sufficient to provide a significant transition probability through optical dipole matrix elements.

Let us consider now the magneto-optical properties of Fe_3O_4 . In Figure 7 we show the experimentally measured

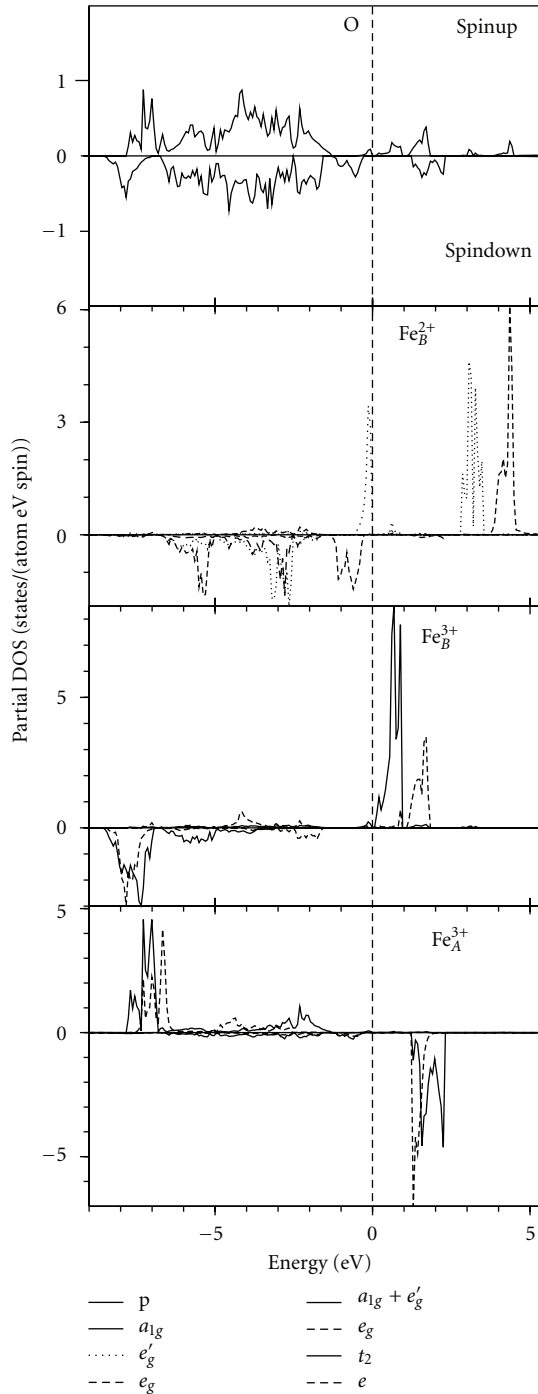


FIGURE 4: LSDA+U partial DOS of Fe_3O_4 [10].

[146] Kerr rotation $\theta_K(\omega)$ and Kerr ellipticity $\epsilon_K(\omega)$ MO spectra of Fe_3O_4 , as well as the off-diagonal parts of the dielectric function calculated with the LSDA and LSDA+U approximations [10]. This picture clearly demonstrates that the better description is achieved with the LSDA+U approach.

One should mention that, although the $\text{O } 2p \rightarrow \text{Fe } 3d$ interband transitions, which start already from about 2.5 eV, play an important role in the formation of the optical

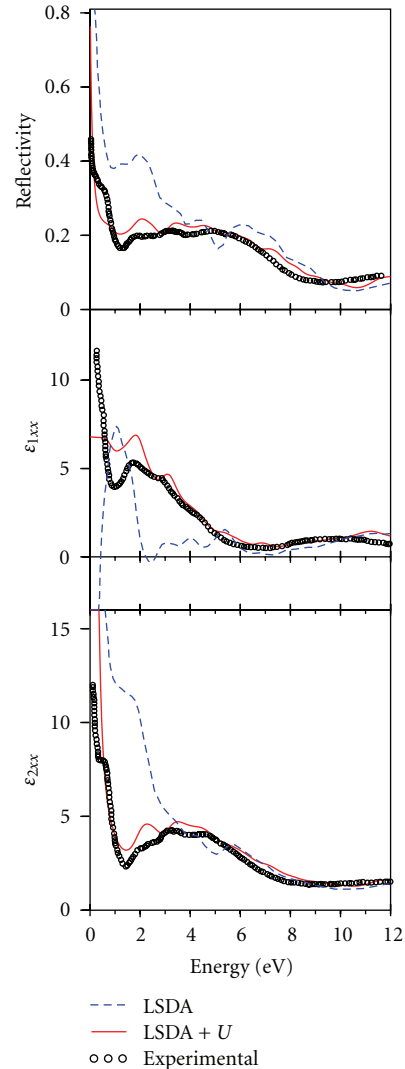


FIGURE 5: Optical reflectivity and diagonal parts of the dielectric function ϵ_{xx} of Fe_3O_4 calculated in the LSDA and LSDA+U approximation [10] compared with experimental data [140] (open circles).

spectra of Fe_3O_4 , the Kerr spectra are mostly determined by transitions between energy bands which have predominantly Fe 3d character. The reason for this is that the spin-orbit and exchange splitting of O 2p states is much smaller in comparison with the Fe 3d ones. The minimum in the Kerr rotation spectrum at 0.9 eV is due to the $\text{Fe}_B^{2+}(a_{1g1}) \rightarrow \text{Fe}_B^{3+}(t_{2g1})$ interband transitions. The second maximum at about 2 eV is associated with the $\text{Fe}_B^{2+}(a_{1g1}) \rightarrow \text{Fe}_B^{3+}(e_{g1})$ interband transitions. The minimum in the Kerr rotation spectrum between 3 and 4 eV can be associated with the $\text{Fe}_B^{3+}(e_{g1}) \rightarrow \text{Fe}_A^{3+}(e_1, t_{21})$ transitions.

All the experimental measurements of the Kerr spectra of Fe_3O_4 [142–147] have been performed at *room temperature*. The LSDA+U calculations, in comparison with the LSDA ones, describe better the electronic structure, optical and MO properties not only in the low-temperature semiconducting phase but also in the high-temperature metallic phase of

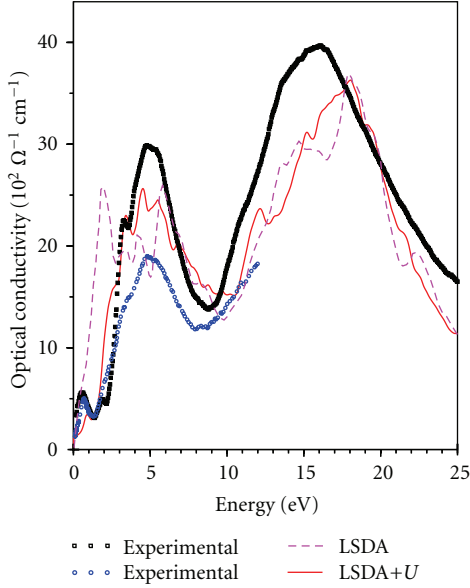


FIGURE 6: The absorptive part of the diagonal optical conductivity of Fe_3O_4 calculated in LSDA (dashed line) and LSDA+ U (solid line) approximations [10] compared with experimental data [141] (solid squares) and [140] (open circles).

Fe_3O_4 . This leads to a conclusion that Fe d electrons remain “correlated” above T_v . The main effect of heating through T_v is a disappearance of the long-range charge order on the B sublattice. This leads to the rearrangement of the electronic states in a small vicinity of the Fermi level and to the closing of the energy gap. However, high-energy Hubbard bands, whose energy position is mainly determined by on-site exchange and correlation interactions, remain almost unaffected ($U_{\text{eff}} \sim 4$ to 5 eV is much larger than $T_v \sim 0.01$ eV). This picture is supported by recent optical measurements [141], which show a strong temperature dependence of the optical properties of Fe_3O_4 only in the range from 0 to 1 eV. The absolute value of the measured prominent peak in the optical absorption for photon energies around 0.6 eV determined by the $\text{Fe}_B^{2+}(a_{1g}) \rightarrow \text{Fe}_B^{3+}(t_{2g})$ interband transitions gradually decreases by about 30% when changing the temperature from 10 K to 490 K. However, the other parts of the spectrum change very little.

Finally, we would like to point out that, while the LSDA+ U approach does a better job than the LSDA in the treatment of correlation effects, it is still unclear how well it performs in evaluating the subtle energies and interactions affecting the charge-ordered ground state and the higher-temperature short-range ordered states.

3.1.5. X-Ray Magnetic Circular Dichroism. The XMCD technique developed in recent years has evolved into a powerful magnetometry tool to separate orbital and spin contributions to element-specific magnetic moments. XMCD experiments measure the absorption of X-rays with opposite (left and right) states of circular polarization. The XMCD spectra in core level absorption are element specific and site selective,

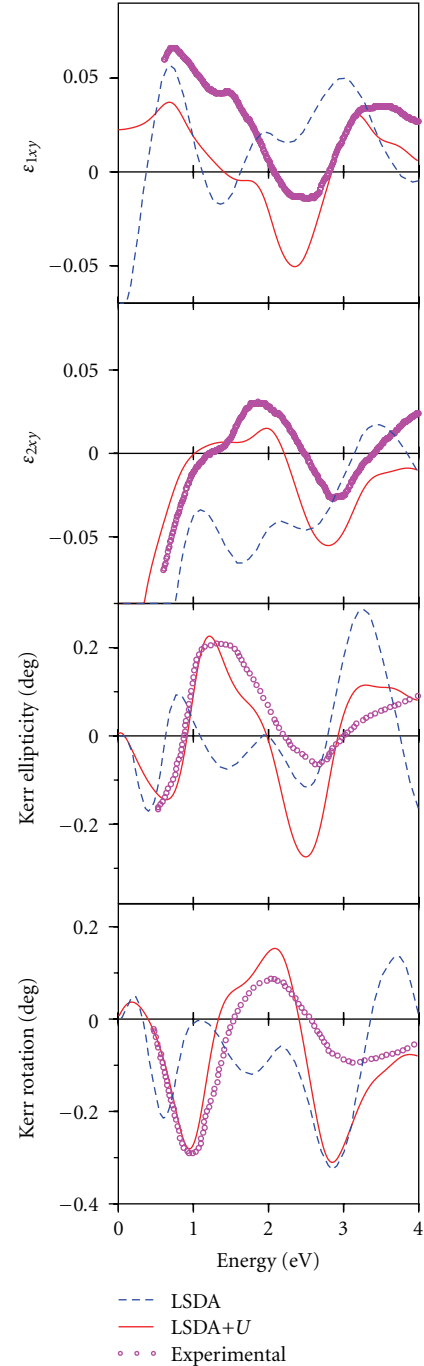


FIGURE 7: Calculated Kerr rotation and Kerr ellipticity spectra of Fe_3O_4 [10] compared with experimental data (circles) [146].

thus providing valuable information on the energy position of empty states in a wide energy interval.

The interpretation of the experimental XMCD spectra of Fe_3O_4 [150, 151] is very difficult due to the existence of three kinds of iron atoms, that is, Fe_B^{2+} , Fe_B^{3+} , and Fe_A^{3+} . The substitution for one of the types of iron ions by another transition metal ion provides a possibility for distinguishing transitions from various sites. There are several such experimental studies in the literature. Koide and coworkers reported the

XMCD spectra at the Fe $M_{2,3}$ and Co $M_{2,3}$ core-absorption edges in Fe_3O_4 and CoFe_2O_4 [151]. For Fe_3O_4 the $M_{2,3}$ prethreshold MCD spectra were measured above and below the Verwey transition temperature. Van Der Laan et al. [192] reported the XMCD spectra at the Ni $L_{2,3}$ edges of NiFe_2O_4 (trevorite). The Ni $L_{2,3}$ edge magnetic circular dichroism measurements of ferrimagnetic $\text{Zn}_x\text{Ni}_{1-x}\text{Fe}_2\text{O}_4$ ($x = 0.0, 0.26, 0.50,$ and 0.75) were reported by Pong et al. [193]. Magnetic circular dichroism is reported for $\text{Mn}_{2/3}\text{Zn}_{1/3}\text{Fe}_2\text{O}_4$ ferrite in [194] with the measurements performed on the $2p$ and $3p$ core levels of Mn and Fe. The electronic structure, spin and orbital magnetic moments, and XMCD spectra of the series Fe_3O_4 , CoFe_2O_4 , NiFe_2O_4 , and MnFe_2O_4 are presented in [191]. The XAS and XMCD spectra at K , $L_{2,3}$ and $M_{2,3}$ edges for transition metals sites were calculated.

In Figure 8 the experimentally measured Fe $L_{2,3}$ XMCD spectra [150] in Fe_3O_4 are compared to the theoretical ones calculated within the LSDA+ U approach [191]. The dichroism at the L_2 and L_3 edges is influenced by the spin-orbit coupling of the initial $2p$ core states. This gives rise to a very pronounced dichroism in comparison with the dichroism at the K edge. Two prominent negative minima of Fe L_3 XMCD spectrum are derived from iron ions at octahedral B sites. The major positive maximum is from Fe_A^{3+} ions. In the LSDA+ U calculations of the charge-ordered Fe_3O_4 , the $L_{2,3}$ XMCD spectra have slightly different shape for the Fe_B^{2+} and Fe_B^{3+} ions. The LSDA+ U calculations are not able to produce the small positive shoulder at the high-energy side of the main peaks of the Fe L_3 XMCD spectrum.

The XMCD spectra at the $L_{2,3}$ edges are mostly determined by the strength of the SO coupling of the initial $2p$ core states and spin-polarization of the final empty $3d_{3/2,5/2}$ states, while the exchange splitting of the $2p$ core states as well as the SO coupling of the $3d$ valence states are of minor importance for the XMCD at the $L_{2,3}$ edge of $3d$ transition metals [195].

To investigate the influence of the initial state on the resulting XMCD spectra, the XAS and XMCD spectra of Fe_3O_4 at the $M_{2,3}$ edge were also calculated. The spin-orbit splitting of the $3p$ core level is about one order of magnitude smaller than for the $2p$ level in Fe_3O_4 . As a result the magnetic dichroism at the $M_{2,3}$ edge is smaller than at the $L_{2,3}$ edge. In addition the M_2 and M_3 spectra are strongly overlapped, and the M_3 spectrum contributes to some extent to the structure of the total $M_{2,3}$ spectrum in the region of the M_2 edge. To decompose a corresponding experimental $M_{2,3}$ spectrum into its M_2 and M_3 parts will therefore be quite difficult in general.

In Figure 9 the experimentally measured Fe $M_{2,3}$ XMCD spectrum [151] in Fe_3O_4 is compared to the theoretical one calculated within the LSDA+ U approach [191]. In Fe_3O_4 the magnetic moments within the A and the B sublattices are ferromagnetically aligned while the two sublattices are antiferromagnetic with respect to each other. The XMCD spectra are positive at the M_3 and negative at the M_2 edge at the tetrahedral A sites and *vice versa* for the octahedral B ones. The interpretation of the experimental Fe $M_{2,3}$ XMCD spectrum is very difficult without a knowledge of the band structure and corresponding transition matrix elements

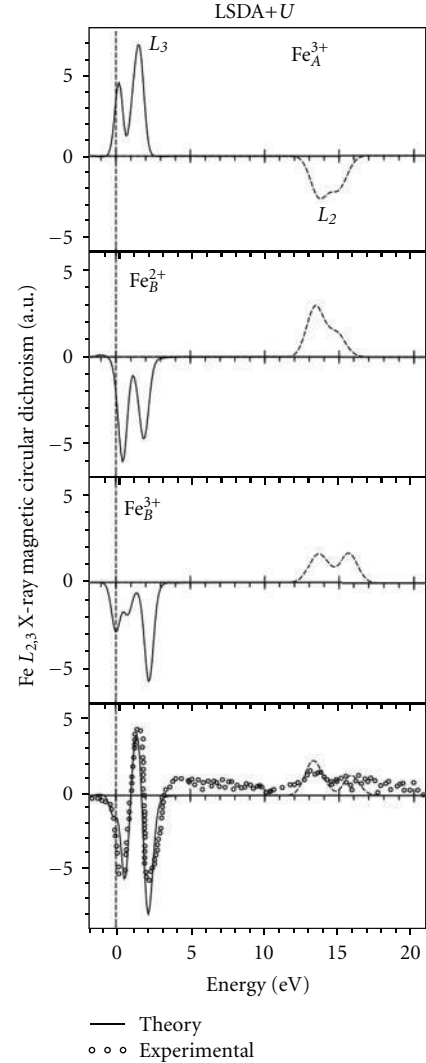


FIGURE 8: Fe $L_{2,3}$ XMCD spectra in Fe_3O_4 calculated with the LSDA+ U approximation [191] in comparison with the experimental data (circles) [150].

because this spectrum is a superposition of six $M_{2,3}$ spectra (from Fe_A^{3+} , Fe_B^{2+} , and Fe_B^{3+} sites) appearing simultaneously in a rather small energy range.

3.2. Low-Temperature Monoclinic Fe_3O_4

3.2.1. Crystal Structure. The low-temperature structure was shown to have a $\sqrt{2}a \times \sqrt{2}a \times 2a$ supercell with space group Cc from X-ray and neutron diffraction [111, 179]. However, recent structural refinement (at 90 K) was only possible in the centric monoclinic space group $P2_1/c$ with $a/\sqrt{2} \times a/\sqrt{2} \times 2a$ of the cubic spinel subcell and eight formula units in the primitive unit cell [111, 179]. Since the refinement for the $P2_1/c$ space group was found to be unstable, additional $Pmca$ orthorhombic symmetry constraints were also applied. This is equivalent to averaging the true superstructure over the additional symmetry operators; that is, each B site in the $P2_1/c$ unit cell is averaged over four nonequivalent subsites

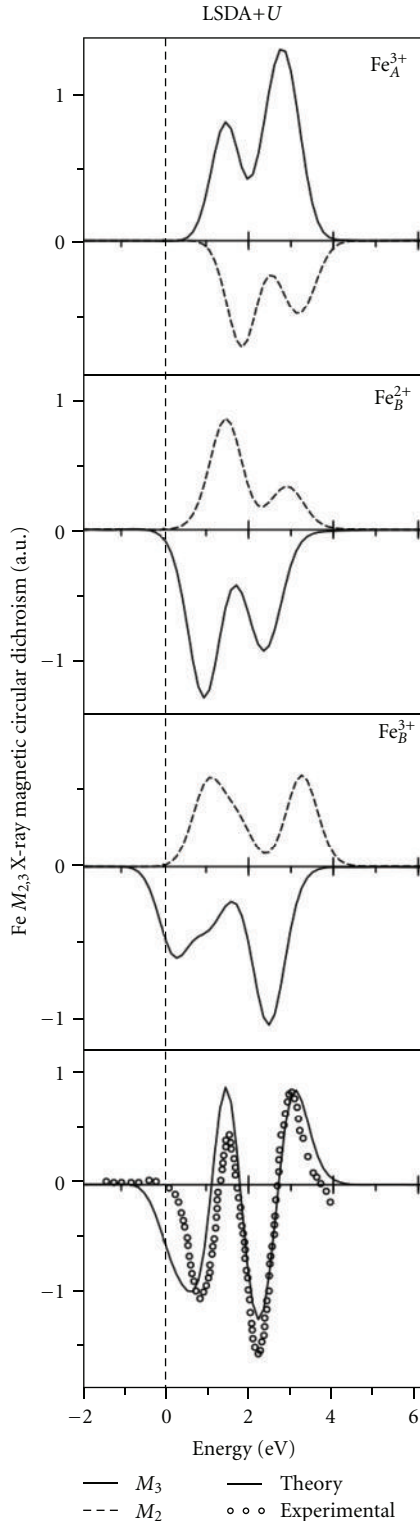


FIGURE 9: Fe $M_{2,3}$ XMCD spectra in Fe_3O_4 calculated with the LSDA+ U approximation [191] in comparison with the experimental data (circles) [151].

in the large $\sqrt{2}a \times \sqrt{2}a \times 2a$ Cc supercell. Note, however, that such an approximation is robust in the sense of smallness of any distortions from the $P2/c$ subcell to the Cc monoclinic

cell (according to [179] these are of $\sim 0.01 \text{ \AA}$). Previous structure refinement below T_V obtained by Iizumi et al. resulted in a $a/\sqrt{2} \times a/\sqrt{2} \times 2a$ subcell of the Cc unit cell and imposed orthorhombic symmetry constraints on the atomic positions [196]. In particular, a refinement based on an approximation of the true crystal structure by a centric space group $Pmca$ or polar $Pmc2_1$ was proposed. But a charge-ordered arrangement has not been identified in this refinement, although large atomic displacements of Fe and O atoms were found. This is in strong qualitative contrast to the recent structure refinement proposed by Wright et al. where clear evidence of CO below the transition has been found [111, 179].

According to the refinement the octahedral Fe_B sites are split into two groups with different values of the averaged Fe–O bond distances, with $B2$ and $B3$ sites being significantly smaller than $B1$ and $B4$ ($B1$ – $B4$ are crystallographically independent Fe_B sites according to the notation in [111, 179]). A different averaged Fe–O bond distance is a sensitive experimental indicator of the cation charge state. Quantitative analysis of the valence state of both Fe_B groups using the bond-valence-sum (BVS) method shows that the octahedral Fe_B sites fall into two clear groups with respect to the estimated value of valence. The result is a charge disproportionation of $0.2\bar{e}$ between large ($B1$ and $B4$) and small ($B2$ and $B3$) sites (which has been referred to as the class I CO model). Another possible class of CO arises from the symmetry-averaging orthorhombic constraint. There are 32 charge-ordered models which are referred to as class II CO because large ($B1$ and $B4$) and small ($B2$ and $B3$) sites could be averaged over ($3\text{Fe}^{2+} + \text{Fe}^{3+}$) and ($\text{Fe}^{2+} + 3\text{Fe}^{3+}$) subsites, respectively. The symmetry averaging results in decrease of the more pronounced charge separation of $0.4\bar{e}$ in the full Cc superstructure (class II CO) down to $0.2\bar{e}$ in the $P2/c$ subcell. The Anderson criterion is not satisfied by any of the class I or class II CO models. This is remarkable because the Anderson criterion has been widely used in many CO models [164, 173]. However, class II, as was shown from electrostatic repulsion energy estimations, appears to be more plausible than the class I arrangement.

Recently this interpretation of the refined crystal structure has been found to be controversial. The lack of atomic long-range CO and, as a result, an intermediate valence regime below the Verwey transition were proposed [112, 180]. It is argued that the difference of the average Fe–O distances between compressed and expanded FeO_6 octahedra, which could be considered as a maximum limit of charge disproportionation, has the same order as the total sensitivity (including experimental errors) of the bond-valence-sum method. This remarkable controversy shows that the understanding of the system is far from satisfactory.

3.2.2. Band Structure. In order to account for the strong electronic correlations in the Fe $3d$ shell, at least on the static Hartree-Fock level, the authors of [155] calculated the electronic structure of the LT phase of Fe_3O_4 using the LSDA+ U method. The value of the U parameter for Fe cations estimated using different experimental and theoretical techniques lies in the range of 4.5–6 eV [154, 173, 197].

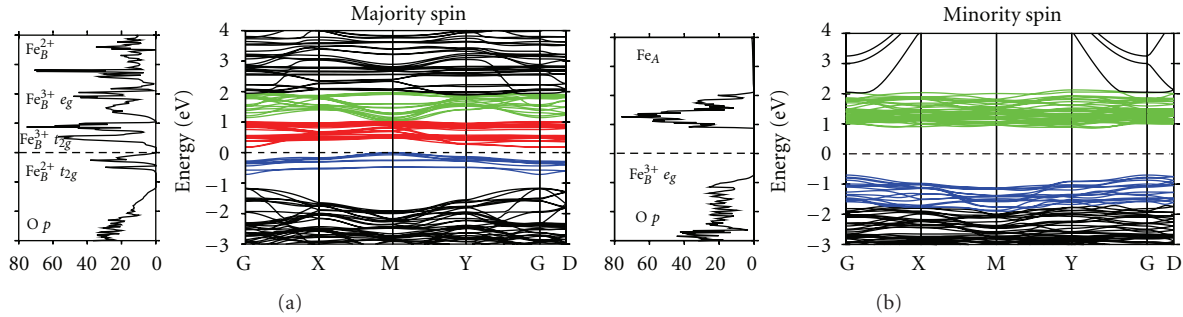


FIGURE 10: Total DOS and band structure of the $P2/c$ phase of Fe_3O_4 self-consistently obtained by the LSDA+ U with $U = 5$ eV and $J = 1$ eV [155]. The Fermi level is denoted by the horizontal line and is taken as the zero of energy. A bandgap of 0.18 eV opens between M and Γ symmetry points. The energy bands predominantly originating from the $\text{Fe}_B^{3+} t_{2g}$ and e_g states are shown in dark gray (red) and light gray (green) colors, respectively, whereas the gray (blue) color corresponds to $\text{Fe}_B^{2+} t_{2g}$ bands. For the majority spin an energy gap of ~ 2 eV opens between $\text{Fe}_B^{2+} e_g$ and Fe_A bands shown in dark gray (red) and light gray (green) colors, respectively. The corresponding contributions to the total DOS are shown (a).

A reasonably good agreement of the calculated gap value of 0.18 eV with the experimental value [141] of 0.14 eV at 10 K was obtained using the U value of 5 eV. Note, however, that the charge and orbital order derived from the LSDA+ U calculations does not depend on the exact U value when it is varied within the above-mentioned limits. The value of the Hund's coupling $J = 1$ eV was estimated from constrained LSDA calculations [27]. In the following all results presented in the paper were obtained using a U value of 5 eV.

Figure 10 shows the LSDA+ U band structure and the total DOS [155] calculated self-consistently for the low-temperature structure of Fe_3O_4 using the Coulomb interaction parameter $U = 5$ eV and exchange coupling $J = 1$ eV. The corresponding partial Fe_B 3d DOSs are shown in Figure 11. The LSDA+ U calculations give results qualitatively distinct from those of the LSDA. An indirect energy gap of 0.18 eV opens in the minority spin channel between M and Γ symmetry points. One of the minority spin t_{2g} states of Fe_{B1} and Fe_{B4} ions becomes occupied while the Fe_{B2} and $\text{Fe}_{B3} t_{2g1}$ states are pushed above the chemical potential. Although, as will be discussed below, the calculated disproportion of Fe_B 3d charges is significantly less than 1, in the following we use the notations Fe^{2+} and Fe^{3+} for $\text{Fe}_{B1,B4}$ and $\text{Fe}_{B2,B4}$ cations, respectively, having in mind the difference of their t_{2g} occupations. The top of the valence band is formed by the occupied t_{2g1} states of B1 and B4 Fe^{2+} cations. The bottom of the conduction band is formed predominantly by the empty t_{2g1} states of B2 and B3 Fe^{3+} cations. The remaining unoccupied t_{2g1} states of B1 and B4 Fe^{2+} cations are pushed by the strong Coulomb repulsion to energies above 2.5 eV. Majority-spin 3d Fe_B states are shifted below O $2p$ states, which form a wide band in the energy interval between -7 and -2 eV. This is in strong contrast with the uniform half-metallic solution obtained by the LSDA.

Bands corresponding to the Fe_A^{3+} cations are fully occupied (empty) for minority- (majority-) spin states, respectively, and already in the LSDA do not participate in the

formation of bands near the Fermi level. The LSDA+ U method does not strongly affect these bands, which lie in the energy interval of -6 eV below and 1-2 eV above the Fermi level.

3.2.3. Charge Ordering. The obtained solution for CO of Fe^{2+} and Fe^{3+} cations on the B sublattice is described by a dominant $[001]_c$ charge (and spin) density wave, which originates from alternating chains of Fe^{2+} ions on octahedral B1 sites and Fe^{3+} ions on B2 sites (see Table 1 and Figure 2 in [181]). A secondary $[001/2]_c$ modulation in the phase of CO, which is formed by the chain of alternately ‘‘occupied’’ Fe^{2+} ions on the B4 sites and ‘‘empty’’ Fe^{3+} ions on B3 sites, was found. This is consistent with a $[001]$ nesting vector instability at the Fermi surface in the Fe_B minority electron states which has been recently revealed by the LSDA calculations for the cubic phase [198]. The calculated CO scheme coincides with the class I CO model proposed by Wright et al. [111, 179]. All the tetrahedra formed by Fe_B cations have either a 3:1 or 1:3 ratio of Fe^{2+} and Fe^{3+} ions. Thus, the LSDA+ U calculations confirm that the Anderson criterion is not satisfied in the LT phase. However, it should be pointed out that the Anderson criterion was introduced under the assumption of equal interatomic distances within each tetrahedron, whereas in the distorted LT structure the iron-iron distances vary from 2.86 to 3.05 Å. The same CO pattern has been recently confirmed by other LSDA+ U calculations [182].

An analysis of the 3d minority occupation matrices of Fe_B cations confirms very effective charge disproportion within the $\text{Fe}_B t_{2g}$ minority-spin subshell. In particular, one of the t_{2g1} states of Fe_{B1}^{2+} and Fe_{B4}^{2+} cations is almost completely filled with the occupation $n \approx 0.8$. On the other hand, the other two t_{2g1} orbitals of the Fe_B^{2+} cations have significantly smaller population of about 0.04. The occupation numbers of t_{2g1} orbitals for Fe_{B2}^{3+} and Fe_{B3}^{3+} cations do not exceed 0.1–0.17, which gives a value of about 0.7 for the largest difference of the populations of Fe_B^{2+} and $\text{Fe}_B^{3+} t_{2g1}$ states. The occupation numbers of the minority-spin Fe_B 3d orbitals and the net

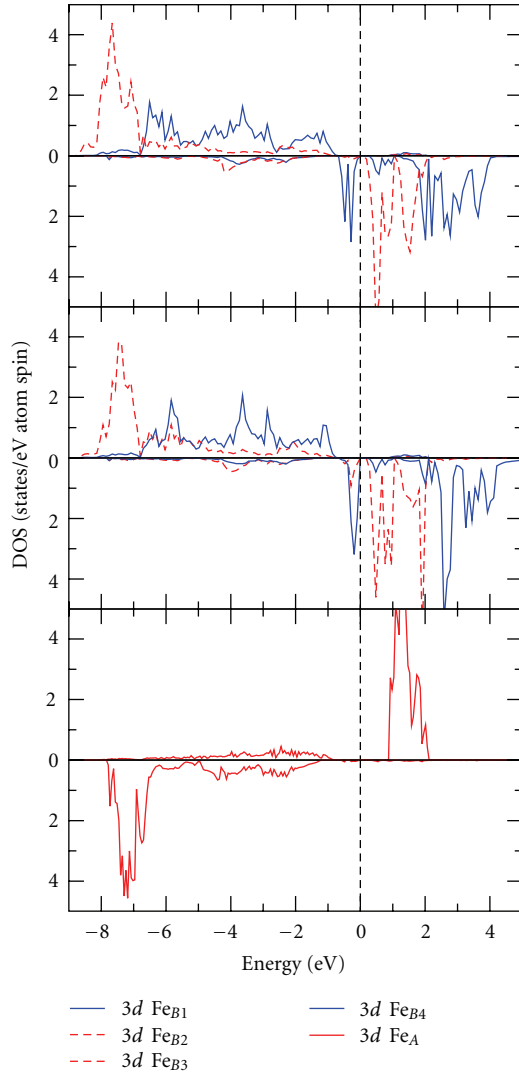


FIGURE 11: Partial DOS obtained from the LSDA+ U calculations with $U = 5$ eV and $J = 1$ eV for the $P2/c$ phase of Fe_3O_4 [155]. The Fermi level shown by dotted lines. A charge-ordered insulating solution is obtained. Fe $3d$ minority states corresponding to B1 and B4 sites are occupied (Fe^{2+}) and located just below the Fermi level, whereas B2 and B3 are empty (Fe^{3+}). The charge difference between 2+ and 3+ Fe_B cations is found to be $0.23\bar{e}$.

occupations of the t_{2g1} and e_{g1} states are given in the last two columns of Table 1.

The change of the t_{2g1} occupations caused by the charge ordering is very effectively screened by the rearrangement of the other Fe electrons. A significant contribution to the screening charge is provided by Fe_B e_g states. Although the bands originating from these states are located well above the energy gap, the minority spin e_g orbitals form relatively strong σ bonds with $2p$ states of the oxygen octahedron and, as a result, give an appreciable contribution to the occupied part of the valence band. The energy of $\text{Fe}_B^{3+} e_{g1}$ states is lower than the energy of corresponding Fe_B^{2+} states, and the former give a significantly larger contribution to the part

of the valence band formed mainly by O $2p$ states. Because of the stronger covalency of the $\text{Fe}_B^{3+} e_g$ -O p bonds, the net occupation of $\text{Fe}_B^{3+} e_{g1}$ states becomes $\sim 0.25\bar{e}$ larger (see the last column of Table 1). The resulting $3d$ charge difference (0.23) and disproportionation of the total electron charges inside the atomic spheres of Fe_B^{2+} and Fe_B^{3+} ions (0.24) are in reasonably good agreement with the value of 0.2 estimated from a BVS analysis of the $P2/c$ structure [111, 179]. The above-mentioned screening of the changes in the Fe_B t_{2g} minority occupations reduces the energy loss due to the development of charge order incompatible with the Anderson criterion in the LT phase of Fe_3O_4 .

Hence, due to the strong screening effects, the order parameter defined as the difference of the net $3d$ charges of Fe_B cations does not provide conclusive evidence for CO. This explains why the BVS analysis does not give a convincing proof of CO existence. Apparently, a well-defined order parameter is the difference of the occupations of the t_{2g} minority-spin states for Fe_B^{3+} and Fe_B^{2+} cations which amounts to 70% of the ideal ionic CO model and clearly indicates the existence of a charge-ordered ground state below the Verwey transition.

The LSDA+ U calculations were also performed for the assumption of Verwey charge order in the $P2/c$ structure [155]. However, instead of the assumed Verwey CO, the same self-consistent solution as the one described above was found. Therefore, the Verwey CO model is unstable in the distorted $P2/c$ structure. It is well known that with increasing U value localization is effectively increased. Remarkably, even for a U value increased up to 7-8 eV no Verwey-like CO pattern was found self-consistently in the distorted $P2/c$ structure. On the contrary, the LSDA+ U calculations performed for an undistorted $P2/c$ supercell of the $Fd\bar{3}m$ structure result in an insulating CO solution which is compatible with the Verwey CO model. Altogether this implies that the Verwey CO model is unstable under a structure distortion from the high-symmetry cubic into the low-symmetry $P2/c$ phase.

Also authors performed LSDA+ U calculations [155] with the same U and J parameters (5 and 1 eV, resp.) for the assumption of one of the 32 class II CO models within Cc supercell of $P2/c$, which is shown in Figure 2 in [179]. But it was found that this kind of CO is unstable and the self-consistent solution coincides with the one found previously for the $P2/c$ structure.

Comparing the LSDA+ U results for the undistorted and distorted $P2/c$ unit cells, we can conclude that the charge-ordering pattern of Fe_B^{2+} and Fe_B^{3+} cations in the LT phase of Fe_3O_4 , derived from the BVS analysis in [179] and confirmed by our study, is mainly forced by the local distortions of the crystal structure. The results of [155] consistently indicate the importance of the small amplitude of atomic displacements (almost of 0.07 Å) recently resolved by X-ray and neutron powder diffraction [111, 179]. The additional displacements leading to the Cc supercell were estimated to be of ~ 0.01 Å but have not been fully resolved so far. They also may be important for full understanding of the CO in Fe_3O_4 . In particular, in the $P2/c$ subcell the true atomic

TABLE 1: $3d$ orbital contribution to the formation of Fe_B minority spin states with occupancy n evaluated by diagonalization of the occupation matrix [155]. Although one of the t_{2g1} states of $B1$ and $B4$ sites is almost occupied with $n \geq 0.7 \bar{e}$ the t_{2g} minority spin occupancies of $B2$ and $B3$ Fe^{3+} cations are less than $0.1 \bar{e}$. The occupied t_{2g1} states of $B1$ and $B4$ Fe^{2+} cations are predominantly of $d_{xz} \pm d_{yz}$ and $d_{x^2-y^2}$ characters, respectively. The sum of t_{2g} (e_g) occupations is given in the last column.

Fe_B ion	Sym.	t_{2g}					e_g		$\sum t_{2g}$ ($\sum e_g$)
		yz	zx	$x^2 - y^2$	$3z^2 - r^2$	xy	n		
Fe_{B1a}	t_{2g}	-0.47	-0.80	0.34	0.00	-0.07	0.81	0.89	
		0.86	-0.33	0.40	-0.01	0.01	0.04		
	e_g	-0.21	0.49	0.84	-0.01	0.04	0.04		
		0.04	0.06	0.01	-0.49	-0.87	0.15		
Fe_{B1b}	t_{2g}	-0.02	-0.03	-0.02	-0.87	0.48	0.11	0.79	
		-0.47	0.83	0.28	-0.03	0.12	0.71		
	e_g	0.83	0.31	0.46	0.00	0.00	0.04		
		0.30	0.45	-0.84	0.00	0.02	0.04		
Fe_{B2a}	t_{2g}	-0.05	0.11	0.02	0.55	-0.83	0.15	0.27	
		0.01	-0.04	0.00	0.83	0.55	0.12		
	e_g	0.00	0.91	0.41	0.00	0.00	0.09		
		-0.99	0.00	0.01	0.00	0.00	0.08		
Fe_{B2b}	t_{2g}	-0.01	0.41	-0.91	-0.04	0.00	0.07	0.52	
		-0.01	0.00	0.00	0.00	0.99	0.27		
	e_g	0.00	-0.02	0.04	-0.99	0.00	0.25		
		0.00	-0.90	0.45	0.01	0.00	0.09		
Fe_{B3}	t_{2g}	-0.99	-0.01	-0.03	0.00	-0.05	0.07	0.23	
		0.03	-0.45	-0.89	-0.04	0.00	0.07		
	e_g	0.00	-0.01	-0.04	0.99	0.00	0.26		
		-0.05	0.00	0.00	0.00	0.99	0.26		
Fe_{B4}	t_{2g}	0.79	-0.18	0.53	-0.09	0.24	0.17	0.36	
		-0.22	0.73	0.63	0.13	-0.10	0.11		
	e_g	0.52	0.65	-0.55	-0.08	-0.04	0.08		
		-0.21	0.12	0.04	-0.91	0.35	0.25		
Fe_{B4}	t_{2g}	0.13	-0.11	0.11	-0.39	-0.90	0.24	0.49	
		-0.55	-0.18	0.82	-0.02	0.02	0.80		
	e_g	0.51	-0.85	0.16	0.01	-0.04	0.04		
		0.66	0.50	0.55	-0.03	0.01	0.03		
e_g	-0.01	-0.02	-0.03	-0.99	-0.12	0.13	0.25		
	-0.02	0.03	0.02	0.12	-0.99	0.11			

positions are averaged over the corresponding number of subsites in the Cc cell. Therefore, the actual arrangement of the locally Fe_BO_6 octahedra in the true Cc structure can be more complex, probably resulting in a more complicated charge and/or orbital order for the LT structure. The calculations in [155] indicate that the competition of the “elastic” and electrostatic energy contributions in the total energy appears to be responsible for the CO, which is realized in the LT structure of Fe_3O_4 [181]. Because of this, the Verwey CO model, which has the lowest electrostatic but significant “elastic” energy contribution in the total energy, becomes less favorable than other arrangements.

3.2.4. Orbital Ordering. The self-consistent solution obtained by the LSDA+ U is not only charge but also orbitally ordered. Table 1 clearly presents which presents the contribution of $3d$ cubic harmonics to the formation of Fe_B minority-spin states with an occupancy n (next to last column in

Table 1) evaluated by diagonalization of the corresponding occupation matrix self-consistently obtained by the LSDA+ U [155].

As shown in the table the most occupied Fe^{2+} $3d$ minority orbitals are centered on the $B1a$, $B1b$, and $B4$ iron sites and have $d_{xz} - d_{yz}$, $d_{xz} + d_{yz}$, and $d_{x^2-y^2}$ characters, respectively. Remarkably, the occupied t_{2g1} orbitals of Fe_B cations are almost orthogonal to each other; that is, their relative orientation corresponds to an anti-ferro-orbital order. Since all Fe_B cations are ferromagnetically coupled the obtained orbital order conforms with the anti-ferro-orbital ferromagnetic state, which is the ground state of the degenerate Hubbard model according to the Kugel-Khomskii theory [199, 200]. This orbital order is consistent with the corresponding distortions of FeO_6 octahedra. In particular, using simple considerations which take into account only the change of the Fe–O bond lengths and neglect the bending of the bonds, it was previously concluded that the calculated

orbital order is mainly determined by the distortions of oxygen octahedra surrounding Fe_B sites [183].

Also this simple analysis shows a remarkable difference between Fe_{B1}^{2+} and Fe_{B4}^{2+} cations; namely, the average Fe_{B1a} –O distance in the plane of occupied $d_{xz} - d_{yz}$ orbital is 2.087 Å, whereas in the planes of two other t_{2g} orbitals they are only 2.063 and 2.067 Å. This difference between the average cation-anion distance in the planes of occupied and unoccupied orbitals is remarkably larger for $\text{Fe}_{B1a,b}$ (more than 0.02 Å), although for Fe_{B4} they are 2.074 and 2.067 Å for occupied $d_{x^2-y^2}$ and unoccupied $d_{xz} \pm d_{yz}$ orbitals, respectively, which gives a difference of only 0.007 Å. This small difference can be changed by applying a uniaxial stress to the $P2/c$ unit cell resulting in modification of the electronic properties [201]. In particular, a few percent of magnitude elongation of the $P2/c$ unit cell along the c -axis with simultaneous (in order to preserve the same unit cell volume) compression in the ab plane gives rise to orbital-order crossover on the Fe_{B4} site from a $d_{x^2-y^2}$ to a d_{xz} occupied orbital. At the same time the charge order and occupied orbitals on the $\text{Fe}_{B1a,b}$ sites remain the same. The pressure-induced spatial reorientation of the occupied $\text{Fe}_{B4} t_{2g}$ orbital was proved by the LSDA+ U calculations for the strained $P2/c$ unit cell. Note, however, that these rough estimations do not take into account the elastic anisotropy in Fe_3O_4 . Moreover, the analysis was performed for the “averaged” $P2/c$ structure. However, they provide insight into the orbital-ordering phenomena behind the Verwey transition in magnetite as well as the problem of an external parameter-controlled electron state (e.g., orbital ordering) in solids [202].

3.2.5. Magnetic Moments. The strong variation of the occupancies of the minority-spin $\text{Fe}_B t_{2g}$ states leads to a pronounced modulation of the spin magnetic moments on the B sublattice. While the total moment per formula unit remains at $4 \mu_B$, the magnetic moments of the $\text{Fe}^{2+} B1$ ($3.50 \mu_B$) and $B4$ ($3.48 \mu_B$) cations become appreciably smaller than Fe_{B2} ($3.94 \mu_B$) and Fe_{B3} ($3.81 \mu_B$) moments. The $[001]_c$ charge and spin modulation on the B sublattice is accompanied by formation of a weak spin modulation on the oxygen ions caused by different strengths of the hybridization of O $2p$ states with the minority-spin $3d$ states of Fe_B^{2+} and Fe_B^{3+} ions. In particular, the oxygen magnetic moment reaches its maximal value of $\sim 0.1 \mu_B$ for O3 and O4 ions, which lie in the plane of Fe_{B2}^{3+} cations. It substantially decreases for other oxygen ions and approaches minimum for O1 and O2 lying in the plane of Fe_{B1}^{2+} cations ($\sim 0.04 \mu_B$).

Recently, an anomalously large value of the Fe_B orbital magnetic moment reaching $0.33 \mu_B$ has been deduced by applying sum rules to experimental $L_{2,3}$ X-ray magnetic circular dichroism spectra of Fe_3O_4 [203]. In addition, the unquenched Fe_B orbital moment was also reported to be confirmed by the LSDA+ U calculations. Later, however, this experimental finding was questioned by Goering et al. [204]. The average orbital moments between $-0.001 \mu_B$ and $0.06 \mu_B$ were found from X-ray magnetic circular dichroism sum rules depending on the integration range. From the spin-polarized relativistic LSDA+ U calculations [155] for the LT

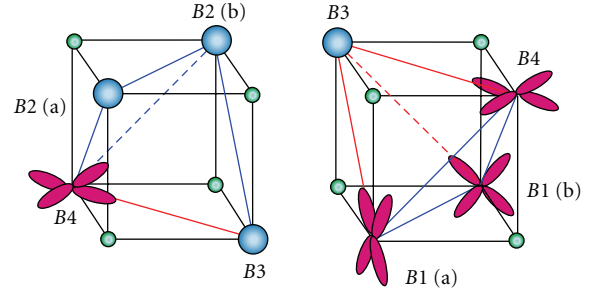


FIGURE 12: Sketch of the spatial arrangement of exchange interaction parameters between the octahedral Fe_B sites [155]. Orbitals approximate the occupied $3d$ minority orbitals of Fe_B^{2+} cations. Fe_B^{3+} cations are shown by large (blue) spheres. Oxygen atoms are shown by small (green) spheres. Ferromagnetic couplings between Fe_B cations are shown by the thick (red) lines, whereas antiferromagnetic exchanges depicted by the thin (blue) lines.

structure it was estimated orbital moments of $0.19 \mu_B$ and $0.014 \mu_B$ for Fe_{B1} and Fe_{B2} ions, respectively. Somewhat larger values of $0.039 \mu_B$ and $0.22 \mu_B$ were calculated for Fe_{B3} and Fe_{B4} cations, respectively. Taking into account the negative Fe_A orbital moment of $-0.021 \mu_B$, this gives the value of $0.07 \mu_B$ for the average orbital moment. Thus, in agreement with the previous theoretical results of [10] and XMCD sum rule data of [204], the calculations give the value of Fe orbital moment of $\sim 0.07 \mu_B$ which is much smaller than reported in [203].

3.2.6. Exchange Coupling Constants. The calculations of the exchange interaction parameters J_{ij} were also performed [155] via the variation of the ground-state energy with respect to the magnetic moment rotation angle [205]. The exchange coupling parameter J_{ij} represents the effective pair exchange interaction between the i th and j th Fe atoms with effective Heisenberg Hamiltonian $H = -\sum_{i>j} J_{ij} \mathbf{S}_i \cdot \mathbf{S}_j$. Here, \mathbf{S}_i and \mathbf{S}_j are the spins at sites i and j ($5/2$ and 2 for Fe^{3+} and Fe^{2+} cations, resp.). Positive (negative) values of J_{ij} correspond to the ferromagnetic (antiferromagnetic) coupling between sites. As shown in Table 2 the exchange couplings between A and B iron sublattices are rather large, of about -70 K, and antiferromagnetic. The Fe_A – Fe_A interactions are weakly antiferromagnetic with the maximal absolute value of 9.3 K (not shown in Table 2). The exchange couplings between the Fe_B sites ($|J_{BB}| \leq 27.5$ K) are substantially smaller than Fe_A – Fe_B ones and almost all of them are ferromagnetic (see Figure 12). Weak antiferromagnetic couplings with $|J_{BB}| \leq 11.6$ K are also obtained (mainly between the sites with the same $2+$ or $3+$ valence state, shown by the thin (blue) lines in Figure 12). The spatial representation of these exchange couplings is presented in Figure 12. Other couplings that are not shown in Table 2 are weaker than 10 K.

Experimental estimation of the exchange couplings in Fe_3O_4 was first performed by Néel on the basis of the two-sublattice collinear model [188]. From analysis of the temperature behaviour of the saturation magnetization and

TABLE 2: Exchange couplings J_{ij} (all with $|J_{ij}| > 10$ K) are presented [155]. The values are given in Kelvin. The spatial representation of the Fe_B - Fe_B exchange couplings is schematically shown in Figure 12. J_{ij} were calculated between the sublattices formed by the translations of the following Fe sites: Fe_{A1} ($1/4, 0.0034, 0.06366$), Fe_{A2} ($1/4, -0.4938, 0.18867$), Fe_{B1a} ($0, 1/2, 0$), Fe_{B1b} ($1/2, 1/2, 0$), Fe_{B2a} ($0, 0.0096, 1/4$), Fe_{B2b} ($1/2, 0.0096, 1/4$), Fe_{B3} ($-1/4, 0.2659, 0.1198$), Fe'_{B3} ($1/4, -0.2659, -0.1198$), Fe''_{B3} ($1/4, 0.2659, 0.3801$), Fe_{B4} ($1/4, 0.2479, -0.1234$), Fe'_{B4} ($-1/4, -0.2479, 0.1234$), and Fe''_{B4} ($1/4, -0.2479, 0.3765$).

i atom	j atom	J_{ij} , K
Fe_{A1}	Fe_{B1a}	-69.7
	Fe_{B1b}	-69.9
	Fe_{B2a}	-42.0
	Fe_{B2b}	-42.1
	Fe_{B3}	-73.7
	Fe'_{B3}	-48.1
	Fe_{B4}	-39.2
	Fe'_{B4}	-52.9
Fe_{A2}	Fe_{B1a}	-40.0
	Fe_{B1b}	-27.0
	Fe_{B2a}	-74.8
	Fe_{B2b}	-77.4
	Fe_{B3}	-89.1
	Fe''_{B3}	-31.1
	Fe'_{B4}	-62.7
	Fe''_{B4}	-27.8
Fe_{B1a}	$\text{Fe}_{B3}, \text{Fe}'_{B3}$	+12.7
Fe_{B1b}	$\text{Fe}_{B3}, \text{Fe}'_{B3}$	+27.5
Fe_{B2a}	Fe_{B2b}	-11.6
Fe_{B3}	Fe'_{B4}	+16.8
Fe_{B4}	Fe'_{B3}	+16.8

paramagnetic susceptibility, he obtained $J_{AA} = -17.7$, $J_{AB} = -23.4$, and $J_{BB} = 0.5$ K, where A and B refer to the tetrahedral and octahedral Fe sites, respectively. These values are qualitatively in accordance with the results presented in Table 2; namely, as in Neel's model, the calculations result in strong antiferromagnetic coupling between the A and B sublattices; J_{AA} couplings (not shown in Table 2) are considerably smaller than J_{AB} ; the exchange couplings in the B sublattice are weak and almost all of them are ferromagnetic. On the other hand, the small antiferromagnetic Fe_{B2a}^{3+} - Fe_{B2b}^{3+} exchange interaction (see Table 2) is in exact agreement with recent estimations using the two-sublattice model [206]. Three-sublattice model calculations give an overall similar result, except, however, the Fe_B^{2+} - Fe_B^{2+} exchange coupling, which seems to be overestimated [207].

3.2.7. Summary. The LSDA+ U study of the $P2/c$ model of the LT phase of Fe_3O_4 [155] shows a charge- and orbitally ordered insulator with an energy gap of 0.18 eV. The obtained charge-ordered ground state is described by a dominant $[001]_c$ charge density wave with a minor $[001/2]_c$ modulation on the Fe_B sublattice. A weak $[001]_c$ spin/charge

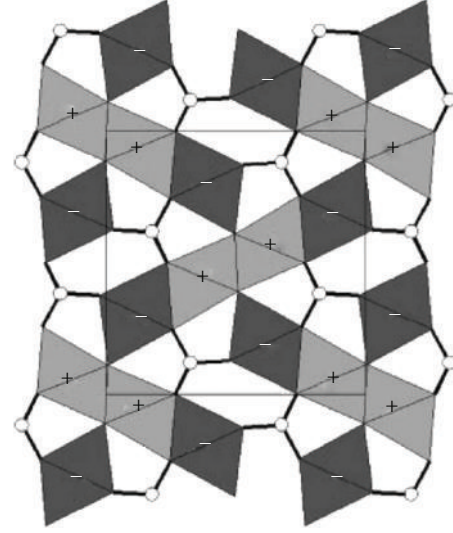


FIGURE 13: The Fe_2OBO_3 structure projected on (100) plane (b vertical, c horizontal). Two structurally distinct $\text{Fe}(1)\text{O}_6$ and $\text{Fe}(2)\text{O}_6$ octahedra shown by light and dark shading, respectively. Plus and minus signs indicate the relative orientation of the moments within each $\text{Fe}(1)$ and $\text{Fe}(2)$ chains in the magnetically ordered phase.

modulation on the oxygen ions was also obtained. The CO coincides with the earlier proposed class I CO [111, 179] and confirms violation of the Anderson criterion [156]. While the screening of the charge disproportion is so effective that the total $3d$ charge disproportion is rather small (0.23), the charge order is well pronounced with an order parameter defined as the difference of t_{2g} occupancies of $2+$ and $3+$ Fe_B cations (0.7). This agrees well with the result of BVS analysis for a monoclinic structure (0.2). The orbital order is in agreement with the Kugel-Khomskii theory [199] and corresponds to the local distortions of oxygen octahedra surrounding Fe_B sites.

Calculations of the effective exchange coupling constants between Fe spin magnetic moments show that the dominating interaction is an antiferromagnetic coupling between Fe_A and Fe_B moments. The coupling between Fe_B^{2+} and Fe_B^{3+} moments is found to be weaker and ferromagnetic.

3.3. Fe_2OBO_3 . Iron borate (Fe_2OBO_3) is a semivalent oxide. It belongs to the homometallic warwickite family with formal chemical formula $\text{MM}'\text{OBO}_3$, where M and M' are, respectively, a divalent and trivalent metal ions. Surprisingly, the homometallic ($M = M'$) warwickites are known only for Fe [208] and Mn [209]. In both compounds the metal has octahedral coordination. These octahedra share edges to form ribbons of four infinite along crystallographic a direction chains of octahedra linked by corner sharing and the trigonal BO_3 groups (see Figure 13).

There are two crystallographically inequivalent sites of the metal ions $\text{Fe}(1)$ and $\text{Fe}(2)$. Fe_2OBO_3 is L -type ferrimagnetic with drastically smaller in comparison with Fe_3O_4 critical temperature of $T_c \approx 155$ K, the $\text{Fe}(1)$ magnetic

moments being aligned antiparallel to the Fe(2) moments. It is almost antiferromagnetic, but a small ferrimagnetic moment of $\sim 0.03 \mu_B$ per Fe atom in a 0.05 T field was found [208]. At room temperature Fe_2OBO_3 is a semiconductor with a thermoactivated conductivity below $e^{-E_a/kT}$ with $E_a \approx 0.35$ eV [208]. Upon further heating a broad semiconductor-to-semiconductor transition occurs at $T_{co} \approx 317$ K, where resistivity drops down by a factor of ~ 3 , and, as a result, a small decrease of the activated energy up to $E_a \approx 0.31$ eV above 350 K is observed [208]. The 317 K transition is assigned to charge ordering of 2+ and 3+ Fe cations on Fe(1) and Fe(2) sites, and accompanied by a structural transition from monoclinic $P2_1/c$ to orthorhombic $Pmcn$ symmetry with increasing temperature. This structural transition is attributed by modification of the β angle from $\beta = 90.220(1)^\circ$ at 3 K to $\beta = 90^\circ$ at 337 K [208]. The change in conductivity and structure are small. But the ^{57}Fe Mössbauer spectra at around 317 K clearly result in the charge localization at the transition with an equal distribution of Fe^{2+} and Fe^{3+} cations over the two structurally distinct Fe(1) and Fe(2) sites with formal chemical formula $\text{Fe}(1)_{0.5}^{2+} \text{Fe}(1)_{0.5}^{3+} \text{Fe}(2)_{0.5}^{2+} \text{Fe}(2)_{0.5}^{3+} \text{OBO}_3$ [208, 210]. Although, there are two types of distorted FeO_6 octahedra with Fe–O bond length varying between 1.92 and 2.23 Å for 3 K, the average Fe(1)–O and Fe(2)–O distances are 2.085 and 2.082 Å, respectively, that is, equal within experimental errors [208]. Such a small difference results in the extremely small value of deviation (≤ 0.01) from the average 2.5+ value of valence of Fe cations estimated by the bond valence sum method. While an electronic transition between charge-ordered and charge-disordered states occurs at around 317 K, as evidenced by the Mössbauer spectroscopy and resistivity measurements, no long-range $\text{Fe}^{2+}/\text{Fe}^{3+}$ ordering is directly observed by X-ray, neutron, or electron diffraction. Thus, a long-range charge ordering such as the simple alternating scheme proposed in [208] destroys the mirror symmetry, which leads to a tilting of the Fe ribbons, consistent with the observed enlargement of the β angle below the transition. However, there is no observation of the increasing of a -axis periodicity (it should increase by a factor of two or another integer factor below T_{co}). Thus, below the transition, a charge ordering is not implicit in the atom coordinates, although it is indirectly evidenced by other experiments. This ambiguity is resolved in our electronic structure study, which reveals an arrangement of Fe^{2+} and Fe^{3+} cations alternately ordered within the chains along the a direction.

Theoretical investigation of the electronic structure and magnetic properties of Fe_2OBO_3 in the low-temperature $P2_1/c$ structure was reported in [211]. An order parameter, defined as the difference between t_{2g} minority-spin occupancies of $\text{Fe}(1)^{2+}$ and $\text{Fe}(1)^{3+}$ as well as the difference between t_{2g} majority-spin occupancies of $\text{Fe}(2)^{2+}$ and $\text{Fe}(2)^{3+}$ cations was proposed. This order parameter was found to be quite large, although the total 3d charge difference between 2+ and 3+ cations is small.

The band structure calculations have been carried out for the low-temperature monoclinic structure of Fe_2OBO_3 . The corresponding $P2_1/c$ unit cell contains four Fe_2OBO_3

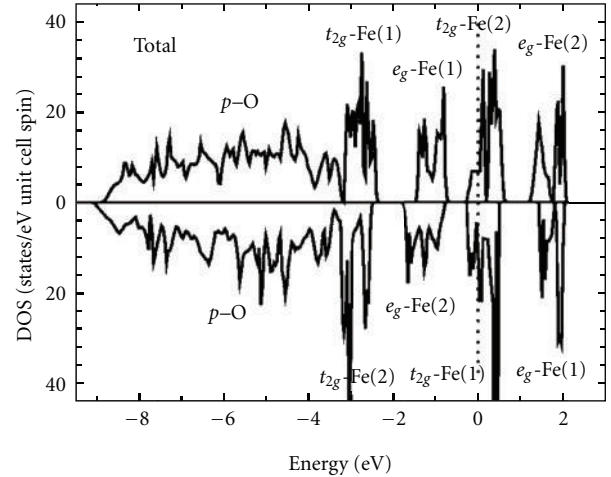


FIGURE 14: Total density of states (DOS) obtained from the LSDA calculations for the low-temperature $P2_1/c$ phase of Fe_2OBO_3 [211]. The top of the valence band is shown by dotted line.

formula units. The LSDA calculations give only a metallic ferrimagnetic solution without charge separation where partially filled bands at the Fermi level originate from the t_{2g} orbitals of Fe cations (see Figure 14).

The lower part of the valence band (below -3.5 eV) is mainly formed by O $2p$ states with a bonding hybridization with Fe $3d$ states. Fe $3d$ states give predominant contribution to the bands at -3.5 eV below and up to 2.5 eV above the Fermi level. The exchange splitting between the spin-up and spin-down Fe $3d$ states is roughly 3 eV which results in a net magnetic moment of $0.31 \mu_B$ per formula unit. Additionally, the fivefold $3d$ levels are split by the crystal field into t_{2g} and e_g subbands. The oxygen octahedra in Fe_2OBO_3 are strongly distorted and the local symmetry of Fe sites is, of course, lower than cubic. Nevertheless, the cubic component of the ligand field, which is determined by the relative strength of Fe d -O p hybridization of π - and σ -type, remains dominant, whereas the splitting within “ t_{2g} ” and “ e_g ” subbands is smaller than the corresponding band-width. This allows one to label the corresponding states as t_{2g} and e_g . The crystal-field splitting is roughly 2 eV, which is less than the exchange splitting. This is consistent with the high-spin state of the Fe cations. The symmetry inequivalence of Fe(1) and Fe(2) sites leads to an inexact cancellation of magnetic moments and results in a small ferrimagnetic moment of $\sim 0.31 \mu_B$ per formula unit.

Fe(1) and Fe(2) t_{2g} and e_g states with the opposite spin projections share nearly the same energy intervals. Thus, Fe $3d$ states between -3.5 and -2.0 eV originate predominantly from majority-spin Fe(1) and minority-spin Fe(2) t_{2g} states whereas the states between -2.0 and -0.5 eV are mainly of e_g character. Partially occupied bands crossing the Fermi level are formed by minority spin Fe(1) and majority-spin Fe(2) t_{2g} states. The nominal occupation of these bands is $1/6$. In the majority-spin channel, however, the Fe(2) t_{2g} state, which is oriented in the plane perpendicular to the shortest Fe(2)–O bond, forms quasi-one-dimensional bands with a

strong dispersion along the a direction. The one-dimensional character of the dispersion is determined by the existence of only two nearest neighbours of the same kind around each Fe(2) ion. The other two Fe(2) t_{2g} states are shifted to higher energy and the corresponding bands are completely unoccupied. As a result, the majority-spin bands crossing the Fermi level turn out to be half filled.

An Fe(1) ion, in contrast to Fe(2) one, has four Fe(1) neighbours at close distances. As a result of the hybridisation between Fe(1) t_{2g} states the situation in the minority-spin channel is more complicated. Twelve t_{2g} bands are split into three groups of 4 bands each. The Fermi level is crossed by lowest bands which show a rather strong dispersion along a but with a two times smaller period.

It should be noted that in contrast to experimental data [212] LSDA predicts Fe₂OBO₃ to be metallic with substantial magnetic moment per unit cell. Apparently, the electron-electron correlations, mainly in the $3d$ shell of Fe cations, play a significant role.

The LSDA+ U calculations have been performed for the $P2_1/c$ unit cell as well as for double ($2a \times b \times c$) and triple ($3a \times b \times c$) $P2_1/c$ supercells of Fe₂OBO₃ (without putting in any local displacements of oxygen atoms around Fe²⁺/Fe³⁺ sites). Thus, for the $2a \times b \times c$ CO pattern proposed in [208] using the classical value of Coulomb and exchange interaction parameters for Fe 5 eV and 1 eV, respectively, a charge-ordered insulator with an energy gap of 0.13 eV was found. This is in a strong contrast with metallic solution without CO obtained by the LSDA. This is a notable result because a CO is not implicit in the atom coordinates, and it shows that LSDA+ U calculations can assist experiments in revealing CO arrangements. To obtain a reasonably good agreement of the calculated gap of 0.39 eV with experimental value of 0.35 eV, the U value has to be increased up to 5.5 eV (see Figures 15 and 16). It does not exceed 10% of the U value, which is in an accuracy of the U calculation. Note, however, that the CO obtained by LSDA+ U within $2a \times b \times c$ supercell does not depend on the U value of 5–5.5 eV. Here and in the following all results are presented for double along a -direction $P2_1/c$ supercell of Fe₂OBO₃.

After self-consistency each of two groups of Fe(1) and Fe(2) atoms is split out in two subgroups of 2+ and 3+ Fe cations with equal number of 2+ and 3+ cations. Thus, one of t_{2g} majority-/minority-spin states of Fe(2)/Fe(1) atom becomes completely occupied, whereas all the rest of t_{2g} states are pushed by strong Coulomb interaction at the energies above 3 eV. The gap is opened between occupied and unoccupied t_{2g} states of Fe(1)²⁺ and Fe(1)³⁺ for spindown and Fe(2)²⁺ and Fe(2)³⁺ for spinup. Majority-spin $3d$ states of Fe(1)³⁺ and minority-spin states of Fe(2)³⁺ cations are shifted below the O $2p$ states, which form the band in the energy range of -8 and -2 eV. In contrast to Fe³⁺ states, the majority-spin Fe(1)²⁺ and minority-spin Fe(2)²⁺ $3d$ states form the broad bands between -8 and -1 eV.

The obtained magnetic structure is almost antiferromagnetic (without spin moment per unit cell) with nearly the same spin moment per Fe(1)²⁺ and Fe(2)²⁺ as well as per Fe(1)³⁺ and Fe(2)³⁺ cations. Using the moment populations

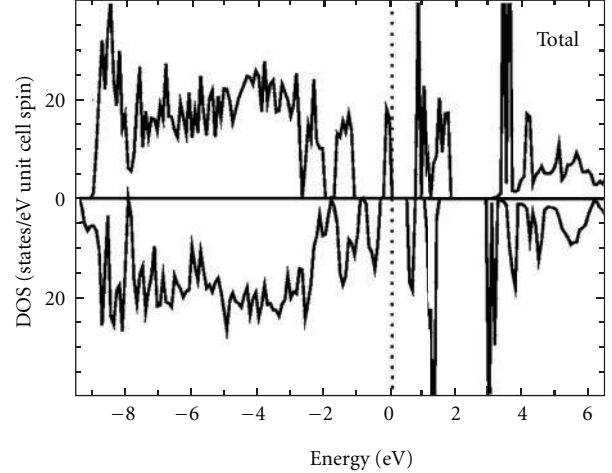


FIGURE 15: The total DOS obtained from LSDA+ U calculations with $U = 5.5$ eV and $J = 1$ eV for the low-temperature $P2_1/c$ phase of Fe₂OBO₃ [211]. The top of the valence band is shown by dotted lines.

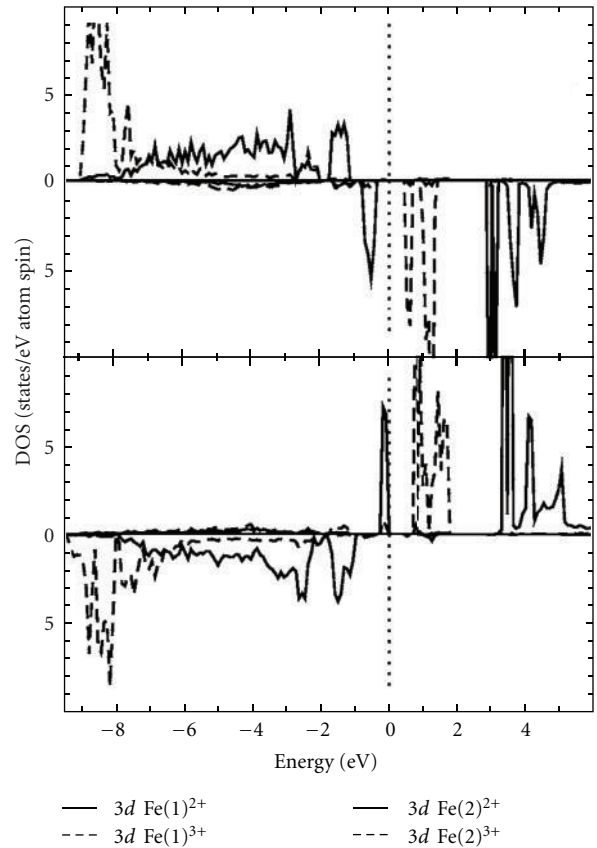


FIGURE 16: The partial DOSs for different Fe cations are shown. The gap is opened between Fe(2)²⁺ and Fe(2)³⁺ for majority spin and Fe(1)²⁺ and Fe(1)³⁺ cations for minority spin states. The gap value of 0.39 eV was obtained by LSDA+ U with $U = 5.5$ eV and $J = 1$ eV [211]. The Fermi level is shown by dotted line.

TABLE 3: Total and l -projected charges, magnetic moments, and occupation of the most populated t_{2g} orbitals calculated for inequivalent Fe atoms in the low-temperature $P2_1/c$ phase of Fe_2OBO_3 [211].

Fe ion	q	q_s	q_p	q_d	M (μ_B)	t_{2g} orbital	n
$\text{Fe}(1)^{3+}$	6.90	0.40	0.55	5.95	-4.16	—	0.10
$\text{Fe}(1)^{2+}$	7.12	0.35	0.50	6.27	-3.62	$d_{xy\uparrow}$	0.91
$\text{Fe}(2)^{3+}$	6.79	0.38	0.54	5.86	4.30	—	0.09
$\text{Fe}(2)^{2+}$	7.04	0.34	0.50	6.21	3.67	$d_{xy\uparrow}$	0.89

in Table 3, the calculated net moment is $\sim 0.03 \mu_B$ per Fe atom, in exact agreement with the experimental value [208].

The charge order obtained by LSDA+ U in $2a \times b \times c$ $P2_1/c$ supercell is consistent with observed enlargement of the β angle below the transition and coincides with charge-ordering scheme proposed earlier by Attfield et al. [208] It is described by the sloping 2+ and 3+ Fe cation lines alternately stacked along a direction and could be considered as a quasi-one-dimensional analog of the Verwey CO model in pyrochlore lattice of Fe_3O_4 . An additional self-consistent LSDA+ U calculations for $P2_1/c$ unit cell as well as for double and triple along a direction $P2_1/c$ supercells was performed using the same U and J values. But only self-consistent solutions with larger value of the total energy or with substantial magnetic moment per unit cell, which contradicts the experimental data, were found. Also it was found that other charge arrangements in $2a \times b \times c$ $P2_1/c$ supercell are unstable, and the stable one coincides with the CO found previously. Thus, the CO obtained for certain value of U and J does not depend on the initial charge arrangement. It is not possible to check all possible CO arrangements including more complex CO scenarios, but our results consistently indicate that the obtained CO solution is more favourable than other simple alternatives and is the ground state of Fe_2OBO_3 in the low-temperature phase.

Although the corresponding total $3d$ charges difference ($0.34 \bar{e}$) and disproportion of the total electron charges inside the atomic spheres of Fe^{2+} and Fe^{3+} cations ($0.24 \bar{e}$) are small, an analysis of occupation matrices of $3d$ Fe(1)/Fe(2) minority-/majority-spin states confirms substantial charge disproportionation. Thus, as shown in Table 3, one of the t_{2g} states of $\text{Fe}(1)^{2+}$ and $\text{Fe}(2)^{2+}$ cations is almost completely filled with the occupation numbers $n \approx 0.9$, whereas the remaining two t_{2g} orbitals of the Fe^{2+} cations have significantly smaller population of about 0.1. According to [181] an order parameter was defined as the largest difference between Fe^{2+} and Fe^{3+} t_{2g} populations. While, due to strong static “screening” effects, the order parameter introduced as the total $3d$ charge difference between 2+ and 3+ Fe cations is ill defined, the well-defined order parameter is the difference of t_{2g} occupancies for Fe^{3+} and Fe^{2+} cations, which amounts to 80% of ideal ionic CO model and clearly pronounces the existence of CO below the transition. The occupation matrices analysis shows that the change of the t_{2g} occupations caused by the charge ordering is very effectively screened by the rearrangement of the other Fe electrons. Thus, significant contribution to the charge screening is provided by Fe e_g states due to relatively strong σ bonds with $2p$ O states and,

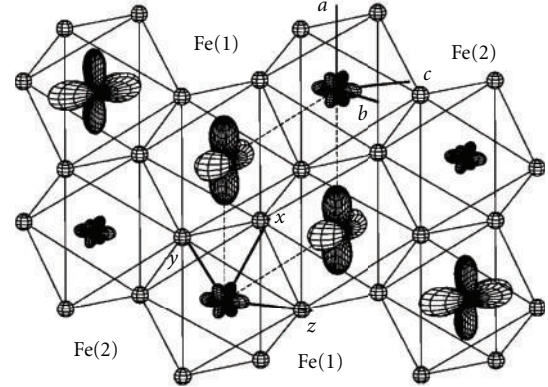


FIGURE 17: The angular distribution of the majority and minority spin $3d$ electron density of the $\text{Fe}(2)$ and $\text{Fe}(1)$ cations, respectively, within Fe ribbon [211]. The size of orbital corresponds to its occupancy. Oxygen atoms are shown by small spheres. x - y - z coordinate system corresponds to the local cubic frame.

as a result, appreciable contribution to the occupied part of the valence band.

The occupied t_{2g} states of Fe^{2+} cations are predominantly of d_{xy} character in the local cubic frame (according to that we later mark the orbital as d_{xy} orbital). This is illustrated in Figure 17, which shows the angular distribution of the majority and minority spin $3d$ electron density of the $\text{Fe}(2)$ and $\text{Fe}(1)$ cations, respectively. Thus, occupied Fe^{2+} and unoccupied Fe^{3+} cations are ordered alternately within the chain which is infinite along a direction. The angular distribution of charge density of the $\text{Fe}(1)$ and $\text{Fe}(2)$ cations, which correspondingly belongs to different Fe ribbons being formed a cross in the Fe_2OBO_3 structure projected on (100) plane (see Figure 13), is shown in Figure 18.

Using the LSDA+ U method the exchange interaction parameters have been calculated via the variation of ground-state energy with respect to the magnetic-moment rotation angle [211]. In Table 4 we have shown the total set of different intraribbon exchange parameters as well as a contribution of different subbands into exchange interactions. The spatial representation of all these exchanges is schematically presented in Figure 19. Surprisingly, only the exchange interaction parameter between $\text{Fe}(2)^{2+}$ and $\text{Fe}(2)^{3+}$ cations is ferromagnetic with relatively small value of $J_6 = 25$ K. In contrast, the nearest sites in quasi-one-dimensional $\text{Fe}(1)$ chain are coupled antiferromagnetically with noticeably larger exchange absolute value of $|J_5| = 275$ K. Furthermore,

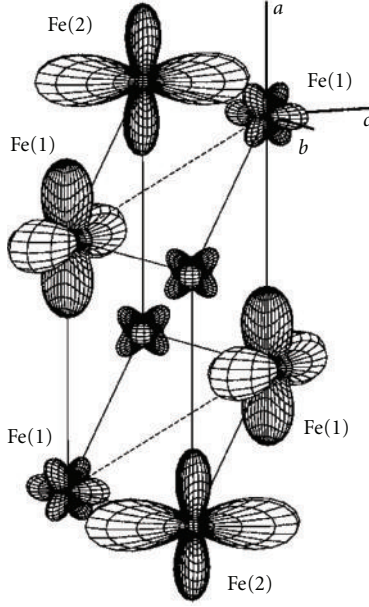


FIGURE 18: The angular distribution of the majority and minority spin $3d$ electron density of the Fe(2) and Fe(1) cations, respectively, from different Fe ribbons [211]. The size of orbital corresponds to its occupancy. The frame of four Fe(1) atoms from the Fe ribbon presented in Figure 17 is shown by dashed lines.

the exchange parameters between the nearest sites of two Fe(1) chains are relatively strong and antiferromagnetic (see J_2 , J_4 , and J_8 in Table 4). Therefore, the Fe(1) sublattice is highly frustrated, while the relatively weak frustrations in the Fe(2) sublattice considerably reduce ferromagnetic interaction within Fe(2) chain. Also it is interesting to note that relatively strong ferromagnetic intrachain interaction between t_{2g} subbands of Fe(2)²⁺ and Fe(2)³⁺ cations (see J_6 in Table 4) is strongly suppressed by the substantial antiferromagnetic $t_{2g} - e_g$ and $e_g - e_g$ exchange.

On the other hand, the interribbon exchange interaction parameters between Fe(1) and Fe(2) atoms are considerably larger. The values of these interactions are shown in Table 5, whereas the spatial representation is schematically presented in Figure 20. Thus, the exchange parameters between Fe(1)³⁺ and Fe(2)²⁺ cations are antiferromagnetic with values of $J_{10} = -917$ K and $J_{14} = -827$ K (see Table 5). Such an appreciable difference between J_{10} and J_{14} arise from geometry. Thus, the former corresponds to the exchange interaction between Fe(1) and Fe(2) atoms, which belongs to an edge, whereas the latter corresponds to the diagonal interaction. It seems that such geometrical reason is also responsible for decrease of absolute value of the exchange interactions between Fe(1)²⁺ and Fe(2)³⁺ cations from $|J_{12}| = 837$ K to $|J_{15}| = 586$ K (see Table 5). Also it is interesting to note that the exchange interaction between Fe(1)³⁺ and Fe(2)³⁺ cations are considerably larger than between Fe(1)²⁺ and Fe(2)²⁺ (J_{11} and J_{13} , correspondingly). We find that the interribbon exchange interactions play predominant role and determine the whole L -type ferrimagnetic spin structure below T_c in

TABLE 4: Total and partial intraribbon exchange interaction parameters are shown [211]. The values are given in kelvin. The spatial representation of all these exchanges is schematically presented in Figure 19.

J_i	$t_{2g} - t_{2g}$	$t_{2g} - e_g$	$e_g - e_g$	Total
J_1	-18	-124	-10	-153
J_2	-78	-101	3	-176
J_3	-66	-17	-46	-129
J_4	-140	-139	0	-279
J_5	-45	-163	-67	-275
J_6	249	-154	-71	25
J_7	-36	-13	-15	-65
J_8	-199	-342	-3	-545
J_9	-12	-138	-3	-154

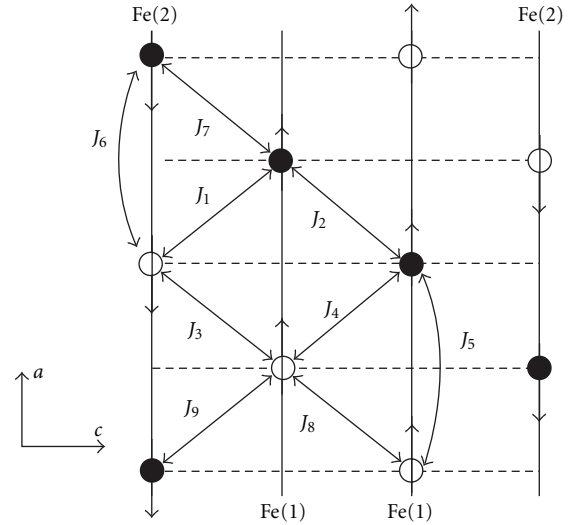


FIGURE 19: The sketch of the arrangement of exchange interaction parameters within the ribbon of iron atoms. Open circles correspond to Fe³⁺, while Fe²⁺ cations are noted by the closed circles. The spin moment direction on each Fe site is shown by an arrow.

contrast with the ferromagnetic intrachain order due to $d^5 - d^6$ superexchange [208].

3.3.1. Summary. In the LSDA+ U study of the low-temperature $P2_1/c$ phase of Fe₂OBO₃ [211] was found a charge-ordered insulator with an energy gap of 0.39 eV. While the screening of the charge disproportion is so effective that the total $3d$ charge disproportion is rather small (0.34), the charge order is well pronounced with an order parameter defined as a difference of t_{2g} occupancies of 2+ and 3+ Fe cations (0.8). The occupied Fe²⁺ and Fe³⁺ cations are ordered alternately within infinite along a -axis chains of Fe atoms. This result is remarkable in view of the absence of directly observed CO atomic displacements in the experimental coordinates and demonstrates the utility of the LSDA+ U method as an aide to experimental studies of CO structures. However, the charge order obtained by LSDA+ U is consistent

TABLE 5: Total and partial interribbon exchange interaction parameters are shown [211]. The values are given in kelvin. The spatial representation of all these exchanges is schematically presented in Figure 20.

J_i	$t_{2g} - t_{2g}$	$t_{2g} - e_g$	$e_g - e_g$	Total
J_{10}	-56	-464	-397	-917
J_{11}	-205	-192	-336	-733
J_{12}	-141	-483	-213	-837
J_{13}	-99	-109	-16	-223
J_{14}	-257	-565	-5	-827
J_{15}	-53	-540	7	-586

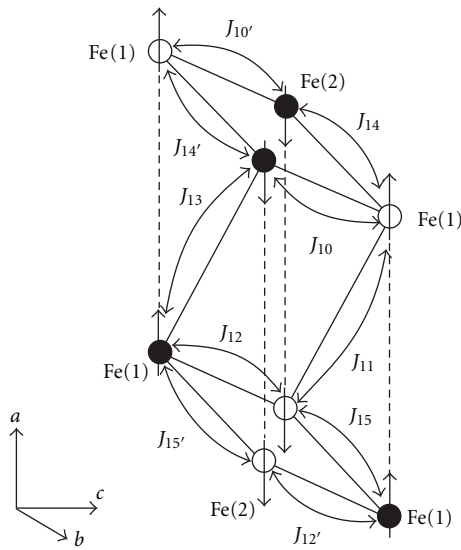


FIGURE 20: The sketch of the arrangement of interribbon exchange interaction parameters [211]. Open circles correspond to Fe^{3+} , while Fe^{2+} cations are noted by the closed circles. The spin moment direction on each Fe site is shown by an arrow. Note that J_i' exchange parameters presented here have the same total values as J_i , while subband contributions are different.

with observed enlargement of the β angle and coincides with charge-ordering scheme proposed earlier by Attfield et al. [208]. It seems certain that Fe_2OBO_3 is charge ordered below T_{CO} , and the absence of the long-range charge ordering from X-ray, neutron, or electron diffraction arises from formation of charge order within small domains, which have been termed “Wigner nanocrystals” [213]. Thus, the superstructure peaks are too weak and broad to be observed against background in diffraction patterns, whereas the observed long-range monoclinic lattice distortion can arise despite a large concentration of defects as these preserve the direction of the monoclinic distortion but do not propagate the coherent doubling of the lattice periodicity. An analysis of the exchange interaction parameters obtained by LSDA+ U method inevitably results in predominance of the interribbon exchange interactions which determine the whole L -type

ferrimagnetic spin structure below T_c , in contrast with the ferromagnetic intrachain order due to $d^5 - d^6$ superexchange proposed earlier in [208].

4. Titanium and Vanadium Oxides

4.1. Ti_4O_7 . The aforementioned phenomena of sharp metal-insulator transitions associated with pronounced charge and/or orbital ordering are characteristic for the *Magnéli* phases $\text{M}_n\text{O}_{2n-1}$ ($\text{M} = \text{Ti}, \text{V}$). These compounds form a homologous series and have been studied recently to understand the differences in crystal structures and electronic properties between the end members MO_2 ($n \rightarrow \infty$) and M_2O_3 ($n = 2$) [214]. In particular, the metal-insulator transition of VO_2 discovered some fifty years ago still is the subject of ongoing controversy and is another “hot topic” in solid-state physics. LSDA calculations have revealed strong influence of the structural degrees of freedom on the electronic properties of VO_2 and neighbouring rutile-type dioxides [215–217]. In this scenario the characteristic dimerization and antiferroelectric displacement of the metal atoms translate into orbital ordering within the t_{2g} states and a Peierls-like singlet formation between neighbouring sites. Recently, this was confirmed by LDA+DMFT calculations, which suggested to regard the transition of VO_2 as a correlation-assisted Peierls transition [218].

Ti_4O_7 titanium oxide is another remarkable member of the *Magnéli* phases with $n = 4$ which shows metal-insulator transitions associated with the spatial charge ordering. It is a mixed-valent compound which has an even mixture of 3+ and 4+ Ti cations ($\text{Ti}_2^{3+}\text{Ti}_2^{4+}\text{O}_7$), corresponding to an average 3d occupation of 1/2 electron per Ti site. Electrical resistivity, specific heat, magnetic susceptibility, and X-ray diffraction data reveal two first-order transitions in the temperature range of 130–150 K [219]. At 150 K a metal-semiconductor transition occurs without measurable hysteresis in resistivity and specific heat. It is followed by a semiconductor-semiconductor transition at 130–140 K, which again is characterized by an almost two orders of magnitude abrupt increase in electrical resistivity and has a hysteresis of several degrees [219]. The magnetic susceptibility shows a sharp enhancement when heating through 150 K. However, it is small and temperature independent below this temperature and does not show any anomaly at 140 K.

The crystal structure of Ti_4O_7 (see Figure 21) can be viewed as rutile-type slabs of infinite extension and four Ti sites thickness, separated by shear planes with a corundum-like atomic arrangement. Below 130 K it crystallizes in a triclinic crystal structure with two formula units per primitive unit cell [220]. Four crystallographically inequivalent Ti sites are found at the centers of distorted oxygen octahedra. They form two types of chains, namely, (a) 1-3-3-1 and (b) 2-4-4-2, which run parallel to the pseudo-rutile c -axis and are separated by the crystallographic shear planes. Although interatomic distances in the (b) chain are almost uniform (3.01 and 3.07 Å between 4-4 and 2-4 Ti sites, resp.) they are remarkably different for the (a) chain (3.11 and 2.79 Å between 3-3 and 1-3 Ti sites).

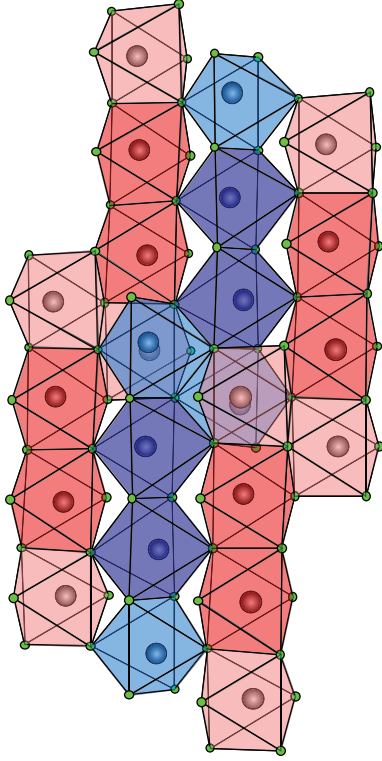


FIGURE 21: The low-temperature crystal structure of Ti_4O_7 . Chains of four Ti sites run parallel to the pseudorutile c -axis. Red and blue (light and dark on the black and white image) chains of four Ti atoms correspond to the (a) and (b) chains of Ti atoms, respectively. Further gradation of red and blue on light and dark subsets indicates inequivalent Ti sites in (a) and (b) chains.

Accurate determination of the crystal structure allowed to elucidate the nature of the three phases distinguished by the two first-order transitions [220]. In particular, in the metallic phase the average Ti–O bond lengths for crystallographically inequivalent TiO_6 octahedra are very similar which results in the average valence state of 3.5+ per each Ti cation. Below 130 K charge has been transferred from the (b) to the (a) chains. In addition, Ti^{3+} cations in alternate (a) chains are paired to form nonmagnetic metal-metal bonds, whereas in the intermediate phase pairing also persists but its long-range order calls for a fivefold supercell [219]. Thus, the 130–140 K transition is associated with a transition to the phase with a long-range order of Ti^{3+} - Ti^{3+} pairs, whereas above 150 K 3+ and 4+ Ti cations are disordered. The presence of the Ti^{3+} - Ti^{3+} pairs strongly differentiates Ti_4O_7 from Fe_3O_4 and results in two steep first-order transitions found in the electrical resistivity.

Recent LSDA band structure calculations of both high- and low-temperature phases of Ti_4O_7 results in significant t_{2g} charge separation between crystallographically independent 3+ and 4+ Ti sites in the low-temperature phase, whereas a rather isotropic occupation of the t_{2g} states has been found at room temperature [221]. While, in addition, an orbital order at the Ti d^1 chains originating from metal-metal dimerization was found, the LSDA gave only metallic

solution with semimetallic-like band overlap instead of the semiconducting gap. This problem is overcome in our work taking into account strong electronic correlations in Ti 3d shell using the LSDA+ U method.

In [187] the authors investigate the electronic structure of the low-temperature phase using the LSDA+ U approach. The LSDA+ U calculations result in a charge- and orbitally ordered insulator with an energy gap of 0.29 eV, which is in a good agreement with an experimental gap value of 0.25 eV. From the results of [187], an orbital-order parameter was proposed as the difference between t_{2g} majority-/minority-spin occupancies of $\text{Ti}(1)^{3+}/\text{Ti}(3)^{3+}$ and $\text{Ti}(2)^{4+}/\text{Ti}(4)^{4+}$ cations respectively. This order parameter is found to be quite large, although the total 3d charge difference between 3+ and 4+ cations, remains small. Also it is interesting to note that the total charge separation between 3+ and 4+ Ti cations is completely lost due to efficient screening by the rearrangement of the other Ti electrons. In addition, we find a strong antiferromagnetic coupling of $J \approx 1700$ K of the local moments within the dimerized Ti^{3+} - Ti^{3+} pairs, whereas an interpair coupling is only of ≈ 40 K. This is in a good agreement with small and temperature-independent magnetic susceptibility in the low-temperature phase of Ti_4O_7 .

4.1.1. LSDA Band Structure. The LSDA band structure calculations [187] for the low-temperature $P\bar{1}$ structure gives a nonmagnetic metallic solution with substantial charge separation between crystallographically independent $\text{Ti}(1)/\text{Ti}(3)$ and $\text{Ti}(2)/\text{Ti}(4)$ cations. The lower part of the valence band below -3 eV is predominantly formed by O $2p$ states with a bonding hybridization with Ti 3d states. Crystal field splitting of the latter is roughly of 2.5 eV. Ti t_{2g} states form the group of bands at and up to 2 eV above the Fermi energy, whereas Ti e_g states give a predominant contribution to the bands between 2.5 and 4.5 eV. Within the t_{2g} group of bands, the symmetry inequivalence of $\text{Ti}(1)/\text{Ti}(3)$ and $\text{Ti}(2)/\text{Ti}(4)$ sites leads to substantial t_{2g} charge separation between these two groups of Ti atoms. In addition, an analysis of the partial density of states reveals significant bonding-antibonding splitting of d_{xy} (in local cubic frame) states of about 1.5 eV for $\text{Ti}(1)/\text{Ti}(3)$ cations, whereas $\text{Ti}(2)/\text{Ti}(4)$ cations show a relatively weak substructure. This substantial bonding-antibonding splitting of $\text{Ti}(1)/\text{Ti}(3)$ t_{2g} states agrees well with the concept of formation of Ti^{3+} - Ti^{3+} spin-singlet pairs proposed earlier by Lakkis et al. [219]. However, the LSDA calculations fail to reproduce an insulating spin-singlet ground state of the low-temperature phase of Ti_4O_7 . Apparently, the electron-electron correlations, mainly in the 3d shell of Ti cations, play a significant role.

4.1.2. LSDA+ U Results and Charge Ordering. In order to take into account strong electronic correlations in Ti 3d shell, authors of [187] perform LSDA+ U calculations for Ti_4O_7 in the low-temperature $P\bar{1}$ structure. The LSDA+ U calculations result in a charge and orbitally ordered insulator with an energy gap of 0.29 eV (see Figure 22). This is in a strong contrast with the metallic solution with a substantial charge

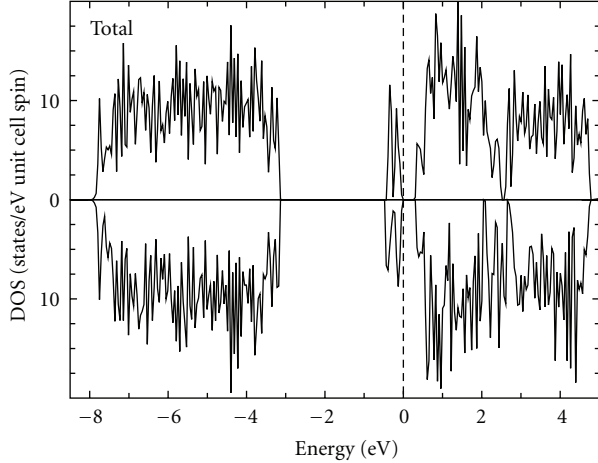


FIGURE 22: The total DOS obtained from LSDA+ U calculations with $U = 3.0$ eV and $J = 0.8$ eV for the low-temperature $P\bar{1}$ phase of Ti_4O_7 [187]. The top of the valence band is shown by dotted lines.

disproportionation between crystallographically inequivalent Ti(1)/Ti(3) and Ti(2)/Ti(4) cations obtained by LSDA and in a reasonably good agreement with an experimental gap value of 0.25 eV. Note, however, that the charge- and orbital-order pattern remains exactly the same for U in the range 2.5–4.5 eV, whereas the energy gap increases considerably up to 1.12 eV for $U = 4.5$ eV. This remarkable increase of the gap value is accompanied by the enhancement of the spin magnetic moment from 0.56 up to $0.8 \mu_B$ per $3+$ Ti(1)/Ti(3) cation as U is increased from 2.5 to 4.5 eV.

In addition, authors perform LSDA+ U calculations for high-temperature metallic phase of Ti_4O_7 [187]. In particular for U of 2.5 eV a metallic self-consistent solution with substantial density of states (76 states/Ry) at the Fermi level has been found, whereas for U of 3 eV the LSDA+ U solution becomes unstable but remains metallic. With further increase of the U value the metallic solution collapses into insulating one.

After self-consistency four crystallographically independent Ti atoms are split out in two subgroups with respect to the spin magnetic moment per Ti site: Ti(1)/Ti(3) with a moment of $0.66/-0.67 \mu_B$, respectively, and Ti(2)/Ti(4) with $0.04/-0.02 \mu_B$. Thus, one of t_{2g} majority-/minority-spin states of Ti(1)/Ti(3) becomes occupied (d^1), whereas all other t_{2g} states are pushed by strong Coulomb interaction above the Fermi level. In contrast, all t_{2g} states of Ti(2) and Ti(4) are almost depopulated (d^0) and form bands up to 2.5 eV above the Fermi level. The occupied Ti(1)/Ti(3) states are strongly localized and form a prominent structure with a bandwidth of 0.25 eV just below the Fermi level (see Figure 23). The strong Coulomb interaction does not affect much the empty Ti e_g states, which give predominant contribution between 2.5 and 4.5 eV. The obtained magnetic structure is almost antiferromagnetic with the spin magnetic moments within $\text{Ti}(1)^{3+}\text{-Ti}(3)^{3+}$ as well as $\text{Ti}(2)^{4+}\text{-Ti}(4)^{4+}$ pairs being of the same magnitude with opposite sign.

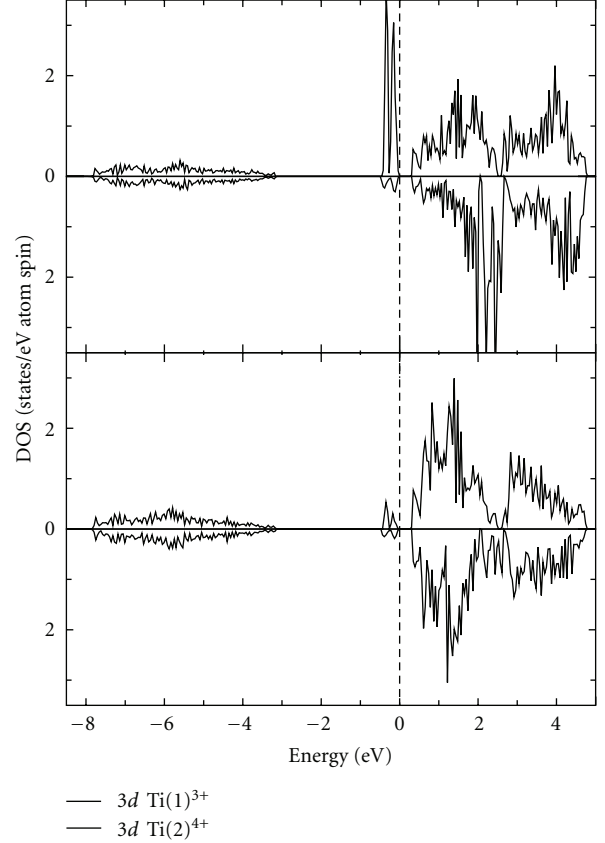


FIGURE 23: The partial DOSs for $\text{Ti}(1)^{3+}$ and $\text{Ti}(2)^{4+}$ cations are shown [187]. The gap value of 0.29 eV was obtained by LSDA+ U with $U = 3.0$ eV and $J = 0.8$ eV. The Fermi level is shown by dotted line.

TABLE 6: Total (q) and l -projected ($q_{s,p,d}$) charges, magnetic moments (M), and occupation of the most populated t_{2g} orbitals (n) calculated for inequivalent Ti atoms in the low-temperature $P\bar{1}$ phase of Ti_4O_7 [187].

Ti ion	q	q_s	q_p	q_d	M (μ_B)	t_{2g} orbital	n
$\text{Ti}(1)^{3+}$	2.27	0.18	0.27	1.83	0.66	d_{xy1}	0.74
$\text{Ti}(2)^{4+}$	2.22	0.22	0.33	1.68	0.04		0.08
$\text{Ti}(3)^{3+}$	2.16	0.18	0.25	1.74	-0.67	d_{xy1}	0.73
$\text{Ti}(4)^{4+}$	2.16	0.21	0.33	1.62	-0.02		0.07

An analysis of occupation matrices of $\text{Ti}(1)^{3+}/\text{Ti}(3)^{3+}$ majority/minority $3d$ spin states confirms substantial charge disproportionation within the Ti $3d$ shell. As shown in Table 6, one of the t_{2g} states of Ti^{3+} cations (d^1) is occupied with the occupation number of 0.74, whereas the remaining two t_{2g} orbitals have a significantly smaller population of about 0.08. Thus, according to [181] we define an orbital-order parameter as the largest difference between $3+$ and $4+$ Ti t_{2g} populations which amounts to 66% of ideal ionic charge-ordering model. The orbital-order parameter clearly shows the existence of substantial charge disproportionation in the Ti $3d$ shell of Ti_4O_7 which is remarkable because of

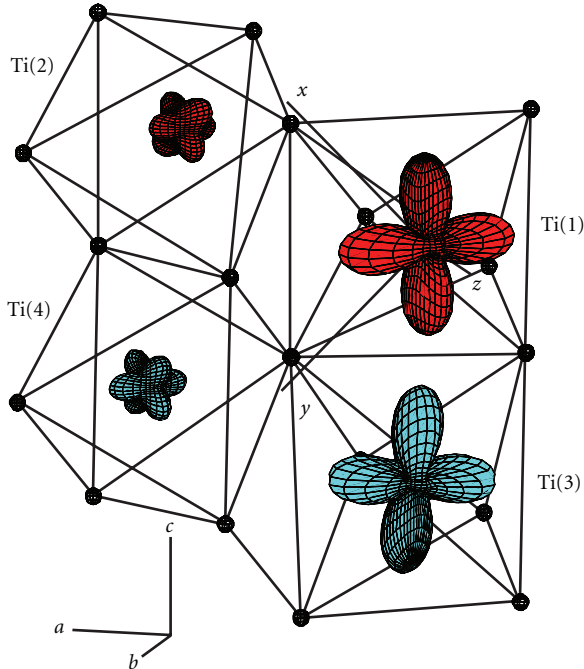


FIGURE 24: Structure of Ti_4O_7 showing the angular distribution of the majority and minority spin $3d$ electron density of Ti cations [187]. Red and cyan (light and dark, resp., on the black and white image) orbitals correspond to the majority and minority $3d$ spin states, respectively. Oxygen atoms are shown by small spheres. The size of orbital corresponds to its occupancy. x - y - z coordinate system corresponds to the local cubic frame.

the complete lack of the total charge separation (see column q in Table 6) between $3+$ and $4+$ Ti cations. The occupation matrices analysis shows that the change of the t_{2g} occupations is very efficiently screened by the rearrangement of the other Ti electrons. A significant portion of the screening charge is provided by Ti e_g states due to formation of relatively strong σ bonds with O $2p$ states, which results in appreciable contribution of the former to the occupied part of the valence band. Ti $4s$ and $4p$ states give additional contributions to the screening of the difference in t_{2g} occupations which leads to complete loss of the disproportionation between the charges at $3+$ and $4+$ Ti sites.

The occupied t_{2g} Ti^{3+} states are predominantly of d_{xy} character in the local cubic frame (according to that we later mark the orbital as d_{xy} orbital). This is illustrated in Figure 24, which shows the angular distribution of the majority- and minority-spin $3d$ electron density of Ti cations, marked by red and cyan color (or light and dark on the black and white image), respectively. Since $\text{Ti}(1)^{3+}$ and $\text{Ti}(3)^{3+}$ cations are antiferromagnetically coupled, the obtained ferro-orbital order is consistent with the formation of a bonding spin-singlet state from the d_{xy} orbitals of two neighboring Ti(1) and Ti(3) sites. The orientation of occupied Ti^{3+} t_{2g} orbitals is consistent with the largest average Ti-O distance in the plane of t_{2g} orbitals. As shown in Table 7 the average Ti(1)-O distance (2.061 Å) in the plane of d_{xy} orbital is

TABLE 7: The averaged Ti-O distances in the plane of t_{2g} orbitals ($d_{\text{orb.}}$) and in the oxygen octahedra ($d_{\text{av.}}$) for $P\bar{1}$ structure of Ti_4O_7 . d_{xy} approximates to the occupied orbital of the $3d^1$ Ti(1) and Ti(3) $3+$ states [187].

Ti atom	orbital	$d_{\text{orb.}}$ (Å)	$d_{\text{av.}}$ (Å)
Ti(1)	d_{xy}	2.061	2.046
	d_{yz}	2.032	
	d_{zx}	2.045	
Ti(2)	d_{xy}	2.012	2.000
	d_{yz}	1.976	
	d_{zx}	2.013	
Ti(3)	d_{xy}	2.047	2.043
	d_{yz}	2.041	
	d_{zx}	2.042	
Ti(4)	d_{yz}	1.976	1.977
	d_{zx}	1.981	

considerably larger than average distances in the other two yz and zx planes (2.032 and 2.045 Å, resp.). The same is also true for the Ti(3) cation but in this case the variation of the average Ti(3)-O distances is much smaller (2.047 versus 2.041 and 2.042 Å), and, as a consequence, the out-of-plane rotation of the occupied t_{2g} minority spin orbital is stronger.

In addition, hopping matrix elements were evaluated via Fourier transformation from reciprocal to real space of the Ti t_{2g} LSDA Wannier Hamiltonian [222]. Remarkably, for the low-temperature phase the Ti(1)-Ti(3) intra-pair d_{xy} - d_{xy} hopping matrix element is found to be of 0.61 eV, whereas all other hoppings are 3-4 times smaller. This strong inhomogeneity of the hopping matrix elements disappears in the high-temperature phase. Thus, according to our calculations hopping elements in the high-temperature phase are 0.23, 0.21, 0.39, and 0.33 eV between 1-3, 2-4, 3-3, and 4-4 Ti sites, respectively.

Estimation of exchange interaction parameters via the variation of the ground-state energy with respect to the magnetic moment rotation angle [17] results in a strong antiferromagnetic coupling of -1696 K between $\text{Ti}(1)^{3+}$ and $\text{Ti}(3)^{3+}$ cations. All other couplings are two orders of magnitudes smaller. This indicates a possible formation of the spin-singlet pairs via direct antiferromagnetic exchange between neighboring Ti(1) and Ti(3) sites. The contribution of the superexchange via O p orbitals to the Ti(1)-Ti(3) exchange coupling is found to be negligible. This was verified by calculating the exchange coupling constants with the subblocks of the LMTO Hamiltonian responsible for the Ti-O hybridization being set to zero. This calculation gave qualitatively same results for the exchange constants although the possibility for the superexchange via O p orbitals was eliminated.

4.1.3. Summary. In the LSDA+ U study [187] of the low-temperature $P\bar{1}$ phase of Ti_4O_7 showi?ehlt? a charge-ordered insulating solution with an energy gap of 0.29 eV. The total $3d$ charge separation is small (less than 0.14), whereas the

orbital-order parameter defined as the difference between t_{2g} occupancies of Ti^{3+} and Ti^{4+} cations is large and gives direct evidence for charge ordering. Ti 4s and 4p states give a strong contribution to the static “screening” of the total 3d charge separation. This effective charge screening leads to complete loss of the disproportionation between the charges at 3+ and 4+ Ti sites which is in remarkable contrast with one finding in Fe_3O_4 and Fe_2O_3 [183]. The occupied t_{2g} states of Ti^{3+} cations are predominantly of d_{xy} character (in the local cubic frame) and form a spin-singlet molecular orbital via strong direct antiferromagnetic exchange coupling between neighboring Ti(1) and Ti(3) sites of $J \approx 1700$ K, whereas the role of superexchange is found to be negligible. This is in a good agreement with small and temperature independent magnetic susceptibility in the low-temperature phase of Ti_4O_7 .

4.2. α' - NaV_2O_5 . Among other transition metal oxides vanadates have recently attracted special attention due to the observation of the low-temperature behavior typical for “heavy-fermion” compounds in LiV_2O_4 [119] and a spin-Peierls (SP) like transition in α' - NaV_2O_5 [223]. From the superstructure formation which gives rise to additional X-ray reflections at $q = (1/2, 1/2, 1/4)$ and a drop of the susceptibility below $T_c = 33$ K, it was concluded that α' - NaV_2O_5 is the second inorganic SP compound after $CuGeO_3$ [224] with the highest transition temperature yet observed. In accordance with the original structure analysis [225], the existence of two sets of inequivalent V^{5+} ($S = 0$) and V^{4+} ($S = 1/2$) sites already above T_c was assumed, and the transition was supposed to be due to singlet formation leading to a dimerization of spin-1/2 V^{4+} chains along the \vec{b} axis.

Further investigations have shown, however, that the compound does not undergo a conventional SP transition. X-ray diffraction experiments [226, 227] revealed that above T_c α' - NaV_2O_5 has a centrosymmetric $Pm\bar{m}n$ structure with one type of V site rather than noncentrosymmetric $P2_1mn$ one as it was previously supposed. This implies that the high temperature phase is a mixed-valence compound and the average oxidation state of V ions is $V^{4.5+}$. Furthermore, only one set of equivalent magnetic V sites is observed in NMR measurements [228, 229]. On the other hand, these experiments show that below T_c there exist two inequivalent V^{5+} and V^{4+} sites which can be explained by assuming that a charge-ordering (CO) transition occurs in α' - NaV_2O_5 . Thermal-expansion and specific-heat measurements [230] also provide evidence for two almost coincident phase transitions around T_c . The appearance of superimposed CO and SP transitions has been proposed within a theoretical model in [231].

Different models for the CO phase which account for spin gap formation have been proposed [231–233]. Although the low-temperature crystal structure is known by now [234], the associated CO model has not yet been determined unambiguously. Relevance of such a model can be verified by comparison of the calculated dispersion of magnetic excitations with the experimental one. Previous neutron scattering data [235] did not yet allow to distinguish between

different possibilities; more recent experiments with higher resolution have improved this possibility. The spin excitation spectra were discussed in [236]. It should be noted that the theoretical spectra are rather sensitive to the actual values of exchange constants and their reliable determination is a very important and challenging task.

The electronic structure of α' - NaV_2O_5 was intensively studied experimentally by means of optical absorption [237] and reflectivity [238, 239] as well as theoretically, based on band structure calculations [227, 240–242]. However, there is a controversial discussion about the origin of the electronic excitations. Concerning the absorption peak occurring at about 1 eV, transitions between bonding and antibonding combinations of V 3d_{xy} states [227, 238, 243], and transitions between vanadium states of different symmetry [239] as well as on-site d-d transitions between crystal-field-split vanadium 3d states [237] are proposed as a source. Furthermore, the information from the experiments appears to be insufficient in order to find a unique parameter set for the description of the electronic structure in α' - NaV_2O_5 .

4.2.1. Structure. α' - NaV_2O_5 crystallizes in an orthorhombic unit cell with the lattice constants $a = 11.318$ Å, $b = 3.611$ Å and $c = 4.797$ Å [244]. The vanadium atoms and their five nearest neighbored oxygen atoms build slightly distorted VO_5 pyramids which are connected by their corners along the b direction as well as by their corners and edges along the a direction as shown in Figure 25(a). The resulting pyramid layers in the ab -plane are separated by sodium atoms. The weak bonds between the vanadium oxide layers and the sodium layers are the reason for the good cleavage behavior in the plane perpendicular to the c direction. The projection of the vanadium and the oxygen atoms of a single pyramid layer onto the ab -plane, excluding the oxygen atoms on the tips of the pyramids, delivers the atomic configuration as illustrated in Figure 25(b). This approach points up the ladder structure in which adjacent ladders are shifted by half of the lattice parameter b in the b direction (see dashed lines in Figure 25(b)).

4.2.2. LDA Bands and TB Parameters. The calculated LDA band structure and total DOS of α' - NaV_2O_5 are presented in Figure 26. The lower part of the valence band is formed mainly by O 2p states with a bonding hybridization with V 3d states. It is separated by a gap of ≈ 3 eV from the bottom of V 3d states which give predominant contribution to the bands at and up to ≈ 4 eV above the Fermi level. It should be noted that in contrast with experimental data LDA predicts α' - NaV_2O_5 to be metallic.

Contributions from states of different symmetry (d_{xy} , d_{xz} , ...) to the density of V d states are shown together with the density of O p states in Figure 27 [245]. Compare again Figure 28 for the orientation of the relevant orbitals with respect to the lattice, in particular the vanadium-oxygen xy -plane. The two V d bands crossing the Fermi level and the next two less than one eV above are formed mainly by V d_{xy} states with O_R p states giving significant contribution to the upper two. In a simplest tight-binding (TB) model which

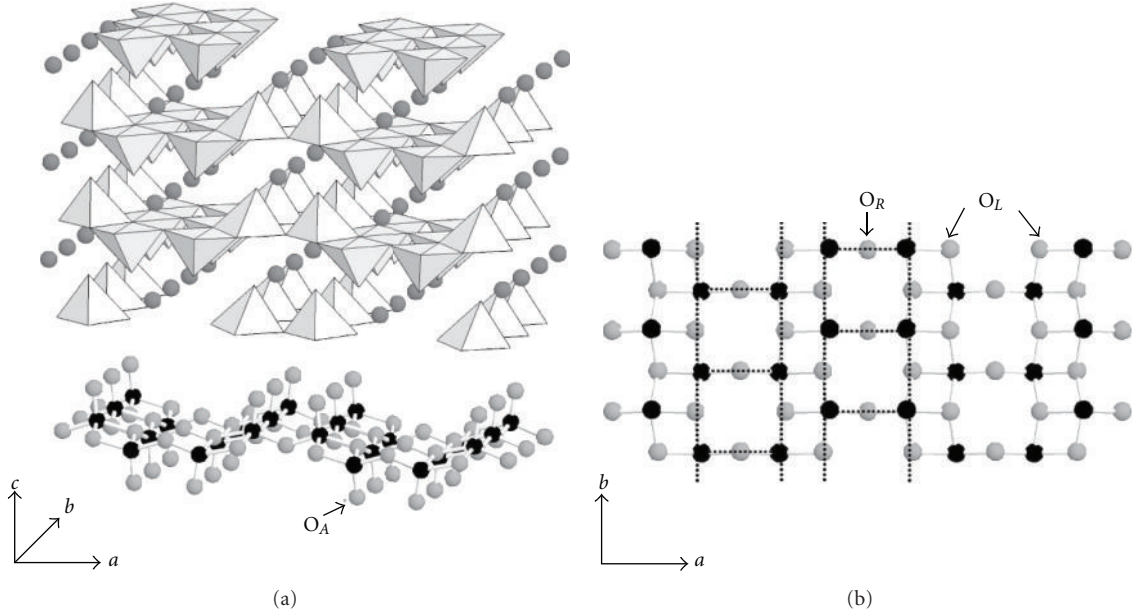


FIGURE 25: Crystal structure of α' - NaV_2O_5 . Vanadium atoms are shown as black spheres and oxygen atoms as grey spheres. (a) Layers of distorted VO_5 pyramids (upper part) separated by sodium ions (dark grey spheres) and the atomic ordering of a single vanadiumoxide layer (lower part). (b) Projection of a single VO layer onto the ab -plane, excluding the apex oxygens. The ladder structure is illustrated by the dashed lines.

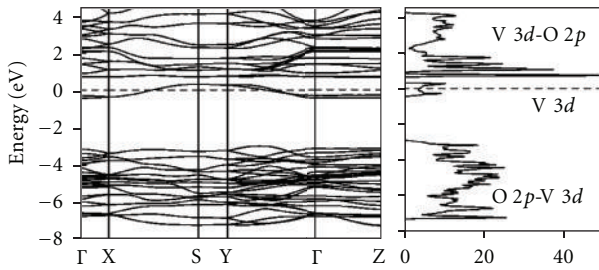


FIGURE 26: LDA band structure and the total DOS calculated for α' - NaV_2O_5 [245].

takes into account only the hybridization of V d states with p states of the nearest O atoms and neglects the distortion and tilting of the VO_5 pyramid, the V d_{xy} orbital forms $dp\pi$ bonds with the p_y orbital of the O_R atom and $p_{x,y}$ orbitals of the O_L atoms in the base of the pyramid and does not hybridize with the nearest to V apex oxygen (O_A above and below the drawing plane of Figure 28). The states in the energy range 1-2 eV are mainly of V $d_{xz,yz}$ character. They are shifted to higher energy relative to V d_{xy} states by a small $dp\sigma$ contribution of antibonding hybridization with $p\sigma$ orbitals of the O atoms forming the base of the pyramid, which is due to a small displacement of the V ions out of the basal plane of the pyramid. Finally, the bands above ≈ 2 eV originate from V $3d_{z^2}$ and $3d_{x^2-y^2}$ states which form $dp\sigma$ antibonding states with $\text{O}_A p_z$ and $\text{O}_{R,L} p_{x,y}$ orbitals, respectively. It is interesting to note that this picture of the chemical bonding in α' - NaV_2O_5 with the bands crossing the Fermi level formed by relatively weakly hybridized V d_{xy} states is in some sense

complementary to the case of layered cuprates where the highest occupied states originate from strongly anti-bonding Cu $d_{x^2-y^2}$ -O $p_{x,y}$ states of $dp\sigma$ character. Here, the V ion resides in the interior of a pyramid whose basal square has its diagonals in x and y directions and whose apex is on the z -axis. Four of the five d -orbitals of vanadium can make bonds partially of σ -character with p -orbitals of oxygen ions at the corners of the pyramid, except for the d_{xy} -orbital, which for symmetry reasons can only make π -bonds. Hence, we have π -bands around the Fermi level in an ionicity gap of σ -bands, and vanadates are π -electron systems. This explains the small bandwidths already on the mean-field level.

The two pairs of bands formed by V d_{xy} are of key importance for understanding the electronic properties of α' - NaV_2O_5 . These bands are separated by a small gap of ≈ 0.2 eV from the higher bands with the splitting between the pairs being $\approx 0.5 - 1$ eV (see Figure 26). The two bands crossing the Fermi level exhibit rather strong dispersion along Γ -Y direction and to a lesser extent along Γ -X, whereas the other two bands are almost dispersionless. All four bands show no appreciable dispersion along Γ -Z direction.

An effective TB model constructed so as to reproduce the calculated band structure is a very useful tool which helps to understand the details of the chemical bonding and can be used as a basis for construction of more involved many-body Hamiltonians. Such a TB model for the four lowest-lying V $3d$ bands in α' - NaV_2O_5 was proposed in [227]. This simple model written in terms of effective V-V hopping integrals reproduces well the dispersion of the lower pair of the bands and the average splitting between the pairs. However, it fails to account for the strongly suppressed dispersion of the upper two bands along Γ -Y direction. Also, the model

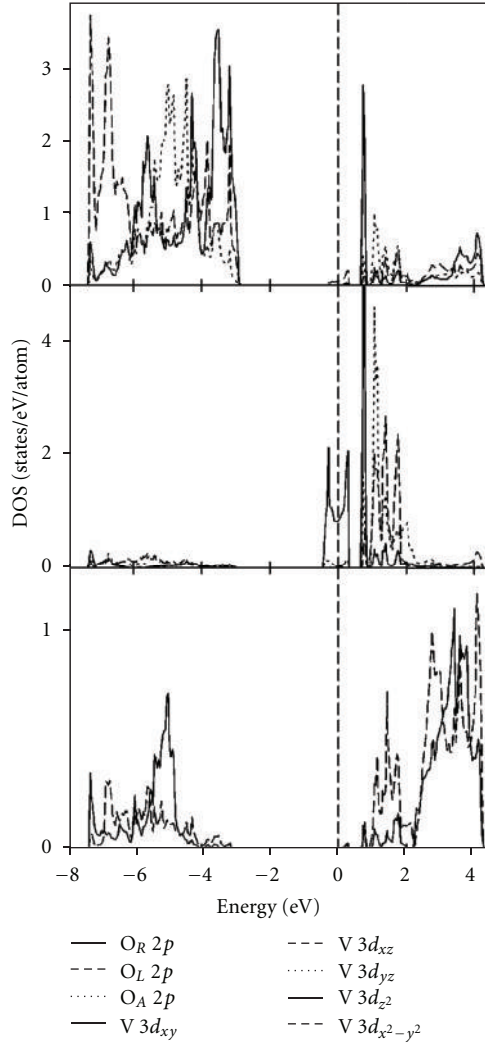


FIGURE 27: DOS curves calculated for V 3d states of different symmetry and for 2p states of inequivalent oxygen sites in α' - NaV_2O_5 [245].

contains the hopping terms between rather distant V atoms, and it is difficult to estimate in advance which of these terms should be included in the model.

As follows from the analysis of DOS (Figure 27) and the LMTO eigenfunctions, relevant for the TB model are V d_{xy} , $O_R p_y$, and $O_L p_{x,y}$ orbitals. To distinguish between two types of O_L atoms surrounding a V site, we shall use where necessary the notation O'_L for the oxygen atom lying at the continuation of the V- O_R -V rung whereas the atoms placed along the V chain running along b direction will be still denoted as O_L . With the appropriate choice of a unit cell neither of V d_{xy} - $O'_L p_y$ bonds crosses the cell boundary and the $O'_L p_y$ orbitals can be excluded from the model, their effect being taken into account implicitly via renormalization of remaining hopping terms. In other words d_{xy} in our model is the antibonding V d_{xy} - $O'_L p_y$ molecular orbital (MO) rather than atomic-like V d_{xy} orbital.

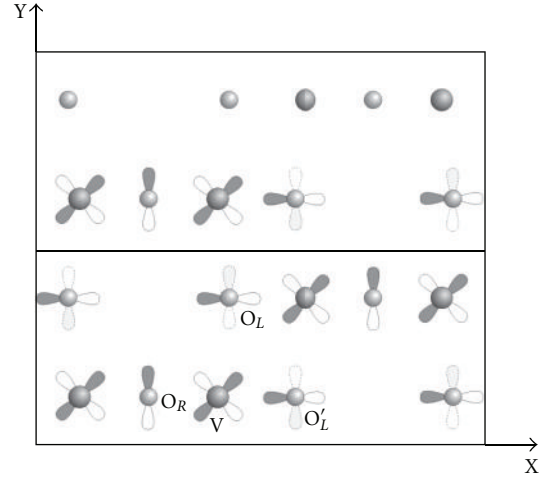


FIGURE 28: Schematic representation of the orbitals used for the extended TB model. $O'_L p_y$ orbitals included implicitly via renormalization of the other hopping terms are plotted by dashed line [245].

The dispersion of the lower pair of V d_{xy} bands can be reproduced already within the TB model which includes only four hopping matrix elements (see Figure 29(a)). Strong V d_{xy} - $O_R p_y$ hybridization ($t_{VO_R} = 1.7$ eV) is responsible for the splitting of the four bands into two subbands. The dispersion along Γ -Y direction is due to V d_{xy} - $O_L p_x$ hopping ($t_{VO_L} = 1.0$ eV), whereas the band crossing in this direction is provided by the direct σ -hopping between $O_L p_x$ orbitals ($t_{O_L O_L} = 0.6$ eV). Finally, the small matrix element $t_{VV} = 0.032$ eV between V d_{xy} orbitals governs the dispersion along Γ -X direction. As was mentioned above we assume in the model that d_{xy} is an antibonding V d_{xy} - $O'_L p_y$ MO and the effective t_{VV} term includes not only direct d_{xy} - d_{xy} hopping but also the hopping term of the same sign between $O_L p_y$ orbitals participating in the MO. Moreover, as O_L atoms are slightly shifted away from the V chains running along b direction the hopping terms between V d_{xy} orbital and p_y orbital of O_L atoms from the same chain give nonvanishing contribution to t_{VV} . The sign of this term is determined by the direction of the out-of-chain displacement of O_L atoms. For the experimentally observed displacement toward the V atom from another ladder the sign is opposite to the sign of the direct d_{xy} - d_{xy} hopping, thus decreasing the effective t_{VV} .

To verify whether the compensation of the individual contributions to t_{VV} really occurs, the calculations with an enlarged out-of-chain displacement of O_L atoms along a direction was performed. As a result of the O_L shift V- O_L and O'_L - O_L distances decrease by 1.5% and 1.8%, respectively, while the V-V distances remain unchanged. If the V d_{xy} - $O_L p_y$ hybridization was weak, one would expect a small increase of the splitting of the lower pair of V d_{xy} bands at the Γ point due to stronger p_y - p_y hopping. The calculated splitting decrease, however, from 0.15 eV for the original structure to 0.08 eV for the distorted one indicating that the effective t_{VV} is very sensitive to the relative position of V and O_L atoms.

As can be seen from Figure 29(a) the TB model with the four hopping terms gives nearly the same dispersion for both lower and upper pairs of the V d_{xy} bands, and additional hopping terms should be included to reproduce the flatness of the upper bands. We found that their strong dispersion along Γ -Y direction can be suppressed (see Figure 29(b)) by “switching on” $O_R p_y$ - $O_L p_x$ ($t_{O_R O_L} = 0.8$ eV) and $O_R p_y$ - $O_R p_y$ ($t_{O_R O_R} = 0.4$ eV) hybridizations, both at least in part of σ -character. As the effect of both of these terms on the dispersion is similar, the values of $t_{O_R O_L}$ and $t_{O_R O_R}$ were determined using their ratio estimated from the distances between the corresponding oxygen atoms and the mutual orientation of the orbitals. The remaining dispersion of the upper pair of bands along Γ -X is canceled by the hopping term $t'_{V O_R} = 0.025$ eV between the V d_{xy} MO and p_y orbital of the O_R atom from another ladder.

The dispersion of the lower pair of the V d_{xy} bands is not affected by the three above-mentioned hopping terms as all of them act via $O_R p_y$ orbitals which give only a small contribution to the corresponding wave functions. The analysis of the eigenfunctions shows that at the Γ point the V d_{xy} orbitals centered at the ends of a rung have the same phases and, consequently, they are orthogonal to the $O_R p_y$ orbital. At the arbitrary k point the orthogonality is not perfect due to the weak interladder coupling along a direction, but as the corresponding hopping term t_{VV} is very small the contribution of $O_R p_y$ orbitals to the wave function remains negligible. On the contrary, the $O_R p_y$ orbitals contribute strongly to the wave functions of the upper pair of the V d_{xy} which are π -antibonding with respect to V d_{xy} - $O_R p_y$ hybridization.

The conclusion can be derived that these additional hopping terms are not important when describing the low-energy electronic excitations in α' - NaV_2O_5 . This is true, however, only for the high-temperature phase in which all V sites are equivalent. Below T_c when V^{4+} and V^{5+} ions can occupy different ends of the same rung, the $O_R p_y$ contribution to the wave functions corresponding to the lowest V d_{xy} bands can be substantial and the dispersion of these bands will be determined to a great extent by the hopping terms in which the $O_R p_y$ orbitals are involved.

Figure 29(b) shows that the proposed extended TB model reproduces the dispersion of all four V d_{xy} bands [245]. The hopping terms obtained from comparison of this model to a TB model written in terms of effective V-V interactions are close to those given in [227]. An important difference is the appearance of an additional hopping term $t_d = 0.085$ eV which couples d_{xy} orbitals of V atoms placed at the opposite ends of consecutive rungs of a ladder. This term has been found to be of the same absolute value as the hopping along the leg of a ladder t_{\parallel} but of the opposite sign and is necessary to compensate the dispersion of the upper pair of bands along Γ -Y direction produced by the later. As both t_{\parallel} and t_d give the contribution of the same sign to the dispersion of the lower bands, we have obtained the value of $t_{\parallel} = -0.085$ eV which is two times smaller compared to the value of -0.17 eV found in [227]. It should be pointed out that the comparatively large t_d can be responsible for exchange coupling of V^{4+} ions along the b direction which is necessary

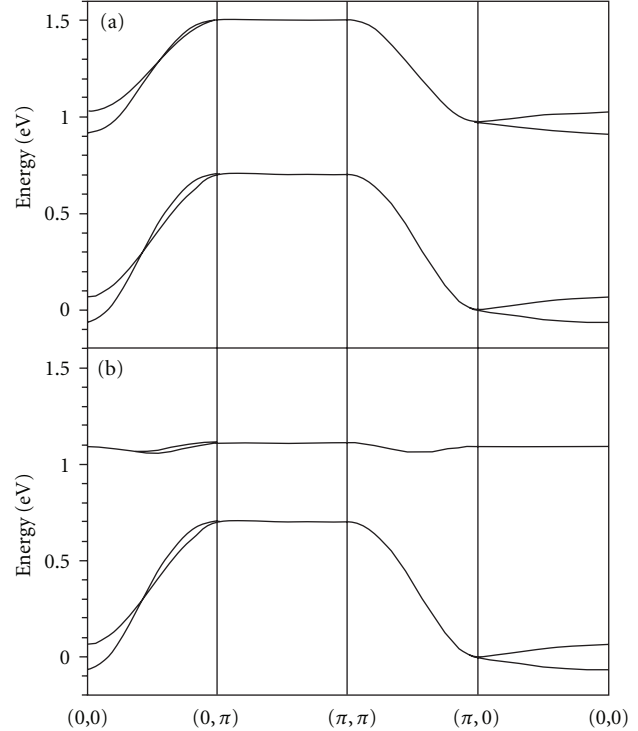


FIGURE 29: (a) The dispersion of the V d_{xy} bands calculated from the extended TB model with four hopping terms $t_{V O_R} = 1.7$ eV, $t_{V O_L} = 1.0$ eV, $t_{O_L O_L} = 0.6$ eV, and $t_{VV} = 0.032$ eV (see text). (b) The same as (a) but with additional hopping terms $t_{O_R O_L} = 0.8$ eV, $t_{O_R O_R} = 0.4$ eV, and $t'_{V O_R} = 0.025$ eV which suppress the dispersion of the upper pair of the bands [245].

to explain the strong dispersion of magnetic excitations along Γ -Y direction in the case of the ordering of V^{4+} into zigzag chains which is considered as a possible low-temperature structure of α' - NaV_2O_5 .

4.2.3. LDA+U Results. The electronic structure of the low-temperature phase of α' - NaV_2O_5 was studied using the LDA+U approach [245]. We restricted ourselves to consideration of CO structures which are possible in the unit cell doubled along the b -axis, thus neglecting the experimentally observed increase of the unit cell along a and c axes. The lattice distortion caused by CO was not taken into account and the atomic positions determined for the high-temperature phase [226] were used. The LDA+U calculations were performed using the value of 3 eV for $U_{\text{eff}} = U - J$. The values of screened on-site Coulomb $U = 4.1$ eV and exchange $J = 1.1$ eV integrals were determined from supercell calculations. The calculated U is significantly smaller than $U = 6.82$ eV used for V^{4+} ions in α' - NaV_2O_5 in [240] which can be explained by the fact that in the super-cell calculations V d_{z^2} and $d_{x^2-y^2}$ orbitals which form rather strong $dp\sigma$ bonds with O p orbitals were allowed to participate in the screening of excessive V d charge, thus providing more perfect screening compared to the case when all V d electrons are treated as localized [246].

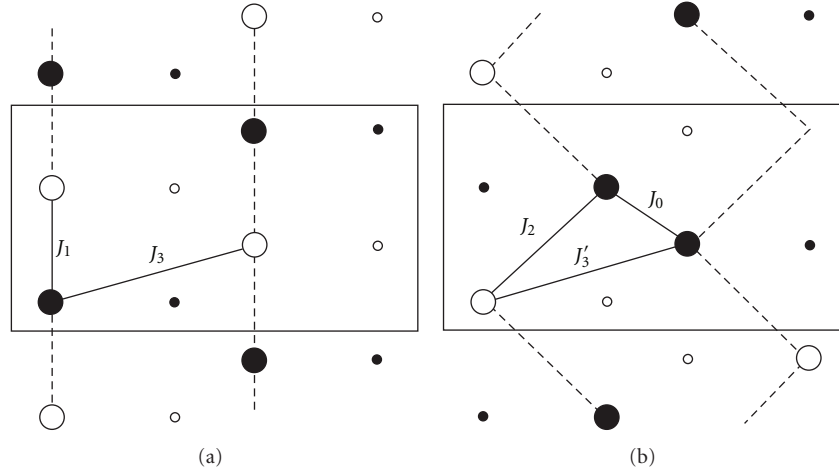


FIGURE 30: (a) In-line charge ordering of V^{4+} ions. (b) Zig-zag charge ordering of V^{4+} ions [245]. Big balls: V^{4+} spinup, big circles: V^{4+} spindown, and small balls and circles: V^{5+} . The nominally V^{5+} ions inherit a small spin moment from their V^{4+} partners in the same rung; see text.

The electronic structure and total energies were calculated for two models for the CO phase which have commonly been considered as possible candidates for the low-temperature structure [245]. In the first model (Figure 30(a)) magnetic V^{4+} ions form in-line chains along b direction separated by nonmagnetic chains of V^{5+} ions. The second one (Figure 30(b)) consists of zig-zag chains of V^{4+} ions occupying alternating ends of consecutive rungs of a ladder. For each of these models different kinds of magnetic ordering of V^{4+} moments were considered.

The band structure and the total DOS for the model with the in-line CO and antiferromagnetic (AF) ordering of V^{4+} magnetic moments along the chains (cf. Figure 30(a)) are shown in Figure 31(a). The two highest occupied bands which are doubly degenerate due to AF order are formed by d_{xy} orbital combinations of the four V^{4+} ions, the d_{xy} states with opposite spin are pushed to higher energies by the on-site Coulomb repulsion U . These almost dispersionless bands are ≈ 2 eV above the Fermi level and separated by an energy gap of ≈ 1 eV from the lowest unoccupied V^{5+} d_{xy} band. In the case of ferromagnetic (F) intrachain ordering and AF ordering along a direction (Figure 31(b)) the hybridization between V^{4+} d_{xy} orbitals along the chains via $O_L p_x$ orbitals leads to appearance of relatively strong dispersion along Γ -Y direction. As a result of the band broadening the correlation gap decreases to 0.7 eV.

The dispersion of the highest occupied V^{4+} and the lowest unoccupied V^{5+} d_{xy} bands calculated for the zig-zag CO model with either AF (Figure 32(a), spin pattern of Figure 30(b)) or F (Figure 32(b)) ordering of V^{4+} magnetic moments along the zig-zag chains is very similar to that obtained for the corresponding cases within the in-line CO model. These results illustrate the importance of the above mentioned effective t_d hopping matrix element which couples d_{xy} orbitals of V ions occupying the opposite ends of consecutive rungs of a ladder. As in the CO phase the V ions at the ends of a rung are no longer equivalent, in

contrast with the LDA calculations $O_R p_y$ orbitals contribute to the wave functions of the lowest V^{4+} d_{xy} bands and the hybridization via $O_R p_y$ orbitals responsible for t_d is “switched on” for these bands. Note that the resulting features of the band structures shown in Figure 32 are obtained from full LDA+ U calculations independent of the tight-binding model and hence prove the correctness of our tight-binding model in this respect.

Another important consequence of the strong hopping across the rung is that the V^{4+} d_{xy} orbital can hybridize via $O_R p_y$ with the unoccupied d_{xy} orbital of the V^{5+} ion from the same rung and the latter give a substantial contribution to the wave functions of the occupied V^{4+} d_{xy} bands. This partial delocalization of V^{4+} d_{xy} states can lead to appearance of relatively long-range terms in a TB model describing the effective V^{4+} d_{xy} - V^{4+} d_{xy} hopping in the case of the CO structure with one V^{4+} ion per rung. The degree of the delocalization depends on the relative energy positions of the V^{4+} and V^{5+} d_{xy} states which can be rather sensitive to the changes of the V-O distances in the VO_5 pyramid caused by charge ordering. As a result of the V^{4+} d_{xy} - V^{5+} d_{xy} hybridization the V^{4+} spin magnetic moment, defined as an integral of the electron spin density over the atomic sphere surrounding the ion, is smaller than the value of $1 \mu_B$ expected for spin 1/2 and is equal to $\approx 0.9 \mu_B$ for both zig-zag and in-line CO models. However, together with the moment of about $0.1 \mu_B$ inside the V^{5+} sphere, this gives the total magnetic moment of $1 \mu_B$ per rung. Just as for the TB model this smearing of the V^{4+} magnetic moment over the rung can affect the parameters of the effective model for exchange interactions between V^{4+} spins in the CO phase of α' - NaV_2O_5 .

The total energies obtained from the LDA+ U calculations for the CO models with different kinds of magnetic order are summarized in Table 8. The lowest total energy is calculated for the zig-zag CO model with AF alignment of

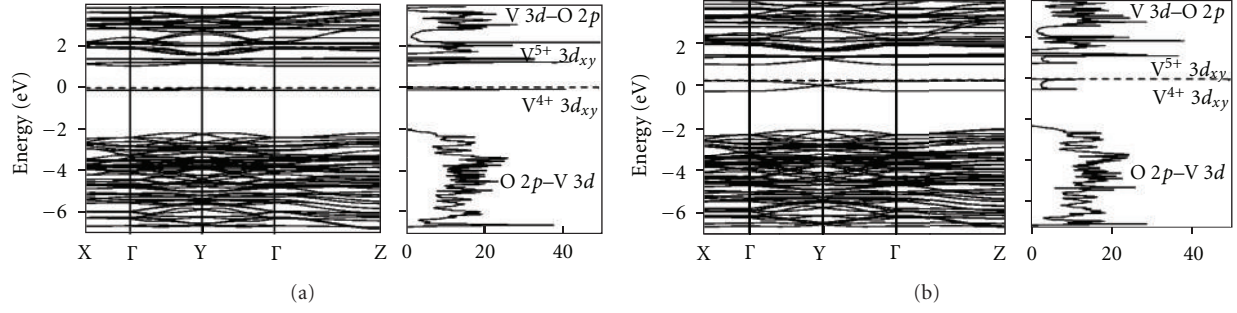


FIGURE 31: LDA+ U band structure and the total DOS for two different kinds of magnetic ordering of V^{4+} moments within the in-line CO model: (a) AF intra-chain ordering; (b) F intra-chain and AF inter-chain ordering [245].

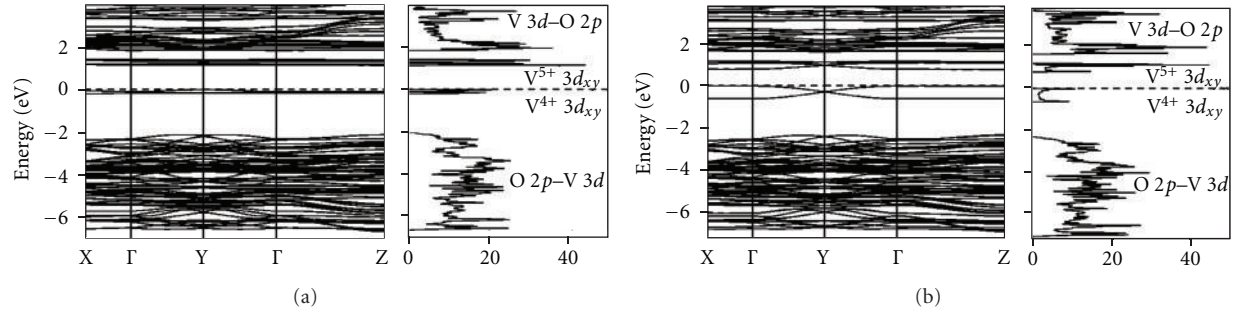


FIGURE 32: LDA+ U band structure and the total DOS for two different kinds of magnetic ordering of V^{4+} moments within the zig-zag CO model with (a) AF intra-chain and F inter-chain ordering and (b) F intra-chain and AF inter-chain ordering [245].

V^{4+} moments along the chains and F interchain ordering (E_{af}^z , Figure 30(b)), the energy of the same model but with AF inter-chain ordering (E_{aa}^z) being only 2 meV higher. The difference between the lowest energies of the considered CO models is found to be 15.5 meV. Comparison of the total energies of the models with different types of magnetic order indicates clearly that AF intra-chain magnetic order is preferable for both in-line and zig-zag CO models. Calculations were also performed for some other models for CO possible in the $1 \times 2 \times 1$ super-cell, but their total energies were found to be much higher than those of the zig-zag and in-line models. For example, an interchange of V^{4+} and V^{5+} at every second ladder in the in-line CO model leads to double chains along b direction. This increases the total energy by 125 meV. Another possible type of CO is a structure with one or two rungs doubly occupied by V^{4+} ions. It was found, however, that formation of the doubly occupied rung results in the energy loss of about 100 meV.

The conclusion derived from the LDA+ U calculations that the zig-zag CO model (Figure 30(b)) is more favorable than the in-line one is supported by recent experimental data on the temperature dependence of the dielectric constant in α' - NaV_2O_5 [247, 248]. The observation of step-like anomalies at T_c suggests that the low-temperature structure is of antiferroelectric type which is consistent with the zig-zag CO model. The in-line CO model, on the other hand, corresponds to the ferroelectric ordering with the spontaneous electric polarization along a -axis in which case a peak in

TABLE 8: The total energies per formula unit calculated with the LDA+ U method for various models for charge and magnetic ordering in α' - NaV_2O_5 [245]. The lowest energy of the zig-zag CO model with AF intrachain and F interchain magnetic ordering is taken as zero energy.

Model	Charge order	Magnetic order		E (meV)
		Intra	Inter	
E_{af}^z	Zigzag	AF	F	0.0
E_{aa}^z		AF	AF	2.0
E_{ff}^z		F	F	13.9
E_{fa}^z		F	AF	20.8
E_a^i	Inline	AF	—	15.5
E_{ff}^i		F	F	27.5
E_{fa}^i		F	AF	32.5

the temperature dependence of the dielectric function should be observed.

4.2.4. Effective Exchange Constants. Effective exchange constants between V^{4+} spins are necessary input values for theoretical models aimed at the description of magnetic excitations in α' - NaV_2O_5 . In [245] they were estimated by mapping the LDA+ U total energies onto the mean-field energy of a localized Heisenberg model. Assuming that the total energy differences between the configurations with the same

CO but different orientations of V^{4+} magnetic moments are due to the change of the magnetic energy written as a sum of pair interactions of the Heisenberg form, one can express the exchange constants in terms of the total energy differences. The corresponding expressions for the exchange parameters introduced for the zig-zag (J_0, J_2) and in-line (J_1) CO models (Figure 30) are

$$\begin{aligned} J_0 &= -2\left(\left(E_{aa}^z - E_{af}^z\right) + \left(E_{fa}^z - E_{ff}^z\right)\right), \\ J_1 &= \left(E_{ff}^i - E_a^i\right) + \left(E_{fa}^i - E_a^i\right), \\ J_2 &= \left(E_{fa}^z - E_{af}^z\right) + \left(E_{ff}^z - E_{aa}^z\right), \end{aligned} \quad (21)$$

where all the energies are given per formula unit, the upper index specifies the CO model, whereas the first and the second letters in the subscript denote the kind of the intra- and inter-chain magnetic ordering, respectively. Here we assume additionally that the absolute value of V^{4+} spin is equal to 1/2 and remains constant. Similar expressions can be written for J_3 and J'_3 exchange parameters.

The effective exchange coupling parameters calculated from the LDA+ U total energies are given in Table 9. It was found that the most important parameters are $J_1 = 29.0$ meV and $J_2 = 32.7$ meV responsible for the exchange coupling along the in-line and zig-zag chains, respectively. While the exchange coupling along the in-line chains is provided by the superexchange via $O_L 2p_x$ orbitals, the mechanism for J_2 is less obvious. It can be explained by the effective hopping of $V^{4+} 3d_{xy}$ orbitals via $O_R 2p_y - O_L 2p_x$ and $O_R 2p_y - O_R 2p_y$ paths taking into account the large values of the corresponding hopping terms $t_{O_R O_L}$ and $t_{O_R O_R}$ obtained from the TB fit to the LDA results. The important point here is that, in contrast to the LDA results, in the case of the CO phase with inequivalent V ions at the ends of a rung, the $O_R 2p_y$ orbital contributes to the wave functions of occupied $V^{4+} d_{xy}$ bands. An additional contribution to J_2 can appear as a result of the above-mentioned partial delocalization of the $V^{4+} d_{xy}$ orbital over the rung due to its hybridization with the d_{xy} orbital of the V^{5+} ion. Then, these delocalized orbitals of adjacent rungs can hybridize via $O_L p_x$ orbitals which gives an additional channel for the interaction between V^{4+} spins.

The calculated exchange constants are smaller than the value of 560 K (48.3 meV) estimated from the high-temperature magnetic susceptibility using the formulas for spin-1/2 chain [223]. However, the present calculations were performed for the case of nearly complete charge-ordering, and it is difficult to compare the results with those obtained for the high-temperature phase with the average oxidation state of V ions being $V^{4.5+}$. Another possible reason for the discrepancy is that the on-site Coulomb repulsion U derived from the super-cell calculations may be overestimated leading to underestimated values of the exchange parameters. Indeed, J_1 and J_2 calculated with $U_{\text{eff}} = 2$ eV are about 60 meV which is already larger than the experimental value.

An important consequence of the fact that the intra-chain exchange coupling for both CO models is of comparable strength is that the experimentally observed strong dispersion of magnetic excitations in Γ -Y direction can be

TABLE 9: The effective exchange coupling constants calculated from the LDA+ U total energies for the in-line and zig-zag CO models [245].

	CO	J (meV)
J_1	In-line	29.0
J_3		-5.0
J_0	Zig-zag	-18.0
J_2		32.7
J'_3		-4.9

explained not only in the case of the in-line CO model but also within the CO model with the zig-zag ordering of V^{4+} ions.

The inter-chain coupling is determined by ferromagnetic effective exchange constants $J_3 = -5.0$ meV for the in-line CO model and $J_0 = -18.0$ meV and $J'_3 = -4.9$ meV for the zig-zag one. This surprisingly large value of J_0 questions the applicability of the model of weakly coupled AF V^{4+} zig-zag chains. However, at least for small deviations from the ground state with AF intra-chain ordering, the energy gain from ferromagnetic alignment of the V^{4+} moments coupled by J_0 is almost exactly compensated by the energy loss due to antiparallel alignment of the moments coupled with J'_3 . As a result of this compensation the total energies E_{af}^z and E_{aa}^z of two configurations with different alignment of the nearest V^{4+} moments differ by 2 meV only.

The effective hopping between d_{xy} orbitals of the nearest V ions is much smaller than the hopping along the ladders, and it can hardly account for the large ferromagnetic J_0 . The dominant mechanism responsible for this interaction is the almost 90-degree exchange caused by the hybridization of $V^{4+} d_{xy}$ orbital via $O_L p_{x,y}$ states to unoccupied $d_{xz,yz}$ and $d_{x^2-y^2}$ orbitals with the same spin projection of the V^{4+} ion from the adjacent ladder. As the latter states are split by ≈ 1 eV by the on-site exchange coupling the energy gain from this hopping depends on the relative orientation of the V^{4+} magnetic moments and reaches its maximal value when the moments are ferromagnetically aligned. To verify that this mechanism is the most important one, we have determined J_0 from test calculations with the on-site exchange interaction switched off which was achieved by averaging the LSDA exchange-correlation potential for majority- and minority-spin electrons. J_0 calculated in this way was found to be ten times smaller in absolute value and of opposite sign which confirms that it is really governed by the on-site exchange. On the other hand, calculated in the same manner J_2 does not change so drastically as it is determined mainly by the on-site Coulomb repulsion U .

As the V^{4+} ions coupled with J_3 and J'_3 occupy equivalent crystallographic positions, one can suppose that the values of these exchange parameters should be close to each other and their difference can be used to check the numerical accuracy of the total energy calculations. Indeed, the calculated values of J_3 and J'_3 differ only slightly which confirms that the calculations were performed with sufficient accuracy.

This relatively strong exchange coupling, considering the large distance between the corresponding V^{4+} ions, is caused by the partial redistribution of a V^{4+} spin between d_{xy} orbitals of V^{4+} and V^{5+} ions from the same rung. The mechanism responsible for J_3 and J'_3 is similar to that for J_0 with the important difference that for the former the hybridization path between d_{xy} and unoccupied $d_{xz,yz}$ orbitals is longer and includes additionally $O_R p_y$ and $V^{5+} d_{xy}$ states which leads to a significant decrease of J'_3 compared to J_0 .

4.2.5. Optical Conductivity. Authors of [249] studied the electronic structure and optical properties of the ladder compound α' - NaV_2O_5 by a joint experimental and theoretical approach. The momentum-dependent loss function was measured using electron energy-loss spectroscopy in transmission. The optical conductivity derived from the loss function by a Kramers-Kronig analysis agrees well with our results from LDA+ U band structure calculations applying an antiferromagnetic alignment of the V $3d_{xy}$ electrons along the legs and an on-site Coulomb interaction U between 2 and 3 eV. The decomposition of the calculated optical conductivity into contributions from transitions between selected energy regions of the DOS reveals the origin of the observed anisotropy of the optical conductivity.

In comparison with V_2O_5 with a similar network of linked VO_5 pyramids, the Na atom provides an additional electron to the valence band of α' - NaV_2O_5 . Since in V_2O_5 the bands, formed by the O $2p$ states, are completely filled and the energetically lowest lying unoccupied bands are formed by the V $3d_{xy}$ states [249], the additional electron in α' - NaV_2O_5 occupies the rather localized V $3d_{xy}$ states, which determine to a great extent the unique properties of the compound. Due to the localized nature of the V $3d$ electrons, the Coulomb correlations between them are rather strong and, as a consequence, conventional LSDA calculations fail to describe properly the electronic structure of α' - NaV_2O_5 . In the unit cell corresponding to the centrosymmetric $Pm\bar{m}n$ structure of the high-temperature phase, a nonmagnetic metallic solution is obtained in contradiction with the experimental data. If an antiferromagnetic (AFM) order of V magnetic moments along the b direction is allowed by an appropriate doubling of the unit cell, an energy gap opens in the LSDA band structure. However, the value of the energy gap is strongly underestimated. Besides, there is no experimental evidence for the existence of AFM order in α' - NaV_2O_5 .

An efficient way to take into account the strong correlations in the V $3d$ shell is to use the LDA+ U approach. However, this method is usually applied to ordered compounds and an additional assumption should be made in order to study the electronic structure and the optical properties of the high-temperature phase of α' - NaV_2O_5 . Since, according to the experimental data, there is no charge ordering above T_c and all V sites are equivalent, we have assumed that the effective one electron potential at each V site is the same and equal to the average of the LDA+ U potentials for V^{4+} and V^{5+} ions. In other words, the orbital-dependent potential is calculated using the occupation numbers averaged formally

over the V^{4+} and V^{5+} orbital occupation numbers. Applying U , the partially occupied V d_{xy} orbitals are the most affected orbitals. The average occupation of the majority-spin d_{xy} orbitals is close to 0.5, and their energy position remains unchanged as compared to LDA, whereas the unoccupied minority-spin d_{xy} orbitals are shifted upwards by $U/2$. As a result, an insulating behavior with the magnetic moment of $0.5 \mu_B$ per V atom or $1 \mu_B$ per rung is immediately obtained which is independent of the kind of magnetic order along the \mathbf{b} axis. One can say that the on-site Coulomb repulsion effectively suppresses the occupation of the d_{xy} orbitals with the opposite spin at each rung.

The effect of the absence of a long-range AFM order in the high-temperature phase of α' - NaV_2O_5 on the electronic structure and optical properties was modeled by performing calculations for spin waves defined by a vector $\mathbf{u} = (0, u_y, 0)$ with u_y varying from 0.5, corresponding to AFM order of V magnetic moments along the b direction, to 0 at which all V magnetic moments are ferromagnetically aligned. In these calculations all θ_t were set to be zero whereas the ϕ_t were chosen in such a way that the V ions situated at the same rung had the same magnetization direction. It has been found that the relative orientation of the magnetization at V sites of neighboring ladders, which is also determined by ϕ_t , has only minor effect on the calculated band structure.

The calculations were iterated to self-consistency for $u_y = 0.5$ and then one iteration was performed for spin waves with other values of u_y [249]. The comparison of the band energies confirmed that the ground state of the system is antiferromagnetic in accordance with previous estimates for the exchange coupling constants between V spins in the b direction.

The densities of the V $3d$ and O $2p$ states, calculated for $U_{\text{eff}} = 3$ eV and AFM order of V magnetic moments along the b direction are shown in Figure 33 [249]. In Figure 33(b) the density of the V $3d$ states calculated for $u_y = 0.3$ (dashed lines) are also shown. Here and in the following we assume that the magnetic moments of the V ions situated at the same rung are ferromagnetically ordered. The states in the energy range from -6.5 to -2 eV are formed mainly by the O $2p$ states (Figure 33(a)) with a bonding hybridization with the V $3d$ states. The V $d_{xz,yz}$ states dominate in the 1.8–3 eV range, while the states with V $d_{3z^2-y^2}$ and V $d_{x^2-y^2}$ characters are shifted to higher energies due to the comparatively strong hybridization with O $2p$ states and form the upper part (>3 eV) of the conduction band, shown in Figure 33(b). The main differences in the structure of the DOS as compared to V_2O_5 are caused by the additional electrons occupying the V d_{xy} bands which are empty in the case of V_2O_5 . Since the change in the occupation of the V d_{xy} states is the main source of the differences between the optical spectra and other physical properties of these compounds, in the following we will focus our attention on the states originating from the V d_{xy} orbitals. The narrow peak in the majority-spin V $3d$ DOS just below the Fermi level (Figure 33(b)) originates from that combination of the $3d_{xy}$ orbitals of the two V atoms on the same rung, which is orthogonal to the $2p_y$ orbital of the O_R atom in the center of the rung. The corresponding antibonding V $3d_{xy}-O_R 2p_y$

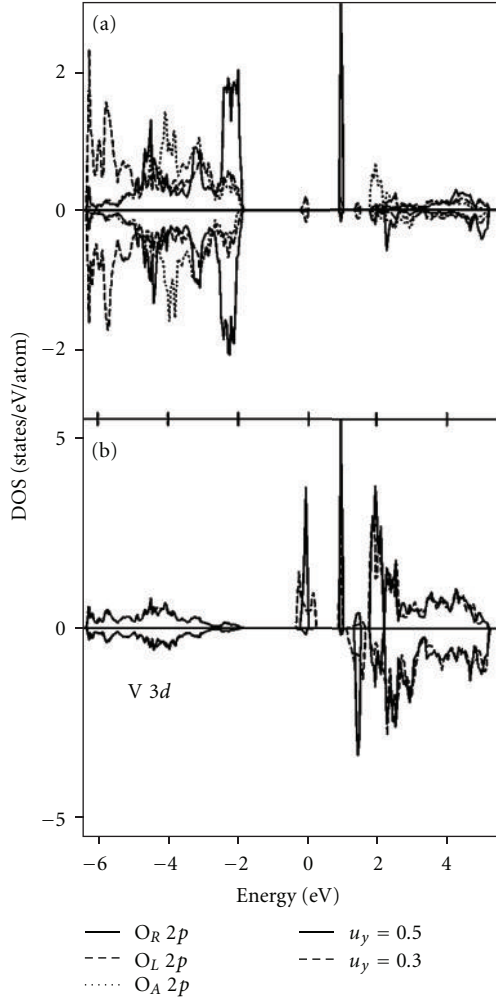


FIGURE 33: Spin-projected densities of the $2p$ states of the three inequivalent oxygen atoms (a) and the $V 3d$ states (b) in α' - NaV_2O_5 calculated for $U_{\text{eff}} = 3$ eV and AFM order of V magnetic moments along the b direction. For comparison the densities of the $V 3d$ states calculated for $u_y = 0.3$ are also shown by dashed lines in (b). All energies are given relative to the valence-band maximum [249].

states are responsible for the DOS peak at 1 eV. In terms of the effective V - V hopping these two peaks result from the bonding and antibonding combination of the $V 3d_{xy}$ states, respectively, and the energy separation between them is determined by $t_a = 0.38$ eV acting across the rung. Here, for the effective V - V hopping terms we use the values obtained from a tight binding fit to the LDA band structure calculated with the LMTO method. The minority spin d_{xy} states of bonding character are shifted to higher energy by the effective Coulomb repulsion and lie above the antibonding $d_{1,xy}$ peak. While the energy of the latter is governed by t_a and thus does not depend on U_{eff} , the relative position of the minority-spin d_{xy} states depends on the exact value of U_{eff} . Finally, the peak at ~ 2.5 eV arising from the antibonding $d_{1,xy}$ states is almost lost in the contributions from the other states of the conduction band, mainly formed by the remaining $V 3d$ states hybridized with $O 2p$ states.

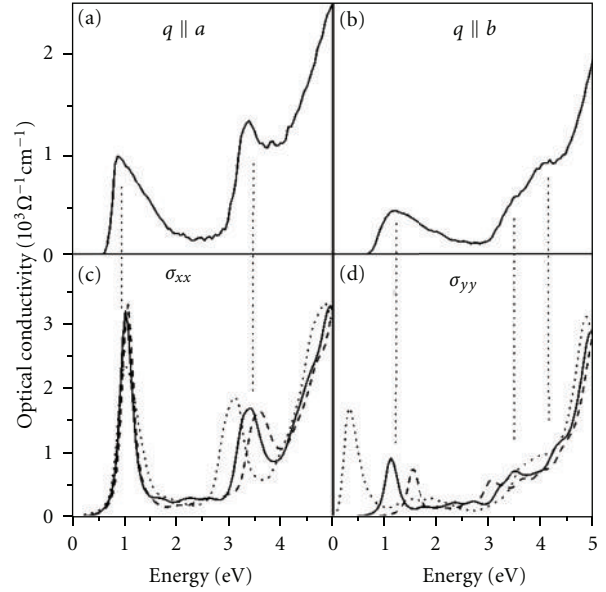


FIGURE 34: The optical conductivity σ_{xx} (c) and σ_{yy} (d) of α' - NaV_2O_5 determined by LDA and LDA+ U band structure calculations with $U_{\text{eff}} = 0$ (dotted line), 2 (solid line), and 3 eV (dashed line) compared with those derived from the experiment ((a) and (b)). The theoretical curves are broadened with a Lorentzian of 0.2 eV width. The vertical dotted lines illustrate the correspondence of the peak positions.

It should be noted that for both spin directions the width of the bonding d_{xy} peaks is much smaller than 0.7 eV, obtained from LDA calculations, because the relatively strong hybridization along the b direction governed by $t_b = 0.17$ eV is suppressed due to the AFM order. However, as u_y , which defines the magnetic structure along the b direction, decreases, the width of the peaks increases and reaches the LDA value when V magnetic moments are ordered ferromagnetically. As for the antibonding d_{xy} states, the dispersion of the corresponding bands along the Γ - Y direction is much weaker already in LDA and the width of their DOS does not depend on u_y .

In Figure 34 the optical conductivity derived by means of a Kramers-Kronig analysis from the EELS spectra with small momentum transfers ($q = 0.1 \text{ \AA}$), aligned parallel to the crystallographic a and b directions (Figures 34(a) and 34(b)), is shown together with the σ_{xx} and σ_{yy} spectra, calculated for $u_y = 0.5$ using the LSDA ($U_{\text{eff}} = 0$) and LDA+ U with $U_{\text{eff}} = 2$ and 3 eV (Figures 34(c) and 34(d)) [249]. Comparing the σ_{xx} spectra (Figures 34(a) and 34(c)) one can see that for this polarization the theoretical spectra are weakly affected by U and already the LSDA curve agrees well with the experimental one. The calculated position of the low-energy peak in σ_{xx} centered at 1 eV does not depend on U and coincides almost perfectly with the position of the corresponding experimental maximum. However, the calculations overestimate the magnitude of the peak and fail to reproduce its asymmetric shape. The peak corresponding to the experimental feature at 3.4 eV lies at slightly lower energy in the LSDA calculations and shifts upwards to ~ 3.7 eV with increasing U .

For σ_{yy} (Figures 34(b) and 34(d)) the situation is quite different. In this case the LSDA calculations result in the optical gap of 0.2 eV which is significantly smaller than the experimental value. In contrast with σ_{xx} the position of the low-energy peak is sensitive to U and becomes close to the experimental value for $U_{\text{eff}} = 2$ eV. A less strong but still noticeable dependence on U can be found in the energy range between 2.5 and 4 eV. Comparing the theoretical spectra calculated with different values of U_{eff} to the experimental ones, one can conclude that the best overall agreement between the theory and the experiment is achieved for U_{eff} lying in the range between 2 and 3 eV.

The observed correspondence between the calculated and the experimental spectra allows us to draw additional information from the detailed analysis of the theoretical spectra. In order to understand better the origins of the features of the optical conductivity and the reasons for their different dependence on the value of U , we analyzed the contributions to the optical conductivity originating from the interband transitions between the initial and final states which are formed by the V $3d_{xy}$ states. In Figure 35 the results of the decomposition of σ_{xx} ((a) and (c)) and σ_{yy} ((b) and (d)) calculated with $U_{\text{eff}} = 3$ eV are presented. The grey areas in Figures 35(a) and 35(b) show the contributions of the transitions from the occupied V $3d_{xy}$ bands. In Figures 35(c) and 35(d) the transitions with the final states restricted to the antibonding V $3d_{1xy}$ and the bonding V $3d_{1xy}$ states are denoted by light grey and grey areas, respectively. The hatched areas show the contributions from interband transitions to higher-lying V $3d$ states. The full σ_{xx} and σ_{yy} spectra are drawn by a solid line without shading, respectively.

Comparing the shaded areas in (a), (b) and (c), (d) of Figure 35, one can see that the peaks below 2 eV in both, σ_{xx} and σ_{yy} spectra, are formed by transitions with the initial states given by the occupied V d_{xy} bands (Figures 35(a) and 35(b)). However, due to different selection rules for the dipole optical transitions the final states for these transitions are quite different for both polarizations. The final states for transitions responsible for the 1 eV peak in σ_{xx} are antibonding V d_{xy} bands (Figure 35(c)). As it was mentioned above, the bonding-antibonding splitting of d_{xy} states is determined by the hybridization within a rung and is not affected by U . When the momentum transfer is parallel to the b direction the matrix elements for these transitions are zero, whereas the transitions into the unoccupied bonding d_{1xy} bands become active (Figure 35(d)). The position of the latter is sensitive to the strength of the on-site Coulomb interaction which explains the strong dependence of the position of the low-energy peak in σ_{yy} on the value of U . In a “many-body language” the $d_{1xy} \rightarrow d_{1xy}$ transition can be interpreted as excitations leading to the appearance of doubly occupied rungs.

In order to avoid misunderstanding we have to note here that due to the AFM order along the b direction the states with both spins projections contribute to the Bloch wave functions and the bands are labeled as majority and minority spin only for convenience according to the dominating contribution of the d_{xy} states of a chosen V site. In view of this remark the term “ $d_{1xy} \rightarrow d_{1xy}$ transition” does not imply

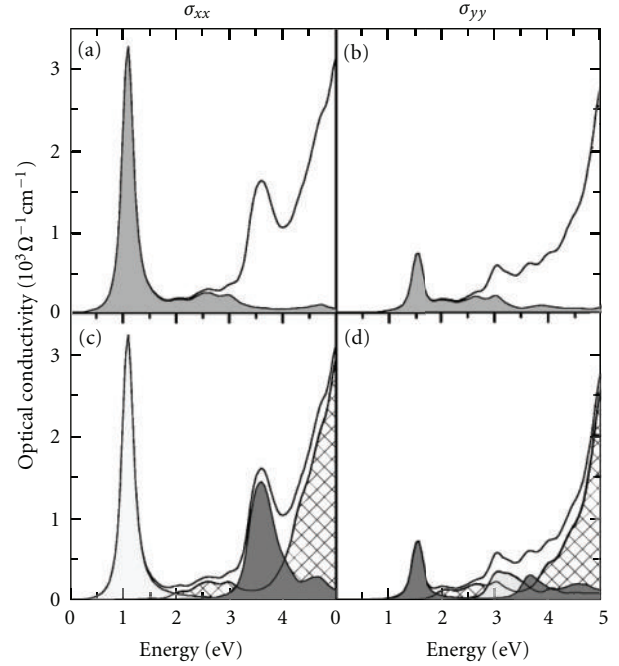


FIGURE 35: Decomposition of the optical conductivity σ_{xx} ((a) and (c)) and σ_{yy} ((b) and (d)) into the contribution from the transitions corresponding to different initial ((a) and (b)) and final states ((c) and (d)), calculated with $U_{\text{eff}} = 3$ eV [249]. The total optical conductivity is shown by the white area, respectively. The grey area in (a) and (b) shows the contribution from the transition with the initial states given by the occupied V d_{xy} bands. In (c) and (d) the transitions with the final states restricted to the antibonding V $3d_{1xy}$ and the bonding V $3d_{1xy}$ states are denoted by light grey and grey areas, respectively. The hatched area shows the contribution from interband transitions to higher-lying V $3d$ states.

that the transition occurs between the states with opposite spins, which would become possible if the relativistic effects were taken into account, but simply specifies the initial and final bands involved in the transition.

Concerning the energy range between 3 and 4 eV, Figures 35(c) and 35(d) illustrate that for both polarizations the spectral features are determined by transitions from the top of the part of the valence band formed mainly by the O $2p$ states. The peak in σ_{xx} at 3.7 eV is due to transitions into the d_{1xy} bands. The initial and final states for these transitions are of the same character as for those which determine the shape of the σ_{xx} spectra of V_2O_5 just above the absorption threshold. The transitions into the antibonding d_{1xy} states are completely suppressed for this polarization, while for σ_{yy} they play an important role in the formation of the shoulder in this energy range, whereas the contribution of the O $2p \rightarrow V d_{1xy}$ transitions are less pronounced. It is striking that these theoretical results explain the double-peak structure in σ_{yy} which is also visible in our experimental data (see Figure 34(b)) but is not resolved in the spectra from optical measurements that we referred to, previously. Finally, the transitions from the occupied d_{xy} states to the part of the conduction band originating from the V $d_{xz,yz}$ states give

rise to the nonvanishing intensity of the calculated spectra in the range between the peaks (1.5–3 eV), also observed in the experiment (see Figure 34).

As mentioned above, the magnitude and the strongly asymmetric shape of the low-energy peak are not reproduced by the calculations (see Figure 34) for both crystallographic directions. The discrepancies are the result of two possible sources: firstly, an oversimplified treatment of the charge fluctuations in the high-temperature phase by using an averaged one-electron potential and secondly the possibly not justified assumption that the V magnetic moments are antiferromagnetically aligned along the b direction. A more rigorous consideration of the charge disorder in the V sublattice of α' - NaV_2O_5 is beyond the capabilities of the LDA+ U approach in its present formulation and thus will be studied in more detail by applying cluster calculations described in the next section. However, the influence of the deviations from the long-range AFM order on the optical spectra can be estimated by performing the calculations for spin waves.

The optical conductivity spectra calculated for different values of u_y are shown in Figure 36. Since the change of the magnetic structure affects most strongly the bands formed by the V d_{xy} states of bonding character (see Figure 33), the spectral features originated from the transitions in which these bands are involved demonstrate the strong dependence on u_y . The change of the shape and the intensity of the peak at 1 eV in σ_{xx} (Figure 36(a)) is the most noticeable. As u_y increases, the peak becomes less intensive and its maximum shifts to higher energy. Since the final states for the corresponding transitions, that is, the antibonding V d_{xy} states, remain very narrow independently of the magnetic order along the b direction, the widening of the peak reflects the change of the density of the occupied V d_{xy} states. The shape of the low-energy peak in σ_{yy} (Figure 36(b)) does not change with increasing u_y , but its intensity rapidly decreases and vanishes completely for $u_y = 0$ when the V magnetic moments order ferromagnetically. The drop of intensity is explained by the decrease of the weight of the majority-spin states in the final-state wave functions. For $u_y = 0$ the initial and final states are formed by pure majority- and minority-spin states, respectively, and the corresponding transitions are forbidden since the relativistic effects were not included in the calculations. The spectral features in the energy range between 3 and 4 eV are also influenced by an increase of u_y , but the changes are less pronounced. The comparison of the spectra for the spin-spiral structures (Figure 36) with the experiment (Figures 34(a) and 34(b)) shows that the accounting for deviations from the AFM order improves the agreement between the theoretical and experimental magnitude of the low-energy peaks of σ_{xx} and σ_{yy} . However, the asymmetric shape of the peaks is not reproduced by the calculations.

For some values of u_y the optical conductivity was calculated for different relative orientations of the magnetization at neighboring ladders (not shown). The changes of the spectra were found to be very small which can be explained by the smallness of the $t_{xy} = 0.012$ eV hopping term which couples the V ions belonging to the consecutive ladders.

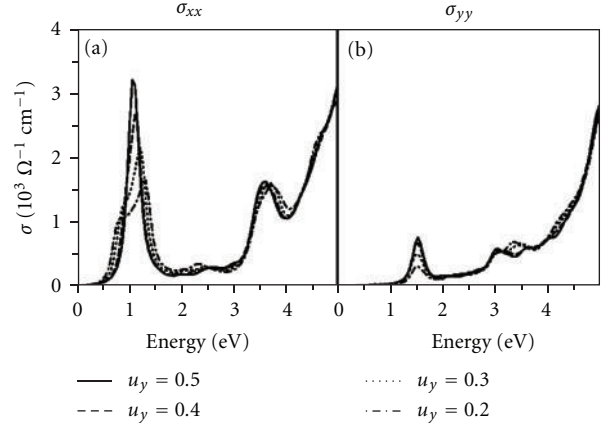


FIGURE 36: Optical conductivity calculated for different values of u_y , which defines the magnetic structure along the b direction [249].

4.2.6. Summary. The extended TB model based on explicit V–O hopping which describes the dispersion of the four bands formed by V d_{xy} states has been constructed by fitting the parameters to the band structure of α' - NaV_2O_5 calculated using the LMTO method [245]. Taking into account the hopping terms between oxygen p orbitals allows to reproduce the suppressed dispersion of the upper pair of V d_{xy} derived bands. The O p –O p hybridization is especially important in the case of the CO phases as it affects the dispersion of the occupied V^{4+} d_{xy} bands and leads to an important additional hopping term in an effective vanadium only tight-binding model, which has not been considered previously.

From the results of LDA+ U calculations performed for different models for the CO phase of α' - NaV_2O_5 , it has been found that the energy of the CO model with zig-zag ordering of V^{4+} ions is lower than the energy of the in-line CO model. Relatively strong dispersion of V^{4+} d_{xy} bands is observed for both CO models when V^{4+} moments are ordered ferromagnetically along the corresponding chains.

Effective exchange constants between V^{4+} magnetic moments were determined from the comparison of the LDA+ U total energies calculated for different kinds of MO within the zig-zag and in-line CO models [245]. It was found that for both CO models the strongest exchange interaction is the AF intra-chain coupling, whereas the coupling between the moments of the nearest V^{4+} ions in the case of the zig-zag CO model was found to be ferromagnetic. The calculated exchange constants are compatible with the experimental values determined from the high-temperature susceptibility. The calculated intra-chain exchange coupling for both in-line and zig-zag CO models is of comparable strength. The important consequence is that the experimentally observed strong dispersion of magnetic excitations in Γ -Y direction can be explained not only in the case of the in-line CO but also within the CO model with the zig-zag ordering of V^{4+} ions.

The LSDA+ U calculations quite well represent the energy positions in the optical conductivity using the on-site

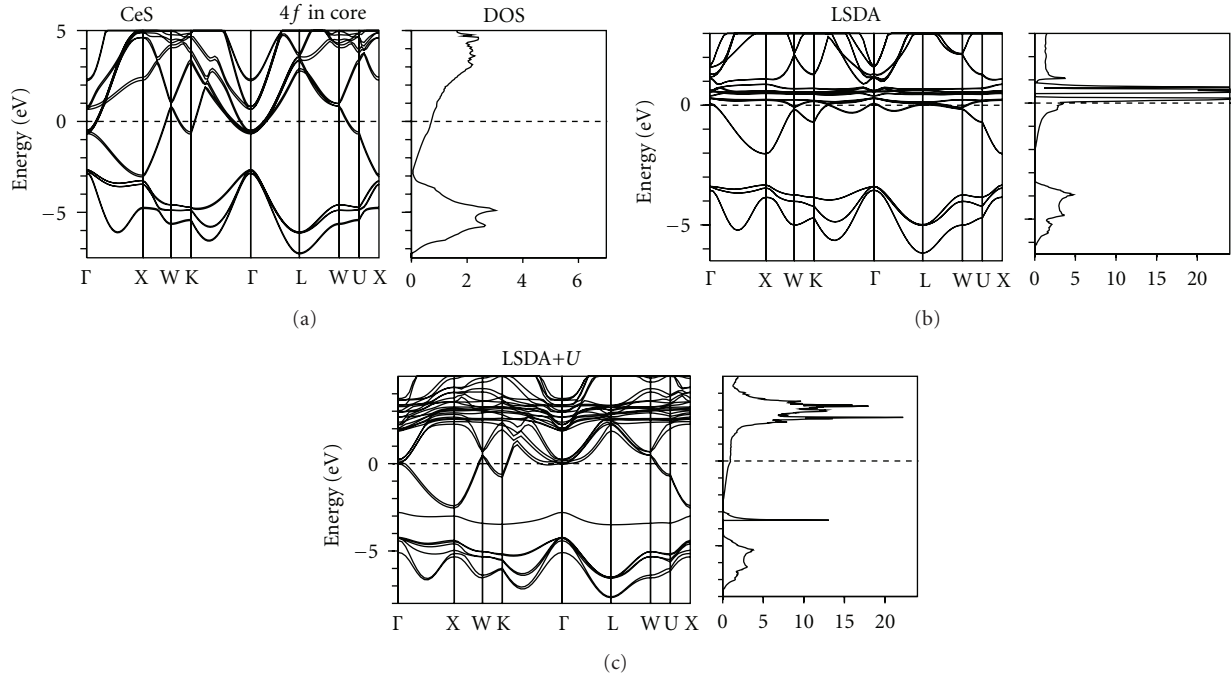


FIGURE 37: Self-consistent fully relativistic, spin-polarized energy band structure and total DOS (in states/(unit cell eV)) calculated for CeS [261] treating the $4f$ states as, (a) fully localized ($4f$ in core), (b) itinerant (LSDA), and (c) partly localized (LSDA+ U).

Coulomb interaction $U = 2\text{--}3\text{ eV}$ and an antiferromagnetic ordering of the electrons along the ladders. The anisotropic behavior of the optical conductivity could be explained by the different characters of the underlying optical transitions. While the transitions between 0.5 and 1.7 eV from the highest occupied band mainly composed by the bonding combination of V $3d_{xy}$ states into the lowest unoccupied band of antibonding V $3d_{xy}\text{--}O_R 2p_y$ states occur on the same rung in the a direction, in the b direction they can be considered as a hopping process to one of the adjacent rungs. The features of σ above 3 eV could be assigned to excitations of the O $2p$ electrons.

5. Ce Compounds

In recent years cerium monopnictides (CeAs, CeSb, and CeBi) and monochalcogenides (CeS, CeSe, and CeTe) attract a great attention partly due to the discovery of the three largest ever measured Kerr rotation angles of 90° , -22.08° , and -9.2° for cleaved single crystals of CeSb, CeS, and CeBi, respectively [250]. Cerium monopnictides and monochalcogenides crystallize in simple rock-salt structure, and each Ce^{3+} ion carries a single $4f$ electron. Furthermore, the cerium monochalcogenides are metals with approximately one conduction $5d$ electron per formula units, as was confirmed from Hall effect measurements [251], while cerium monopnictides are well-compensated semimetals with a low concentration of conduction $5d$ electrons and valence holes in the p band [252]. The temperature dependence of the electrical resistivity of the cerium monochalcogenides exhibit Kondo behavior [253], indicating nonnegligible $d\text{--}f$ mix-

ing. Furthermore, the Ce monochalcogenides order magnetically at low-temperature in the antiferromagnetic fcc type-II structure [254]. The ordered magnetic moments are rather small and equal to 0.31 , 0.45 , and $0.66\mu_B$ for SeS, CeSe, and CeTe, respectively. The Ce monopnictides have magnetic moments of 0.57 , 2.06 , and $2.10\mu_B$ for CeAs, CeSb, and CeBi, respectively.

5.1. CeS, CeSe, and CeTe. The optical and polar Kerr spectra of Ce monochalcogenides were measured by Reim [255] and Pittini et al. [256, 257]. All three Ce chalcogenides exhibit sharply peaked Kerr rotations and ellipticities at the energies of their plasma minima. The largest Kerr rotation was observed for CeS, for which -22.08° was reported by Pittini et al. [257]. Smaller peak rotations up to -6° were observed for CeSe and CeTe.

Theoretical investigations of the optical and MO of some of the Ce monochalcogenides were carried out by Lim et al. [258], Cooper et al. [259], Yaresko et al. [62], Price et al. [260], and Antonov et al. [261].

Figure 37 shows the energy band structure of CeS for three independent fully relativistic spin-polarized band structure calculations treated the $4f$ electrons as: (a) itinerant electrons using the local spin-density approximation; (b) fully localized, putting them in the core; and (c) partly localized using the LSDA+ U approximation. The energy band structure of CeS with the $4f$ electrons in the core can be subdivided into three regions separated by energy gaps. The bands in the lowest region around -13 to -14.5 eV (not shown in Figure 37) have mostly S s character with some amount of Ce sp character mixed in. The next six energy

bands are $S p$ bands separated from the s bands by indirect energy gap. The highest region can be characterized as Ce spin-split $5d$ bands. The sharp peaks in the DOS at the Fermi energy and at around 2 eV above are due to $4f_{5/2}$ and $4f_{7/2}$ states, respectively (see Figure 37). There is a single $4f$ energy band crossing the Fermi level.

The LSDA+ U band structure calculations [261] started from a $4f^1$ configuration for the Ce^{3+} ion with one on-site $4f$ energy shifted downward by $U_{\text{eff}}/2$ and 13 levels shifted upwards by this amount. The energies of occupied and unoccupied f levels are separated by approximately U_{eff} . However, the $4f$ states are not completely localized, but may hybridize, and together with all other states their energy positions relax to self-consistency. The LSDA+ U energy bands and total DOS of CeS [261] for $U_{\text{eff}} = 6$ eV are shown in Figure 37. For Ce^{3+} ions one $4f$ band is fully occupied and situated between $S p$ and $Ce 5d$ states, but the other thirteen $4f$ bands are well above the Fermi level hybridizing with $Ce 5d$ states.

Figure 38 shows the calculated imaginary part of the energy-loss function $\text{Im}[-1/\epsilon(\omega)]$, absorptive diagonal part of the optical conductivity σ_{1xx} , and the optical reflectivity compared with experimental data [257]. The calculated spectra have been convoluted with a Lorentzian whose width is 0.2 eV to approximate a lifetime broadening.

The predominant structure of CeS as well as CeSe and CeTe reflectivity spectra is the edge near 3 eV [257]. This sudden drop is characteristic for metallic rare-earth chalcogenides and is due to a plasma oscillation interfering with interband excitations. This plasma resonance causes the golden color for all metallic rare-earth sulfides. The energy of the conduction electron plasma resonance in the presence of the interband excitations is given by $\epsilon_{1xx}(\omega) = 0$. In the particular case of CeS this condition is fulfilled at $\hbar\omega = 2.9$ eV for the LSDA+ U calculations, and the maximum peak of the energy-loss spectrum in Figure 38 is shifted only very little from this energy as a result of damping. The correct energy position of the plasma edge in CeS can be obtained only by taking into account $5d \rightarrow 4f$ interband transitions. The calculations treating $4f$ electrons as core electrons place the zero crossing energy of $\epsilon_{1xx}(\omega)$ at higher energies (at 3.2 eV) in comparison with the LSDA+ U calculations, hence gives a wrong energy position for the major minimum in the optical reflectivity spectrum (Figure 38). On the other hand, the calculations with the $4f$ electrons in core produce more sharp conduction electron plasma resonance than the LSDA+ U calculations (Figure 38). As a result, the former calculations give better agreement with the experiment in the absolute value of the minimum of the reflectivity spectrum. The best agreement between theory and the experiment for the optical reflectivity was found to be when we used the LSDA+ U approximation (Figure 38). The Coulomb repulsion U_{eff} strongly influences the electronic structure and the optical spectra of CeS. Due to removing the $4f$ states from the Fermi level, the diagonal part of the optical conductivity σ_{1xx} in the energy interval of 0 to 3.5 eV has only small infrared peak (see Figure 38). This peak originates from interband transitions between eigenvalue surfaces that are quasiparallel around the Γ symmetry point.

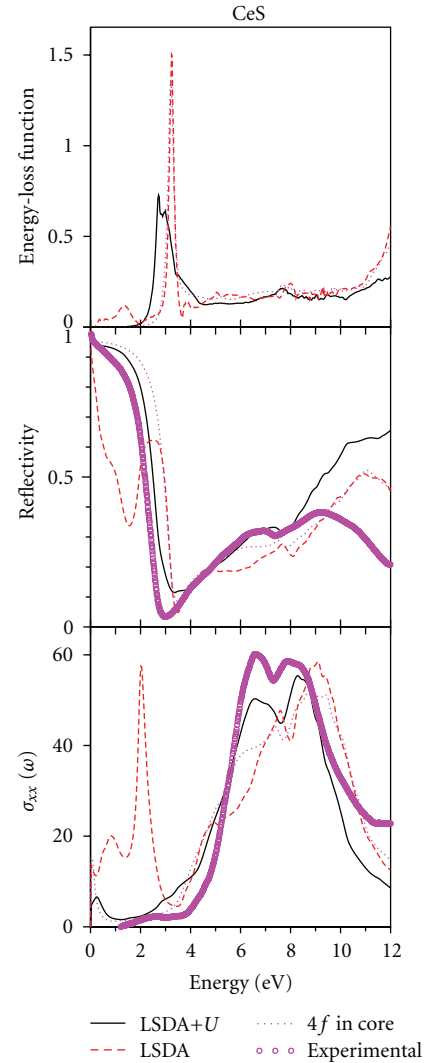


FIGURE 38: Calculated absorptive diagonal part of the optical conductivity σ_{1xx} (in 10^{14} s^{-1}), the optical reflectivity R , and energy-loss function of CeS [261] compared with experimental data [257].

These quasiparallel bands are visible along Γ -L and Γ -K symmetry directions (see Figure 37). The very broad double-peak structure observed between 4 and 10 eV is due to transitions from bands with predominantly $S 3p$ character to unoccupied $Ce 5d(t_{2g})$ and $5d(t_{2g})$ bands, respectively.

The calculation of the optical conductivity where the $4f$'s are treated as band states reproduces two additional structures in the 0.0 to 3.5 eV energy interval, namely, the peaks at 0.9 and 2.0 eV (Figure 38). Both of the peaks involve the $5d \rightarrow 4f$ interband transitions. The second peak is responsible for the deep minimum in the optical reflectivity at 1.8 eV which is not observed in the experiment [257] (Figure 38).

After consideration of the band structure and optical properties we, turn to the magneto-optical spectra. The polar magneto-optical Kerr effect was measured on CeS, CeSe, and CeTe in [257]. All three spectra are quantitatively very similar. They are dominated by a sharp and large negative

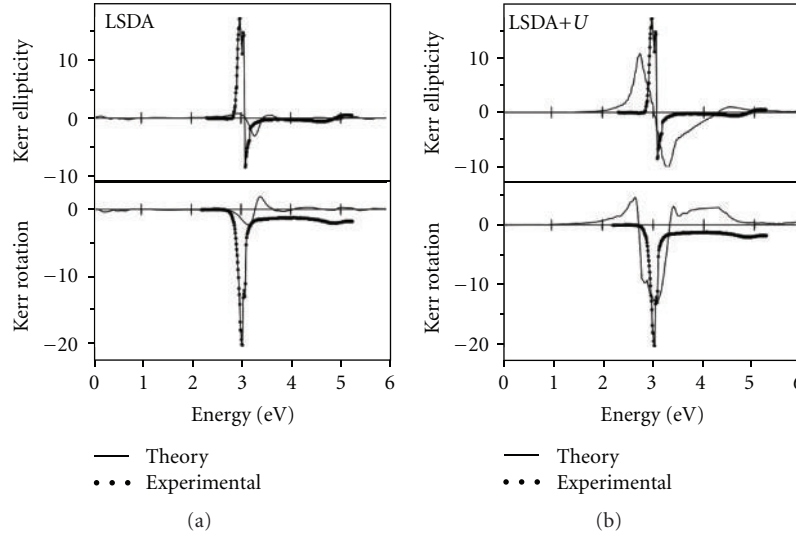


FIGURE 39: Calculated and experimental Kerr rotation (θ_K) and Kerr ellipticity (ϵ_K) spectra (in degrees) of the CeS with the $4f$ electrons treated as itinerant electrons (LSDA) and partly localized (LSDA+ U) [261]. The experimental data are those from [257].

Kerr rotation peak of -22.08° , -5.51° , and -3.32° detected at photon energies of 3.04, 2.60, and 1.99 eV for CeS, CeSe, and CeTe, respectively, with a remarkably small width of 0.1 eV [257]. These Kerr rotation peaks are significant, in particular if one considers the small magnetic moment achieved in the sample at the condition of the experiment. Particularly meaningful is the Kerr rotation peak of -22.08° observed in CeS [257] with a magnetic moment of only $0.31 \mu_B/\text{Ce}$. This extraordinary peak corresponds to the highest ever observed specific Kerr rotation of $71.23^\circ/\mu_B$ and to the second largest ever measured Kerr rotation after the record of 90° recently detected on CeSb [262]. In Figure 39 we show the experimental [257] $\theta_K(\omega)$ and $\epsilon_K(\omega)$ MO Kerr spectra of CeS, as well as the spectra calculated with LSDA and LSDA+ U approximations. This picture clearly demonstrates that the better description is unambiguously given by the LSDA+ U approach. The LSDA spectra have extra peaks at 0 to 1 eV which is caused by extra structure present in the interband dielectric tensor. Responsible are interband transitions involving the hybridized $4f$ states, which in the LSDA approach exhibit a maximum resonance near E_F . In the LSDA+ U approach, the $4f$ state energies are shifted due to the on-site Coulomb interaction U_{eff} . As a result, the transitions involving the $4f$ states do not take place at small photon energies any more, and the structures at 0 to 1 eV disappear from Kerr spectra. The calculations in which the $4f$ electrons are treated as quasicore (not shown) are able to reproduce a very similar structure as the LSDA+ U calculations, but, due to the lack of corresponding $5d \rightarrow 4f$ interband transitions, the off-diagonal part of the optical conductivity σ_{2xy} is nearly zero, so that a very small Kerr rotation is obtained. Although the LSDA+ U calculations made much better work in the comparison with LSDA one, they still produce the less-sharp plasma resonance and hence give smaller rotation angle of -13° than experimentally observed -22.08° .

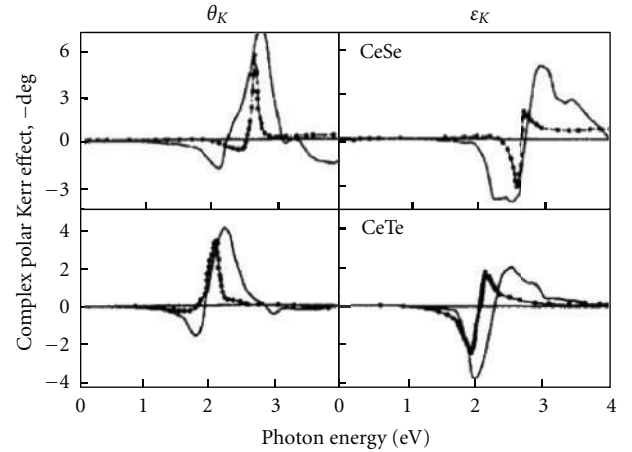


FIGURE 40: Theoretical and experimental [250] Kerr angle (θ_K) and Kerr ellipticity (ϵ_K) spectrum of CeSe and CeTe. The theoretical spectrum (solid curve) was calculated using the LSDA+ U approach with $U = 6$ eV.

In Figure 40 we show the experimental [257] and LSDA+ U results for Kerr spectra of CeSe and CeTe. The results of the LSDA approach are not shown here, but we mention that these do by far not reproduce the experimental data as good as LSDA+ U approaches [62]. The main peak in the Kerr rotation spectra in Figure 40 is not found to be due to optical transitions stemming directly from the nearly localized $4f^1$ level. Instead, these peaks are due to a plasma minimum in the denominator $D(\omega) \equiv \sigma_{xx}(1 + (4\pi i/\omega)\sigma_{xx})^{1/2}$ and nonzero σ_{xy} .

5.2. *CeSb and CeBi*. The optical and MO properties of CeSb were investigated by Schoenes and Reim [263] and Reim et al. [264], whereas its optical conductivity to 20 eV was measured

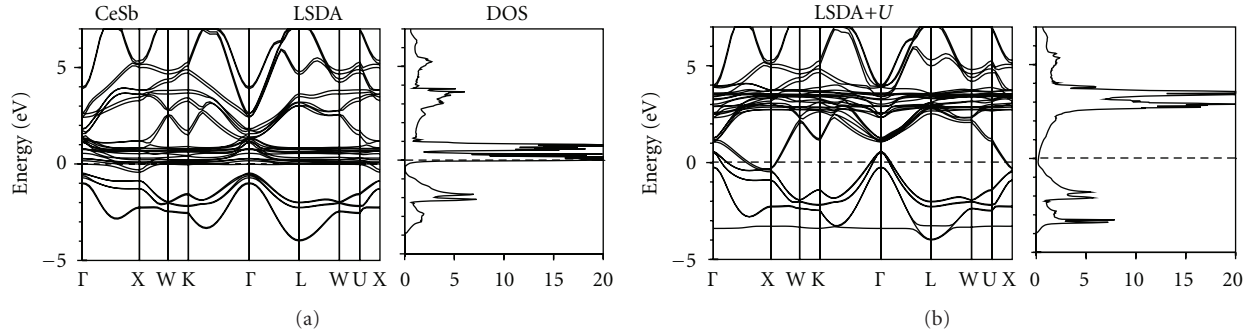


FIGURE 41: Self-consistent fully relativistic, spin-polarized energy band structure and total DOS (in states/(unit cell eV)) calculated for CeSb in the LSDA and LSDA+ U ($U_{\text{eff}} = 6$ eV) approximations [62].

by Kwon et al. [265]. Reim et al. [264] observed the onset of a large Kerr rotation that reached -14° at 0.5 eV, but that energy was the lower end of the spectral range they could measure. Pittini et al. [262] extended the low-energy limit to 0.23 eV and observed a record Kerr rotation which increased to reach -90° at 0.46 eV, and then jumped to $+90^\circ$ at the same energy, and decreased with increasing photon energy. Note that the reflectivity of CeSb at the maximum of Kerr rotation was found to be 28% [262]. 90° is the absolute maximum value that can be measured. It is two orders of magnitude larger than the values that are commonly measured for transition-metal compounds and about one order of magnitude larger than values maximally achieved for other lanthanide and actinide compounds [46]. Later on Salghetti-Drioli et al. [266] prepared well-characterized single crystals of CeSb but could not reproduce the record Kerr rotation on these crystals. Instead only a peak of -17° at 0.46 eV was observed. They remeasure the CeSb specimen on which record Kerr rotation was found and obtained for this sample the 90° rotation. Salghetti-Drioli et al. polished the surface of the sample on which Pittini had measured the record rotation, in order to exclude surface oxidation effects, but after the surface treatment only a small Kerr rotation could be measured from the sample [266]. Salghetti-Drioli et al. suggest that the observed 90° Kerr rotation might not be the intrinsic rotation of CeSb but could be caused by a surface oxide layer.

The discovery of 90° Kerr rotation in CeSb attracts a great interest from theorists. Several groups tried to produce the Kerr rotation spectrum from the first principles or analyze theoretically the possibility of attaining a 90° Kerr rotation. Using the exact equation for the polar Kerr rotation Uspenskii et al. [267] pointed out that a 90° rotation can occur only when the absorptive parts of the diagonal and off-diagonal permittivities are zero. The absolute maximum value of Kerr rotation can be achieved at energy with zero reflectivity, and it is also attainable for the reflectivity of the order of 30–50% and hence the observation of 90° rotation in principle be possible in CeSb with its 28% reflectivity at 0.46 eV. Pustogowa et al. [268] also examined the possibility of a 90° rotation using the modeled MO conductivity and reflectivity with a singular oscillator strength and the SO

coupling as a parameter. She was able to obtain a 90° rotation for various values of the SO parameter.

To investigate the nature of a record polar Kerr rotation in CeSb several first-principle calculations of the diagonal and off-diagonal optical conductivity and polar Kerr effect of CeSb were carried out in [62, 258–260, 269, 270].

The energy band structure of CeSb in the LSDA and LSDA+ U approaches is presented in Figure 41 from [62, 270]. The LSDA calculations place the $4f$ DOS at and just above the Fermi level. The Coulomb repulsion U_{eff} strongly influences the electronic structure of CeSb. For Ce^{3+} ions thirteen unoccupied $4f$ states are situated at 2 to 4 eV above the Fermi level hybridizing with Ce $5d$ states. A single occupied $4f$ state is located at -3.2 eV in good agreement with photoemission measurements which detected the $4f^1$ level slightly deeper than -3 eV [271–273]. The LSDA+ U calculations also improve the magnetic moments producing spin and orbital magnetic moment equal to -1.012 and $2.960 \mu_B$, which yield a total moment of $1.948 \mu_B$. The experimental value obtained for the antiferromagnetic ground state is equal to $2.10 \pm 0.04 \mu_B$ [274, 275]. The LSDA strongly underestimates the magnetic moments producing spin, orbital, and total magnetic moments equal to -0.897 , 1.511 , and 0.614 , respectively [270].

Liechtenstein et al. [269] and Yaresko et al. [62] show that LSDA+ U calculations also give a substantial improvement over LSDA result in diagonal and off-diagonal optical conductivity of CeSb.

The complex polar Kerr spectra of CeSb were evaluated by Yaresko et al. [62] and Antonov et al. [270]. The maximal Kerr angle calculated with the LSDA approach was relatively large, about -12° to -22° depending on value of life-time broadening. The LSDA+ U approach produces a relatively larger polar Kerr angle. The results for the Kerr spectra of CeSb from [62] are shown in Figure 42(a). A giant Kerr rotation of 60° is less than the observed value of 90° . Pittini et al. [262] observed that the maximum Kerr rotation depends on the magnetization and that therefore the intrinsic quantum state plays an important role. In addition, the record Kerr effect occurs close to a plasma minimum. Both observations agree with what was found in the calculations (Figure 42). The denominator $D(\omega) \equiv \sigma_{xx}(1 + (4\pi i/\omega)\sigma_{xx})^{1/2}$

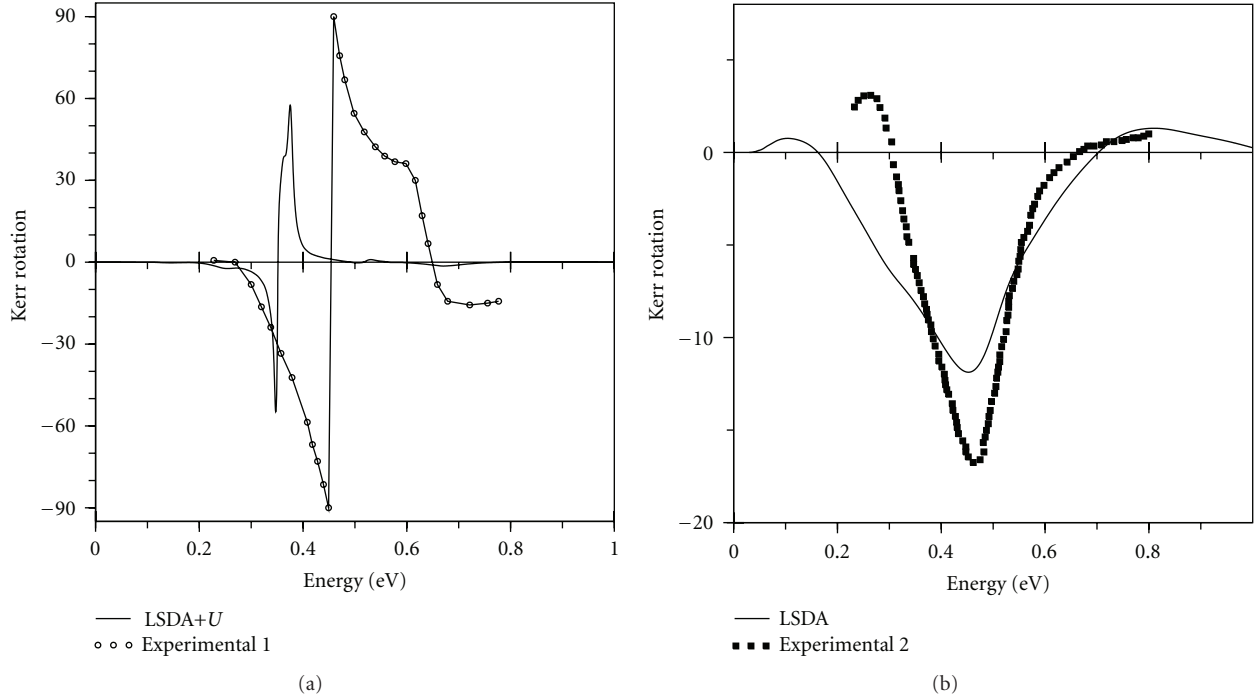


FIGURE 42: (a) Experimental [257] Kerr rotation (in degrees) of CeSb in comparison with LSDA+ U calculations [62]; (b) the LSDA theoretical spectrum [270] and experiment [266].

nearly vanishes due to the particular frequency dependence of σ_{xx} . A small denominator is in itself not sufficient for obtaining a large Kerr rotation. Also σ_{xy} , which relates to the magnetic polarization, is important. The $4f^1$ level in CeSb is a completely spin and orbitally polarized state, which has a large magnetic moment of about $2\mu_B$. The $4f^1$ level is, however, located 3.2 eV beneath E_F , and therefore it cannot contribute directly to the peak rotation. It was found that the $4f^1$ level plays nevertheless a crucial role, because, due to hybridization of valence states with the anisotropically polarized $4f^1$ state, the valence bands become anisotropically polarized. This anisotropic polarization leads to an asymmetrical coupling of the left- and right-hand circularly polarized light at small photon energies. The asymmetrical light coupling leads in turn to a relatively large σ_{xy} , which causes the huge Kerr rotation. To emphasize the importance of the anisotropic hybridization, it was performed also quasicore calculations for the $4f^1$ level [62]. One was obtained a very similar σ_{xx} , but due to the lack of anisotropic $4f$ hybridization, σ_{xy} becomes nearly zero. Consequently, only a very small Kerr rotation is obtained in quasicore calculations (not shown). We should note that the large angle of -60° represents the maximal Kerr rotation that could be achieved in the LSDA+ U calculations. In this case no lifetime broadening was included and the plasma frequency was slightly changed. The first-principles LSDA+ U calculations give smaller but still substantial Kerr angle of -45° [62]. We also should mention that the theoretical Kerr spectrum is more narrow and shifts toward smaller energies in comparison with the experiment.

Figure 42(a) shows the results for the Kerr spectra of CeSb calculated in LSDA approximation [270] in comparison with latest experimental data obtained by Salghetti-Drioli et al. [266] on well-characterized single crystals of CeSb. The theoretical spectrum is convoluted on lifetime effect using the parameter of 0.1 eV. Surprisingly LSDA theory produces the experimental spectrum rather good in the shape, position, and amplitude.

The MO Kerr spectra of CeBi has also a considerable interest. In most compounds the magnitude of the Kerr effect is proportional to the spin-orbit (SO) coupling interaction. The MO Kerr effect in MnBi is, for example, larger than that in MnSb, because the SO coupling on Bi is larger than that on Sb. One could thus expect that the Kerr angle in CeBi should be as large as, or even larger than, that of CeSb. However, this is not found to be the case [257].

In Figure 43 we show the experimental [257] and theoretical Kerr spectrum of CeBi [276]. The measured maximal Kerr rotation amounts only to -9° . The LSDA+ U approach (with $U = 6$ eV) explains the measured MO Kerr spectrum of CeBi fairly well. There is a small energy difference of 0.1 eV in the position of the rotation maximum, and the calculated Kerr ellipticity deviates above 0.5 eV from the experimental curve.

The fact that the Kerr rotation of CeBi is far less than that of CeSb is fully reproduced by the calculations [62, 276], but it is not consistent with our experience that the Kerr effect is proportional to the magnitude of SO coupling. The imaginary part of σ_{xy} is for CeBi as large as that of CeSb, but if we compare the σ_{xx} of CeBi to that of CeSb, then we find that the

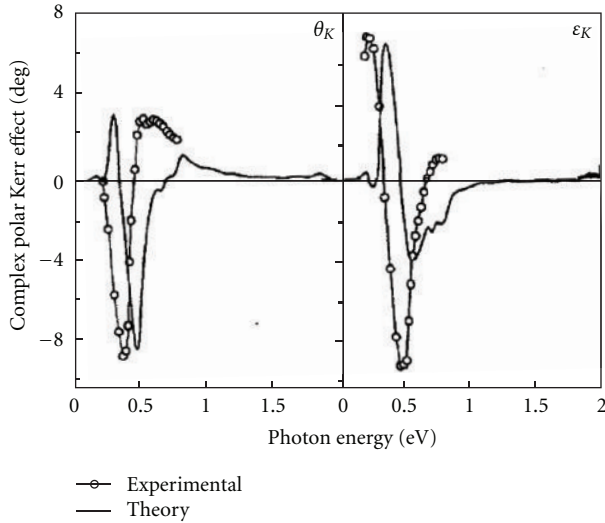


FIGURE 43: Theoretical [276] and experimental [257] Kerr angle (θ_K) and Kerr ellipticity (ϵ_K) spectrum of CeBi. The theoretical spectrum (solid curve) was calculated using the LSDA+ U approach with $U = 6$ eV.

denominator does not become as small for CeBi. The resulting Kerr angle of CeBi is therefore not as large as that of CeSb.

5.3. *CeFe₂*. Among the Ce–T series the C15 Laves phase compounds, CeT₂ (T = Ni, Co, Fe), which stand out as archetype of the α –Ce class, have been studied intensively [277].

CeFe₂ compound presents a strong anomaly in physical properties in comparison with other RFe₂ compounds, which originates from $3d$ – $4f$ hybridization. Firstly, there is a strong reduction in the lattice parameter in comparison with the expected smooth decrease through the RFe₂ series, leading to a lattice constant for CeFe₂ as small as that for HoFe₂. Secondly, the magnetic properties present characteristic features. The Curie temperature ($T_c = 230$ K) is depressed by a factor of nearly 3 as compared to LuFe₂ ($T_c = 610$ K, La–Fe compounds do not exist). The magnetic moments are also anomalously low ($\mu_{Fe} \approx 1.4 \mu_B$, $\mu_{Ce} \approx 0.7 \mu_B$, coupled antiferromagnetically to each other). The saturation magnetization is equal to $2.30 \mu_B/\text{f.u.}$, the magnetic susceptibility follows the Curie-Weiss law with an effective moment of $7.4 \mu_B/\text{f.u.}$ [278]. Moreover, magnetic and neutron-diffraction studies have shown that the substitution of small amount (only a few %) of Fe by Co, Al, Si, or Ru reveals a second magnetic transition with an abrupt loss of ferromagnetism at Neel temperature T_N , lower than the bulk-ordering temperature T_c . In particular, with Co substitution an antiferromagnetic phase appears for $T \leq 80$ K [279]. From recent neutron scattering experiments for CeFe₂, Paolasini et al. reported that there is an AFM spin fluctuation with a propagation vector $q = (1/2, 1/2, 1/2)$ below about 100 K even in the FM state [280]. They also revealed that the AFM spin fluctuation with the same q vector exists in the FM state for Ce(Fe_{0.93}Co_{0.07})₂, and that it changes into a typical AFM spin wave in the AFM state at low temperatures [281]. The AFM spin fluctuation

and the AFM spin wave observed by them are associated with the Fe spins. They also showed that the AFM state of Ce(Fe_{0.93}Co_{0.07})₂ is not a simple collinear AFM structure but a noncollinear one. From magnetization measurements using a CeFe₂ single crystal, Fukuda et al. revealed that the magnetization along the $\langle 111 \rangle$ direction at 5 K is anisotropically suppressed by applying hydrostatic pressure [282]. According to their conclusion, such anisotropic suppression of the magnetization originates from the anisotropic Ce $4f$ –Fe $3d$ hybridizations with the strong magnetoelastic effect. Fujiwara et al. [283] carried out the magnetization measurements of single-crystal CeFe₂ under hydrostatic pressures up to 8 kbar and show that the magnetization is quite anisotropically suppressed at 5 K even in the cubic symmetry by applying the hydrostatic pressure, while the neutron diffraction studies indicate that the antiferromagnetic spin fluctuation with a propagation vector $q = (1/2, 1/2, 1/2)$ is enhanced by applying hydrostatic pressure of 15 kbar.

All anomalous physical properties of CeFe₂ suggest that the Ce $4f$ states in CeFe₂ hybridize strongly with the other valence electrons, notably the Fe $3d$ valence states [277].

The band structure investigations of the CeFe₂ were carried out by several authors [284–287]. Already first band structure calculation by Eriksson et al. [284] using the LMTO method within atom sphere approximation (ASA) shows that total magnetic moments at the Fe and Ce sites are aligned antiferromagnetically. It was an indication on itinerant character of the $4f$ states in CeFe₂. The relativistic effects was found to be relatively small. Trygg et al. [286] provided the energy band structure calculations of CeFe₂ including spin-orbit coupling and orbital polarization using the full potential linear muffin-tin orbital (FP-LMTO) method. Later on Konishi et al. [287] obtained similar results using also the FP-LMTO. The Ce $4f$ electrons were treated as itinerant band electrons. They also reported on results from high-energy spectroscopic measurements using core-level and valence-band photoemission, inverse photoemission, and soft X-ray absorption techniques. It was found that the Ce $4f$ partial density of states obtained from the band structure calculations agree well with the experimental spectra concerning both the $4f$ peak position and the $4f$ bandwidth, if the surface effects are properly taken into account. Combined analysis of the experimental and theoretical results indicate very strong hybridization of the Ce $4f$ states with the delocalized band states, mainly the Fe $3d$ states.

In [288], authors focus their attention on the theoretical investigation of the X-ray magnetic circular dichroism in CeFe₂ compound. Actually XMCD is one of the most promising techniques to reveal local electronic and magnetic properties in a variety of magnetic materials, essentially because of its element as well as shell selectivities. In fact, with the help of circular polarized X-rays of good quality, arising from third-generation synchrotron facilities, a lot of data have been accumulated up to now on XAS and XMCD of transition-metal and rare-earth compounds [6, 289, 290].

The first experimental XMCD measurements of CeFe₂ at the Ce $M_{4,5}$ absorption edges were carried out by Schillé et al. [291]. The uncertainty of these experiments was too large to allow a reliable quantitative determination of the absolute

value of the local $4f$ moments on Ce. Later, using high-quality sample and better experimental conditions, Delobbe et al. [292] measured the X-ray magnetic circular dichroism at the Fe $L_{2,3}$, Ce $M_{4,5}$, and Ce $L_{2,3}$ absorption edges of CeFe_2 . Application of the sum rules yields both the magnitude and the direction of the magnetic contributions to the total moment in CeFe_2 . A total Ce magnetic contribution of $-0.29 \mu_B$ ($M^{5d} = -0.13 \mu_B$, $M^{4f} = -0.16 \mu_B$) and a ratio for the $4f$ contribution $\langle L_z \rangle / \langle S_z \rangle \approx -1$ were found, which confirmed that the $4f$ states are highly hybridized in CeFe_2 . The experimental results of XAS and XMCD spectra for CeFe_2 at the Ce $L_{2,3}$ and Fe K absorption edges were presented in [279, 291]. Mizumaki et al. [293] measured Ce $L_{2,3}$ XMCD spectra in $\text{Ce}(\text{Fe}_{1-x}\text{Co}_x)_2$ compounds for $x = 0.0, 0.2$, and 0.3 . Klose with coworkers investigated magnetic circular dichroism on Ce/Fe multilayers at the Fe K and Ce $L_{2,3}$ absorption edges [294].

As for the XMCD and photoemission spectroscopy (PES) studies of R compounds, it is widely believed that the spectra are well described by the single-impurity Anderson model (SIAM) [295, 296]. Indeed during many years Kotani's group demonstrates remarkable agreement between theoretically calculated and the experimentally measured XMCD spectra in the rare-earth compounds with different degree of the $4f$ localization using the SIAM approximation [297–301]. To describe the hybridization of $R5d$ states with spin-polarized transition metal $3d$ states of surrounding ions, they used a cluster model. The method contains several adjustable parameters (such as the energy of the $4f$ level, ϵ_{4f} , Coulomb interaction between the $4f$ electrons, U_{ff} , and between $4d$ and $5d$ states, U_{fd} , core hole potentials U_{fc} and U_{dc} , and hybridization parameter between $4f$ and conducting states V_{fd}). By proper choice of these parameters they were able to describe quite well the shape of the R XMCD spectra at the $L_{2,3}$ edges for the considered series of $R - \text{T}$, including CeFe_2 compound (see review paper [302]). Recently, however, it has been argued that for systems, in which the Ce $4f$ states hybridize strongly with the other valence electrons, calculations based on the density-functional theory (DFT) may give an equally good or even better description of the PES and XMCD spectra than the SIAM analysis [6, 287, 303]. However, one should bear in mind that calculations based on DFT are not strictly applicable for excited state properties, in contrast to the ground-state properties, such as the magnetic moments of the ground state, which are typically the focus of these calculations. Nevertheless, the electronic structure obtained from such calculations is often compared with photoemission or XMCD data, and good agreement between experiment and calculations is frequently observed. In the limit of complete screening of the excited state, one would expect ground-state density-functional calculations to be able to describe the spectra well. Still there are only a few *ab initio* calculations of the XMCD spectra in rare-earth compounds [304–308] and no such calculations for the CeFe_2 compound in literature as far as we know.

CeFe_2 crystallizes in the cubic $Fd\bar{3}m$ structure (space group no. 227) and belongs to the large class of C15 Laves-phase compounds. The unit cell consists of two formula units

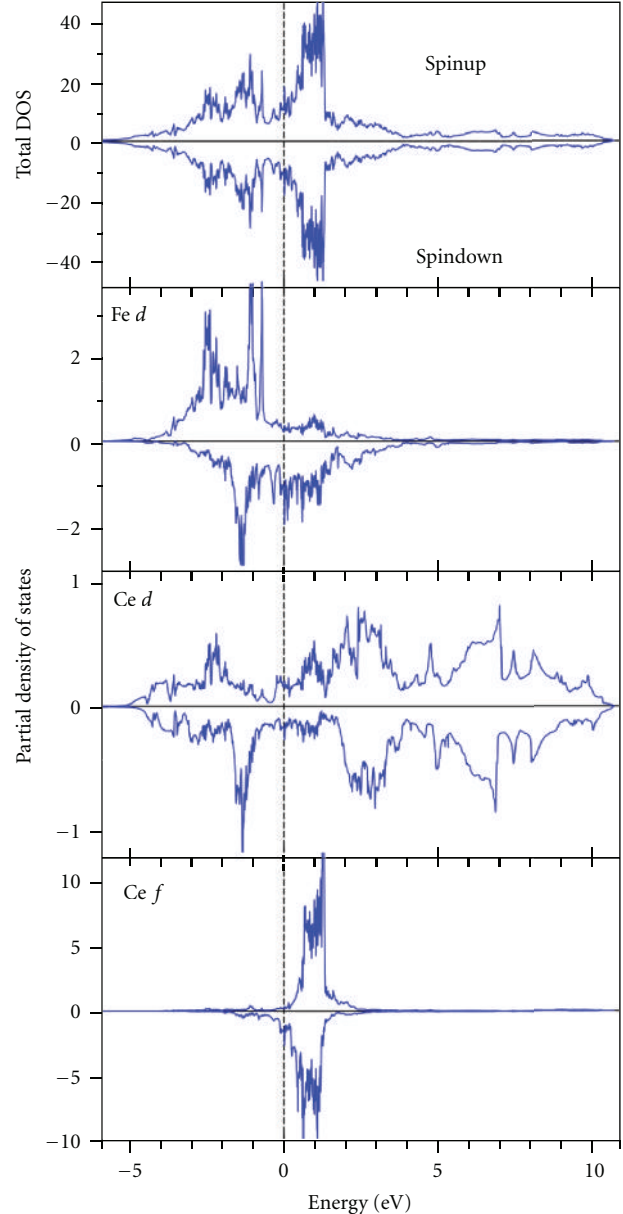


FIGURE 44: The total (in states/(cell eV)) and partial (in states/(atom eV)) densities of states of CeFe_2 [288]. The Fermi energy is at zero.

(i.e., six atoms) with a lattice constant $a = 7.3 \text{ \AA}$ [309], Ce ions occupy the $8a$ Wyckoff positions ($x = 0, y = 0, z = 0$). Fe ions occupy the $16d$ positions ($x = 5/8, y = 5/8, z = 5/8$). The Ce atoms have twelve Fe atoms as nearest neighbors (at 3.0265 \AA distance), while for Fe there are six Fe atoms (at 2.581 \AA distance) and six Ce atoms (at 3.0265 \AA distance).

5.3.1. Energy Band Structure. The fully relativistic spin-polarized total and partial density of states (DOSs) of cubic ferromagnetic CeFe_2 are presented in Figure 44 for the LSDA approximation. The results agree well with previous band structure calculations [284, 286, 287].

There is a visible Ce $4f$ -Fe $3d$ as well as Ce $4f$ -Ce $5d$ hybridization at 0 to 2 eV above the Fermi level. The Ce $5d$ empty states possess two major peaks at around 3 eV and 7 eV above the Fermi level. As we will see later these two peaks are responsible for the double structure of the Ce XAS at the $L_{2,3}$ edges.

A large magnetic moment at the Fe site induces spin splitting of the itinerant Ce $5d$ and Ce $4f$ states through exchange and hybridization effect. From our LSDA calculations, it has been deduced that the total moment $\mu = 2.253 \mu_B/f.u.$ (experimental saturation magnetization is $2.30 \mu_B$ [287]) is the result of the antiparallel coupling between Fe moment ($1.473 \mu_B$) and cerium moment ($-0.693 \mu_B$). The total Ce moment corresponds to a $4f$ contribution of $-0.275 \mu_B$ and a $5d$ contribution of $-0.221 \mu_B$. The orbital Ce $4f$ moment was calculated to be $0.151 \mu_B$. The spin and orbital Fe $3d$ moments are $1.502 \mu_B$ and $0.064 \mu_B$, respectively.

The LSDA calculations show an unusual antiparallel magnetic coupling between R and transition metal moments. The first experimental evidence of an ordered Ce moment in CeFe₂ antiferromagnetically aligned with respect to the Fe moments was obtained from powder neutron diffraction experiments [310]. Few years later, a combination of polarized and unpolarized neutron diffraction measurements on a CeFe₂ single crystal [311] confirmed the previous results obtained on powder samples. The partial magnetic moments in CeFe₂ have been studied also using Compton scattering [312] and X-ray magnetic circular dichroism [292]. In all experiments, an antiparallel coupling of the Ce and Fe moments is found. This coupling is also reproduced in band structure calculation [284, 286–288]. The antiparallel coupling of the moments is a strong indication that the Ce $4f$ states in CeFe₂ are delocalized. Indeed, in CeFe₂ Fe $3d$ and Ce $5d$ states strongly hybridize to form bonding and antibonding bands. When a moment develops at the Fe sites the energy of spin-up $3d$ states is lowered, reducing the $3d - 5d$ hybridization for the spin-up states. The opposite effect occurs for the spin-down states, and the induced Ce $5d$ spin moment is therefore antiparallel to the Fe $3d$ spin moment [284]. The hybridization between the Fe $3d$ and Ce $5d$ states is more pronounced in the minority channel (see Figure 44). When a Ce $4f$ electron is localized, the direction of the $4f$ spin moment is dictated by the polarization of the $5d$ electrons so that the Ce and Fe spin moments are always antiparallel. In a Ce³⁺ ion with the f^1 configuration, the $4f$ spin moment is accompanied by an orbital moment which is larger than the spin moment and, according to Hund's third rule, is antiparallel to it. Hence, for the localized $4f$ electrons, the coupling of the total Ce and Fe moments is ferromagnetic. When the Ce $4f$ orbital moment is quenched due to band formation, the coupling becomes antiparallel. It should be mentioned that the band structure calculations for CeFe₂ [288] show that the Ce spin moment is partially induced by the direct Ce $4f$ -Fe $3d$ hybridization, which is an additional argument in favor of the delocalized character of the Ce $4f$ electrons.

Figure 45 shows the comparison of the experimental photoemission spectrum with the $4f$ partial DOS calculated by the LSDA and LSDA+ U approximations. The LSDA

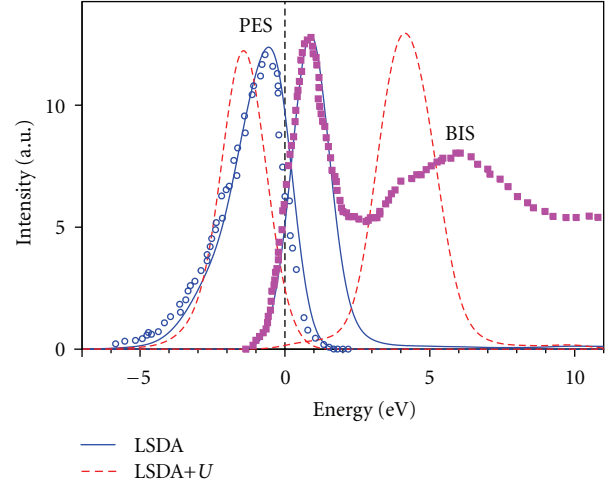


FIGURE 45: Comparison of the experimental photoemission (open circles) [287] and X-ray bremsstrahlung isochromat (full squares) spectra [287] with the $4f$ partial DOS calculated by the LSDA (full line) and LSDA+ U (dashed line) approximations.

approach better represents the energy position of the occupied part of Ce $4f$ bands. The principal question is the energy position of the empty $4f$ states, which is usually answered by optical or X-ray bremsstrahlung isochromat spectroscopy (BIS) measurements. BIS spectrum is consisted from two major peaks. The first peak situated at around 1 eV above Fermi energy is derived from Ce empty $4f$ bands. From analysis of Figure 45 we can conclude that the LSDA calculations place the $4f$ empty bands in better agreement with the experiment than the LSDA+ U approach.

5.3.2. Ce $L_{2,3}$ XMCD Spectra. For various ferromagnetic Ce intermetallic compounds, X-ray absorption spectra and their X-ray magnetic circular dichroism have been extensively studied for Ce $L_{2,3}$ edges [302]. According to experimental observations, both XAS and XMCD spectra for strongly mixed-valence Ce compounds, which also include CeFe₂ exhibit a double-peak structure. According to the atomic-like consideration the two peaks in the XAS are associated with a mixed-valence state in CeFe₂: in the presence of the hole at the core level the lower energy peak corresponds to the $4f^1 5d^n$ configuration and the higher energy peak to the $4f^0 5d^{n+1}$ configuration. One should mention, however, that Ce $5d$ states in CeFe₂ having definitely band character extend at more than 15 eV (see Figure 44). Therefore, one would expect that the calculations based on density-functional theory may give an equally good or even better description of the R XAS and XMCD spectra at the $L_{2,3}$ edge than the atomic-like SIAM analysis.

The XMCD spectra at the Ce $L_{2,3}$ edges are mostly determined by the strength of the spin-orbit (SO) coupling of the initial Ce $2p$ core states and spin-polarization of the final empty $5d_{3/2,5/2}$ states, while the exchange splitting of the Ce $2p$ core states as well as the SO coupling of the $5d$ valence states are of minor importance for the XMCD at the Ce $L_{2,3}$ edges of CeFe₂. A qualitative explanation of

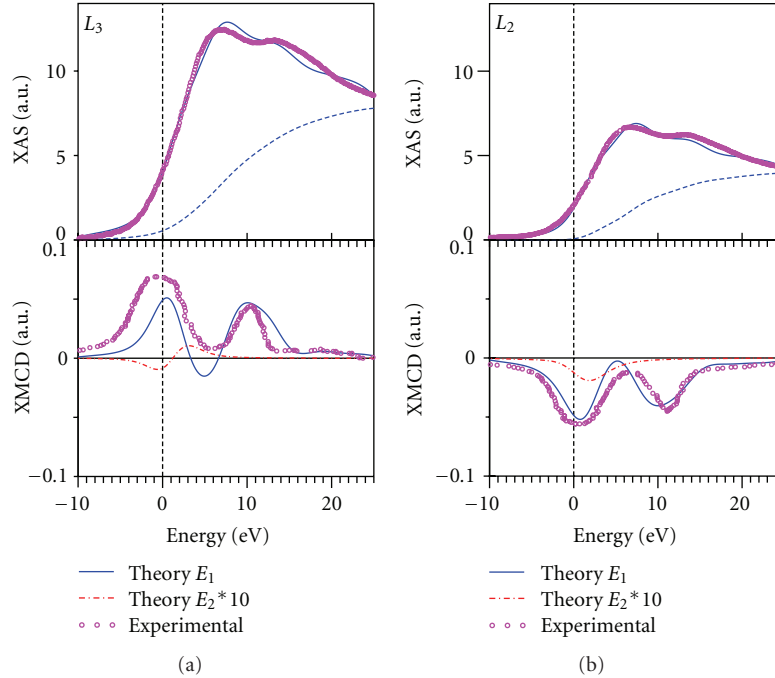


FIGURE 46: (upper panel) the experimental [293] (circles) and theoretically calculated [288] with the LSDA approximation (full lines) isotropic absorption spectra of CeFe_2 at the Ce $L_{2,3}$ edges. Dashed lines show the background spectra; (lower panel) experimental [293] (circles) XMCD spectra of CeFe_2 at the Ce $L_{2,3}$ edges in comparison with the ones calculated using the LSDA (full lines) approximation; the dashed-dotted lines show the contribution from the quadrupole E_2 ($2p \rightarrow 4f$) transitions multiplied by a factor of 10.

the XMCD spectra shape can be provided by the analysis of the corresponding selection rules, orbital character, and occupation numbers of individual $5d$ orbitals (see detailed analysis in [307]).

The LSDA approximation reasonably well describes the shape of the XAS and XMCD spectra at the Ce $L_{2,3}$ edges (Figure 46); however, it slightly overestimates the first low energy peak and underestimates the intensity of the dichroic signal between two positive peaks of the L_3 XMCD spectrum.

5.3.3. Summary. The Ce $4f$ electrons in the CeFe_2 hybridize strongly with the Fe $3d$ electrons. A large magnetic moment at the Fe site induces spin splitting of the itinerant Ce $5d$ and Ce $4f$ states through exchange and hybridization effect. From our LSDA calculations, it has been deduced that the total moment is the result of the antiparallel coupling between Fe moment and cerium moment. This conclusion agrees well with the neutron diffraction, Compton scattering, and X-ray magnetic circular dichroism experiments.

The theoretically calculated X-ray absorption spectra at the Ce $M_{4,5}$ edges have a rather simple line shape composed of two white line peaks with additional fine structures at the high-energy part of the spectra which can be assigned to multiplet structures. The dichroism at the Ce $M_{4,5}$ edges is very large due to strong spin orbit coupling of the initial Ce $3d$ core states and large spin polarization of the final empty $4f_{5/2,7/2}$ states.

The XAS and XMCD spectra at the Ce $L_{2,3}$ edge reflect the energy distribution and the orbital character of the

Ce $5d$ band-like states. The LSDA calculations show good agreement in the shape of the X-ray absorption spectra at the Ce $L_{2,3}$ edges with the experimental measurements and reproduce the observed two-peak structure of the Ce XMCD spectra.

6. Sm Monochalcogenides and Borides

6.1. Sm Monochalcogenides. The Sm monochalcogenides offer the interesting possibility to study the transition from semiconductor to the mixed-valence state as a function of pressure. First, it is of great importance to characterize the semiconducting state.

The energy band structure of SmS presented in Figure 47 with the $4f$ electrons in the core can be subdivided into three regions separated by energy gaps. The bands in the lowest region around -11 eV have mostly S s character with some amount of Sm sp character mixed in. The next six energy bands are S p bands separated from the s bands by an energy gap of about 7 eV. The width of the S p band is about 3.2 eV. The unoccupied electronic states can be characterized as Sm $5d$ bands. The sharp peaks in the DOS calculated in the LSDA just below and above the Fermi energy are due to $4f_{5/2}$ and $4f_{7/2}$ states, respectively (Figure 47).

The LSDA+ U band structure calculations [313] have been started from a $4f^6$ configuration for the Sm^{2+} ion with six on-site $4f$ levels shifted downward by $U_{\text{eff}}/2$ and eight levels shifted upward by this amount. The energies of occupied $4f_{5/2}$ and unoccupied $4f_{7/2}$ levels are separated by

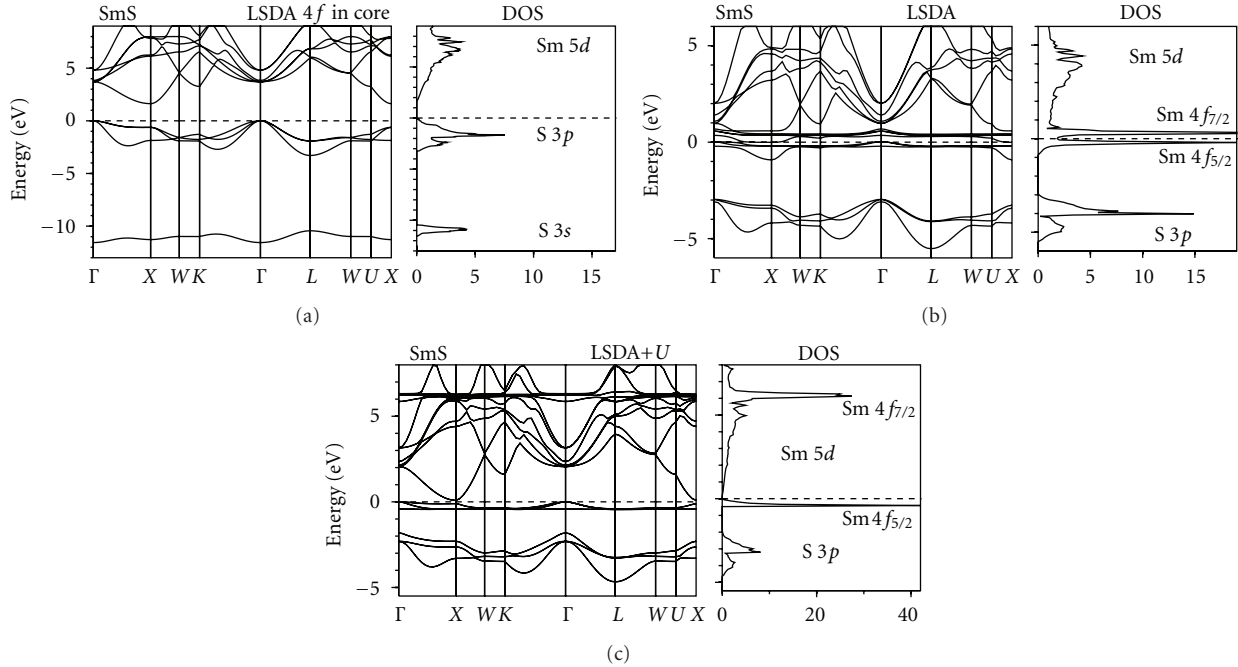


FIGURE 47: Self-consistent fully relativistic, spin-polarized energy band structure and total DOS (in states/(unit cell eV)) calculated for SmS [313] treating the 4f states as (a) fully localized (4f in core), (b) itinerant (LSDA), and (c) partly localized (LSDA+U).

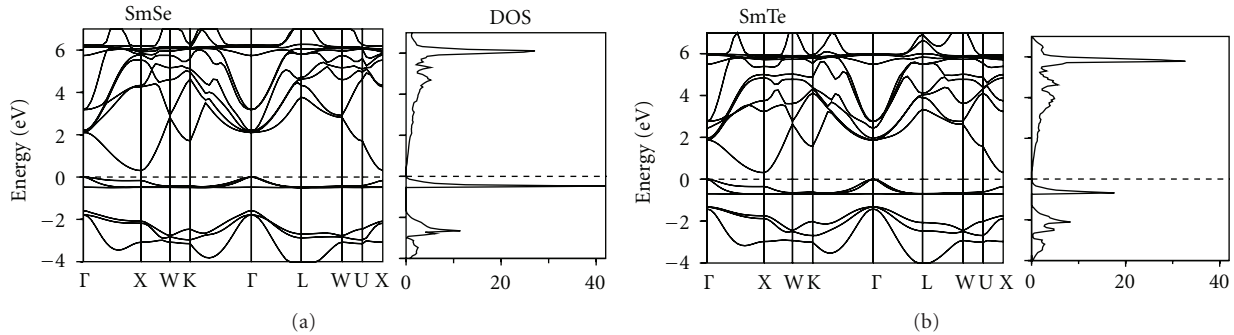


FIGURE 48: Self-consistent fully relativistic, spin-polarized energy band structure and total DOS (in states/(unit cell eV)) calculated for SmSe and SmTe in LSDA+U approximation [313].

approximately U_{eff} . The LSDA+U energy bands and total density of states of SmS for $U_{\text{eff}} = 6$ eV are shown in Figure 47. The Coulomb repulsion U_{eff} strongly influences the electronic structure of SmS. For Sm^{2+} ions six $4f_{5/2}$ bands are fully occupied and situated in the gap between S p and Sm $5d$ states, while the $4f_{7/2}$ hole levels are completely unoccupied and well above the Fermi level hybridized with Sm $5d$ states which results in a nonmagnetic ground state with the Sm ion in the divalent state. The theoretically calculated energy gap $\Delta E = 0.18$ eV which is formed between Sm $4f_{5/2}$ and Sm $5d$ states is in good agreement with the experimentally estimated 0.15 eV derived from the activation energy [5].

The LSDA+U energy bands and total density of states of SmSe and SmTe for $U_{\text{eff}} = 6$ eV are shown in Figure 48. Their electronic structures are very similar to the SmS one with six

Sm $4f_{5/2}$ bands fully occupied and the $4f_{7/2}$ hole bands completely unoccupied and well above the Fermi level hybridized with Sm $5d$ states. Theory gives energy gaps between Sm $4f_{5/2}$ and $5d$ bands equal to 0.47 and 0.67 eV in SmSe and SmTe, respectively. The corresponding experimental values are equal to 0.45 and 0.65 eV [5].

Photoemission experiments, both X-ray (XPS) and ultraviolet (UPS), have been of central importance for understanding mixed-valence materials. The partial 4f DOS of the occupied part of the SmS calculated in LSDA and LSDA+U approximations is compared with XPS measurements [314] in Figure 49. The theoretically calculated 4f DOS cannot, of course, fully account for the multiplet splitting. Therefore, Figure 49 presents the 4f DOSs taking into account the multiplet structure of the $4f^5$ final-state. This multiplet structure consists of 3 terms ${}^6\text{H}$, ${}^6\text{F}$, and ${}^6\text{P}$ [314]. In Figure 49 the XPS

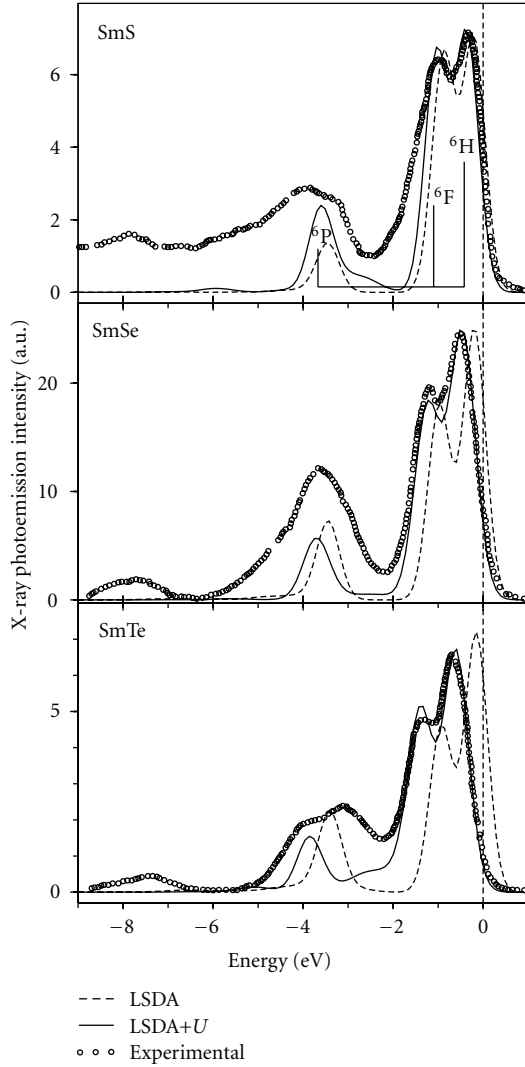


FIGURE 49: Comparison of the calculated $4f$ DOS in LSDA and LSDA+ U approximations [313] with the experimental XPS spectra from [314] taking into account the multiplet structure of the $4f^5$ final state (see explanations in the text).

spectrum is modeled by a weighted sum of three $4f$ DOS curves. We aligned the centroid of the calculated occupied $4f$ DOS peak with the centroid of the atomic final state multiplet. Although LSDA calculations produce almost the same picture as LSDA+ U calculations in the case of SmS, for SmSe and SmTe the LSDA calculations place the $4f_{5/2}$ energy bands too close to the Fermi level which leads to disagreement with measured XPS spectra (Figure 49).

In Figure 50 we show the experimental [315] real and imaginary parts of the dielectric function, $\epsilon_{1xx}(\omega)$ and $\epsilon_{2xx}(\omega)$, the optical reflectivity and optical conductivity $\sigma_{1xx}(\omega)$ spectra, as well as the spectra calculated with LSDA, LSDA+ U , and the $4f$ electrons in the core. This picture clearly demonstrates that the better description is unambiguously given by the LSDA+ U approach. As was mentioned above, the LSDA theory produces a metallic solution and, therefore, gives the wrong asymptotic behavior for the optical

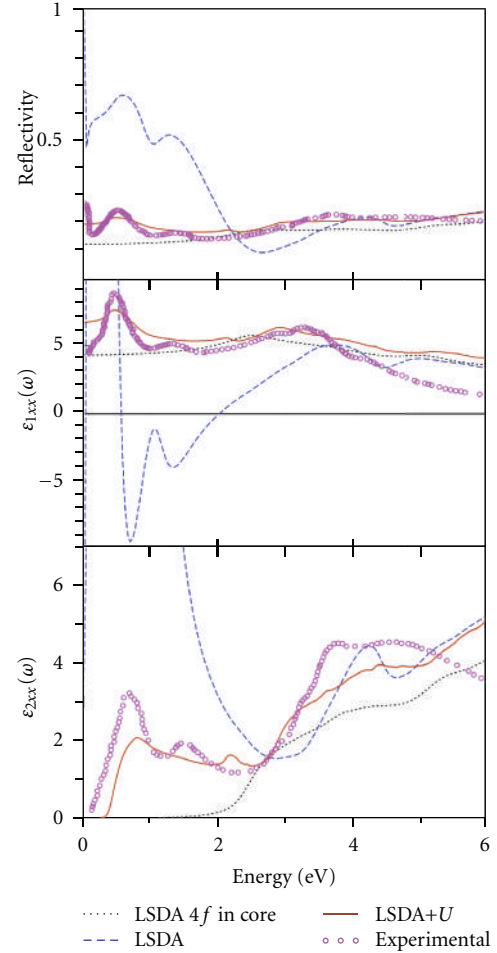


FIGURE 50: Calculated optical reflectivity R , real and imaginary parts of the diagonal dielectric function, ϵ_{1xx} , ϵ_{2xx} of SmS [313] treating $4f$ states as (1) fully localized ($4f$ in core) (dotted line), (2) itinerant (dashed line), and (3) partly localized (LSDA+ U approximation) (solid line) compared with experimental data (open circles) [315].

reflectivity and the dispersive part of the dielectric function ϵ_{1xx} as $\omega \rightarrow 0$. The most prominent discrepancy in the LSDA spectra is the extra peaks between 0 and 1.5 eV in the $\epsilon_{1xx}(\omega)$, $\epsilon_{2xx}(\omega)$, and optical conductivity $\sigma_{1xx}(\omega)$ caused by interband transitions involving the occupied $4f_{5/2}$ and unoccupied $4f_{7/2}$ hybridized states. In the LSDA+ U approach, the empty $4f_{7/2}$ state energies are shifted upward due to the on-site Coulomb interaction U_{eff} . As a result, the transitions involving the unoccupied $4f_{7/2}$ states do not take place at small photon energies, and the erroneous peak structures around 0 to 1.5 eV disappear from the optical spectra.

The calculations in which the $4f$ electrons are treated as quasicore are able to reproduce correct asymptotic behavior for the optical reflectivity and the dispersive part of the dielectric function ϵ_{1xx} as $\omega \rightarrow 0$ similar to the LSDA+ U calculations, but it fails in producing a peak at around 0.6 eV in the absorptive part of the dielectric function ϵ_{2xx} and optical conductivity spectra. This peak is mostly determined by the $4f \rightarrow 5d$ interband transitions.

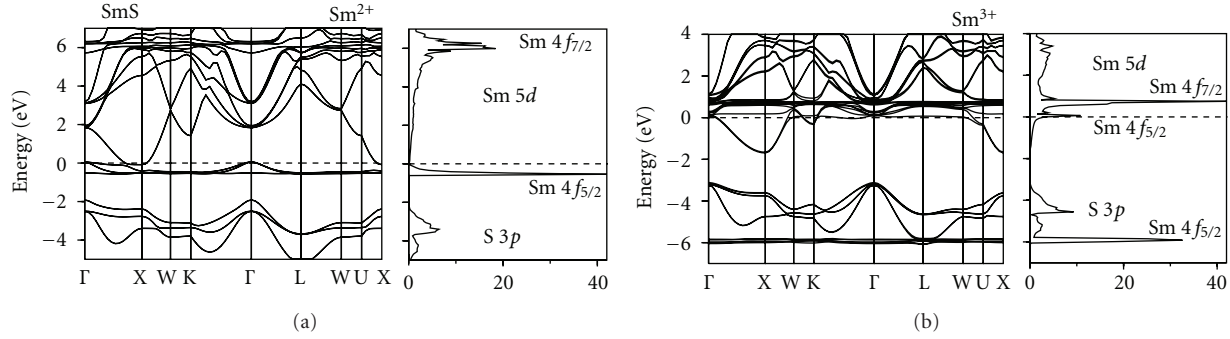


FIGURE 51: Self-consistent fully relativistic, spin-polarized energy band structure and total DOS (in states/(unit cell eV)) calculated for SmS with the LSDA+ U approximation for divalent and trivalent Sm atoms [313].

6.2. *High-Pressure Golden Phase of SmS.* The history of the Sm monochalcogenides as MV materials started at the beginning of the 1970s when Jayaraman et al. [316] and then Bucher et al. [317] discovered a pressure-induced semiconductor-metal transition and suggested that the metallic state would be mixed valent. It was a surprise that SmS showed this transition occurring at the incredibly low pressure of 6.5 kbar. Starting the pressure above the phase transition and decreasing, a large hysteresis is observed and the MV state snaps back to a semiconductor state at 1.5 kbar. For SmSe and SmTe the pressure-induced valence transition is continuous and is completed at higher pressures, about 45 and 60 kbar, respectively [5].

By increasing external pressure and hence, decreasing the lattice constant, the widths of Sm 5d and 4f bands are increased. In addition, the crystal-field splitting of the 5d states $e_g - t_{2g}$ in SmS is also increased. At a given pressure the 5d band overlaps with the 4f_{5/2} states and the energy gap becomes zero (Figure 51). It happens at a lattice constant around 5.70 Å [5]. Starting from the overlap of 4f and 5d states, 4f electrons will spill into the 5d band leaving a 4f⁵ state behind. The ionic radius of Sm³⁺ is about 15% less than the radius of Sm²⁺, so that simultaneously with more electrons in the 5d conduction band the lattice will shrink, thus further increasing the crystal-field splitting of the 5d states, resulting in an avalanche effect and a first-order valence transition. However, the valence transition does not go all the way to trivalency but stops where the gain in electronic energy is compensated by an increase in lattice strain energy [5].

The LSDA+ U energy bands and total density of states of SmS for Sm³⁺ are shown in Figure 51. There are five 4f_{5/2} bands fully occupied and hybridized with the bottom of the S p states. The 4f_{7/2} unoccupied states are well above the Fermi level. The initially empty 6th 4f_{5/2} hole level became partly occupied and pinned at the Fermi level in the process of self-consistent relaxation with occupation number equal to 0.25 (valence 2.75+). It is a typical situation for mixed-valent crystals.

We can use two different representations in the construction of the LSDA+ U method, namely, (j, m_j) and (l, m_l) representations. Most of rare earths and their compounds

have a rather large 4f spin magnetic moment; therefore, it is natural to use the (l, m_l) representation in the calculations of their electronic structure. In this case one chooses the projection of the orbital momentum onto the spin direction m_l for the occupied states. The SmS black phase as well as SmSe and SmTe have a nonmagnetic ground state; therefore, it was used in that case the (j, m_j) representation [313]. For fully occupied 4f_{5/2} states the z projections of the total moment were equal to $m_j = -5/2, -3/2, -1/2, 1/2, 3/2$, and 5/2.

The situation is not clear for golden SmS. It was used both of the representations for the calculation of the electronic structure of the golden high-pressure phase of SmS in [313]. Figure 51 presents the energy band structure of golden SmS in the (j, m_j) representation with $m_j = -1/2$ for the hole state. Due to the existence of a hole in the 4f_{5/2} shell, the LSDA+ U gives a so-called low magnetic moment ground state with total magnetic moment equal to $0.240 \mu_B$ (spin and orbital moments have opposite directions with values equal to -0.305 and $0.545 \mu_B$, resp.). The (l, m_l) representation gives a high-spin magnetic moment ground state in SmS with total magnetic moment equal to $4.636 \mu_B$ at each Sm³⁺ site (spin and orbital moments have opposite directions with values equal to 5.501 and $-0.865 \mu_B$, resp.). We should mention, however, that, although the LSDA+ U band structure calculations give always a nonzero samarium magnetic moment, in golden SmS all the efforts to find a magnetic superstructure in high-pressure SmS using neutron experiments have remained unsuccessful. However, one cannot exclude either a weak magnetic component below the limit of the experimental sensitivity (samples for high-pressure measurements are very tiny) or an incommensurate structure giving peaks at positions not searched in the neutron experiments. The evaluation of the magnetic ground state of golden SmS from first principles requires further investigation.

The pinning of a partly occupied 6th 4f level strongly depends on the lattice constant. The increasing of the valency with decreasing of the lattice constant which was found in the band structure calculations [313] can be considered as qualitative theoretical support of the conclusion derived from various experimental measurements [5] that the application

of pressure enhances the Sm^{3+} state relative to Sm^{2+} state in SmS. The theoretically calculated samarium valency was found to be equal to 2.55+ and 2.86+ for high- and low-spin solutions, respectively. The experimentally estimated one is about 2.6+ from spectroscopic methods and susceptibility measurements [318–320] and about 2.8+ from Vegard's law analysis of lattice constant measurements [320].

Some experimental results indicate that the golden phase of SmS could be a narrow-gap semiconductor. Evidence for a gap comes from the activation behavior of the electrical resistivity and point contact measurements [5]. The estimations from the point-contact spectra shows a possible gap of about 6.4 meV [5]. On the other hand, some experiments indicate that there may not be a gap but rather a pseudogap, and the hybridization does not occur over whole Brillouin zone. Although the temperature dependence of the resistivity in the golden phase of SmS is semiconductor-like, the resistivity is increased only one order of magnitude with cooling from room temperature to several K 's, whereas, for example, in SmB_6 it is 5 orders of magnitude [5]. Direct optical measurements of mechanically polished (high-pressure golden phase) SmS by Travaglini and Wachter [321] show that, in contrast to SmB_6 , the reflectivity does not tend to a constant value for $\omega \rightarrow 0$, but it seems to rise toward 100% as for a metal. Besides, there is a linear with $T\gamma$ term in the specific heat presumably due to conduction electrons [322]. The LSDA+ U band structure calculations of golden SmS [313] produce a pseudo gap at the Fermi level with a peak just above and a shoulder below the Fermi level with predominantly f character. It should be mentioned that, when the density of states at E_F is small compared to the giant density of states of the f peaks, the resistivity may nevertheless appear activated over a certain temperature range as experimentally observed, but for the lowest temperatures metallic conductivity should persist [321].

6.3. SmB_6 . SmB_6 is classical mixed-valence narrow gap semiconductors. This class of materials is characterized by their electronic properties, which at high temperatures are associated with a set of independent localized (f) moments interacting with a sea of conduction electrons, while at low temperature the electronic properties resemble those of a narrow gap semiconductor. SmB_6 is the first compound in which the phenomena of MV was detected directly by X-ray absorption [323]. Despite more than 35 years of experimental and theoretical efforts, many fundamental aspects of the microscopic description of the MV ground state and the nature of valence fluctuations are still under discussion [5, 324, 325]. The main problem is the origin of the MV ground state, which seems intimately connected with the gap formation. One question is whether Kondo insulating materials actually are true insulators at low temperatures or whether an intrinsic small conduction-electron carrier concentration is present [326]. Infrared absorption [327, 328], inelastic neutron scattering [329–332], optical conductivity [333], electron tunneling [334], and electrical transport [335–337] measurements all detect a small electronic gap $\Delta = 3\text{--}20$ meV. However, the low-temperature transport properties of SmB_6 are manifestly metallic, having a large but

finite resistivity below ~ 4 K [335–337]. There is considerable controversy whether these in-gap states are intrinsic and present in pristine SmB_6 [329–332, 338, 339], or extrinsic and dictated entirely by sample quality [335–337, 340, 341]. The size of the energy gap determined by different methods varies considerably. For example, the value of the gap in SmB_6 is equal to 2.7 meV by tunneling spectroscopy [334], 5 meV from the temperature dependence of the electrical resistivity [335–337], and 16 meV by point-contact spectroscopy [342]. Direct measurements of the low-temperature dynamical conductivity and dielectric permittivity of single crystalline SmB_6 give evidence for a 19 meV energy gap and an additional narrow donor-type band lying only 3 meV below the bottom of the upper conduction band [343].

The average valence of Sm in the hexaboride was established to be 2.56 at room temperature and to vary slightly with temperature by measurements of X-ray absorption [323, 344], lattice constant [345], X-ray photoemission [346], and the Mössbauer isomer shift [347].

The energy band structures of SmB_6 have been calculated by Yanase and Harima [348] in the local spin density approximation and in [349] using the LSDA+ U approximation.

The compound SmB_6 has the CaB_6 type crystal structure with space group $Pn3m$ (no. 221) and lattice constant equal to 4.1333 Å. The structure of samarium hexaboride may be viewed as a CsCl-type lattice with the cesium replaced by samarium and the chlorine by a B_6 octahedron. Figure 52 shows the energy band structure of SmB_6 calculated within the LSDA and the LSDA+ U approximations [349]. The energy band structure of SmB_6 with the LSDA approximation can be subdivided into three regions separated by energy gaps. The bands in the lowest region around -14 to -16 eV (not shown) have mostly B $2s$ character with some amount of Sm sp character mixed in. The next group of energy bands are B $2p$ bands separated from the $2s$ bands by an energy gap of about 3 eV. The width of the B $2p$ band is about 8.8 eV. The Sm $5d$ bands are partly occupied. They are also separated from B $2p$ states by the energy gap of around 0.7 eV. The sharp peaks in the DOS calculated in the LSDA just below and above the Fermi energy are due to $4f_{5/2}$ and $4f_{7/2}$ states, respectively (Figure 52). They cross the Sm $5d$ bands and hybridize with them. There is a small direct energy gap at the Fermi level of around 23 meV.

The LSDA+ U energy bands and total DOS of SmB_6 for $U_{\text{eff}} = 7$ eV are shown in Figure 52. The Coulomb repulsion U_{eff} strongly influences the electronic structure of SmB_6 . For Sm^{3+} ions five $4f_{5/2}$ bands are fully occupied and hybridized with the B $2p$ states. The $4f_{7/2}$ unoccupied states are above the Fermi level at around 1 eV. A single $4f_{5/2}$ level is fully unoccupied and situated at about 0.34 eV above the Fermi level.

The LSDA+ U band structure calculations [349] have been started from a $4f^6$ configuration for the Sm^{2+} ion with six on-site $4f$ energies shifted downward by $U_{\text{eff}}/2$ and eight levels shifted upward by this amount. The energies of occupied $4f_{5/2}$ and unoccupied $4f_{7/2}$ levels are separated by approximately U_{eff} (Figure 52). For Sm^{2+} ions eight $4f_{7/2}$ hole levels are completely unoccupied and well above the Fermi level and hybridized with Sm $5d$ states. The $4f_{5/2}$ bands are

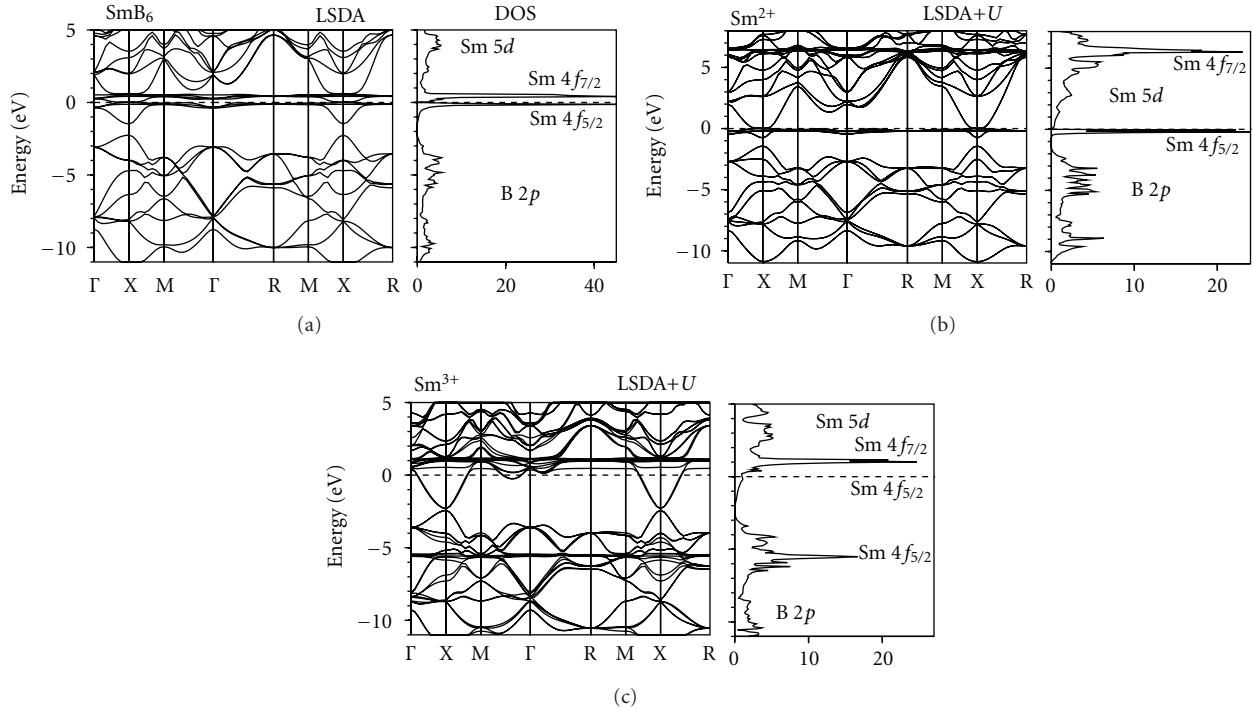


FIGURE 52: Self-consistent fully relativistic, spin-polarized energy band structure and total DOS (in states/(unit cell eV)) calculated for SmB₆ with LSDA and LSDA+*U* approximations [349].

situated in close vicinity of the Fermi level. They cross the bottom of Sm 5*d* band. Figure 53 shows an expanded view of the LSDA+*U* energy band structure and total DOS for SmB₆ with Sm²⁺ ions. There is a hybridization gap at the Fermi level $\Delta E = 27$ meV. Although the LSDA+*U* calculations [349] used a starting configuration with fully occupied 4*f*_{5/2} bands, in the process of self-consistent relaxation, one of the 4*f*_{5/2} doubly degenerate bands becomes partly unoccupied and situated above the Fermi level around the X symmetry point (Figure 53) due to Sm 5*d*–4*f* hybridization. There is a small peak in the DOS above the Fermi level at around 0.03 eV with predominantly 4*f* character. This peak contains 0.02 4*f* holes. In other words, the LSDA+*U* calculations produce a semiconducting ground state in SmB₆ with noninteger Sm valency equal to 2.02+.

The XPS spectra for SmB₆ indicate multiplet structure which can be identified with both Sm²⁺ and Sm³⁺ configurations being present. Figure 54 shows the SmB₆ XPS spectrum [346] in comparison with the occupied part of the partial LSDA+*U*4*f* DOS calculated with a multiplet structure of the final states taken into account in the same way as for SmS in previous section. Figure 54 shows the final-state multiplet structure presented in [346]. Sm²⁺ (4*f*⁵ final state) has the multiplets ⁶H, ⁶F, and ⁶P. Sm³⁺ (4*f*⁴ final state) has the multiplets ⁵I, ⁵F, G, and ⁵D [346]. It is clear that the structures between 0.0 and –5.5 eV binding energy should be assigned to the final-state multiplet structure derived from six fully occupied 4*f* bands (Sm²⁺), and the structures between –5.5 and –13 eV are associated with the final-state

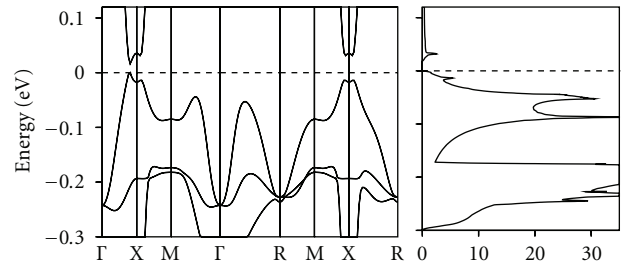


FIGURE 53: Expanded view of the energy band structure and total DOS (in states/(unit cell eV)) of SmB₆ for Sm²⁺ ions calculated in LSDA+*U* approximations [349].

multiplet structure of the Sm³⁺ ions. The agreement with the positions of the multiplet peaks indicates that the LSDA+*U* is giving reasonably correct average positions for the occupied 4*f* states.

Let us turn now to the optical properties of SmB₆. Experimental investigation of the reflectivity spectra of SmB₆ was performed by Kierzek-Pecold [350] in a narrow energy range from 1 to 5.6 eV. After that, Travaglini and Wachter measured the reflectivity spectrum of SmB₆ in the energy range from 1 meV to 12 eV at 300 K and 4 K for investigation of the energy gap [333]. Kimura with coworkers measured the optical spectra of all single-crystal rare-earth hexaborides RB₆ (*R* = La, Ce, Pr, Nd, Sm, Eu, Gd, Th, Dy, Ho, Yb, and Y) in the energy region from 1 meV to 40 eV at 300 K and 13 K [328, 351–353].

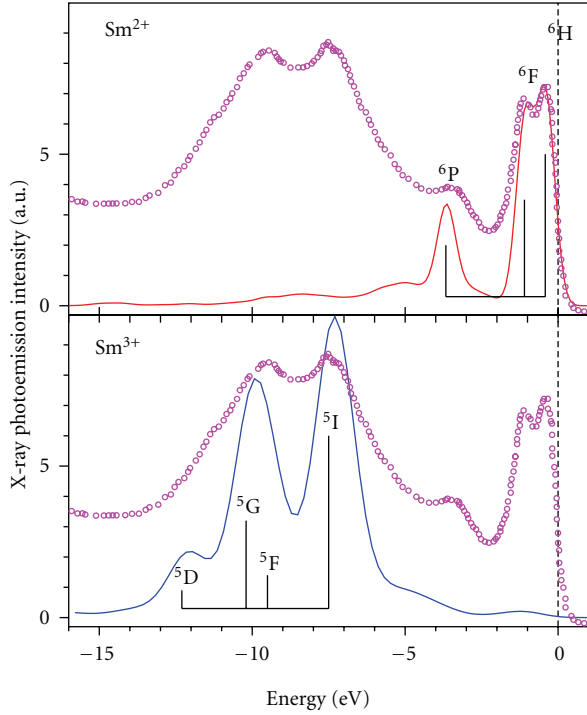


FIGURE 54: Comparison of the calculated $4f$ DOS of SmB_6 using LSDA+ U approximation [349] with the experimental XPS spectra from [346] taking into account the multiplet structure of the $4f^5$ and $4f^4$ final states (see explanations in the text).

Figure 55 shows with a logarithmic scale the calculated optical conductivity spectra of SmB_6 compared with experimental data measured at 13 K [328]. Calculations were performed for both the divalent and trivalent phases of SmB_6 . The experimentally measured optical conductivity spectrum has two strong peaks at 0.12 and 0.5 eV and a steep rise at 3 eV (Figure 55). As might be expected the experimental optical conductivity spectrum contains key features of both the divalent and trivalent theoretically calculated spectra. However, the three major peaks have different origins in the divalent and trivalent phases. A step increase of optical conductivity starting at around 3 eV is mostly determined by $B 2p \rightarrow \text{Sm } 5d$ interband transitions around the X symmetry point in the divalent samarium compound. The same feature in the trivalent phase can be described as a combination of the $B 2p \rightarrow \text{Sm } 5d$ and $\text{Sm } 5d \rightarrow \text{Sm } 4f$ interband transitions. These transitions also occur mostly around the X symmetry point (Figure 52). The low-energy peak at 0.12 eV in the divalent phase can be explained as interband transitions between occupied $\text{Sm } d-f$ mixed states and unoccupied $\text{Sm } 5d$ states near the X symmetry point. The same structure in the trivalent Sm phase is due to interband transitions among hybridized $\text{Sm } 5d$ bands along Γ -X, Γ -M, X-M, and X-R symmetry directions. This peak is shifted at around 0.1 eV toward smaller energies in comparison with the experimental measurements. The peak at 0.5 eV in the divalent phase arises from interband transitions between occupied $\text{Sm } d-f$ mixed states and unoccupied $\text{Sm } 5d$ states near the X symmetry

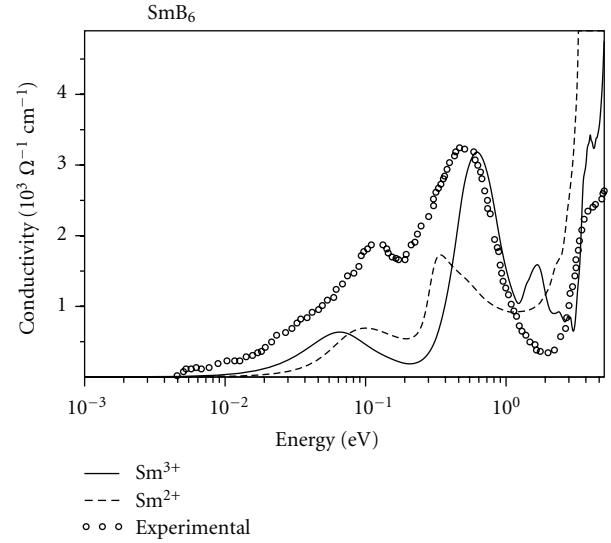


FIGURE 55: Calculated diagonal part of the optical conductivity $\sigma_{1xx}(\omega)$ of SmB_6 in the LSDA+ U approximation [349] compared with the experimental measurements at 13 K (open circles) [328].

point and Γ -X and X-M symmetry directions. The same structure in the trivalent samarium phase is due to interband transitions between occupied $\text{Sm } 5d$ states and the empty 6th $4f$ hole band along Γ -X, Γ -M, and X-M symmetry directions.

As we mentioned above, the XPS measurements cannot distinguish between an inhomogeneously mixed or a homogeneously mixed compound, that is, whether Sm^{2+} and Sm^{3+} ions are integer valent and statically mixed or the charge between them just fluctuates slower than the time resolution of XPS. The experimental optical conductivity spectrum also can be considered as a mixture of both the divalent and trivalent spectra. From other experiments, SmB_6 is known to be a homogeneous mixed-valence semiconductor compound with a small energy gap [5]. Mössbauer isomer shift versus temperature measurements for SmB_6 by Cohen et al. clearly shows that above 700 K and down to 4.2 K the degree of valence mixing is a constant of around 2.56 [347]. The LSDA+ U band structure calculations [349] produce a metallic state with trivalent samarium ions if we start the self-consistent procedure from Sm^{3+} . On the other hand, if we used as starting configuration with fully occupied $4f_{5/2}$ levels (Sm^{2+}), we will be able to produce a correct semiconductor ground state for SmB_6 with a small hybridization energy gap and a theoretically calculated valency $2.02+$. A comprehensive theory for the MV state is needed to provide a quantitative measure of the mixing between the two configurational states. The LSDA+ U calculations are only able to provide specific details for the individual configurational states.

6.4. YbB_{12} . The compound YbB_{12} has the UB_{12} type crystal structure with space group $Fm\bar{3}m$ (no. 225) and lattice constant equal to 7.464 Å. The crystal structure of YbB_{12} can be understood as fcc NaCl type with the sodium replaced by ytterbium and the chlorine by 12 B atoms.

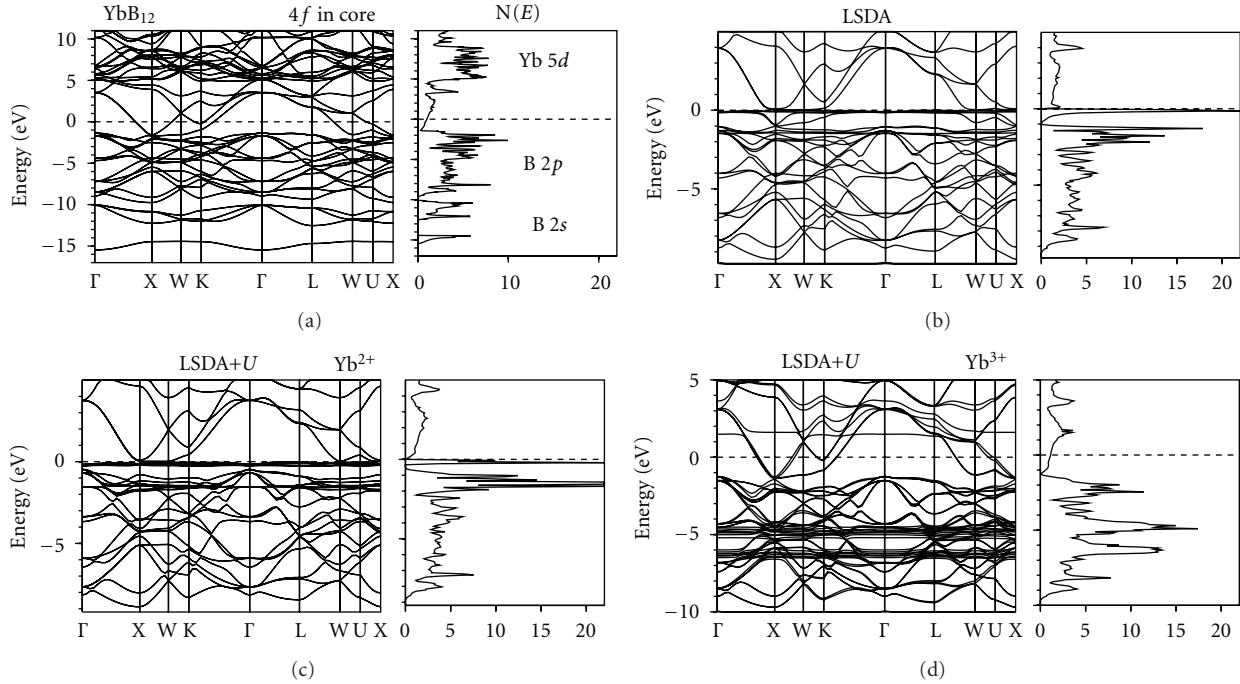


FIGURE 56: Self-consistent fully relativistic, spin-polarized energy band structure and total DOS (in states/(unit cell eV)) calculated for YbB_{12} with LSDA and LSDA+ U approximations [349].

The band structure calculations in [349] have been performed using three independent fully relativistic spin-polarized calculations. The $4f$ electrons have been considered as (1) itinerant electrons using the local spin-density approximation (2) fully localized, putting them in the core, and (3) partly localized using the LSDA+ U approximation. Figure 56 shows the energy band structure of YbB_{12} for all three approximations. The energy band structure of YbB_{12} with $4f$ electrons in core can be subdivided into three regions. The bands in the lowest region around -15.5 to -10 eV have mostly B $2s$ character with some amount of Yb sp character mixed in. The next group of the energy bands are B $2p$ bands separated from the $2s$ bands by a small energy gap of about 0.4 eV. The width of the B $2p$ band is about 8 eV. The Yb $5d$ bands are partly occupied and cross the Fermi energy. They slightly overlap with B $2p$ states. The sharp peaks in the DOS calculated in the LSDA just below the Fermi energy are due to Yb $4f_{5/2}$ and $4f_{7/2}$ states (Figure 56). They cross Yb $5d$ bands and hybridize with them. There is a small direct energy gap of about 65 meV at the Fermi level.

The LSDA+ U energy bands and total density of states of YbB_{12} for $U_{\text{eff}} = 8$ eV are shown in Figure 56. For divalent Yb ions all 14 $4f$ bands are fully occupied and situated closely below the bottom of Yb d band. They are split due to spin-orbit coupling by $\Delta\varepsilon_{\text{so}} = 1.4$ eV. There is a small hybridization gap at the Fermi level. In other words, the calculations indicate a nonmagnetic semiconducting ground state in YbB_{12} for Yb atoms in the divalent state. The theoretically calculated energy gap $\Delta E = 65$ meV is formed between Yb $4f_{7/2}$ and Yb $5d$ states. The experimentally estimated energy gap is about 10 meV from the activation energy [355–357],

25 meV from optical measurements [358], and 200–300 meV from tunneling experiments [359].

For the trivalent Yb ion, thirteen $4f$ electron bands are well below the Fermi energy and hybridized with the B $2p$ states (Figure 56). The 14th $4f$ unoccupied hole level is above the Fermi level at around 1.5 eV. It should be mentioned that such an electronic structure is appropriate for the development of the Kondo scenario.

The partial $4f$ DOS of the occupied part of YbB_{12} calculated in the LSDA+ U approximation is compared with ultraviolet photoelectron spectra (UPS) [354, 360] in Figure 57 [349]. The experimental spectra were measured using both single-crystalline [354] and polycrystalline [360] samples. The double-peak structure at 0.1 and 1.5 eV binding energy reflects the spin-orbit doublet of the Yb^{2+} density of states. The corresponding spin-orbit doublet for the Yb^{3+} DOS is situated at -6.0 and -7.6 eV (Figure 57(a)).

Theoretically calculated $4f$ DOS cannot, of course, fully account for the multiplet splitting. Therefore, we present in Figure 57(b) the $4f$ DOSs taking into account the multiplet structure in the same way as for SmB_6 . We used the theoretical final-state multiplet structure presented in [361]. Yb^{2+} has the configuration $4f^{14}$. The $n-1$ state $4f^{13}$ has one hole in $4f$ shell and cannot reproduce the experimentally measured four-peak structure in the XPS. One would expect only the spin-orbit doublet, and the 4-peak structure is almost certainly due to surface effects.

After consideration of the band structure and UPS spectra of YbB_{12} , we turn to the optical spectra. Optical reflectivity experiments have been conducted by Okamura et al. on single crystals of YbB_{12} [358]. They found that upon cooling

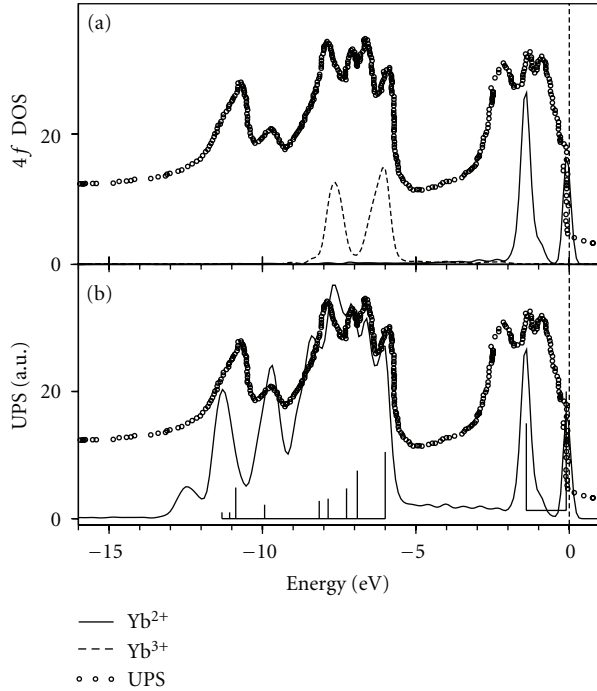


FIGURE 57: (a) The calculated $4f$ DOS of YbB_{12} for Yb^{2+} and Yb^{3+} configurations [349] in comparison with the experimental UPS spectra from [354]; (b) the calculated $4f$ DOS of YbB_{12} taking into account the multiplet structure of the $4f^{13}$ and $4f^{12}$ final states (see explanation in the text) in comparison with the experimental UPS spectra from [354].

below 70 K, a strong suppression of the optical conductivity $\sigma(\omega)$ was seen in the far-infrared region, reflecting the opening of an energy gap of ~ 25 meV. A narrow, asymmetric peak was observed at ~ 40 meV in $\sigma(\omega)$, which was attributed to optical transitions between the Yb $4f$ -derived states across the gap [358]. They also measured the optical spectra of single crystalline LuB_{12} as a reference material.

Figure 58 shows with a logarithmic scale the calculated optical reflectivity $R(\omega)$ and diagonal part of optical conductivity $\sigma_{1xx}(\omega)$ spectra of LuB_{12} compared with the experimental data [358]. To incorporate the intraband contribution to the optical conductivity tensor, the phenomenological Drude model [362] with intraband Drude relaxation time $\gamma_D = 0.3$ eV was used. A sharp onset is seen in the LuB_{12} reflectivity spectrum $R(\omega)$ near 1.6 eV, which can be identified as the plasma edge (ω_p) due to a metallic response of free carriers. The peak structures above ω_p are due to interband transitions between electronic states far apart from E_F . Figure 58 clearly shows the important role of intraband transitions in formation of the optical conductivity spectrum in LuB_{12} .

Figure 59 shows the calculated optical reflectivity spectra of YbB_{12} compared with experimental data measured at 290 K [358]. Calculations were performed for both the divalent and trivalent phases of YbB_{12} . The intraband optical transitions in Drude form with inverse intraband Drude relaxation time $\gamma_D = 0.1$ eV also included. The optical reflec-

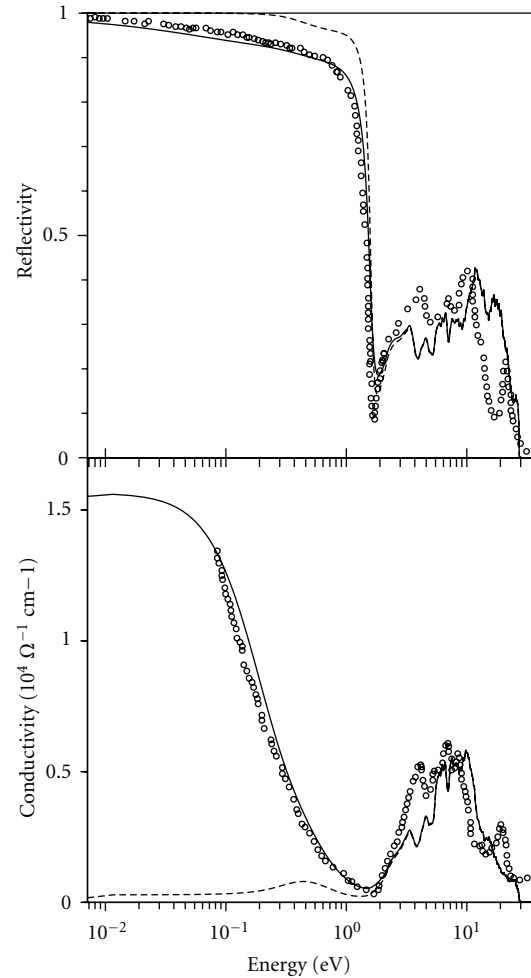


FIGURE 58: Calculated optical reflectivity $R(\omega)$ and diagonal part of the optical conductivity $\sigma_{1xx}(\omega)$, of LuB_{12} in the LSDA approximation: dashed line without and solid line with Drude term [349] compared with the experimental data (open circles) [358]. Above ~ 1 eV the dashed and solid lines coincide.

tivity spectrum of YbB_{12} measured at 290 K has a metallic character, very similar to LuB_{12} $R(\omega)$ with the same plasma edge at 1.6 eV. The two spectra are almost identical for the energy interval above ω_p . Below ω_p , in contrast, the spectra are strictly different for the two compounds. In LuB_{12} , $R(\omega)$ is nearly flat and $\sigma(\omega)$ shows a sharp rise, which is typical of a good metal, while in YbB_{12} there is a broad dip in $R(\omega)$ giving rise to a prominent peak at 0.25 eV in $\sigma(\omega)$. As can be seen from Figure 59 a broad dip in $R(\omega)$ comes from YbB_{12} with divalent Yb ions. Our LSDA+ U calculations produce the reflectivity spectrum in YbB_{12} with trivalent ytterbium ions very similar to the LuB_{12} spectrum. The experimentally measured optical reflectivity spectrum of YbB_{12} can be considered as a mixture of two spectra coming from di- and trivalent ytterbium ions. Good agreement between theory and experiment can be reached if one uses the sum of the optical reflectivity spectrum consisting of 20% ytterbium divalent and 80% ytterbium trivalent spectra (Figure 59).

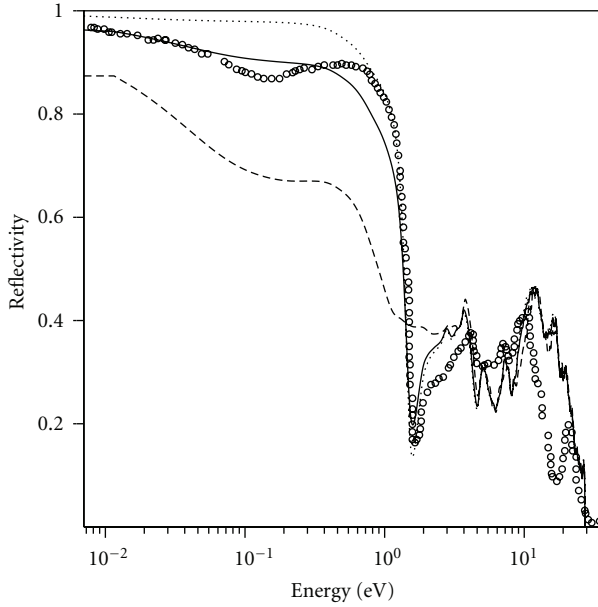


FIGURE 59: The experimental optical reflectivity spectrum $R(\omega)$ of YbB_{12} (open circles) measured at 290 K [358] in comparison with theoretical calculations in the LSDA+ U approximation: dotted line for Yb^{3+} , dashed line for Yb^{2+} ions, and solid line for $R = 0.2 * R^{2+} + 0.8 * R^{3+}$ [349].

The experimental investigations of the temperature dependence of the optical spectra of YbB_{12} presented in [358] show that, as the temperature is lowered from 290 K to 78 K, there is no drastic change in the optical conductivity spectrum. The IR peak becomes slightly enhanced and blue-shifted. At 78 K the spectra are still metallic. However, at 20 K the spectral weight below ~ 40 meV in $\sigma(\omega)$ is strongly depleted and the spectrum becomes typical of a semiconductor with an energy gap of around 25 meV. The reflectivity spectrum at 20 K is also typical of a semiconductor having the asymptotic value at $\omega \rightarrow 0$ of 0.83. The gap development coincides with the rapid decrease of the magnetic susceptibility in exactly the same temperature range [358].

Figure 60 shows the calculated diagonal part of optical conductivity $\sigma_{1xx}(\omega)$ spectra of YbB_{12} [349] compared with experimental data [358]. Calculations were performed for both the divalent and trivalent phases of YbB_{12} . The experimentally measured optical conductivity spectrum in the 0 to 0.6 eV energy interval has two peaks at 0.05 and 0.25 eV (Figure 60). The experimental optical conductivity spectrum of YbB_{12} contains key features of both the divalent and trivalent theoretically calculated spectra. The low-energy peak at 0.05 eV in the optical conductivity spectrum originates from trivalent phase and can be explained as interband transitions between occupied and unoccupied Sm $5d$ states along Γ -X and X-W symmetry directions (Figure 56). The prominent peak in $\sigma_{1xx}(\omega)$ spectrum at around 0.4 eV (the corresponding experimental peak situated at 0.25 eV) is mostly derived from the interband transitions between occupied Yb $4f$ bands and empty Yb $5d$ bands of divalent phase in the vicinity of the W symmetry point as well as along the X-W

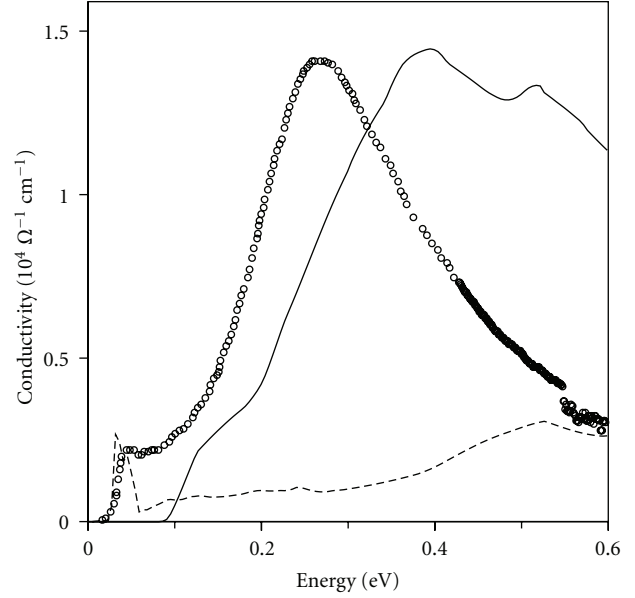


FIGURE 60: Calculated diagonal part of the optical conductivity σ_{1xx} , of YbB_{12} in the LSDA+ U approximation for Yb^{2+} ion (full line) and Yb^{3+} ion (dashed line) [349] compared with the experimental data (open circles) [358].

symmetry direction (Figure 56). The theoretically calculated $\sigma_{1xx}(\omega)$ spectrum in divalent phase is shifted toward higher energies due to the larger theoretically calculated energy gap (65 meV) in comparison with the experimental one (25 meV).

6.4.1. Summary. The Sm monochalcogenides SmS, SmSe, and SmTe constitute a very interesting system exhibiting behavior due to strongly correlated electrons. While the standard LSDA approach is unable to correctly describe the electronic structure of these materials because of the strong on-site Coulomb repulsion, U_{eff} , the LSDA+ U approach is remarkably accurate in providing detailed agreement with experiment for a number of properties.

In contrast to LSDA, where the stable solution for Sm monochalcogenides at ambient pressure is metallic, the LSDA+ U method gave an insulator with energy gaps of 0.15, 0.45, and 0.65 eV (the experimental gaps are 0.18, 0.47, and 0.67 eV) for SmS, SmSe, and SmTe, respectively. The Coulomb repulsion U_{eff} strongly influences the electronic structure of Sm monochalcogenides. For Sm^{2+} ions six $4f_{5/2}$ bands are fully occupied and situated in the gap between chalcogen $3p$ and Sm $5d$ states. The $4f_{7/2}$ hole levels are completely unoccupied and well above the Fermi level hybridized with Sm $5d$ states. The LSDA+ U theory predicts that the samarium ion in these compounds is in an integer divalent state. It also shows a gradual decrease of the energy gap with reduction of the lattice constant. The LSDA+ U theoretical calculations describe well the optical spectra of Sm monochalcogenides.

When applying external pressure to SmS and, hence, decreasing its lattice constant, the widths of Sm $5d$ and $4f$ bands are increased and the crystal-field splitting of the $5d$ states $e_g - t_{2g}$ is also increased. At a given pressure the $5d$ band overlaps with the $4f_{5/2}$ states. This leads to a first-order valence $\text{Sm}^{2+} \rightarrow \text{Sm}^{3+}$ phase transition. The gap in SmS is closed at $a = 5.70 \text{ \AA}$ in good agreement with experimental measurements of SmS transport properties under pressure. For SmS with Sm^{3+} ions five $4f$ bands are fully occupied and hybridize with chalcogenide p states. The initially empty hole 6th $4f$ level in the process of self-consistent relaxation becomes partly occupied with the $4f$ DOS maximum situated in close vicinity of the Fermi level in the golden phase of SmS. The occupation number of the 6th $4f$ hole level is equal to 0.45 (valence 2.55+) in a good agreement with the experimental estimates from spectroscopic methods and susceptibility measurements.

In conclusion we would like to point out that, while the LSDA+ U approach does a very good job in the treatment of correlation effects in SmS, SmSe, and SmTe at normal pressure, it is still unclear how well it performs in describing the mixed-valence state in golden SmS in the pressure range from 6 to 20 kbar. On one hand, we found the pinning of a partly occupied 6th $4f$ level at the Fermi level, which is the typical situation for mixed-valence systems. On the other hand, the LSDA+ U calculations always produce a nonzero magnetic moment in the high-pressure phase of SmS, although all attempts to find any sign of magnetic ordering in this system gave no positive results for the last 30 years. It is more likely that our LSDA+ U calculations describe well the situation in the metallic phase of SmS at pressure $P \geq 20$ kbar with trivalent samarium ions.

We should mention that the experimental situation in golden SmS differs from that in SmB_6 in the sense that in the later system a new generation of samples of much better quality became available during recent years, and more reliable data about transport properties and infrared spectroscopy were obtained. In SmS we still use old experimental data, and it is difficult to ascertain the full validity of measured gaps or pseudogaps as well as other properties based on the experiments of the early 1970s. The physical nature of the mixed-valence state in golden SmS requires further investigation theoretically as well as experimentally.

As classical mixed-valence narrow gap semiconductors SmB_6 and YbB_{12} constitute very interesting systems exhibiting behavior due to strongly correlated electrons. The LSDA calculations provide an inadequate description of the $4f$ electrons in SmB_6 and YbB_{12} due to improper treatment of the correlation effects.

The Coulomb repulsion U_{eff} strongly influences the electronic structure of SmB_6 . For Sm^{2+} ions eight $4f_{7/2}$ hole levels are completely unoccupied and well above the Fermi level hybridized with Sm $5d$ states. The $4f_{5/2}$ bands are situated in close vicinity of the Fermi level. One of the $4f_{5/2}$ levels is slightly unoccupied and extends just above the Fermi level around the X symmetry point, producing a noninteger Sm valency equal to 2.02+. There is a small hybridization gap at the Fermi level $\Delta E = 27 \text{ meV}$. The theoretically calculated energy gap is larger than the experimentally estimated one

of around 3.6 to 5.2 meV determined from the activation energy and optical measurements. For Sm^{3+} five $4f$ bands are fully occupied and situated at around 6 eV below the Fermi level. A 6th $4f$ hole level is fully unoccupied and situated at about 0.34 eV above the Fermi level. The average positions of the occupied $4f$ states in Sm^{2+} and Sm^{3+} calculations are in agreement with XPS measurements.

In the LSDA+ U energy band structure calculations of the electronic structure of YbB_{12} with divalent Yb ions all 14 $4f$ bands are fully occupied and situated closely below the bottom of the Yb $5d$ band. They are split due to spin-orbit coupling by $\Delta\epsilon_{so} = 1.4 \text{ eV}$. There is a small hybridization gap at the Fermi level. The theoretically calculated energy gap $\Delta E = 65 \text{ meV}$ between Yb $4f_{7/2}$ and Yb $5d$ states is somewhat larger than the gap estimated from the activation energy and optical measurements and smaller than observed in tunneling experiments. For the trivalent Yb ion, thirteen $4f$ electron bands are well below the Fermi level and hybridized with the B $2p$ states. They are separated from a $4f$ hole state by the correlation energy U_{eff} . The 14th $4f$ unoccupied hole level is well above the Fermi level at around 1.5 eV.

The optical spectra of YbB_{12} can be considered as a mixture of two spectra coming from di- and trivalent ytterbium ions. Good agreement between theory and high-temperature optical reflectivity spectrum can be reached if one uses the sum of the optical reflectivity spectrum consisting of 20% ytterbium divalent and 80% ytterbium trivalent spectra. Low temperature measurements show that below 20 K there is a gap development in the optical conductivity and reflectivity spectra of YbB_{12} . The low energy peak at 0.05 eV in the optical conductivity spectrum originates from the trivalent phase and can be explained as interband transitions between occupied and unoccupied Sm $5d$ states along Γ -X and X-W symmetry directions. The prominent peak in the $\sigma_{1xx}(\omega)$ spectrum at around 0.4 eV is mostly derived from interband transitions between occupied Yb $4f$ bands and empty Yb $5d$ bands of the divalent phase in the vicinity of the W symmetry point as well as along the X-W symmetry direction.

We should mention that the situation in YbB_{12} is still vague both experimentally and theoretically, and that more experimental data may help clarify the picture. If ytterbium in this compound is practically trivalent, as is claimed based on recent measurements of X-ray absorption and inelastic neutron-scattering by Alekseev et al. [363], then the gap in the tunneling and other experiments could be ascribed only to a Kondo insulator (KI) state. However, it is difficult to understand this. The necessary precondition for the KI state is a nearly half-filled single conduction band, but LSDA+ U band structure calculations with Yb^{3+} ions produce several sheets of Fermi surface. The influence of the degree of valence mixing on the formation of the Kondo insulator state in YbB_{12} will require further theoretical and experimental investigations.

7. Tm Monochalcogenides

The Tm monochalcogenides TmS, TmSe, and TmTe constitute a well-known family of strongly correlated electron

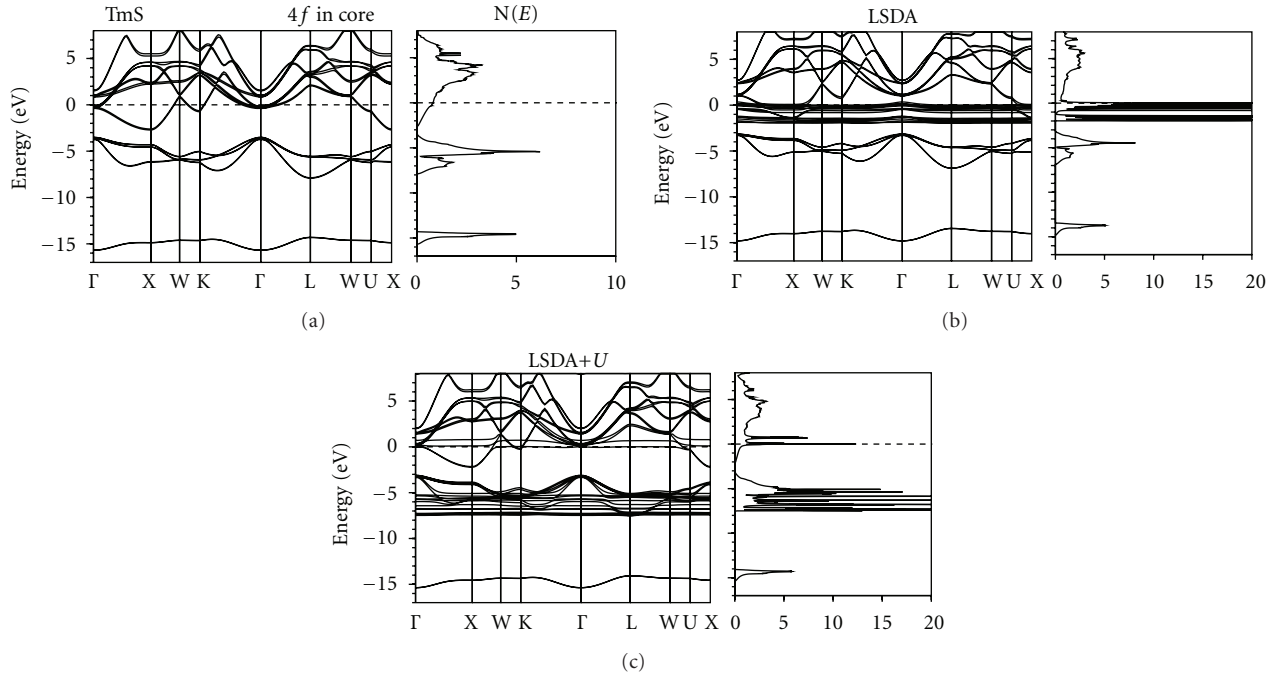


FIGURE 61: Self-consistent fully relativistic, spin-polarized energy band structure and total DOS (in states/(unit cell eV)) calculated for TmS [384] treating the $4f$ states as (a) fully localized ($4f$ in core), (b) itinerant (LSDA), and (c) partly localized (LSDA+ U).

systems. They form a very interesting group of materials in which many characteristic phenomena are expressed. In the series of the Tm monochalcogenides one has the interesting possibility to go from integer trivalent metallic TmS to integral divalent semiconducting TmTe through intermediate-valence TmSe [5, 364, 365]. The unique feature of thulium compounds compared with intermediate-valence materials containing cerium, samarium, or europium is that both ground-state configurations of thulium have a nonzero magnetic moment. TmS exhibits antiferromagnetic order which is an almost type II sinusoidally modulated structure below $T_N = 6.2$ K [366]. It has been classified as a Kondo lattice compound due to a metallic resistivity which increases Kondo-like down to about 15 K [4, 367–369]. TmSe has attracted interest because of the valence fluctuation between $4f^{12}$ and $4f^{13}$ configurations, Kondo effects, antiferromagnetic order, and a possible metal-insulator transition. This compound has the peculiarity that two magnetic valence states Tm^{2+} and Tm^{3+} are involved in the valence fluctuation. Evidence comes from photoemission experiments [346, 364, 365, 370–373] and also from measurements related to magnetic properties, resistivity, and specific heat [374–378]. However, the situation is so complicated that there is no overall consistent explanation of the physical properties of this compound. The resistivity of TmSe shows a Kondo-like logarithmic temperature dependence at high temperatures followed by a sharp increase at $T_N = 3.5$ K, which is thought to be a transition into an insulating state [377, 379, 380]. This anomaly in the vicinity of T_N shows a very complicated response to external magnetic fields and to pressure [376, 381].

TmTe is a magnetic semiconductor with a localized 13th f level between a filled Te $5p$ valence band and an empty Tm $5d$ conduction band [365]. The lattice constant and the Curie constant show that the Tm ions are divalent at ambient pressure [364]. TmTe is interesting in its own right, especially since it was recently reported [382] to undergo a phase transition at $T_Q = 1.7$ K, far above the magnetic-ordering temperature ($T_N \sim 0.2$ – 0.4 K depending on the specimen). This transition was ascribed to the onset of long-range ordering among the Tm quadrupolar moments, but the exact mechanism is still controversial [383].

7.1. TmS

7.1.1. Band Structure. The theoretical study of the electronic structure, optical and magneto-optical spectra of TmX ($X = \text{S}, \text{Se}, \text{and Te}$) have been done in [384]. It was performed three independent fully relativistic spin-polarized band structure calculations. The $4f$ electrons have been considered as (1) itinerant electrons using the local spin-density approximation, (2) fully localized, putting them in the core, and (3) partly localized using the LSDA+ U approximation. An important difference with respect to treating the $4f$ electrons as core electrons is that in the LSDA+ U calculation all optical transitions from the $4f$ states are taken into account.

Figure 61 shows the energy band structure of TmS for all three approximations. The energy band structure of TmS with the $4f$ electrons in the core can be subdivided into three regions separated by energy gaps. The bands in the lowest region around -15 eV have mostly S s character with some amount of Tm sp character mixed in. The next six energy

bands are $S p$ bands separated from the s bands by an energy gap of about 6.5 eV. The width of the $S p$ band is about 3.7 eV. The spin splitting of the $S p$ bands is very small (about 0.06 eV at the X symmetry point (Figure 61)). The highest region can be characterized as Tm spin-split d bands. It is important that the top of the $S p$ bands is at -3.5 eV below the Fermi level since it means that all the interband transitions in the energy interval of 0.0 to 3.5 eV take part within the Tm d bands (see below). The sharp peaks in the DOS calculated in the LSDA at the Fermi energy and near 2 eV below are due to $4f_{7/2}$ and $4f_{5/2}$ states, respectively (Figure 61).

The LSDA+ U band structure calculations [384] have been started from a $4f^{12}$ configuration for the Tm^{3+} ion with twelve on-site $4f$ energies shifted downward by $U_{\text{eff}}/2$ and two levels shifted upward by this amount. The energies of occupied and unoccupied f levels are separated by approximately U_{eff} . We emphasize, however, that the $4f$ states are not completely localized, but may hybridize, and together with all other states their energy positions relax to self-consistently.

The LSDA+ U energy bands and total density of states (DOSs) of TmS for $U_{\text{eff}} = 6$ eV are shown in Figure 61. The Coulomb repulsion U_{eff} strongly influences the electronic structure of TmS. For Tm^{3+} ions twelve $4f$ bands are fully occupied and hybridize with $S p$ states. The 14th f hole level is completely unoccupied and well above the Fermi level. A hole 13th f level is pinned at the Fermi level. Although it was used a starting configuration with zero occupation of 14th f and 13th f levels, in the process of self-consistent relaxation initially empty 13th f level become partly occupied due to pinning at the Fermi level with occupation number equal to 0.12 (valence 2.88+) in good agreement with the experimental estimations (2.91+) by off-resonance UPS [373]. A fundamental aspect of this observation is the pinning of the 13th f state at E_F to be a robust property of the TmS compound: it happens irrespective of the precise value of U_{eff} .

Photoemission experiments, both X-ray (XPS) and ultraviolet (UPS), have been of central importance for understanding mixed-valence materials (see the review of the early work by Campagna et al. [346]). In rare-earth photoemission, when the photon ejects an electron from the $4f^n$ shell it leaves behind a $4f^{n-1}$ configuration, hence the kinetic energy distribution curve of the emitted electron measures the spectra of the final-state hole. The final-state $4f^{n-1}$ has a characteristic multiplet splitting which serves as a fingerprint, and these are accurately resolved and calculable in rare-earth photoemission. By identification of the final-state hole the initial state can be inferred.

The partial $4f$ DOS of the occupied part of the TmS calculated in LSDA and LSDA+ U approximations is compared with UPS measurements [371] in Figure 62. The calculated $4f$ DOS has been broadened to account for lifetime effects and for the experimental resolution. The Tm $4p$ states essentially do not contribute to XPS and UPS because of the low ionization cross-section compared with that of the Tm $4f$ states [385]. Hence, the measurements only indicate the f excitation energies of trivalent and divalent Tm, relative to the Fermi level. The LSDA calculations places the $4f$ energy band right at the Fermi level (Figure 61) producing in the $4f$ DOS a double peak between 0 and -3 eV (Figure 62).

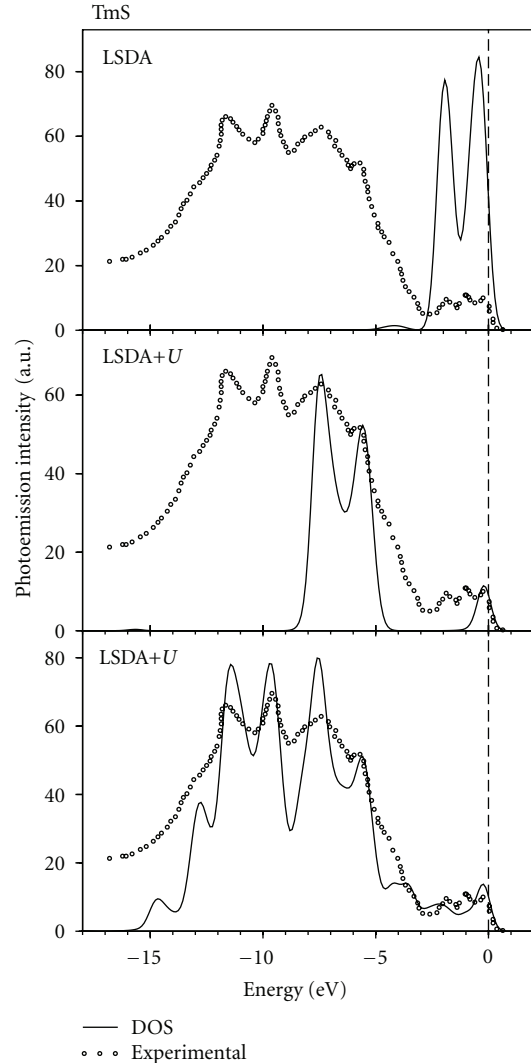


FIGURE 62: Comparison of the calculated $4f$ DOS in LSDA and LSDA+ U approximations [384] with the experimental UPS spectra from [373]. The bottom panel shows the LSDA+ U $4f$ DOS taking into account the multiplet structure of the $4f^{11}$ final state (see explanations in the text).

In the LSDA+ U calculations twelve fully occupied $4f$ bands are situated between -4 and -8 eV in the DOS and a partly filled 13th $4f$ band produces a small peak at around -0.5 eV binding energy (Figure 62).

The LSDA+ U DOS cannot, of course, fully account for the multiplet splitting. Therefore, we present at the bottom panel in Figure 62 the LSDA+ U $4f$ DOS taking into account the multiplet structure of the $4f^{11}$ final state. The multiplet structure consists of 15 terms, nine of which are the most intensive ($^4I_{15/2}$, $^4I_{13/2}$, 4F , 2H , 4G , 2K , 4D , 2L , and 2F) [346]. The relative intensities for the multiplet peaks were obtained on the basis of Cox calculations [387] who used the fractional parentage method [388]. In this method Hund's rule ground state is assumed for $n4f$ electrons and then the coefficients of fractional parentage (Racah's) for the $n-1$ configurations are calculated. The intensities for

the various configurations (multiplets) are just the square of the coefficients of fractional parentage. In the bottom panel in Figure 62 UPS spectrum is modeled by a weighted sum of nine LSDA+ U $4f$ DOS curves. The centroid of the DOS has been aligned with each term of the atomic final-state multiplet and summed up the spectra scaling them according to the relative intensities of the multiplets. The agreement between theory and the UPS measurements is very good. It is clear that the structures between -4.5 and -16 eV binding energy should be assigned to the final-state multiplet structure derived from twelve fully occupied $4f$ bands (Tm^{3+}) and the structures between 0.0 and -4.5 eV are associated with the final-state multiplet structure of the partly occupied 13th f level.

From the good agreement between theory and UPS measurements we may conclude that the LSDA+ U calculations give an accurate position for the occupied $4f$ bands. Figure 63 shows the experimental BIS spectrum of TmS [386] compared with the calculated energy distribution for the unoccupied partial Tm $4f$ ($N_f(E)$) and $5d$ ($N_d(E)$) density of states in the LSDA and LSDA+ U approximations. The experimental spectrum consists of two maxima at about 0.9 eV and 4 eV above the Fermi level. The first narrow peak was identified as having f character, whereas the second broad peak was associated with $5d-6s$ states [386]. The LSDA places the empty $4f$ states right at the Fermi level which contradicts the experimental data (Figure 63). The LSDA+ U calculations place the maximum of the 14th f hole level well above the Fermi level around 0.7 eV. The 13th f hole level is partly occupied with its maximum DOS situated 0.025 eV above the Fermi level (Figure 61). Due to a rather large experimental resolution of the BIS spectra (~ 1 eV) [386] one experimentally observes essentially only a single BIS $4f$ peak instead of two, although, a shoulder can be discerned split off from the main peak [386]. The LSDA+ U calculations give the correct position of both the $4f$ and $5d$ states (Figure 63) within the experimental resolution.

7.1.2. Optical Spectra. More precise information on the band positions may be obtained from optical measurements. Although such measurements have much better resolution (the experimental resolution in optics is always in the meV range) in comparison with XPS and BIS, they produce complex functions containing information of both the initial and final states simultaneously (joint density of states) and are strongly influenced by the optical transition matrix elements

Figure 64 shows the calculated real and imaginary parts of the dielectric function, $\epsilon_{1xx}(\omega)$ and $\epsilon_{2xx}(\omega)$, the optical reflectivity and imaginary part of the energy-loss function $\text{Im}[-1/\epsilon(\omega)]$ compared with experimental data [389]. On the basis of the results of the LSDA+ U band structure calculation, the observed optical reflectivity spectrum (Figure 64) can be sorted into the respective interband transition groups: (1) metallic high reflectivity below ~ 1 eV, (2) a steep edge between ~ 1 and ~ 2.5 eV, and (3) above the minimum at ~ 2.7 eV some less pronounced structures with a broad maximum of R between 5 and 7 eV mostly caused by $3p \rightarrow 5d$ interband transitions.

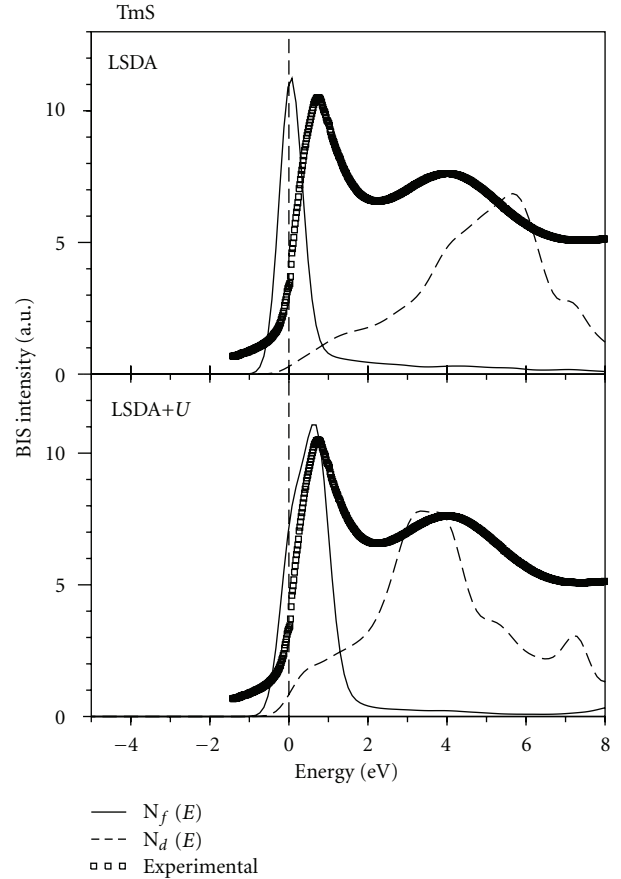


FIGURE 63: Comparison of the calculated partial $4f$ ($N_f(E)$) and $5d$ ($N_d(E)$) DOS in the LSDA and LSDA+ U approximations [384] with the experimental BIS spectrum of TmS from [386].

The predominant structure of the TmS as well as TmSe reflectivity spectra is the edge at 2 eV. This sudden drop is characteristic for metallic rare-earth chalcogenides and is due to a plasma oscillation interfering with interband excitations [389]. This plasma resonance causes the golden color of TmS crystals as it does for all metallic rare-earth sulfides. The energy of the conduction electron plasma resonance in the presence of the interband excitations is given by $\epsilon_{1xx}(\omega) = 0$. In the particular case of TmS this condition is fulfilled at $\hbar\omega = 2.15$ eV, and the maximum peak of the energy-loss spectrum in Figure 64 is shifted only very little from this energy (by -0.05 eV) as a result of damping. The correct energy position of the plasma edge in TmS can be obtained only by taking into account $5d \rightarrow 4f$ interband transitions. The calculations treating $4f$ electrons as core electrons place the zero crossing energy of $\epsilon_{1xx}(\omega)$ at higher energies in comparison with the LSDA+ U calculations and as a result give a wrong energy position for the plasma resonance (Figure 64).

To search for possible optical $5d \rightarrow 4f$ interband transitions, the reflectivity of a TmS single crystal has been measured between 2 meV and 12 eV at room temperature and at 6 K [386]. One should mention that the observation of an optical $5d \rightarrow 4f$ transitions is quite rare, especially when the metal has a large carrier concentration as in the case

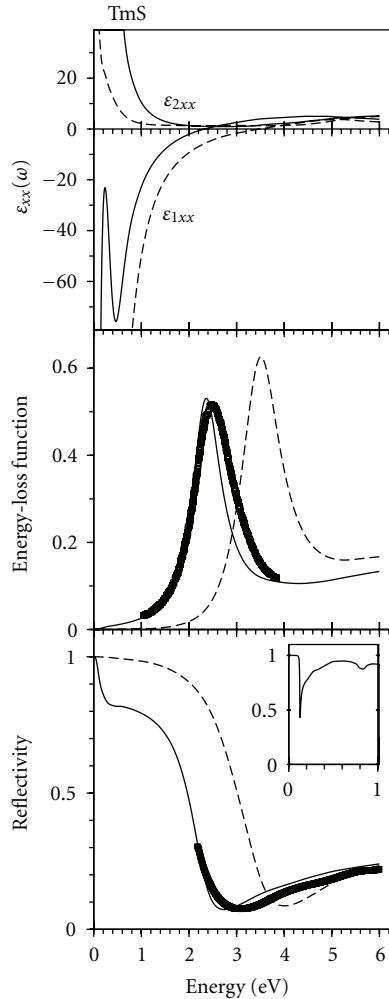


FIGURE 64: Calculated real and imaginary parts of the diagonal dielectric function, $\epsilon_{1xx}, \epsilon_{2xx}$, energy-loss function, and the optical reflectivity R of TmS [384] treating $4f$ states in core (dashed line) and by the LSDA+ U approximation (solid line) compared with experimental data (solid circles) [389].

of TmS with about one carrier per formula unit. The large amount of carriers effectively screen the optical transition as most of the light intensity gets reflected by the plasmons. The chances to observe the optical $5d \rightarrow 4f$ transitions in a metal become only realistic when the energy of the optical transitions is very small since the intensity of the transition scales with ω^{-2} [386]. Such a situation occurs in TmS where the partly occupied 13th f hole level is very close to the Fermi level with its maximum DOS situated 25 meV above the Fermi level (Figure 61). Reflectivity measurements of TmS single crystals in the mid-infrared region reveal two lines near 53 and 90 meV [386]. The authors interpreted these features as optical transitions from the partly filled $5d$ conduction states near the Fermi level into the empty crystal-field split 13th band f states (acoustic and optical phonon modes are situated at 13 and 37 meV resp. according to Raman scattering measurements [386]).

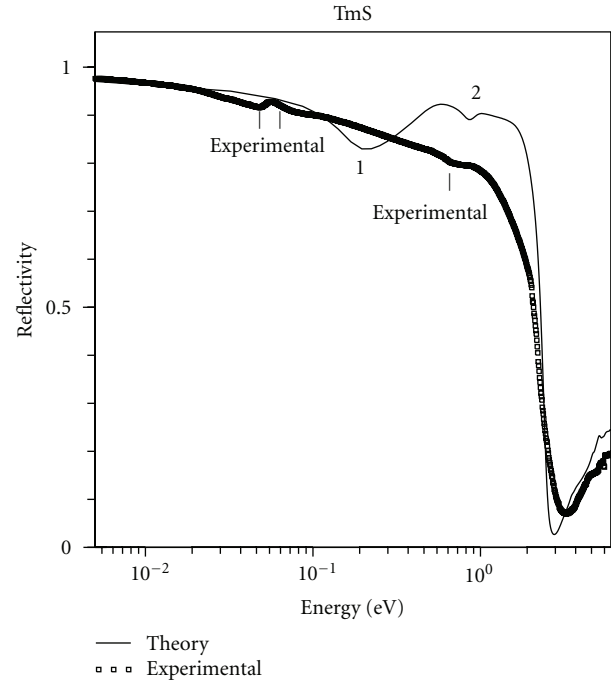


FIGURE 65: Calculated optical reflectivity spectrum of TmS [384] compared with experimental data [386].

Another less pronounced feature was observed in the reflectivity spectrum measured at 6 K around 0.9 eV. The insert of Figure 64 shows the unbroadened theoretically calculated optical reflectivity in the 0 to 1 eV energy interval with two well-pronounced minima at 0.11 and 0.9 eV. These features reflect the interband transitions from occupied $5d$ states to empty 13th f and 14th f hole levels situated at 0.025 and 0.7 eV, respectively (Figure 61). In real optical experiments such transitions are obscured by broadening from intraband Drude-like transitions, life-time effects, and to a lesser extent the experimental distortion. Figure 65 shows with a logarithmic scale the experimental optical reflectivity spectrum of TmS [386] in comparison with the theoretically calculated one.

The position of the second less-pronounced minimum that arises from the $5d$ to 14th f interband transitions is in good agreement with the experimental measurements (Figure 65). The crystal-field effects have not been included in the band structure calculation [384], so only a single feature in the optical reflectivity at 110 meV was obtained instead of experimentally measured two ones at 53 and 90 meV due to crystal field splitting [386]. The small shift of the theoretically calculated feature towards larger photon energies in comparison with the optical measurements may be due to a valence band electron-hole interaction in the optical spectrum which is absent in photoemission or BIS experiments as well as in our one-particle LSDA+ U calculations. We should mention that the incorporation of the electron-hole excitations in the band structure calculations is a nontrivial task and requires an effective two-body approach. It is beyond our capacity now.

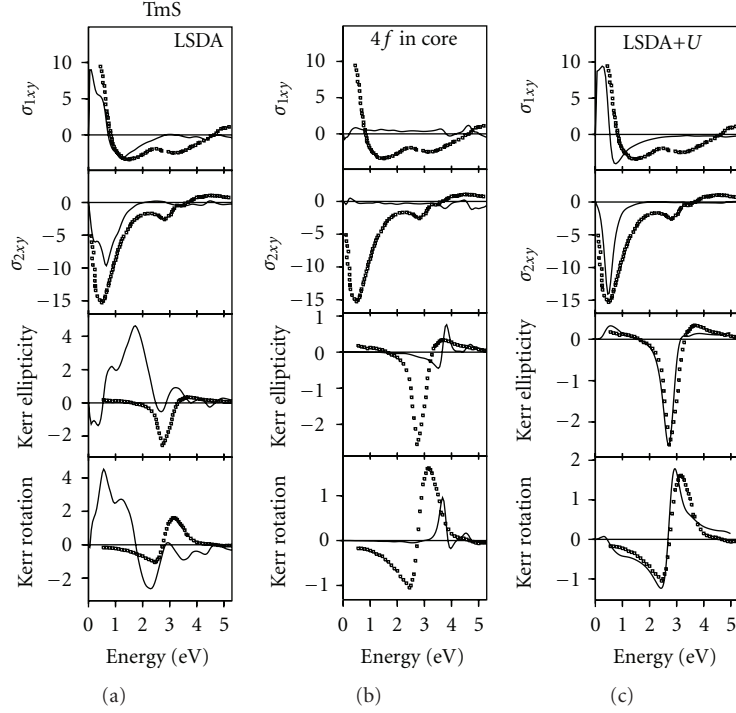


FIGURE 66: Calculated off-diagonal parts of the dielectric function ϵ_{xy} (in 10^{29} s^{-2}), Kerr rotation and Kerr ellipticity spectra (in degree) for TmS treating the $4f$ states as a core electrons, LSDA and LSDA+ U approximations [384] compared with experimental data (circles) [390].

7.1.3. Magneto-Optical Spectra. After consideration of the band structure and optical properties, we turn to the magneto-optical spectra. In the polar geometry, where the z -axis is chosen to be perpendicular to the solid surface and parallel to the magnetization direction, the expression for the Kerr angle can be obtained easily for small angles and is given by [46]

$$\theta_K(\omega) + i\epsilon_K(\omega) = -\frac{\sigma_{xy}(\omega)}{D(\omega)}, \quad (22)$$

$$D(\omega) = \sigma_{xx}(\omega) \sqrt{1 + \frac{4\pi i}{\omega} \sigma_{xx}(\omega)}, \quad (23)$$

with θ_K , the Kerr rotation and ϵ_K the so-called Kerr ellipticity. $\sigma_{\alpha\beta}$ ($\alpha, \beta \equiv x, y, z$) is the optical conductivity tensor, which is related to the dielectric tensor $\epsilon_{\alpha\beta}$ through

$$\epsilon_{\alpha\beta}(\omega) = \delta_{\alpha\beta} + \frac{4\pi i}{\omega} \sigma_{\alpha\beta}(\omega). \quad (24)$$

In Figure 66 we show the experimental [390] $\theta_K(\omega)$ and $\epsilon_K(\omega)$ MO Kerr spectra of TmS, as well as the spectra calculated with LSDA, LSDA+ U , and the $4f$ electrons in the core. This picture clearly demonstrates that the better description is unambiguously given by the LSDA+ U approach. The most prominent discrepancy in the LSDA spectra is the extra peaks between 0 and 2 eV caused by interband transitions involving the hybridized $4f$ states, which in the LSDA approach exhibit a maximum resonance near E_F . In the LSDA+ U approach, the occupied $4f$ state energies are shifted downward due

to the on-site Coulomb interaction U_{eff} . As a result, the transitions involving the occupied $4f$ states do not take place at small photon energies, and the erroneous peak structures around 0 to 2 eV disappear from the Kerr spectra. The calculations in which the $4f$ electrons are treated as quasi-core are able to reproduce structure similar to the LSDA+ U calculations, but in the wrong positions. Besides, due to the lack of corresponding $5d \rightarrow 4f$ interband transitions, the off-diagonal part of the optical conductivity σ_{2xy} is nearly zero, so that a very small Kerr rotation is obtained.

Off-diagonal optical conductivity of TmS shows very large values at low energies with a marked extremum in $\sigma_{2xy}(\omega)$ near 0.5 eV and it is almost constant in the 2 to 4 eV energy interval (Figure 66). As a result the shape of the Kerr ellipticity and Kerr rotation spectra in this compound are completely determined by a shape of the function $[\omega D(\omega)]^{-1}$ in the (22).

The situation is clearly seen in Figure 67 where we show the theoretically calculated Kerr rotation and ellipticity of TmS using the LSDA+ U approximation and the frequency dependence of real and imaginary parts of the function $[\omega D(\omega)]^{-1}$ multiplied by a constant to normalize the spectra. Obviously the shape of the Kerr spectra in TmS results mostly from the resonance structure of the function $[\omega D(\omega)]^{-1}$. Actually the first-principles band structure calculations [384] confirm the idea already drawn by Feil and Haas in [391] on the basis of model calculations that the sharp Kerr effect in some magnetic metallic rare-earth compounds including TmS and TmSe is not due to the electronic interband transitions, but rather to the influence of a plasma resonance.

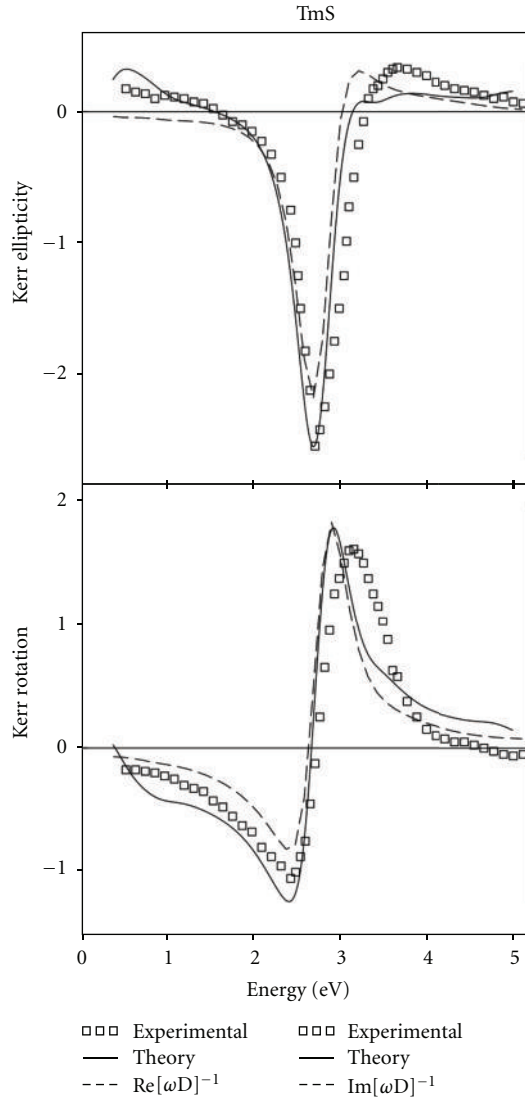


FIGURE 67: Calculated Kerr rotation and Kerr ellipticity spectra (in degree) for TmS in the LSDA+ U approximation, and real and the imaginary parts of the function $[\omega D(\omega)]^{-1}$ [384] compared with experimental data [390].

7.2. TmTe. Figure 68 shows the energy band structure and total density of states of TmTe calculated in LSDA and LSDA+ U approximations. Although TmTe is known as a magnetic semiconductor, LSDA calculations gave a metallic solution. The LSDA+ U calculations predict a correct ground state of TmTe, namely, a magnetic semiconductor with direct energy gap of 0.86 eV at the Γ symmetry point and an indirect energy gap of 0.58 eV between the top of Tm 4*f* valence band at the Γ point and the bottom of Tm 5*d* conduction band at the X symmetry point. Theory produces a somewhat larger energy gap in comparison with the optical measurements of 0.35 eV [365]. Thirteen completely occupied Tm 4*f* energy bands located between 0.0 and -2.2 eV are hybridized with Te 5*p* states. The empty 14th *f* energy level is situated around ~ 5.8 eV above the Fermi level hybridized with Tm 5*d* states

(Figure 68). In other words theory predicts the Tm atom in TmTe to be in divalent state.

The most striking evidence for the absence of any mixed-valence state in TmTe comes from photoemission measurements. It was shown in [365] that the amount of detectable Tm^{3+} in UPS measurements depends strongly on the surface condition and that the ratio of $\text{Tm}^{3+}/\text{Tm}^{2+}$ increases after cleavage as a function of time from a value $\leq 6\%$. Also, the absorption spectrum of vacuum-cleaved TmTe, as derived from the reflectance, shows clear evidence for transitions from Tm^{2+} in the energy region 0 to 7 eV, but no conclusive indication of transitions from Tm^{3+} in the energy region 7 to 14 eV [365].

A recent more precise photoemission study of TmTe [373] gives the mean valence value equal to 2.15+ and 2.35+ from study the total yield and off-resonance photoemission spectra, respectively, although the mean valence of the same sample obtained from the result of magnetic susceptibility measurement is 2.017+. The valency of the Tm ion in TmTe from lattice constant considerations was found to be 2.0+ [364]. Thus, it would seem that the trivalent component observed in photoemission measurements mainly comes from the surface. Besides, the valence structure of such samples strongly depends on the stoichiometry. Figure 69 shows TmTe UPS spectrum [373] in comparison with the occupied part of the partial LSDA+ U 4*f* DOS calculated with a multiplet structure of 4*f*¹² final state taken into account in the same way as for TmS. The multiplet structure consisting of six terms (³H, ³F, ³P, ¹I, ¹G, ¹D, and ¹S) was taken from [346]. We conclude that the structures between 0.0 and -8 eV binding energy is associated with the 4*f*¹² final-state multiplet structure. The structures with higher binding energies should be assigned to the final-state 4*f*¹¹ multiplet structure of the Tm^{3+} ions mainly coming from the surface. To check this the energy band structure and 4*f* DOS of TmTe was calculated using a starting configuration with zero occupation of the 14th *f* and 13th *f* levels (Tm^{3+} configuration) and with taking into account a multiplet structure of the 4*f*¹¹ final state [384]. As can be seen from Figure 69 the 4*f*¹¹ final-state multiplet structure corresponds to structures seen in the -4 to -16 eV energy interval. Hence, the contribution to the peaks at around -5.5 and -7.5 eV binding energy in UPS measurements comes from both the Tm^{2+} and Tm^{3+} ions. Besides, there are also contributions to the main feature of the UPS spectrum at 0 to -3 eV binding energies coming from the partly filled 13th *f* level of the Tm^{3+} ions.

The pressure effects on transport properties of TmTe were investigated by Matsumura et al. [392]. It was found that, at room temperature, the resistivity of TmTe showed an exponential decrease up to 2 GPa, indicating a linear closing of the energy gap (with $d\Delta/dP = -207$ meV/GPa), followed by an almost pressure-independent metallic regime. In order to investigate the influence of pressure on the electronic structure of TmTe, the self-consistent energy band structure calculations for several reduced lattice constants were performed. It was found a gradual decrease of the energy gap and closing of the indirect gap at $a = 6.05$ Å in a good agreement with experiment. The semiconductor-metal phase transition

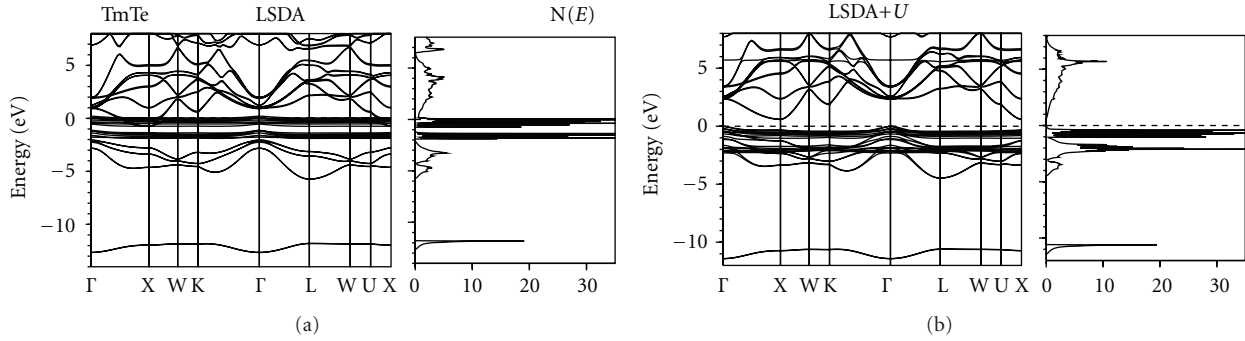


FIGURE 68: Self-consistent fully relativistic, spin-polarized energy band structure and total DOS (in states/(unit cell eV)) calculated for TmTe [384].

for pure TmTe takes place at around ~ 2.5 GPa [392]. The *compositionally induced* semiconductor—metal transition in the TmSe $_{1-x}$ Te $_x$ system takes place for $x = 0.4$ with the lattice constant equal to ~ 6.02 Å [5] (see what follows).

There is no experimental measurements of the MO spectra for TmTe. The measurements have been performed only for the TmSe $_{0.32}$ Te $_{0.68}$ system [46]. The theoretical analysis of the MO spectra of TmSe $_{0.32}$ Te $_{0.68}$ will be considered below.

7.3. TmSe. The simplest argument that TmS is trivalent, TmSe intermediate valent, and TmTe divalent under normal conditions comes from comparing the lattice constants of rare-earth sulfides, selenides, and tellurides as done by Bucher et al. [364]. The lanthanide contraction is the cause for the general trend in the curves, and the standard divalent Sm, Eu, and Yb ions with their larger ionic radius are the obvious deviations. TmTe lies on the divalent curve, TmS on the trivalent one, and TmSe is intermediate, and by linear interpolation between a hypothetical divalent and trivalent TmSe one obtains a valence of Tm $^{2.75+}$. Further evidence that TmSe is intermediate-valence comes from X-ray and ultraviolet photoemission spectroscopy measurements [346, 373]. The photoemission study of TmSe [373] gives the mean valence value equal to 2.79 and 2.68 from study of the total yield spectra and off-resonance photoemission, respectively, although the mean valence of the same sample obtained from magnetic susceptibility measurement is 2.53. It should be mentioned that the total yield spectra reflect more bulk information than photoemission spectra and the values obtained from transport properties or magnetic susceptibility are mostly bulk and not surface sensitive [373].

The ground state of an intermediate valence compound is a quantum mechanical mixture of both the $4f^n$ and the $4f^{n-1}5d$ configuration on each rare-earth ion. Such compounds need theoretical consideration beyond the mean field one-particle LSDA+ U approximation due to possible configuration interaction between different $4f$ valence states. Although such interaction should be less in Tm compounds in comparison, for example, with mixed-valent Ce compounds due to contraction of the $4f$ wave function, it can lead to a spontaneous interconfiguration fluctuations (ICFs), introduced first by Hirst [393]. As briefly discussed by Varma

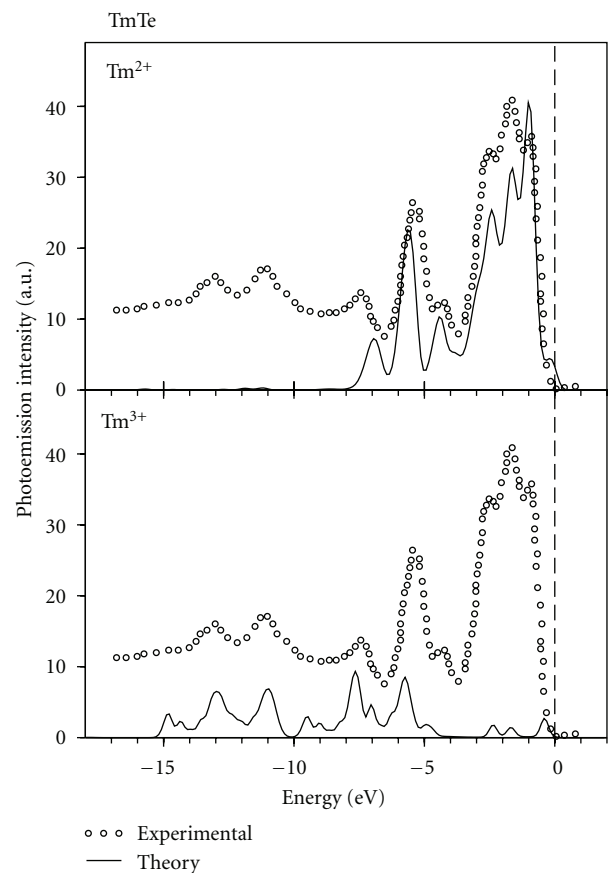


FIGURE 69: Comparison of the calculated Tm $^{2+}$ and Tm $^{3+}4f$ DOS of TmTe in LSDA+ U approximation [384], taking into account the multiplet structure of $4f^{12}$ and $4f^{11}$ final states with the experimental UPS spectra from [373].

[3], at $T = 0$, fluctuations could be either static or dynamic. In the static case the system is spatially “inhomogeneous” in the sense that at inequivalent sites different valence states are present. Examples among the rare-earth compounds are Eu $_3$ S $_4$ or Eu $_3$ O $_4$ [346]. Such static charge “fluctuations” have been known for a long time in the $3d$ -series; Fe $_3$ O $_4$, magnetite, being a typical example (see [10] and references

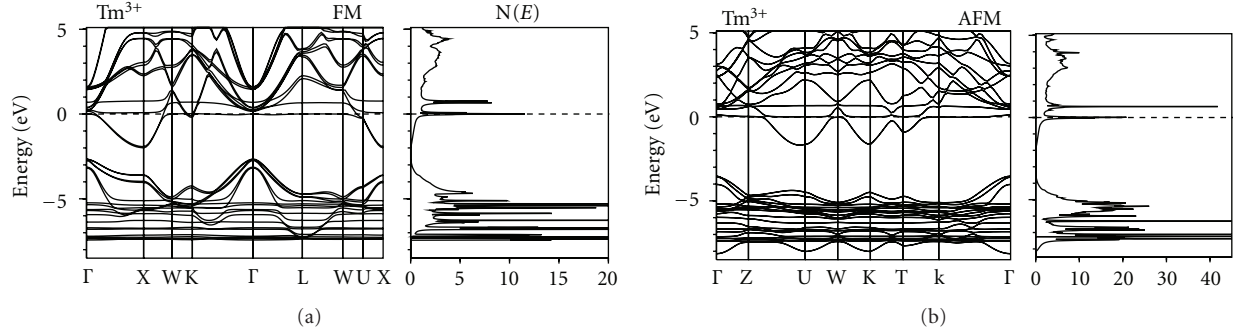


FIGURE 70: Self-consistent fully relativistic, spin-polarized energy band structure and total DOS (in states/(unit cell eV)) calculated for TmSe in ferromagnetic (FM) and antiferromagnetic (AFM) ordering [384].

therein). In the dynamic case the system shows fast local fluctuations which give an intrinsic width to the f levels. At any given site $4f$ charge fluctuations between the two configurations occur on a time scale τ_{ICF} , the so-called *inconfiguration fluctuation time*. The system on time average is “homogeneous,” that is, all sites are equivalent. TmSe is known to be a homogeneous mixed-valence compound [346]. Experiments such as lattice constant and isomer shift measurements which probe the sample on a time scale much longer than τ_{ICF} will see only one intermediate configuration, but experiments such as XPS or UPS measurements which take place in a time much shorter than τ_{ICF} (up to 10^6 - 10^7 times shorter [370]) will see the instantaneous picture of a mixture of the ions in the two valence states.

7.3.1. Band Structure. The LSDA+ U energy bands and total density of states of TmSe for $U_{\text{eff}} = 6$ eV are shown in Figure 70 both for the ferromagnetic and antiferromagnetic ordering for the Tm^{3+} ions. The electronic structure of TmSe for the Tm^{3+} ions is very similar to the TmS one with twelve $4f$ bands fully occupied and hybridized with chalcogenide p states. The 14th f hole level is completely unoccupied and well above the Fermi level. A hole 13th f level is partly occupied and pinned at the Fermi level. The occupation number of the 13th f level is equal to 0.27 (valence 2.73+) in good agreement with estimations from the lattice constants (2.75+) as done by Bucher et al. [364] and from UPS measurements (2.79+ and 2.68+ from total yield and photoemission spectra, resp.) [373].

Figure 71 shows the expanded view of the total DOS of TmSe and TmS both in the ferromagnetic (FM) and antiferromagnetic (AFM) states [384]. An important feature of the FM electronic structure is a high DOS at the Fermi energy E_F in both TmS and TmSe. A large DOS at E_F signals an instability with respect to metamagnetic phase transitions. Indeed, total energy calculations show that the ground state for TmSe as well as for TmS is an antiferromagnetic ordering in agreement with experiment [366, 377]. Through the FM-AFM phase transition a pseudogap at the Fermi level is opened in both TmS and TmSe (Figure 71). The opening of such a pseudo gap may explain the increase of the electrical

resistivity below Néel temperature [377, 379, 380], as well as an enormous negative magnetoresistivity associated with the metamagnetic transition to the high-field aligned state and decrease of the Hall coefficient in an external magnetic field [381].

The pinning of a partly occupied 13th f level is different in TmS and TmSe. In contrast to TmS, the Fermi level crosses the 13th f hole level in the vicinity of its DOS maximum in TmSe, both in the FM and the AFM states. The maximum DOS of the 13th f hole level is situated above the Fermi level, as close as 4 meV (~ 45 K) in the AFM ground state of TmSe. The energy position of the 13th f level is in a good agreement with low-temperature far infrared optical measurements by Marabelli and Wachter [394]. According to their measurements the first interband transition appears at about 3 meV. It should be mentioned here that when we speak about partial occupation of the 13th f hole level in TmS we mean that such an occupation is due to the hybridization effect between $5d$ and $4f$ energy states. The peak position of the 13th f hole level DOS in TmS is relatively far away from the Fermi level. A different situation occurs in TmSe where the Fermi level crosses the shoulder of the 13th f hole level DOS (see Figure 71); hence, the 13th f level is really pinned at the Fermi level. It is a typical situation for mixed-valent crystals.

The Tm monochalcogenides offer the unique opportunity to follow the evolution of intermediate valence as a function of composition. The driving force is the change of lattice constant upon exchanging the anion. In order to separate the influence of the lattice constant from the influence of the ionic potential of the chalcogenide component on the electronic structure of TmX ($X = \text{S}$ and Se), we present in Figure 71 also the DOS of TmSe evaluated with the lattice constant of TmS [384]. The partial occupation of the 13th hole f level in this case is similar to the situation for TmS, although the energy positions of the maxima is not the same as in actual TmS. The mean valency of TmSe with the lattice constant of TmS is equal to 2.90+, very close to valency in actual TmS (2.88+). It can be considered as qualitative theoretical support of the conclusion derived in [383] that the application of pressure enhances the Tm^{3+} state relative to Tm^{2+} state in the TmSe.

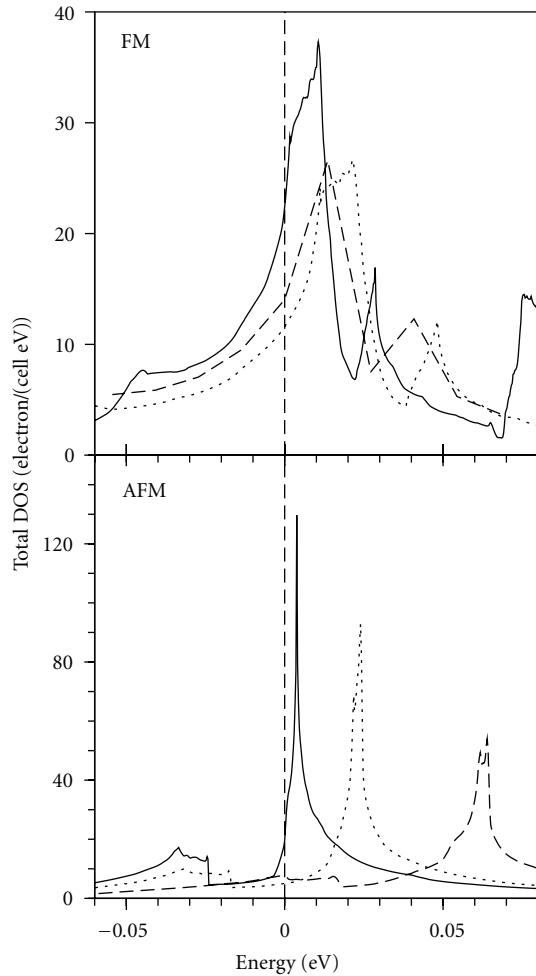


FIGURE 71: Expanded view of the DOS of TmSe (solid line), TmS (dotted line), and TmSe with the lattice constant of TmS (dashed line) calculated in the LSDA+ U approximation for ferromagnetic (FM) and antiferromagnetic (AFM) ordering [384].

In Figure 72 the partial $4f$ DOS of the occupied part of the TmSe band structure is compared with XPS measurements [346] for two single crystals with different lattice constants. An off-stoichiometric violet TmSe single crystal, with lattice constant $a = 5.640 \text{ \AA}$, contains almost entirely Tm^{3+} ions [346]. The theory calculations using a starting configuration with zero occupation of 14th and 13th f levels (Tm^{3+} configuration) well describe this experimental XPS spectrum.

The XPS spectrum of TmSe with $a = 5.689 \text{ \AA}$ has a sizable divalent signal between 0 and -3 eV binding energy. The middle panel of Figure 72 shows the theoretically calculated $4f$ DOS of the Tm^{2+} Se taking into account the multiplet structure of the $4f^{12}$ final state. The bottom panel shows the experimental XPS spectrum for $a = 5.689 \text{ \AA}$, in comparison with the sum of Tm^{3+} and Tm^{2+} $4f$ DOSs in the proportion of fifty-fifty. These results suggest that the valency of the sample with $a = 5.689 \text{ \AA}$, is close to 2.5 as comes from the analysis of the DOSs. Of course it is difficult to make quantitative conclusions about the possible Tm $4f$ configuration in

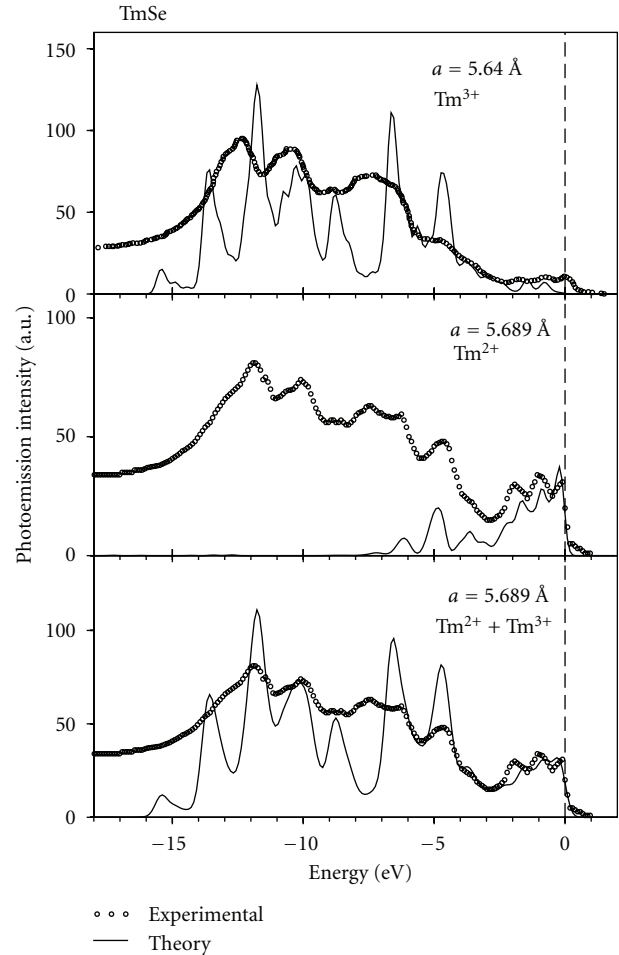


FIGURE 72: The calculated Tm^{3+} and $\text{Tm}^{2+} 4f$ DOS of TmSe in LSDA+ U approximations, taking into account the multiplet structure of the $4f^{12}$ and $4f^{11}$ final states [384]. Comparison is made with the experimental XPS spectra from [346] measured for two different lattice constants.

TmSe from comparison of theoretically calculated $4f$ DOS with XPS or UPS spectra. From such a comparison we can only derive an energy position of final-state multiplet structures from Tm^{3+} and Tm^{2+} ions. The XPS and UPS spectra are strongly affected by the transition matrix elements which have been omitted in the consideration for simplicity. Besides, the relative intensities of Tm^{3+} and Tm^{2+} ion final-state multiplet structures depend on the excitation photon energy. This was shown in [373] where the intensity ratio between the trivalent and divalent components in Tm monochalcogenides changes significantly depending on resonance or off-resonance conditions. Finally, UPS and XPS spectroscopies are strongly surface-sensitive methods. The escape depth of a photoelectron with kinetic energy of a kilovolt is about 15 \AA . For the softer radiation typical for the UPS measurements ($\leq 100 \text{ eV}$) the escape depth is only about 4 \AA [4]; hence, only the surface layers are probed. A recent advance in our understanding of mixed-valent photoemission comes from the recognition that surface spectra can be markedly different from that of the bulk. In

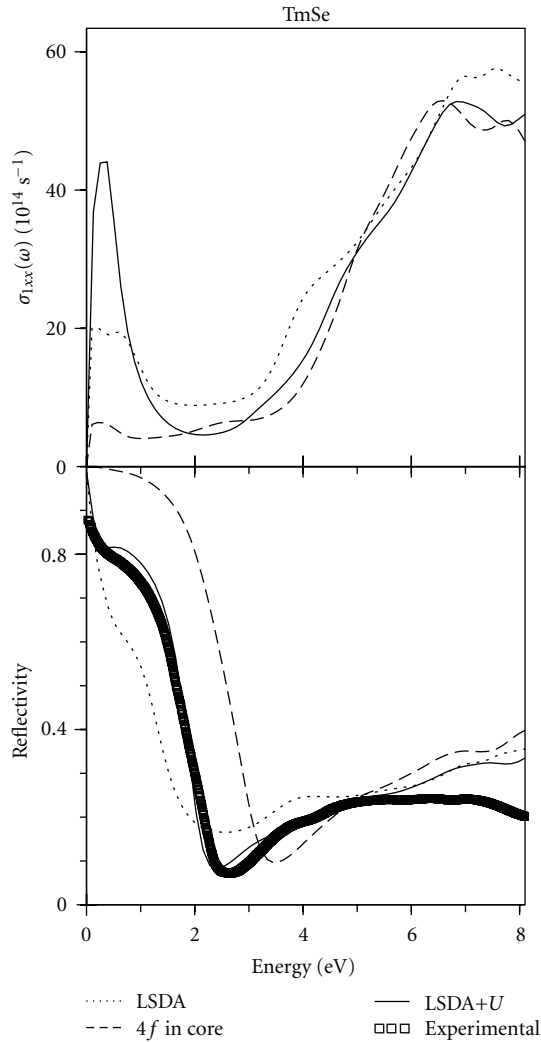


FIGURE 73: Calculated diagonal part of the optical conductivity σ_{1xx} and the optical reflectivity R of TmSe treating the $4f$ states as (1) fully localized ($4f$ in core) (dashed line), (2) itinerant (LSDA) (dotted line), and (3) partly localized (LSDA+ U) (solid line) [384] compared with the experimental data [389] (open squares).

particular the valence at the surface can be very different [4].

In the optical reflectivity measurements the depth of penetration is given by the inverse absorption coefficient and typically amounts from 10^2 to 10^3 Å. This means that the optical measurements are not so surface sensitive.

7.3.2. Optical Spectra. Figure 73 shows the calculated diagonal part of the optical conductivity σ_{1xx} and the optical reflectivity of TmSe treating the $4f$ states as (1) fully localized ($4f$ in core), (2) itinerant (LSDA), and (3) partly localized (LSDA+ U) in comparison with experimental data [389]. The calculations treating $4f$ electrons as core electrons place the zero crossing energy of $\epsilon_{1xx}(\omega)$ at higher energies in comparison with the LSDA+ U calculations and as a result give a wrong energy position for the plasma resonance

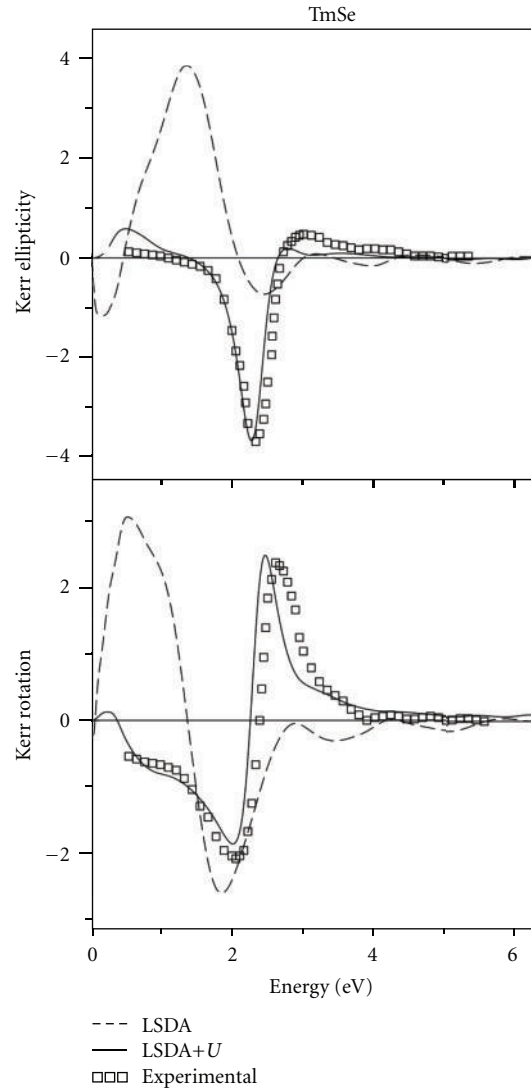


FIGURE 74: Calculated Kerr rotation and Kerr ellipticity spectra (in degrees) for TmSe in the LSDA (dashed line) and LSDA+ U (full line) approximations [384] compared with experimental data (open squares) [263].

which determines a deep minimum in the optical reflectivity (Figure 73). Due to the wrong position of $4f$ energy bands in the LSDA calculations, this approximation is not able to produce the correct optical reflectivity in the infrared spectral region. Figure 73 clearly demonstrates that the better description of the optical reflectivity spectrum is given by the LSDA+ U approach. The $5d \rightarrow 4f$ interband transitions play an essential role in the fast decrease of the optical reflectivity in 0 to 0.5 eV energy interval.

7.3.3. Magneto-Optical Spectra. In Figure 74 we show the experimental [263] $\theta_K(\omega)$ and $\epsilon_K(\omega)$ MO Kerr spectra of TmSe, as well as the spectra calculated with LSDA and LSDA+ U . The better description is unambiguously given by the LSDA+ U approach. The most prominent discrepancy in the LSDA Kerr spectra is the extra peak at 0.5 eV which

is caused by extra structure present in the dielectric tensor. Responsible are interband transitions involving the hybridized $4f$ states, which in the LSDA approach exhibit a maximum resonance near E_F . In the LSDA+ U approach, the occupied $4f$ state energies are shifted downward due to the on-site Coulomb interaction U_{eff} . As a result, the transitions involving the occupied $4f$ states do not take place at small photon energies, and the erroneous peak structure around 0.5 eV disappears from Kerr spectra.

Some experimental results [5, 394–396] indicate that TmSe could be a narrow-gap semiconductor below the Neel temperature. Evidence for a hybridization gap comes from the activated behavior of the electrical resistivity [4] and from a large negative value of the Hall coefficient at 3.5 K [4], suggesting fewer than 10^{18} carriers per cm^3 . Another evidence that stoichiometric TmSe might be a narrow-gap semiconductor comes from point contact measurements [395]. The dynamic resistance $dV/dI(V)$ which for intermediate-valence materials is proportional to $1/N(E)$ has a peak at E_F in the AFM state. Such a peak disappears in an external magnetic field above 10 kOe where TmSe exhibits a ferromagnetic order. A maximum in $dV/dI(V)$ corresponds to a minimum in $N(E)$ —a gap or at least a pseudogap. The estimations from the activation energy in electrical resistivity measurements and from point-contact spectra show a possible gap of about 1 to 2 meV [5].

On the other hand, some experiments indicate that there may not be a gap but rather a pseudogap, and the hybridization does not occur over whole Brillouin zone. The electrical resistivity is raised only about one order of magnitude through the FM \rightarrow AFM phase transition [5]. Direct optical measurements by Battlog et al. [397] show a metallic reflectivity in Tm_{1-x}Se with a reflectivity edge which shifts about 0.5 eV as x varies from thulium deficiency to excess. Such studies as a function of stoichiometry give convincing evidence that the intrinsic TmSe behavior is metallic. More recent optical measurements by Marabelli and Wachter [394] show that during the measurements they always found a free carrier behavior for the lowest energies, then a gap or a pseudogap followed by a first interband transition at about 3 meV.

In our LSDA+ U band structure calculations of TmSe we used as a starting configuration with zero occupation of 14th and 13th f levels. In the process of self-consistent relaxation, the 14th f hole level is situated well above the Fermi level, but the initially empty hole 13th f level becomes partly occupied due to pinning at the Fermi level with occupation number equal to 0.27 (valence 2.73+) producing a metallic AFM-ordered ground state with a pseudo gap at the Fermi level. Such an energy band structure well describes the energy distribution curve of the UPS spectrum, as well as the optical and MO spectra of TmSe (see Figures 72, 73, and 74, resp.). We should mention that the more sophisticated LDA++ method [398] which takes into account the energy dependence of the electron self-energy also failed to obtain an insulating AFM ground state in TmSe. The possible appearance of such an energy gap in TmSe might be caused by both hybridization and exciton effects due to the Coulomb attraction of the $5d$ conduction electron

and $4f$ hole [398]. This effect is not described in the LSDA+ U and LDA++ methods. This mechanism requires further theoretical investigations. Additional experimental low-temperature optical ir measurements on good quality single crystals of TmSe are highly desired.

7.3.4. Summary. In contrast to LSDA, where the stable solution for TmTe is a metal, the LSDA+ U method gave an insulator with an indirect energy gap of 0.58 eV. LSDA+ U theory predicts that the thulium ion in TmTe is in an integer divalent state. It also shows a gradual decrease of the energy gap with reduction of the lattice constant. The gap is closed at $a = 6.05 \text{ \AA}$ in a good agreement with experimental measurements of TmTe transport properties under pressure and the compositionally induced semiconductor-metal transition in the $\text{TmSe}_{1-x}\text{Te}_x$ system.

For the Tm^{3+} ions of TmS and TmSe twelve $4f$ bands are fully occupied and hybridize with chalcogenide p states. The 14th f hole level is completely unoccupied and well above the Fermi level. The initially empty hole 13th f level in the process of self-consistent relaxation becomes partly occupied with $4f$ DOS maximum situated in close vicinity of the Fermi level in TmS and TmSe. A fundamental aspect of this observation is the partial occupation of the 13th f state to be a robust property of TmS and TmSe compounds: it happens irrespective of the precise value of U_{eff} . The positions of the 13th and 14th f hole levels in TmS and TmSe are in good agreement with BIS and optical measurements. The degree of occupation and position of the partly occupied 13th f level with respect to the Fermi level is different in TmS and TmSe. In TmS the hole level is almost empty and situated significantly far from the Fermi level. Such a situation is appropriate for achieving the Kondo lattice scenario. In TmSe the upper hole 13th f level is pinned at the Fermi level; therefore, TmSe is expected to be an intermediate-valent compound in agreement with experimental data. The occupation number of the 13th f hole level is equal to 0.12 and 0.27 (valency 2.88+ and 2.73+) in TmS and TmSe, respectively, in a good agreement with the experimental estimates from lattice constant and XPS and UPS measurements.

The LSDA+ U theoretical calculations describe well the measured XPS and UPS Tm monochalcogenides spectra only after taking into account the multiplet structure of final $4f^{11}$ and $4f^{12}$ states for Tm^{3+} and Tm^{2+} ions, respectively. It was shown that the structures in the XPS and UPS spectra of TmS and TmSe between -4.5 and -16 eV binding energy should be assigned to the final-state multiplet structure derived from twelve fully occupied $4f$ bands (Tm^{3+}), and the structures between 0.0 and -4.5 eV are associated with the final-state multiplet structure of the partly occupied 13th $4f$ state.

The MO spectra of TmX ($X = \text{S, Se, Te}$) are very sensitive tools for drawing conclusions about the appropriate model description. On account of the calculated MO spectra, we conclude that TmS and TmSe MO spectra are best described using the LSDA+ U approach. The shape of the Kerr spectra in TmS and TmSe is mostly due to a resonance structure of the function $[\omega D(\omega)]^{-1}$ due to a steep plasma edge. The analysis indicates that the available experimental Kerr spectra

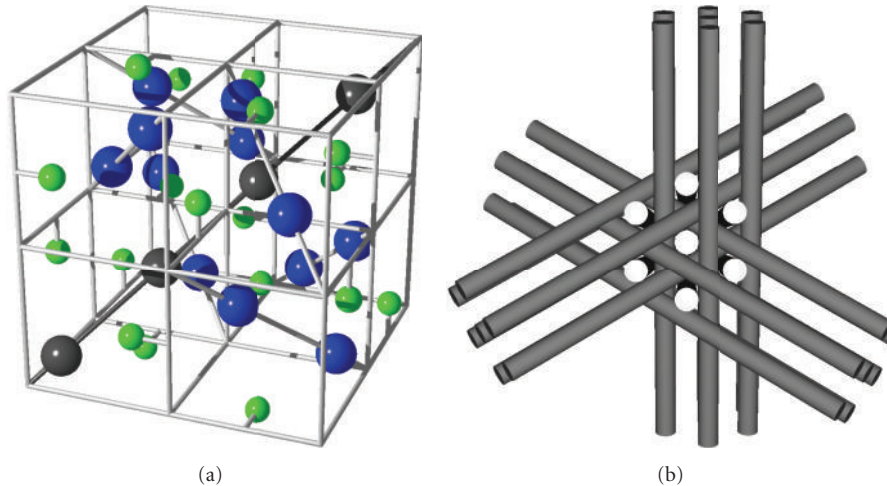


FIGURE 75: (a) Structure of Yb_4X_3 . Large balls: Yb ions, small balls: pnictide ions. In the trigonal charge-ordered phase the black large balls indicate Yb^{2+} sites and the gray large balls Yb^{3+} sites. (b) The four families of chains formed by the Yb atoms.

for $\text{TmSe}_{0.32}\text{Te}_{0.68}$ is a complex mixture of the divalent and trivalent Tm ion spectra.

8. Yb_4As_3 and Related Compounds

The rare-earth pnictides Yb_4X_3 ($X = \text{P}, \text{As}, \text{Sb}, \text{Bi}$) exhibit unusual physical properties [399–406]. The high-temperature phases of these compounds have the cubic anti- Th_3P_4 structure with space group $I4\bar{3}d$. The Yb ions occupy the P sites with Wyckoff positions $12a, \bar{4}, \dots, x = 0.069$, and the X ions occupy the Th sites with special Wyckoff positions $16c, \dots, 3, \dots$, fixed by symmetry ([407], see Figure 75(a)). All Yb-atoms are aligned on four families of chains oriented along the four diagonals of the cubic unit cell ([408], Figure 75(b)). All four ytterbium pnictides have anomalously large lattice constants ($a = 8.56, 8.788, 9.322, \text{ and } 9.573 \text{ \AA}$ for $X = \text{P}, \text{As}, \text{Sb}, \text{ and Bi}$, resp.) [399, 400]. Because the pnictide ion is trivalent, three of the four Yb ions have a filled $4f$ shell (valency 2+), while one ion is in a $4f^{13}$ (valency 3+) configuration. When all Yb sites are equivalent, the hole in the $4f$ shell is moving between different Yb ions and the system is a mixed-valent metal. Its average Yb-valence $Z = 2.25$ is rather close to the observed one ($Z_{\text{exp}} = 2.20$), obtained from the Mössbauer experiments [401].

The most interesting material is Yb_4As_3 . At about $T_s = 300 \text{ K}$ it undergoes a weak first-order phase transition with a trigonal distortion. This transformation was clearly established by susceptibility measurements [399], the Mössbauer spectra [401], polarised neutron diffraction [409], and elastic constant measurements [410]. At the structural transformation, the crystal shrinks in a volume-conserving way along one of the four Yb-chain directions ($\langle 111 \rangle$, say). The resulting trigonal unit cell with the trigonal angle $\alpha = 90.8^\circ$ has the *short chain* along its main diagonal. The centered trigonal space group is now $R3c$ with two inequivalent Yb sites at Wyckoff positions $2a, 3, \dots$, and two further inequivalent Yb sites at Wyckoff positions $6b, 1$, as well as

two inequivalent As sites at Wyckoff positions $6b, 1$. The distortion is accompanied by charge ordering with Yb^{3+} ions occupying the short chains [406]. So the $4f$ electronic state of Yb_4As_3 changes from a valence-fluctuating state in the cubic phase to a charge-ordered state $\text{Yb}^{3+}\text{Yb}_3^{2+}\text{As}_3^{3-}$ in the trigonal phase, although the charge ordering is not complete [401, 409]. The Yb^{2+} ions have a closed $4f$ shell with no spin magnetic moment. The Yb^{3+} ions have the $4f^{13}$ configuration with spin magnetic moment equal to one. Inelastic neutron scattering experiments on Yb_4As_3 revealed the existence of low-energy excitations that are characteristic of a one-dimensional antiferromagnetic coupling at low-temperatures [409].

Below 100 K, Yb_4As_3 exhibits heavy-fermion behavior: the resistivity shows a T^2 behavior ascribed to electron-electron interaction involving the heavy quasiparticle band, the Sommerfeld coefficient γ of the electronic specific heat C_{el} has a relatively high value of about $200 \text{ mJ mol}^{-1} \text{ K}^{-2}$, and the extrapolated magnetic susceptibility at 0 K has a rather large value $\chi(0) \approx 3 \times 10^{-2} \text{ emu/mol}$ ([399]). The Sommerfeld-Wilson ratio is found to be of the order of unity, indicating Fermi-liquid behavior. Below 2 K and for moderate applied magnetic fields ($>2 \text{ T}$), the “high field” magnetic susceptibility of Yb_4As_3 drops considerably as compared to the low field value [411]. There is also a rapid decrease observed in the specific heat at an applied field of about 1 T [402], both observations indicating the destruction of the heavy electron behavior.

The Hall coefficient R_H of Yb_4As_3 , extrapolated to $T = 0$, is equal to $7 \times 10^{18} \text{ cm}^{-3}$ (see [399]). It would correspond to a carrier concentration of about 0.001 per formula unit if only one type of carriers was present.

The pressure effects on transport properties of Yb_4As_3 were investigated by Okunuki et al. [412] and by Mōri et al. [413]. A clear increase of the carrier concentration is observed with increasing pressure which leads to a rapid decrease of the resistivity ρ . The maximum in the

temperature dependence of both ρ and R_H also decreases with pressure. However, the inverse Hall mobility, that is, the resistivity divided by the Hall coefficient, is found to increase with increasing temperature without any anomaly in the low-temperature phase even under high-pressure. This demonstrates that the mobility is not affected by pressure.

Summarizing all the experimental data, we can conclude that there is a strong dependence of the transport properties of Yb_4As_3 on doping, pressure, and sample preparation, but the specific heat and magnetic susceptibility do not change very much. This observation suggests that Yb_4As_3 is not an ordinary heavy-fermion system. The latter are usually interpreted within the context of a Kondo lattice model. The heavy quasiparticle bands are thought to originate from Kondo resonance states at the Fermi level which evolve into coherent band states below a characteristic temperature. However, this mechanism leads to a similar behavior of the specific heat coefficient γ and the carrier number as functions of doping. As explained above the opposite behavior is observed which is a strong argument against the Kondo scenario in this class of compounds.

The electronic structure of Yb_4As_3 has been investigated experimentally by means of photoemission [414], X-ray bremsstrahlung isochromat spectroscopy [415], optical properties [416–418]. The optical measurements [416, 417] show a strong temperature dependence of the optical reflectivity in the far infrared energy region below 10 meV. The plasma frequency ω_p derived from optical measurements [418] is very small. It varies from 0.08 eV for 10 K to 0.14 eV for 70 K indicating again an extremely small carrier number. Photoelectron spectroscopy in the X-ray and ultraviolet ranges (XPS and UPS) provide information on the energy position of Yb^{2+} and $\text{Yb}^{3+}4f$ states in charge-ordered Yb_4As_3 . Structures in UPS and XPS spectra with binding energy between 0 and 4 eV were identified [414] to be the spin-orbit doublet of the $4f^{13}$ final states and the structures between 6 and 13 eV to be the multiplet structures of the $4f^{12}$ final states. The low-temperature photoemission also does not show any evidence for Kondo resonance states close to the Fermi level, confirming the exclusion of the Kondo scenario for Yb_4As_3 .

Two approaches have been proposed to explain the properties of Yb_4As_3 . One is based on a one-electron picture and was applied by Ochiai et al. [399] in form of a four-band model and by Kasuya [419] in form of a two-band model. A characteristic feature of this approach is a hole band of As $4p$ states and a Yb $4f$ band with a high density of states near the Fermi level. The second approach treats the $4f$ electrons as being strongly correlated [420–422]. Charge ordering of the Yb^{3+} ions and the associated structural phase transition are a consequence of reducing the sum of the Coulomb repulsion and exchange to a minimum and are described by a band Jahn-Teller effect of correlated electrons. The observed heavy-fermion behavior is ascribed to spin-like excitations in the Yb^{3+} chains.

These two approaches have been combined in [423] by studying the electronic structure and the physical properties of Yb_4As_3 in the trigonal low-temperature R3c phase within an *ab initio* band structure approach which takes strong

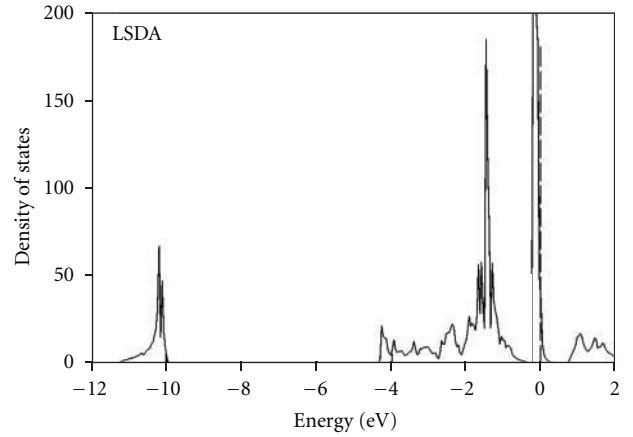


FIGURE 76: LSDA total DOS of Yb_4As_3 [423] (in states per cell and eV).

correlations into account. This was achieved by applying a local spin density approximation to the density-functional theory supplemented by a Hubbard U term (LSDA+ U). The electronic structure of the related compounds Yb_4X_3 ($X = \text{P}, \text{Sb}, \text{Bi}$, and $\text{P}_{0.5}\text{As}_{0.5}$) was also considered.

8.1. Yb_4As_3 . The LSDA total DOS of Yb_4As_3 is shown in Figure 76. The occupied part of the valence band can be subdivided into three regions separated by energy gaps. The bands in the lowest region have mostly As s character with some amount of Yb s character mixed in. The next group of bands is formed by As p states with little admixture of Yb p and d states. The large narrow peak close to the Fermi energy is formed by Yb $4f$ states. Unoccupied $5d$ bands of Yb are separated from the $4f$ states by an energy gap, a characteristic and important feature of the ytterbium pnictides. The position of the LSDA $4f$ states close to the Fermi energy is, on the other hand, in contradiction to the findings of XPS and UPS experiments [414].

The LSDA+ U band structure calculations in [423] were started from the $4f^{14}$ configuration for three Yb^{2+} ions, where all 14 on-site $4f$ energies are shifted downwards by $U_{\text{eff}}^{(2+)}/2$, and from the $4f^{13}$ configuration for one Yb^{3+} ion with 13 on-site $4f$ energies shifted downwards by $U_{\text{eff}}^{(3+)}/2$ and one level shifted upwards by this amount. The energies of occupied and unoccupied $\text{Yb}^{3+}f$ bands are separated by approximately $U_{\text{eff}}^{(3+)}$.

The LSDA+ U energy bands of AF Yb_4As_3 for $U_{\text{eff}}^{(2+)} = 5.3$ eV and $U_{\text{eff}}^{(3+)} = 8.8$ eV are shown in Figure 77. For three divalent Yb ions the $4f$ bands are fully occupied and hybridize with As p states in the energy range between -0.5 and -2.5 eV. They are split due to spin-orbit coupling by $\Delta\epsilon_{\text{so}} = 1.40$ eV. For the trivalent Yb ion, thirteen $4f$ electron bands per ion are well below the Fermi level and separated from a $4f$ hole state by the correlation energy $U_{\text{eff}}^{(3+)}$. One $4f$ hole band per Yb^{3+} ion, doublydegenerate due to AF ordering, appears closely below the top of the As p band. Since the As p band is separated from the Yb $5d$ band by an ordinary

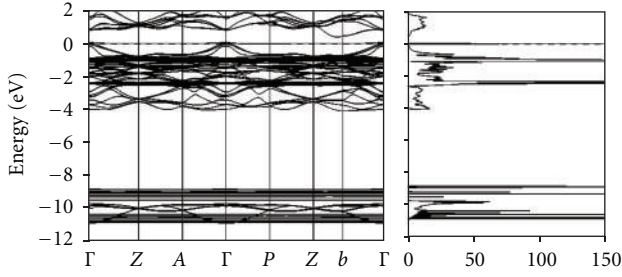


FIGURE 77: Self-consistent LSDA+ U energy band structure and total DOS (per unit cell and eV) of Yb_4As_3 [423] ($U_{\text{eff}}^{(2+)} = 5.3$ eV, $U_{\text{eff}}^{(3+)} = 8.8$ eV).

band gap, the Fermi level must be pinned at the bottom of the $4f$ hole band. This feature in combination with the small mass of the As p electrons close to the top of the p band appears to be a clue feature for the physics of the ytterbium pnictides. Due to the very small phase space for hybridization and the very small Yb $4f$ –As p orbital overlap, the DOS peak of the hole band is as narrow as 0.007 eV right above the Fermi level. It is now clear why the usual Kondo lattice scenario is inappropriate for these pnictide compounds. For a Kondo resonance to develop both the occupied and empty $4f$ -states must be sufficiently far away from the Fermi level. Quite opposite to this situation the (almost) empty level is pinned slightly above the Fermi energy. But due to the very small phase space for hybridization around the Γ point one still has an almost stable moment of the nearly integer occupation of the f shell.

Since the $4f$ binding energy of the Yb^{2+} ions is larger than 0.5 eV and hence larger than the Yb $4f$ –As p orbital hybridization energy both in experiment and in the calculated band structure, the $4f$ shell of the Yb^{2+} ions has been treated as a core shell in the following detailed numerical analysis. It has been checked that this simplification does not affect the issue. Therefore, we are left with a charge balance between Yb $4f$ states of the Yb^{3+} ions and pnictide p states only. Any charge transfer between these states causes a change in the Hartree potential which is governed by the bare Coulomb integral U_f of the $4f$ state being as large as 30 eV. Thus, an artificial shift via tuning $U_{\text{eff}}^{(3+)}$ of the hole f level by 3 eV, say (corresponding to a change of $U_{\text{eff}}^{(3+)}$ itself by 6 eV), will completely be compensated by a charge transfer as small as 0.1 electron charge. For this reason *the $4f$ hole level, to which the Fermi level is pinned, is itself very rigidly pinned close to the top of the pnictide p band.*

In Figure 78 the band structure in the vicinity of the Fermi level is shown for $U_{\text{eff}}^{(3+)} = 9.6$ eV. It corresponds to a ground state with a hole pocket around the Γ point ($k = 0$) holding 0.0058 As p holes per formula unit. For chosen values $U_{\text{eff}}^{(3+)} = 5.3, 7.0, 9.6,$ and 9.8 eV the obtained hole numbers are 0.0717, 0.0225, 0.0058, and 0.0005, respectively. Only for $U_{\text{eff}}^{(3+)} \geq 10$ eV the As p band would be filled and the Fermi level would lie in a gap between this band and the f hole state. This *generic* feature is obtained independent

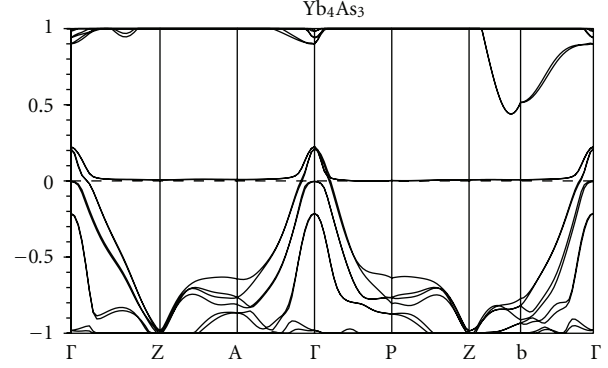


FIGURE 78: Self-consistent LSDA+ U energy band structure of Yb_4As_3 along the high-symmetry directions and for energies close to the Fermi level [423], (here, $U_{\text{eff}}^{(3+)} = 9.6$ eV, and the f shell of the Yb^{2+} ions is treated as a core shell).

of whether the filled f shell of the Yb^{2+} ions is treated as core or as valence, whether AF or ferromagnetic order is assumed on the Yb^{3+} chains or whether spin-orbit coupling is taken into account or not, all the involved energies being small compared to the unscreened U_f . Figure 79 shows the obtained partial DOS close to the Fermi level for a number of cases.

The carrier density in Yb_4As_3 at low temperature is extremely low, for which the following findings give evidence: (1) a large value of the resistivity up to 10 m Ω [399], (2) a very low plasma frequency obtained from optical reflectivity [418], (3) a large value of the Hall coefficient [399] which corresponds to about 0.001 holes per Yb^{3+} ion, assuming the single carrier model. Yb_4As_3 is a compensated semimetal, so the number of As p holes exactly equals the number of excess Yb $4f$ electrons in the partially filled $4f$ hole level. However, the mobility of heavy $4f$ electrons is assumed to be negligible in comparison with the mobility of As p electrons [399]. So the transport properties of Yb_4As_3 are mostly determined by the number of As p holes. In the analysis of [423], a carrier number of 0.001 per formula unit would result from a $U_{\text{eff}}^{(3+)}$ value between 9.6 and 9.8 eV which would not be in contradiction with photoemission.

The small mass at the top of the pnictide p band results in a very low p DOS of 0.015 states per eV, atom, and spin, at the f hole level for $U_{\text{eff}}^{(3+)} = 9.6$ eV. This means that there are very few p band states to broaden the f level by hybridization. The width of the hole state equals to about 0.007 eV (80 K) and decreases with increasing $U_{\text{eff}}^{(3+)}$. The total DOS at the Fermi level, resulting essentially from the $4f$ hole states, yields for $U_{\text{eff}}^{(3+)} = 9.6$ eV a large band structure contribution to the Sommerfeld constant of $\gamma = \pi^2 k_B^2 N_A N(\epsilon_F)/3 = 40$ mJ mol $^{-1}$ K $^{-2}$. The calculated γ is substantial, yet it corresponds only to the experimental value in a sufficiently strong magnetic field which suppresses magnetic moment fluctuations [402]. Since Yb_4P_3 , although a semiconductor, has an even larger value of the Sommerfeld constant than Yb_4As_3 , a large part of γ must be due to fluctuations of the magnetic moments in charge-ordered $\langle 111 \rangle$ chains.

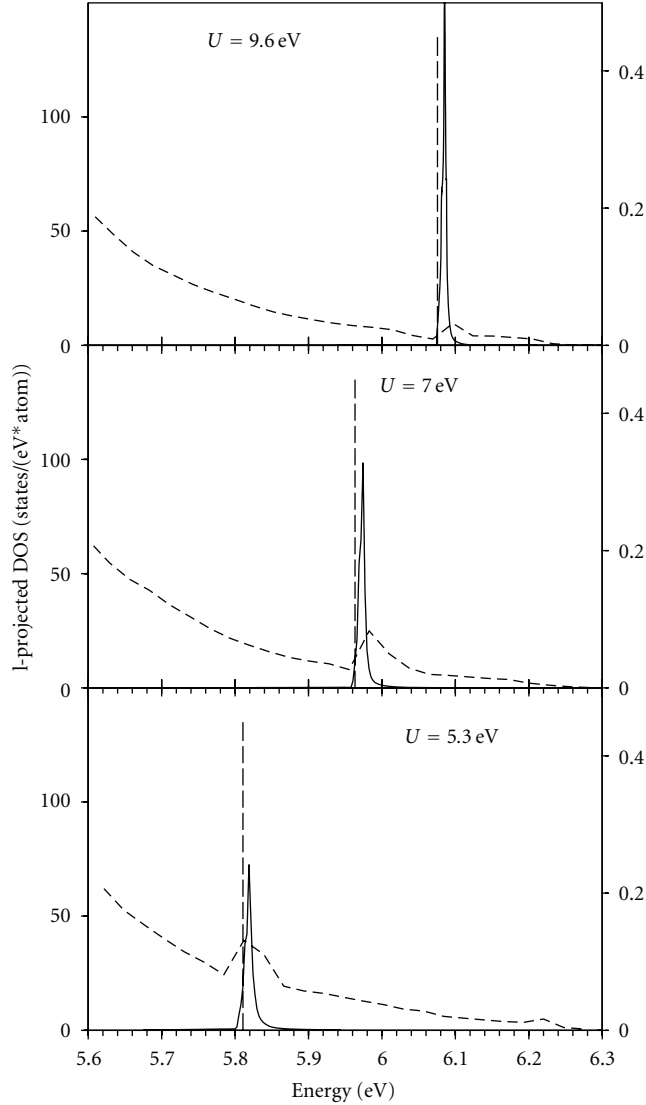


FIGURE 79: Yb $4f$ partial DOS and As $4p$ partial DOS of Yb_4As_3 on an expanded energy scale around the Fermi level (dashed vertical line) for various values of $U_{\text{eff}}^{(3+)}$ [423]. The left ordinate scale is for the f DOS and the right one for the p DOS.

Beyond LSDA+ U , further many-body interactions need to be invoked to account for the full Sommerfeld constant of the specific heat [420, 424].

8.2. Yb_4X_3 ($X = \text{P}, \text{Sb}, \text{and Bi}$). Figure 80 shows the energy band structure and total density of states near the Fermi level for Yb_4P_3 , Yb_4Sb_3 , and Yb_4Bi_3 calculated in the trigonal R3c AF crystal structure in the LSDA+ U approximation with $U_{\text{eff}}^{(3+)} = 9.6$ eV. Only Yb_4P_3 , and Yb_4As_3 reveal the charge-ordering cubic-to-trigonal structural transformation. The other two compounds remain in the cubic structure down to lowest temperatures with the Yb^{3+} ions being randomly distributed among the four chains. Such a valence fluctuating system is presently outside the scope of our investigation.

TABLE 10: The centers of gravity E_c relative to the Fermi energy and widths (in eV) of pnictogen np bands ΔE_{np} in Yb_4X_3 compounds.

Compound	E_c	ΔE_{np}
Yb_4P_3	-2.01	4.00
Yb_4As_3	-1.79	4.20
Yb_4Sb_3	-2.18	4.45
Yb_4Bi_3	-2.28	4.65

The main trend in the electronic structure of the sequence of Yb_4X_3 compounds ($X = \text{P}, \text{As}, \text{Sb}, \text{or Bi}$) results from the characteristic trend in the pnictide p wave functions and from the systematic change of the lattice parameters. The counteraction of screening by inner atomic shells and of relativistic effects leads to the characteristic trend in the position of the atomic p state and hence of the center of gravity of the pnictide p band, first increasing from P to As and then monotonically decreasing from P to Bi. The p bandwidth is monotonically increasing from P to Bi due to the increasing extension of the atomic wave function, although the lattice constant increases too (see Table 10). Therefore, if one moves from Yb_4Bi_3 to Yb_4P_3 through the series, the unoccupied $4f$ level moves from below towards the top of the pnictide p band and beyond, implying a reduction of metallicity and finally a transition to semiconducting behaviour, which is experimentally found in $\text{Yb}_4(\text{As}_{1-x}\text{P}_x)_3$ for $x \geq 0.4$ [400]. Figure 80 shows the energy band structure of the series, including also, $\text{Yb}_4(\text{As}_{0.5}\text{P}_{0.5})_3$. In this compound, treated as ordered, two AF ordered Yb^{3+} ions are no longer chemically equivalent and the system becomes ferrimagnetic. This leads to a splitting of the $4f$ hole bands. These bands are already well above the top of the valence band.

Experimentally, Yb_4Sb_3 and Yb_4Bi_3 show the typical valence-fluctuating behaviour [399]. Their energy band structures calculated for hypothetical trigonal R3c symmetry differ significantly from that of Yb_4As_3 . With the increasing pnictide p band widths, already in Yb_4Sb_3 the indirect gap between the top of the Sb $5p$ valence band and the bottom of the Yb $5d$ conduction band is closed (Figure 80). In Yb_4Bi_3 the direct gap has also disappeared due to further broadening of the Bi $6p$ conduction band. However, there is still no overlap between the partly filled narrow Yb $4f$ band and the Yb $5d$ conduction band in both compounds.

8.2.1. Summary. Using the LSDA+ U approach to band structure calculations with a U value adjusted to experiment but close to theoretical estimates, it was found a band gap between the As p band and the Yb $5d$ band in Yb_4As_3 . As a consequence, a very narrow marginally occupied $\text{Yb}^{3+}4f$ hole band is pinned close to the top of the As p valence band via the charge balance between Yb and As which is governed by the large (~ 30 eV) bare Coulomb integral of the Yb $4f$ state. The same charge balance pins the Fermi level close to the bottom of this $4f$ hole band which has a width of 0.007 eV (80 K). It lead to an extremely low carrier density in Yb_4As_3 . The Fermi surface of Yb_4As_3 consists of two almost spherical sheets: a hole pocket of As p states with a relatively

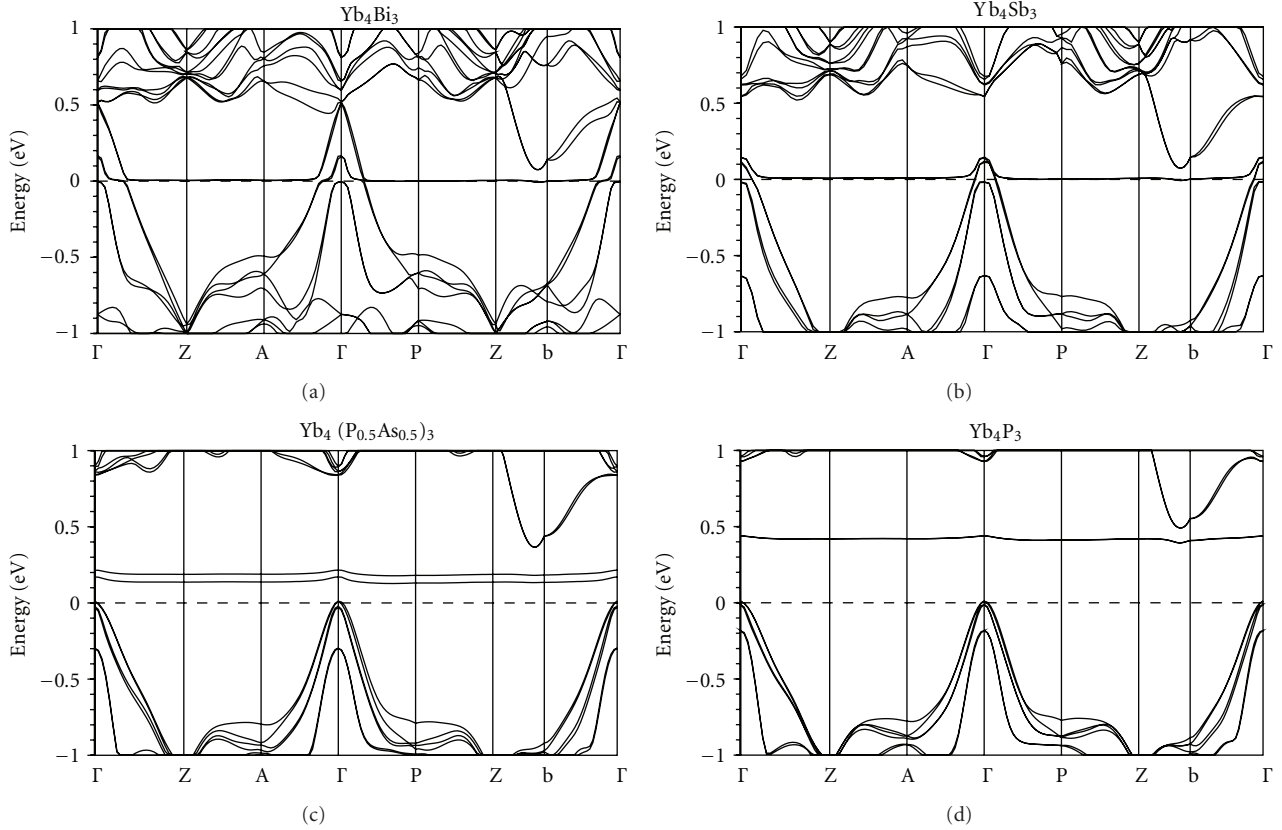


FIGURE 80: Self-consistent LSDA+ U ($U_{\text{eff}}^{(3+)} = 9.6$ eV) energy band structure of Yb_4Bi_3 , Yb_4Sb_3 (hypothetical R3c symmetry), $\text{Yb}_4(\text{P}_{0.5}\text{As}_{0.5})_3$, and Yb_4P_3 [423].

small effective mass, centered at the Γ point of the BZ, and an electron ellipsoid of Yb $4f$ states with a relatively heavy mass, centered on the symmetry line Γ -P.

The systematic trends in the position and width of the pnictide p band when going through the pnictogen group of the Periodic Table leads to a transition to semiconducting behavior towards the light pnictogen end with a charge transfer gap between the pnictide p band and the Yb $4f$ state, and to an increasing carrier number and hence increasing metallicity with valence-fluctuating Yb ions towards the heavy pnictogen end. Already in $\text{Yb}_4(\text{As}_{0.5}\text{P}_{0.5})_3$ semiconducting behavior is found. In Yb_4Sb_3 and in Yb_4Bi_3 the band gap between the pnictide p valence band and the Yb $5d$ conduction band is closed.

For Yb_4As_3 , the LSDA+ U band structure calculations provide a two-band model of the electronic structure: (1) a wide, nearly fully occupied As $4p$ valence band and (2) a very narrow, marginally occupied Yb $4f$ band, very weakly hybridized with the As $4p$ band in a small k space region near the Γ point of the BZ. Pressure, doping and so forth. may slightly change the relative position of these two bands and hence strongly affect the low carrier density and the transport properties. But the $4f$ shell of the Yb^{3+} ions is little influenced as long as the charge order is maintained.

In the LSDA+ U band structure calculations the Yb_4X_3 compounds have been treated as ideal systems with perfect

charge and AF-order. The real situation is much more complicated. Yb_4As_3 shows no magnetic ordering down to a very low temperature of 0.2 K. However, experimental evidence for existence of short-range AF correlations was found. An external magnetic field strongly affects the magnetic excitations suppressing the heavy-fermion properties of Yb_4As_3 . Going from Yb_4As_3 to Yb_4P_3 , the number of Yb^{3+} ions increases, the degree of charge and AF ordering also increases, and despite of the decrease of the number of free carriers (Yb_4P_3 is a semiconductor) the heavy-fermion properties are more pronounced which is reflected in the increasing value of the Sommerfeld constant γ from about $200 \text{ mJ mol}^{-1} \text{ K}^{-2}$ in Yb_4As_3 to $250 \text{ mJ mol}^{-1} \text{ K}^{-2}$ in Yb_4P_3 . Going to heavier pnictogen ions, metallicity increases and the tendency to moment and charge order is lost, and a typical mixed-valence behavior is found instead.

The large γ value of the semimetal Yb_4As_3 cannot be incorporated into Landau's Fermi-liquid theory for the following reason. In Landau's theory it is essential that the linear specific heat coefficient γ is related to the density of states at the Fermi level which depends on the quasiparticle masses. This relation does not hold here as seen by realizing that a large γ value is found even in the absence of any Fermi surface like in $\text{Yb}_4(\text{As}_{1-x}\text{P}_x)_3$ for $x \geq 0.4$. This is not surprising as the huge γ value can be assigned to spin excitations in the Heisenberg chains and can therefore be unrelated to the

quasiparticle excitations near the Fermi surface. It depends on the characteristic energy for the fluctuations of magnetic moments in the charge-ordered $\langle 111 \rangle f^{13}$ chains which is given by the superexchange of f^{13} moments along chains via pnictide orbitals. Note that only the effective moments of the lowest crystal-field doublets are relevant here. We speculate that, if the complete Fermi surface and the effective masses of Yb_4As_3 could be measured, one would find that they do not explain the specific heat in contradiction with Landau's Fermi-liquid theory. Therefore, this concept requires a generalization. One of the strong points of Landau's theory is that it is a phenomenological approach, which does not require a microscopic model for a given material. It is within that spirit that a generalization is suggested by postulating in addition to the charged fermions (electrons or holes) a liquid of neutral fermions with a density of states $N^*(0)$. This density of states is fitted to the γ value of the specific heat. The underlying physical picture is, of course, that the magnon-like spin excitations in the chains, although of bosonic character, can be transformed into charge neutral fermionic excitations giving rise to the large γ value. But, as pointed out above, we are dealing with a phenomenological theory, and therefore no microscopic justification of the postulate is required. A liquid of neutral fermions for the description of a metallic system was suggested before by Kagan et al. [425] in connection with Kondo lattices. In the present case, the neutral fermions do not contribute to electric transport, but, for example, to the thermal conductivity. They contribute also to the compressibility and to the spin susceptibility. The observed $\rho(T) = AT^2$ behavior at low temperature [399] with $A = 0.75 \mu\Omega \text{ cm/K}^2$ has to be interpreted as resulting from the scattering of the charged quasiparticles off the neutral fermions. A more detailed analysis of these features is left to a future investigation.

9. Sm and Eu Pnictides and Chalcogenides

Cubic Sm_4Bi_3 with the anti- Th_3P_4 structure undergoes a first-order transition into a trigonal $R3c$ phase at about 260 K. This change has been ascribed to a charge-ordering transition from the thermal valence-fluctuating state into a static mixture of di- and trivalent sites as one of the diagonals of the cube shrinks by approximately 1.4% [405, 426–428]. In charge-ordered Sm_4Bi_3 , smaller Sm^{3+} ions occupy the short chains [428]. Similar to Yb_4As_3 , each magnetic Sm^{3+} chain is isolated from other Sm^{3+} chains by Sm^{2+} ions for which the total angular momentum (J) equals zero. However, Sm_4Bi_3 shows a three-dimensional antiferromagnetic order at 2.7 K [429] as opposed to Yb_4As_3 , where a one-dimensional antiferromagnetic coupling at low temperatures has been predicted [420] and later discovered [409]. At this point, it is of great interest to characterize the nature of the phase transition occurring in Sm_4Bi_3 , because the physical properties of its distorted phase have been found to differ from those of Yb_4As_3 . In particular, no maximum occurs in the temperature dependence of the electrical resistivity, nor is there any appreciable linear term in its electronic specific heat.

Contrary to Sm_4Bi_3 , two other samarium pnictides Sm_4As_3 and Sm_4Sb_3 show no evidence of charge-ordering in

a wide temperature range [427]. The change of the character of charge ordering in Sm_4Bi_3 due to pressure has been studied in [427, 430]. With increasing pressure the resistivity anomaly at the charge ordering transition moves to lower temperatures, becomes weaker, and completely disappears at 2.8 GPa. Above that pressure the crystal undergoes a first-order, isostructural phase transition characterized by an abrupt decrease of the resistance by a factor of three and a volume by about 10%. The behavior of the electrical resistivity in the high-pressure phase (at 3 GPa) of Sm_4Bi_3 is similar to that of Sm_4As_3 and Sm_4Sb_3 [427]. The effect of high pressure can be reproduced by substitution of Bi atoms by smaller Sb atoms. Such an investigation has been reported in [431]. It was found that, with increasing Sb content in the $\text{Sm}_4(\text{Bi}_{1-x}\text{Sb}_x)_3$ system, the carrier concentration decreases and the charge-ordering temperature slightly increases, while by applying pressure the ordering temperature decreases. This relationship between the substitution and pressure effect in Sm_4Bi_3 is very similar to that in Yb_4As_3 . So, it was suggested that Sm_4Bi_3 is a semimetal in the same way as Yb_4As_3 . Although the substitution effect may be different from the pressure effect, both effects finally lead to enhancement of the Sm^{3+} state relative to Sm^{2+} state. The electronic states of Sm_4As_3 and Sm_4Bi_3 were studied with photoemission spectroscopy in [432, 433].

Recently experimental evidence for charge ordering in Eu_4As_3 has been reported. A first following from this result is the observation of trigonal distortion with $a = 9.176 \text{ \AA}$, $\alpha = 90.855^\circ$, which would indicate a periodic arrangement of the Eu^{2+} and Eu^{3+} ions [434]. Important information concerning the charge ordering of Eu_4As_3 was given by the Mössbauer spectroscopy measurements done by Wortmann et al. [435]. They found two absorption peaks separated clearly below $T = 340 \text{ K}$ corresponding to the di- and trivalent Eu ions. Above 340 K, these two peaks suddenly unite and the line width narrows with increasing temperature. Therefore, they concluded that Eu_4As_3 is a thermal valence-fluctuating compound which goes into a charge-ordered state below 340 K. Discontinuous changes corresponding to the structural transition are observed in the magnetic susceptibility, too [429]. However, the change of the magnetic susceptibility of Eu_4As_3 at the structural transition temperature is opposite to that of Yb_4As_3 that is, the magnetic susceptibility of Yb_4As_3 is larger in the low-temperature phase while that of Eu_4As_3 is smaller. The temperature dependence of the specific heat of Eu_4As_3 shows that, at the structural transition temperature, a sharp δ -like peak is observed [429]. This indicates that the structural transition is of first order. Eu_4As_3 orders ferromagnetically at $T = 18 \text{ K}$ in contrast to Yb_4As_3 and Sm_4Bi_3 which possess antiferromagnetic order at low temperatures. Anomalies in the structural, transport, and thermal properties in Eu_4As_3 associated with this transition are similar to those found in Yb_4As_3 and Sm_4Bi_3 .

The samarium chalcogenides Sm_3X_4 ($X = \text{S}, \text{Se}$ or Te) with the cubic Th_3P_4 structure are well known as typical examples of valence-fluctuation compounds, where two different valence ions, Sm^{2+} and Sm^{3+} , coexist [436]. Such a possibility was mentioned already in the early work of Picon et al. [437]. They noted that the lattice constants of Sm_3S_4

and Eu_3S_4 are too large in comparison with those of the trivalent $\text{R}_3^{3+}\text{S}_4$ compounds, indicating that cations with two different valence states 2+ and 3+ coexist in a ratio of 1 : 2.

Unlike most other Th_3P_4 -type rare-earth chalcogenides, which are trivalent and metallic [364], the Sm_3X_4 compounds behave as semiconductors, with a room-temperature electrical resistivity already of the order of $1\ \Omega\text{cm}$. The activation-type temperature dependence of the dc resistivity $\rho = \rho_0 \exp(E/k_B T)$ has a unique value of the activation energy $E \approx 0.14\ \text{eV}$ for Sm_3X_4 ($X = \text{S}, \text{Se}, \text{or Te}$) [315, 438]. The optical measurements reveal a direct energy gap in Sm_3S_4 and Eu_3S_4 equal to $0.2\ \text{eV}$ and $1.7\ \text{eV}$, respectively [439, 440]. The analysis for the dielectric response confirmed that Sm_3Se_4 is an insulator, that is, without free carriers at low-temperature [441]. But the gap is so small that it is easily smeared by imperfections like in La-doped SmB_6 [427]. From X-ray diffraction experiments [436], both types of Sm ion were found to occupy the same crystallographic site. The magnetic susceptibility of Sm_3X_4 is explained by a sum of the susceptibility of the Van Vleck term for Sm^{2+} with $J = 0$ (0 K) and $J = 1$ (400 K) and of the Curie term for Sm^{3+} with $J = 5/2$ in the coexistence ratio 1 : 2 [442]. Assuming ideal stoichiometry, simple charge balance for the nominal formula $\text{Sm}^{2+}(\text{Sm}^{3+})_2(\text{X}^{2-})_4$ implies that no free carriers are available to populate the conduction band, which explains the lack of metallic conduction observed experimentally. Thermally activated electrical transport takes place, however, through the hopping of electrons among the rare-earth sites [443]. Thus, near room temperature, the Sm ions fluctuate rapidly between two configurations $4f^5$ and $4f^6$, giving rise to the so-called “thermal valence fluctuations.” This mechanism differs markedly from the “quantum valence fluctuations” occurring in homogeneously mixed-valence compounds [3–5, 7]. Here, the fluctuations slow down drastically as T decreases, as evidenced by the upswing in the transverse nuclear relaxation rate $1/T_2$ on cooling below $160\ \text{K}$ [444] or the frequency-dependent stiffening of the elastic constants, [445] and an activation-type temperature dependence of the relaxation time, $\tau = \tau_0 \exp(E/k_B T)$. The relaxation time corresponding to the hopping rate in the thermal motion of the $4f$ electron from Sm^{2+} to neighboring Sm^{3+} ions in Sm_3X_4 becomes longer and longer on lowering the temperature; however, no sign of a phase transition to a charge-ordered state has been found. On lowering the temperature, the fluctuation of the $4f$ electrons freezes gradually into a charge glass state, which is characterized by the random distribution of Sm^{2+} and Sm^{3+} ions in space. In fact, it has been reported that the broad peaks of the magnetic susceptibility and specific heat around $T_{\text{sg}} = 1.3\ \text{K}$ in Sm_3Te_4 occur at the transition into the spin-glass state because of the random ordering of the magnetic moments of Sm^{2+} and Sm^{3+} ions [446].

This result is in contrast with the low-temperature properties of the isomorphous Eu_3S_4 compound. This compound possesses a first-order phase transition near $T_{\text{co}} = 186\ \text{K}$ [447]. The transition exhibits the configurational entropy of an order-disorder transition. The structural changes at the phase transition of Eu_3S_4 were found to be very small compared, for example, to these of the second-order structural

phase transition in La_3S_4 [447]. The carrier concentration drops by roughly 3 orders of magnitude in Eu_3S_4 upon cooling below T_{co} [448]. Eu_3S_4 has also a phase transition to a ferromagnetic state below $T_c = 3.8\ \text{K}$ [449]. A recent synchrotron X-ray diffraction study for single crystals of Eu_3S_4 has revealed that a Th_3P_4 -type $I\bar{4}3d$ structure transforms to a charge-ordered $I\bar{4}2d$ one at $T_{\text{co}} = 188.5\ \text{K}$ [450]. In the $I\bar{4}2d$ crystal structure, all Eu^{2+} ions mix with half the Eu^{3+} in the $8d$ sites, and the remaining Eu^{3+} ions occupy the $4a$ sites.

No such effect has been observed in the Sm chalcogenides down to temperatures of less than $1\ \text{K}$. This intriguing result has raised interesting speculations as to the nature of the low-temperature state in the Sm_3X_4 compounds [403]. From the AC conductivity, it has been suggested that, as thermal fluctuations die out at low temperatures, tunneling of $4f$ electrons between neighboring sites may become the dominant transport mechanism. It is known that the tunnel motion of the $4f$ electrons is relevant when the initial and final states possess nearly equal energies [7]. Various spectroscopic probes (Mössbauer effect [451], NMR [444], μSR [452]) have been used to determine the charge and magnetic response of these compounds with different characteristic time scales. It now seems most likely that, in Sm_3X_4 , the Sm^{3+} moments freeze at low temperature into a spin-glass state [444, 446], possibly associated with a static, or quasistatic, spatial disorder of the two $4f$ configurations. According to this interpretation, the huge linear term, $\gamma = 0.6\ \text{J K}^{-2}/\text{mol}$ and $\gamma = 0.79\ \text{J K}^{-2}/\text{mol}$, observed in the low-temperature specific heat in Sm_3Te_4 and Sm_3Se_4 , respectively [453], can be ascribed to magnetic disorder rather than to heavy-fermion phenomena as proposed initially.

Why does Sm_3X_4 favor the charge glass state and does not exhibit charge ordering with the usual first-order transition with symmetry-breaking character like Eu_3S_4 or Yb_4As_3 ? To answer this question, the microscopic details about the $4f$ electron states and their degree of hybridization with conduction states are highly relevant.

Crystal Structure. The high-temperature phases of R_4X_3 ($\text{R} = \text{Sm}, \text{Eu}; \text{X} = \text{As}, \text{Sb}, \text{Bi}$) compounds have the cubic anti- Th_3P_4 structure with space group $I\bar{4}3d$ (no. 220). The R ions occupy the P sites with Wyckoff positions $16c$, ($x = y = z = u$), and the X ions occupy the Th sites with special Wyckoff positions $12a$ ($x = 3/8, y = 0, z = 1/4$) [454]. All R-atoms are aligned on four families of chains oriented along the four diagonals of the cubic unit cell [408].

The high-temperature phases of Eu_3S_4 and Sm_3X_4 ($X = \text{S}, \text{Se}, \text{or Te}$) compounds have the bcc Th_3P_4 structure with space group $I\bar{4}3d$ (no. 220). Conventional unit cell of Eu_3S_4 includes four formula units. Both ions Eu^{2+} and Eu^{3+} in Eu_3S_4 occupy crystallographically equivalent $12a$ sites ($x = 3/8, y = 0, z = 1/8$) with S_4 symmetry. S occupies the $16c$ sites ($x = y = z = u$). Only the x -coordinate of sulfur (u parameter) is a variable among positional parameters. We used the experimentally determined values of $u = 0.0721, 0.0722, 0.0724$, and 0.0724 for $\text{Eu}_3\text{S}_4, \text{Sm}_3\text{S}_4, \text{Sm}_3\text{Se}_4$, and Sm_3Te_4 , respectively [454]. It gives a slight deviation from an ideal Th_3P_4 structure ($u = 1/12 = 0.0833$). An Eu ion is

coordinated by eight sulfur ions in a distorted cube while a sulfur ion is coordinated by six Eu ions.

A recent synchrotron X-ray diffraction study for single crystals of Eu_3S_4 has revealed a low-temperature charge-ordered structure with tetrahedral symmetry and a space group of $I\bar{4}2d$ (no. 122). The cell dimensions are $a = 8.508 \text{ \AA}$ and $c = 8.514 \text{ \AA}$ [450]. Eu ions occupy crystallographically two nonequivalent positions, namely, $4a$ ($x = y = z = 0$) and $8d$ ($x = 3/8, y = 1/4, z = 1/8$) sites. S ions occupy the $16e$ sites ($x = 0.572, y = 0.823, z = 0.449$) [450]. Both Eu sites are coordinated by eight sulfur ions. The $4a$ sites are distributed as in the diamond structure. The mean Eu-S distance for the $8d$ sites is about 0.3% larger than for the $4a$ sites.

9.1. Sm_4Bi_3 . The LSDA+ U partial DOSs of antiferromagnetic (AF) Sm_4Bi_3 are shown in Figure 81 [455]. In order to imitate the nonmagnetic ($J = 0$) ground state of Sm^{2+} ion the exchange-correlation potential is taken to be the same for both spin states within the corresponding atomic spheres. For three divalent nonmagnetic Sm ions, six $4f_{5/2}$ energy bands per ion are fully occupied and hybridize with Bi p states at around -2.0 eV below Fermi energy. The other eight $4f_{7/2}$ divalent Sm energy bands are situated far above the Fermi level at 6.5 eV and hybridize with Sm $5d$ states. Both the occupied and empty $\text{Sm}^{2+}4f$ states are very narrow which indicates that their hybridization with Bi p and Sm $5d$ states is rather weak. For the trivalent Sm ion seven spin-down $4f$ electron bands per ion are well above the Fermi level and hybridize with Sm $5d$ states. Five spin-up $\text{Sm}^{3+}4f$ states are below the Fermi level situated right in the energy gap between Bi s and p states (not shown). The other two spin-up $4f$ energy bands for the trivalent Sm ion, doubly degenerate due to AF ordering, appear just below the top of the Bi p band. One of them is completely empty and above the Fermi energy at around 0.15 eV , but the other one is pinned to the Fermi level. The 6th and 7th $4f$ spin-up energy bands have different orbital characters, $m_j = -5/2$ and $m_j = -7/2$, respectively, and their splitting is mainly caused by the nonspherical part of the Coulomb interaction.

The pinning of the 6th spin-up $\text{Sm}^{3+}4f$ state to the Fermi level is a robust feature of the electronic structure of the Sm_4Bi_3 compound. As an example, we present in Figure 82 the energy bands of Sm_4Bi_3 for different values of Coulomb parameter U . The 6th spin-up $\text{Sm}^{3+}4f$ state just slices near the top of the Bi p band when U is varied from 3 to 10 eV . Only for $U \geq 10.5 \text{ eV}$ does the Sm $4f$ band become empty. Such pinning of the $4f$ state to the Fermi level may be explained by the charge balance between Sm $4f$ states of the Sm^{3+} ions and pnictide p states. This feature in combination with the small mass of the Bi p electrons close to the top of the p band appears to be a key point for the physics of the Sm pnictides.

In Figure 82 for drawing of the $4f$ bands we used the so-called *fat-bands* representation. The size of the circles indicates the degree of the $4f$ orbital character in a band. Such a representation can help to visualize also the hybridization between Sm $4f$ and Bi p states. The largest Sm $4f$ -Bi p hybridization was found to be near the Γ symmetry point

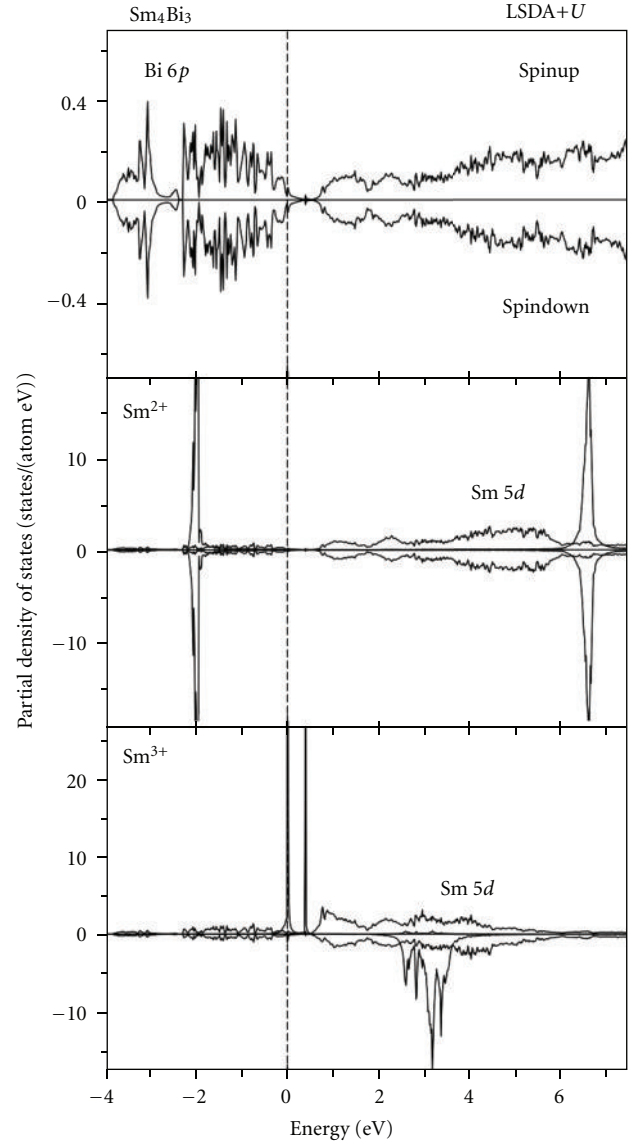


FIGURE 81: The partial density of states (in states/(atom eV)) of Sm_4Bi_3 calculated in LSDA+ U approximation ($U = 7.0 \text{ eV}$) for the low-temperature $R3c$ phase [455].

in the Γ -P direction. Due to the very small phase space for hybridization and the very small Sm $4f$ -Bi p orbital overlap, the DOS peak of the 6th hole spin-up $4f$ band pinned at the Fermi level is as narrow as 0.01 eV .

This situation is similar to that found in the charge ordering of Yb_4As_3 [423], where a very narrow marginally occupied $\text{Yb}^{3+}4f$ hole band is also pinned close to the very top of the As p valence band via the charge balance between Yb and As. One should mention, however, that there are also some important differences. There are two $4f$ energy bands crossing the top of the Bi p band in Sm_4Bi_3 but only a single one in the Yb_4As_3 compound. The latter case corresponds to a ground state with a hole pocket around the Γ -point ($\mathbf{k} = 0$) holding 0.0058 As p holes per formula unit. In the case of Sm_4Bi_3 a hole pocket around the Γ -point contains

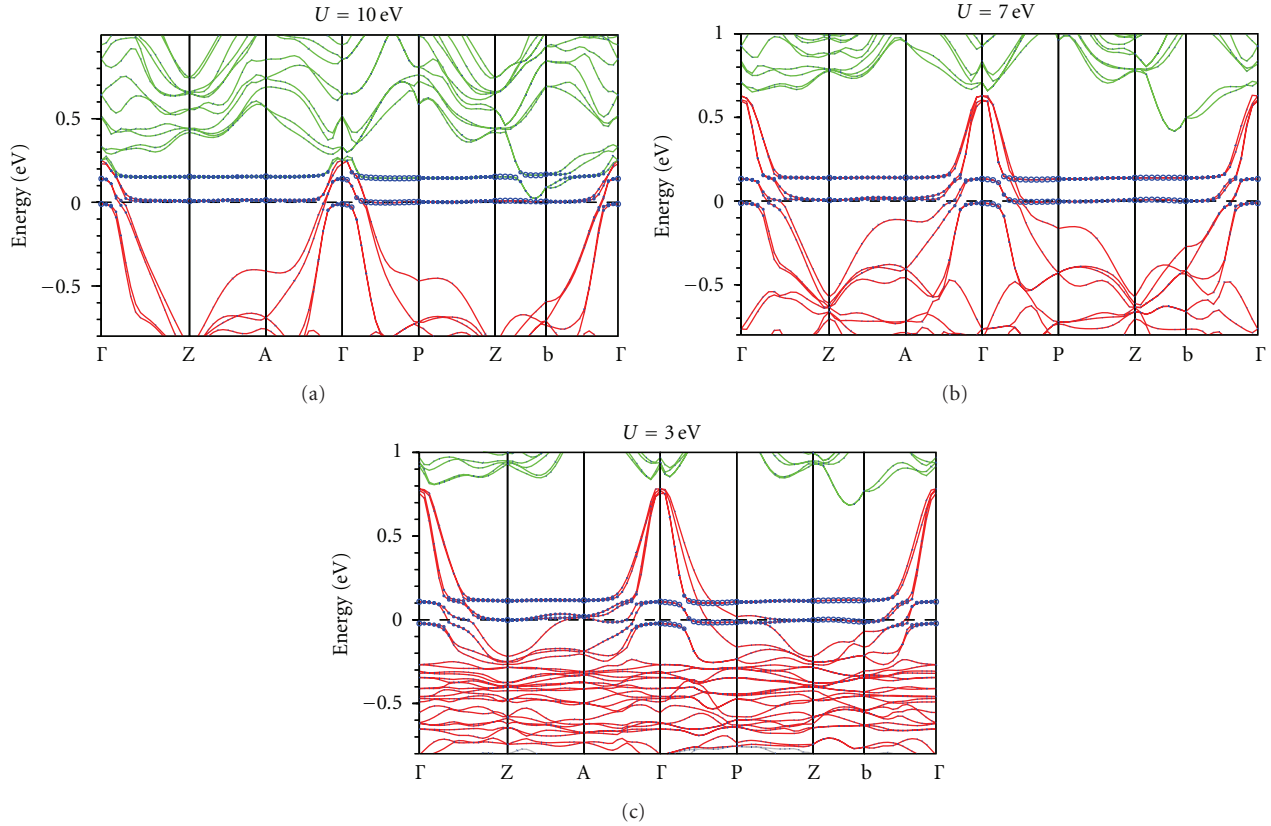


FIGURE 82: The energy band structure of Sm_4Bi_3 calculated in LSDA+ U approximation around the Fermi level for various values of U [455].

0.25 Bi p holes per formula unit. As a consequence the carrier concentration is relatively large in Sm_4Bi_3 . However, the most prominent difference in the electronic structure of the Sm_4Bi_3 in comparison with the Yb_4As_3 compound is the value of the spin moment of the corresponding magnetic ions. The Yb^{3+} ions occupying short chains in Yb_4As_3 have the $4f^{13}$ configuration with an effective spin of $s = 1/2$. This leads to appearance of one-dimensional spin 1/2 chains with antiferromagnetic coupling at low temperatures [409]. The trivalent Sm^{3+} ions with the $4f^5$ configuration have a spin moment $s = 5/2$, and Sm_4Bi_3 possesses a three-dimensional antiferromagnetic order [429]. The Fermi surface of Sm_4Bi_3 consists of two closed hole pockets of Bi p states centered at the Γ point and two electron ellipsoids of Sm f states centered at P and A symmetry points. The corresponding Fermi surface of Yb_4As_3 consists of a hole pocket of As p states centered at the Γ point and an electron ellipsoid of Yb f states centered on the symmetry line Γ -P.

The mobility of heavy $4f$ holes is assumed to be negligible in comparison with the mobility of pnictide p electrons. So the transport properties of Sm_4Bi_3 are mostly determined by the number of pnictide p holes.

9.2. Sm_4As_3 and Sm_4Sb_3 . The main trend in the electronic structure of the sequence of Sm_4X_3 compounds ($X = \text{As}, \text{Sb},$ or Bi) results from the characteristic trend in the pnictide p wave functions and from the systematic change of the lattice

parameters. The counteraction of screening by inner atomic shells and of relativistic effects leads to the characteristic trend in the position of the atomic p state, and hence the center of gravity of the pnictide p band decreases from As to Bi. The p bandwidth is monotonically increasing from As to Bi due to the increasing extension of the atomic wave function, although the lattice constant increases too. The degree of pinning of Sm 6th $4f$ spin-up energy band to the Fermi level in Sm_4Sb_3 and Sm_4As_3 is similar to that obtained for the Sm_4Bi_3 compound. An artificial shift via tuning U of the hole f level by changing U by 6 eV is completely compensated by a charge transfer as small as 0.2 electron.

The most prominent difference in the electronic structure of the Sm_4Bi_3 compound in comparison with the other two samarium pnictides is in the position and occupation of the 6th hole $4f$ spin-up energy level. Figure 83(a) shows the expanded view of the total DOS of Sm_4X_3 ($X = \text{As}, \text{Sb},$ or Bi) compounds. If one moves from Sm_4Bi_3 to Sm_4As_3 through the series, the peak position of the 6th hole $4f$ spin-up level shifts toward higher energy from the Fermi level. The occupation of the 6th hole $4f$ spin-up level reduces from 0.25 electrons in Sm_4Bi_3 to 0.15 electrons in Sm_4Sb_3 and to 0.01 electrons in Sm_4As_3 . Therefore, the Sm^{3+} state is enhanced relative to the Sm^{2+} one in the series. This is consistent with the conclusion derived in [431] on the $\text{Sm}_4(\text{Bi}_{1-x}\text{Sb}_x)_3$ system. We should mention here that when we speak about partial occupation of the 6th f hole level

in Sm_4X_3 compounds we imply that such an occupation is due to the hybridization effect between pnictide p and Sm $4f$ energy states.

The Sm_4X_3 pnictides offer the unique opportunity to follow the evolution of intermediate valence as a function of composition. The driving force is the change of lattice constant upon exchanging the anion. In order to separate the influence of the lattice constant from the influence of the ionic potential of the pnictide component on the electronic structure of Sm_4X_3 ($X = \text{As}, \text{Sb}, \text{and Bi}$), we present in Figure 83(b) the DOS of Sm_4Bi_3 evaluated with the lattice constant of Sm_4Sb_3 ($a = 9.308 \text{ \AA}$) and for $a = 9.561 \text{ \AA}$. The peak positions of the 6th hole $4f$ spin-up level of Sm_4Bi_3 with lattice parameter equal to that of the Sm_4Sb_3 compound and real samarium antimonide are almost the same indicating the major role played by the lattice constant in this case. On the other hand, the occupation number of the 6th hole $4f$ spin-up level in the compressed Sm_4Bi_3 is 1.5 times larger than in Sm_4Sb_3 compound. The reason is the larger Sm $4f$ -pnictide p hybridization in the former case due to larger extension of the atomic Bi $6p$ wave function in comparison with the Sb $5p$ one. It can be concluded that in the cases of the Sm_4X_3 compounds the type of pnictide ion potential plays an essential role.

The results of the band structure calculations for Sm_4As_3 and Sm_4Sb_3 presented above were obtained with the assumption that the compounds contain three Sm^{2+} and one Sm^{3+} ions in the unit cell similar to Sm_4Bi_3 . In this case it is still not clear why Sm_4As_3 and Sm_4Sb_3 show no trace of charge ordering at low temperatures. On the other hand, in earlier work, Ochiai et al. [427] suggested that Sm_4As_3 and Sm_4Sb_3 are typical dense Kondo systems with all four Sm ions being in the trivalent state. From the volume collapse in the high-pressure phase of Sm_4Bi_3 , it was deduced that all Sm ions must be close to trivalency in this phase [426, 430].

The electronic structure of Sm_4As_3 with trivalent Sm ions (not shown) differs significantly from the band structure with only one Sm ion in the trivalent state. In the former case As $4p$ states are completely occupied and are far below the Fermi level. On the other hand, the previously empty Sm $5d$ states become occupied due to $4f \rightarrow 5d$ charge transfer. A similar band structure was found also in Sm_4Sb_3 with trivalent Sm ions.

Independently of the number of trivalent Sm ions the 6th $4f$ hole level is always pinned at the Fermi energy. It makes the usual Kondo lattice scenario inappropriate for Sm_4As_3 and Sm_4Sb_3 because, for a Kondo resonance to develop, both the occupied and empty $4f$ states must be sufficiently far away from the Fermi level.

In conclusion we note that the question of how many Sm ions are in the trivalent state in Sm_4As_3 and Sm_4Sb_3 compounds as well as in the high-pressure phase of Sm_4Bi_3 (above 2.8 GPa) is still open. Analysis of the lattice constants suggests that all four Sm ions are probably in the trivalent state [426, 427]. On the other hand, the magnetic susceptibility at room temperature in Sm_4As_3 is definitely larger than the theoretical value for Sm^{3+} , which can be explained by over 10% mixing of Sm^{2+} [427]. Moreover, high-resolution $4d - 4f$ resonance photoemission spectra of Sm_4As_3 have

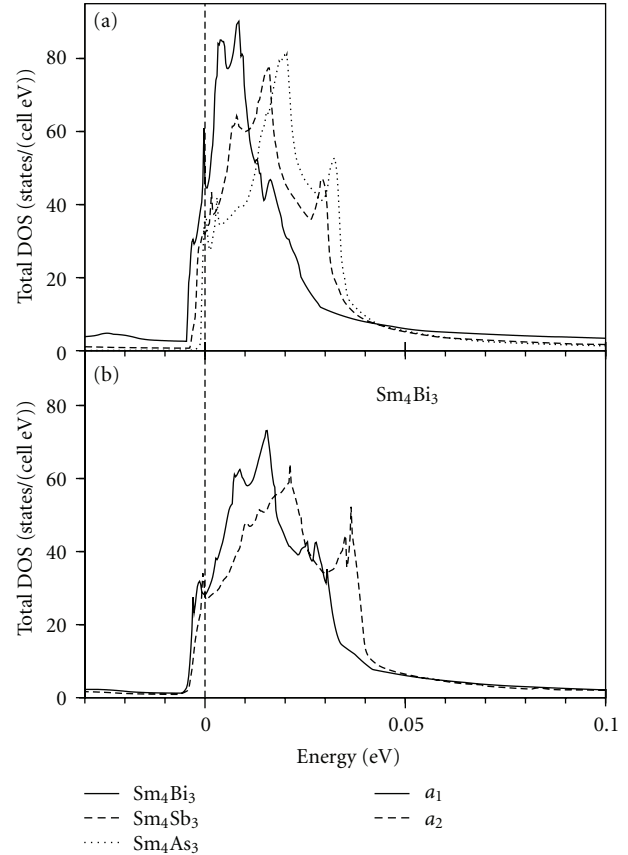


FIGURE 83: Expanded view of the DOS of (a) Sm_4X_3 ($X = \text{As}, \text{Sb}, \text{Bi}$) and (b) Sm_4Bi_3 for the lattice constants $a_1 = 9.308 \text{ \AA}$ and $a_2 = 9.561 \text{ \AA}$ [455].

quite intensive components at 0 to 4 eV binding energy [5, 6], which indicates a significant amount of Sm^{2+} ions in the compound.

The principal question about the degree of Sm valency might be answered also by optical measurements. In Figure 84 we show the optical reflectivity and conductivity spectra of Sm_4As_3 calculated in the LSDA+ U approximation for different Sm valencies. The most prominent difference in the spectra is the extra peak between 0 and 1 eV in the optical conductivity with all four Sm ions in the trivalent state caused by interband transitions involving the occupied $5d$ hybridized states. In Sm_4As_3 with only one Sm ion being in the trivalent state Sm $5d$ states are completely empty. As a result, the transitions involving the occupied $5d$ states do not take place at small photon energies, and the erroneous peak structures around 0 to 1 eV disappear from the optical spectra. A small peak at around 0.15 eV presented in the optical conductivity spectrum with one Sm ion in the trivalent state is mostly determined by the interband transitions involving occupied states with predominantly As p character to unoccupied states with predominantly Sm $4f$ character situated in close vicinity of the Fermi level. Experimental measurements of the optical spectra in Sm_4As_3 and Sm_4Sb_3 are highly desired.

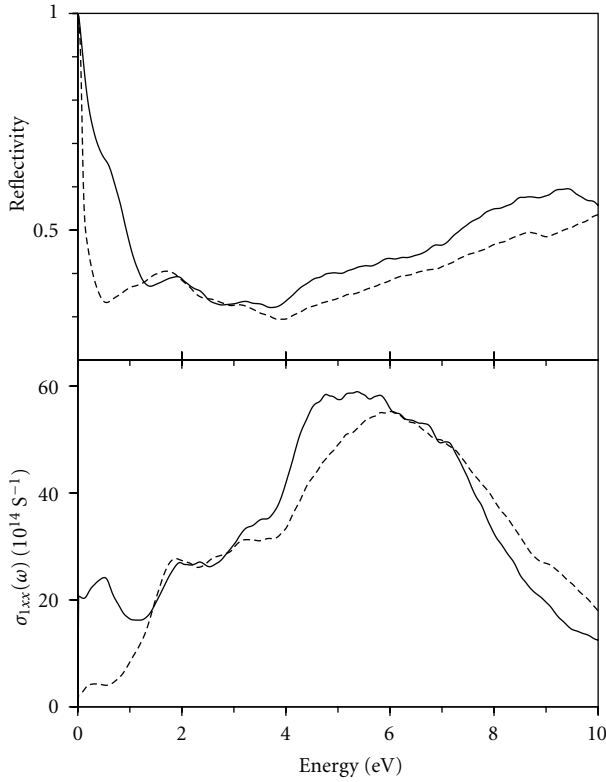


FIGURE 84: Calculated optical reflectivity $R(\omega)$ and conductivity $\sigma(\omega)$ in Sm_4As_3 with one (dashed line) and all four Sm ions in the trivalent state (full line) [455].

It should be mentioned that the experimental situation in Sm_4X_3 differs from that, for example, in Yb_4As_3 or Eu_4As_3 in the sense that in the later systems a new generation of samples of much better quality became available during recent years, and more reliable data about transport properties, optical and photoemission spectra were obtained. In Sm_4X_3 we still use old experimental data, and it is difficult to ascertain the full validity of measured properties based on the experiments of the early 1980s. The physical nature of the mixed-valence state in Sm_4As_3 and Sm_4Sb_3 compounds as well as in the high-pressure phase of Sm_4Bi_3 requires further investigation theoretically as well as experimentally.

9.3. Eu_4X_3 ($X = \text{As}, \text{Sb}, \text{and Bi}$). Figure 85 shows the energy band structure and total density of states near the Fermi level for Eu_4As_3 , Eu_4Sb_3 , and Eu_4Bi_3 calculated in the LSDA+U approximation [455]. For divalent ferromagnetic Eu ions seven $4f$ spin-up energy bands per ion are fully occupied and hybridize with the bottom of the pnictide p states (not shown). The other seven $4f$ spin-down divalent Eu energy bands are situated far above the Fermi level at 7 to 7.5 eV and are hybridized with Eu $5d$ states. The six $4f_{5/2}\text{Eu}^{3+}$ bands are fully occupied and situated in the gap between the pnictide s and p states, while eight $4f_{7/2}$ hole levels are completely unoccupied and cross the top of pnictide p band and bottom of the Eu $5d$ band. There is a hybridization energy gap of

$\Delta E = 0.05$ eV in Eu_4Bi_3 which is formed between Bi p and $\text{Eu}^{3+}4f_{7/2}$ states.

The Fermi surface of Eu_4Bi_3 consists of small closed hole pockets of Bi p states centered at the Γ point and an electron ellipsoid of Eu $5d$ states centered at the Z -b symmetry direction. There are no $4f$ states at the Fermi level.

As in the case of Sm_4X_3 the main trend in the electronic structure of the sequence of Eu_4X_3 compounds ($X = \text{As}, \text{Sb}, \text{or Bi}$) results in a monotonic increase of the p bandwidth going from As to Bi due to an increasing extension of the atomic wave function. Therefore, as one moves from Eu_4Bi_3 to Eu_4As_3 through the series, the unoccupied $4f_{7/2}$ levels for nonmagnetic Eu^{3+} move from below toward the very top of the pnictide p band. If Eu_4Bi_3 is a semimetal, Eu_4As_3 and Eu_4Sb_3 are both semiconductors. The direct gap is equal to 0.41 eV and 0.12 eV and the indirect gap -0.26 eV and 0.02 eV in Eu_4As_3 and Eu_4Sb_3 , respectively. These gaps are between pnictide p and Eu $5d$ bands.

The temperature dependence of the Hall coefficient single crystal Eu_4As_3 is presented in [429]. Large values of the Hall coefficient indicate a very low carrier concentration of this system. The same holds true for the electrical resistivity, which is, for instance, estimated as about 0.005 carriers/Eu ion at 200 K, assuming a one band model. Its positive sign suggests dominant hole conductivity in a wide temperature range. On the other hand, from our band structure calculations, Eu_4As_3 is a semiconductor, although the calculated indirect gap is rather small in this system and any crystal imperfections or small doping can easily close the gap.

Among Eu_4X_3 ($X = \text{As}, \text{Sb}, \text{and Bi}$) compounds only Eu_4As_3 reveals the charge-ordering cubic-to-trigonal structural transformation. There is no information on the charge ordering for the other two compounds in the literature [456].

9.4. Eu_3S_4 . The analysis on the site preference of Eu^{2+} and Eu^{3+} ions presented in [450] shows that Eu^{2+} ions do not occupy the $4a$ sites within the error estimates. The ionic radii of Eu^{2+} and Eu^{3+} ions are 1.25 and 1.07 Å [457]. Larger Eu^{2+} ions prefer the slightly larger $8d$ sites, although both sites are surrounded by eight sulfur atoms in the coordination of a distorted cube. The ordering scheme is that the Eu^{3+} ions occupy the $4a$ sites, while both Eu^{2+} and Eu^{3+} ions occupy the $8d$ sites in the ratio of 1:1. The chemical formula involving the information on the valence is given as $[\text{Eu}^{3+}]_{4a}[\text{Eu}^{2+}\text{Eu}^{3+}]_{8d}(\text{S}^{2-})_4$. Two isomer shift peaks of the Mössbauer spectra of Eu_3S_4 support the separation of Eu^{2+} and Eu^{3+} ions below $T = 228$ K [458]. Since the observation temperature is higher than $T_{\text{co}} = 188.5$ K, the gradual freezing of electron hopping occurs independently of the crystal-structural change, where the crystal still maintains the Th_3P_4 -type structure. The frequency of hopping can be described as a relaxation time τ to exchange the electrons in the observation of the Mössbauer spectra. Exponential temperature dependence of τ was reported with a continuous change through the phase transition. The τ values are 1.010^{-7} , 3.510^{-8} , 8.510^{-10} , and 3.510^{-11} sec at $T = 83, 200, 250$ and 325 K, respectively [458]. It should be noted that the hopping of electrons still exists at $T = 83$ K even below

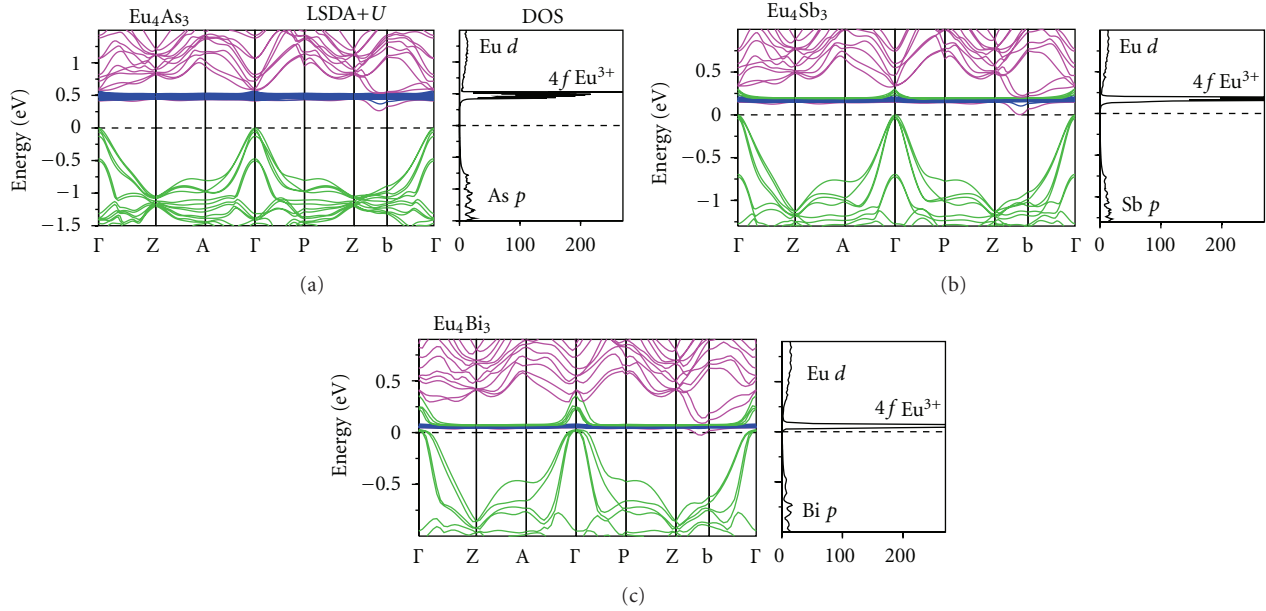


FIGURE 85: The energy band structure and total DOS (in states/(cell eV)) of Eu_4As_3 , Eu_4Sb_3 , and Eu_4Bi_3 calculated in LSDA+ U approximation ($U = 7.47, 7.35$, and 7.25 eV, resp.) [455].

the phase-transition temperature of $T_{\text{co}} = 188.5$ K. Similar gradual freezing of electron hopping was observed in the neutron and X-ray Huang scattering of magnetite [124, 459].

Although the distribution of Eu^{2+} and Eu^{3+} ions at $8d$ sites is random below $T_{\text{co}} = 188.5$ K, the energy barrier to enable the electron hopping is relatively small even in the low-temperature phase so far examined. Therefore, a new charge ordering between Eu^{2+} and Eu^{3+} ions may exist for Eu_3S_4 [450].

Figure 86 shows the partial density of states of Eu_3S_4 for the low-temperature $I\bar{4}2d$ phase calculated in the LSDA+ U approximation for $U_{\text{eff}} = U - J = 7.63$ eV [455]. In the LSDA+ U band structure calculations of Eu_3S_4 , it was assumed an additional charge ordering of the Eu^{2+} and Eu^{3+} ions in $8d$ sublattice (see Figure 87) in a way which has been done in the case of the low-temperature charge-ordered magnetite Fe_3O_4 in B sublattice for Fe^{2+} and Fe^{3+} ions [10]. In contrast to LSDA, where the stable solution for Eu_3S_4 is metallic, the LSDA+ U method gave an insulator consistent with the experimental situation described in the introduction.

For divalent magnetic Eu_{8d}^{2+} ions seven $4f$ spin-down energy bands per ion are situated at the top of Eu $5d$ states at 10 to 11 eV above Fermi level. The $4f$ spin-up energy bands per ion are fully occupied and hybridized with about a half of the $S p$ band. There is a quasi-energy gap between hybridized and nonhybridized parts of $S p$ bands at -2.1 to -2.4 eV (Figure 86). Six $4f_{5/2}\text{Eu}^{3+}$ nonmagnetic bands for both the $4a$ and $8d$ sites are fully occupied and situated in the gap between $S s$ and p states, while eight $4f_{7/2}$ hole levels are completely unoccupied and cross the very bottom of the $\text{Sm } 5d$ states at around 2 eV above the Fermi level (Figure 86). Both the occupied and empty $4f$ Eu_{4a}^{3+} states

are shifted downward at around 0.1 eV in comparison with the position of the $4f\text{Eu}_{8d}^{3+}$ states due to slightly different chemical bonding.

9.5. Sm_3S_4 . The inhomogeneous mixed-valence state on the Sm sublattice was modeled by lowering the crystal symmetry in such a way that $12a$ sites split into two groups consisting of 4 and 8 equivalent sites. The former were occupied by Sm^{2+} and the latter by Sm^{3+} ions.

In contrast to LSDA, where the charge-inhomogeneous solution for Sm_3S_4 is metallic, the LSDA+ U method gave an insulator. Sm^{2+} nonmagnetic $4f_{5/2}$ bands are fully occupied and situated at the very top of $S p$ energy band (Figure 88). The $4f_{7/2}$ hole levels are completely empty and well above the Fermi level hybridized with $\text{Sm } 5d$ states at around 9 eV (Figure 88). For trivalent Sm ions seven $4f$ spin-down energy bands per ion are situated above Fermi level at 2.2 to 4.0 eV hybridized with $\text{Sm } 5d$ states. Five $4f$ spin-up energy bands per ion are fully occupied and situated in the gap between $S s$ and p energy bands (not shown). The other two empty $4f$ spin-up energy bands are situated just above the Fermi level in the gap between occupied nonmagnetic $4f_{5/2}\text{Sm}^{2+}$ bands and empty $\text{Sm } 5d$ bands (Figure 88).

Photoemission experiments, both X-ray (XPS) and ultraviolet, are of central importance for understanding mixed-valence materials (see the review of the early work by Campagna et al. [346]). In rare-earth photoemission, when the photon ejects an electron from the $4f^n$ shell, it leaves behind a $4f^{n-1}$ configuration; hence, the kinetic energy distribution curve of the emitted electron measures the spectra of the final-state hole. The final state $4f^{n-1}$ has a characteristic multiplet splitting which serves as a fingerprint, and these are accurately resolved and calculable for rare-earth

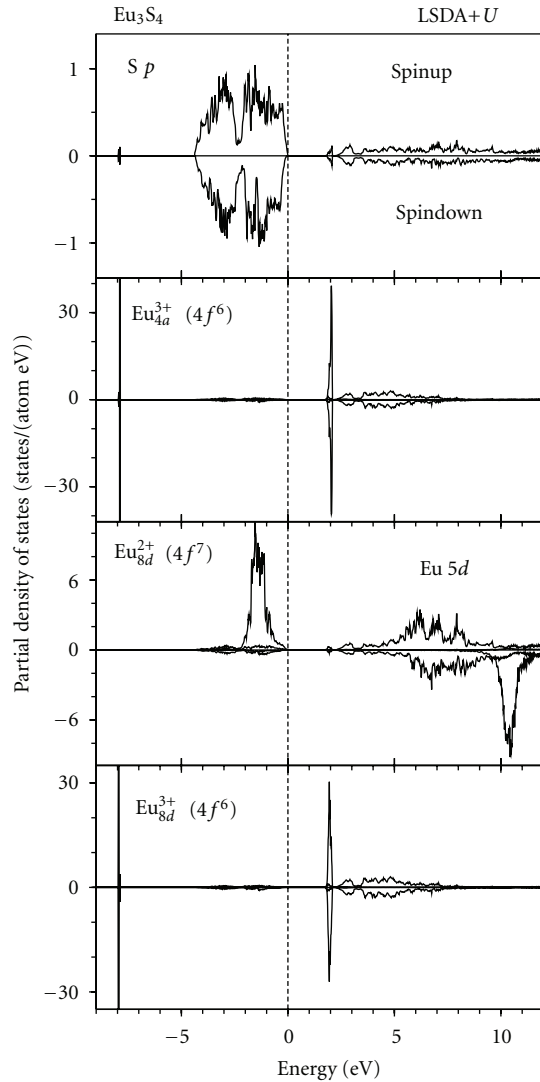


FIGURE 86: The partial density of states (DOS) (in states/(atom eV)) of Eu_3S_4 in $I42d$ phase calculated in LSDA+U approximation [455].

photoemission. By identifying the final-state hole the initial state can be inferred.

The partial $4f$ DOS of the occupied part of the Sm_3S_4 calculated in the LSDA+ U approximations is compared with XPS measurements [314] in the top panel of Figure 89 [455]. The calculated $4f$ DOS has been broadened to account for lifetime effects and for experimental resolution. The S $3p$ states essentially do not contribute to the XPS spectra because of the low ionization cross-section compared with that of the Sm $4f$ states [385]. Hence, the measurements only indicate the f excitation energies relative to the Fermi level.

The theoretical $4f$ DOS calculated using one-electron approximations cannot, of course, fully account for the multiplet splitting. Therefore, we present in the two other panels of Figure 89 the $4f$ DOSs taking into account the multiplet structure of Sm^{2+} and Sm^{3+} ions. We used the final state multiplet structure presented in [370]. The multiplet

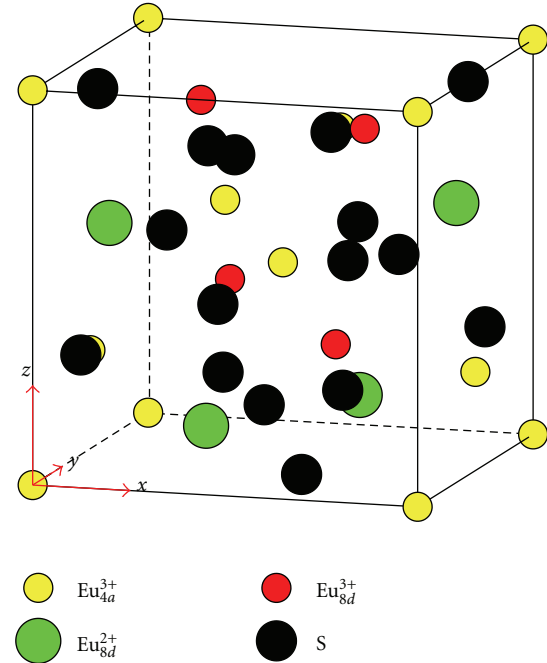


FIGURE 87: Crystal structure of a low temperature phase of Eu_3S_4 . Small yellow balls: Eu^{3+} ions in the $4a$ crystallographic positions. Large green balls: Eu^{2+} ions in the $8d$ positions, small red balls: Eu^{3+} ions in the $8d$ positions. Large black balls: S ions [455].

structure for Sm^{2+} ion ($4f^5$ final state) consists of 3 terms 6H , 6F , and 6P . The Sm^{3+} ion ($4f^4$ final state) has the multiplets 5I , 5F , 5G , and 5D . The relative intensities for the multiplet peaks were obtained on the basis of Cox calculations [387] using the fractional parentage method [388]. In this method Hund's rule ground state is assumed for $n4f$ electrons, and then the coefficients of fractional parentage (Racah's) for the $n-1$ configurations are calculated. The intensities for the various configurations (multiplets) are just the square of the coefficients of fractional parentage. In Figure 89 the XPS spectrum is modeled by a weighted sum of $4f$ DOS curves. We aligned the centroid of the calculated occupied $4f$ DOS peak with the centroid of the atomic final state multiplet and summed up the spectra scaling them according to the relative intensities of the multiplets. The agreement between LSDA+ U theory and the XPS measurements is reasonably good. The disagreement in the intensity of some peaks might be explained by the influence of transition matrix elements which have not been included in the theoretical calculations. It is clear that the structures between -4.5 and -16 eV binding energy should be assigned to the final-state multiplet structure derived from five fully occupied $\text{Sm}^{3+}4f$ spin-up bands and the structures between 0.0 and -4.5 eV are associated with the final-state multiplet structure of the divalent $\text{Sm}^{2+}4f$ DOS. The LSDA calculations place $4f$ energy bands in close vicinity of the Fermi level for both the Sm^{2+} and Sm^{3+} ions and hence are not able to produce the structures of the XPS spectrum in the -4.5 to -16 eV energy interval.

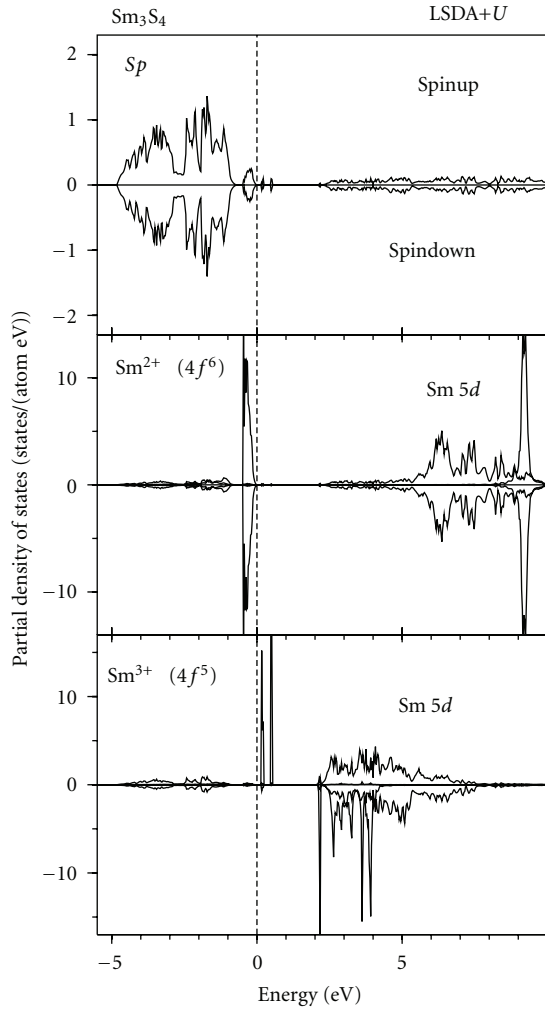


FIGURE 88: The partial density of states (DOS) (in states/(atom eV)) of Sm_3S_4 calculated in LSDA+ U approximation [455].

From the good agreement between theory and XPS measurements, we may conclude that the LSDA+ U calculations give an accurate position for the occupied $4f$ bands. The principal question is the energy position of the empty $4f$ states, which is usually answered by optical or BIS measurements. In Figure 90 we show the experimental [439] real refractive index $n(\omega)$, extinction coefficient $k(\omega)$ and optical reflectivity $R(\omega)$ spectra of Sm_3S_4 , as well as the spectra calculated with LSDA, LSDA+ U and with the $4f$ electrons in the core. This picture clearly demonstrates that the best description is unambiguously given by the LSDA+ U approach. As was mentioned previously, the LSDA theory produces a metallic solution and, therefore, gives the wrong asymptotic behavior for the optical reflectivity and the extinction coefficient $k(\omega)$ as $\omega \rightarrow 0$. The most prominent discrepancy in the LSDA spectra is the extra peaks between 0 and 1.5 eV in the extinction coefficient $k(\omega)$ caused by interband transitions involving the occupied $4f_{5/2}$ and unoccupied $4f_{7/2}$ hybridized states. In the LSDA+ U approach, the empty $4f_{7/2}$ state energies are shifted upward due to the on-site Coulomb interaction U_{eff} . As a result,

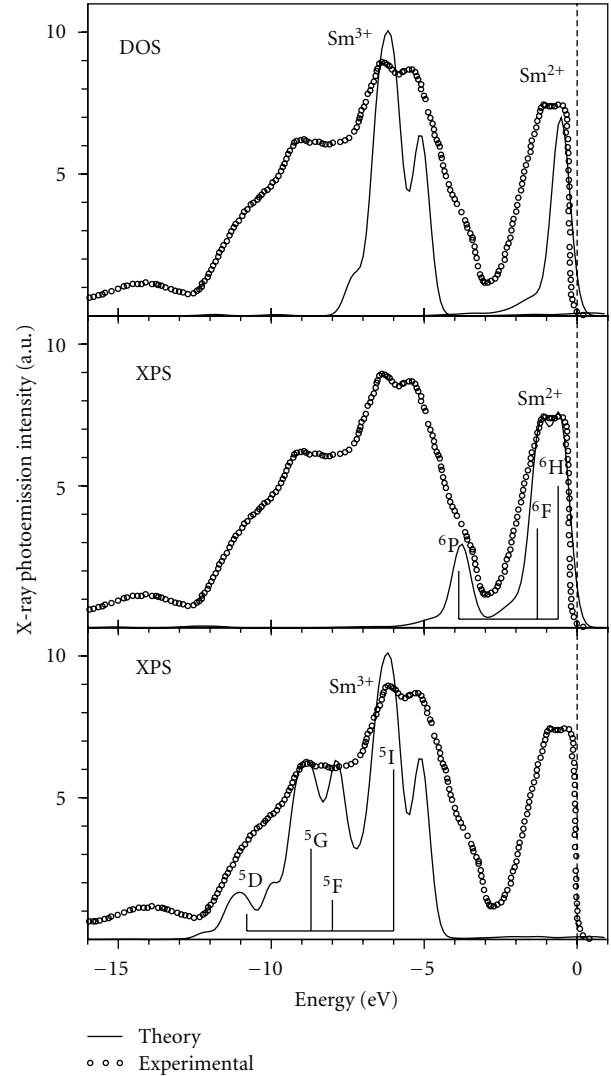


FIGURE 89: Comparison of the calculated $4f$ DOS of Sm_3S_4 in the LSDA+ U approximations with the experimental XPS spectrum from [5] taking into account the multiplet structure of the $4f^5$ final state (see explanations in the text) [455].

the transitions involving the unoccupied $4f_{7/2}$ states do not take place at small photon energies, and the erroneous peak structures around 0 to 1.5 eV disappear from the optical spectra.

The calculations in which the $4f$ electrons are treated as quasicore are able to reproduce correct asymptotic behavior for the optical reflectivity and the refractive index $n(\omega)$ as $\omega \rightarrow 0$ similar to the LSDA+ U calculations, but they fail in producing a peak at around 0.6 eV in the refractive index $n(\omega)$ and the extinction coefficient $k(\omega)$. This peak is mostly determined by the interband transitions between occupied $4f_{5/2}$ states hybridized with $S p$ states and two empty $4f_{\text{spin-up}}$ bands situated in close vicinity of the Fermi level.

9.6. Comparison between Sm_3S_4 , and Eu_3S_4 . Samarium chalcogenides Sm_3X_4 ($X = \text{S}, \text{Se}, \text{Te}$) do not exhibit any

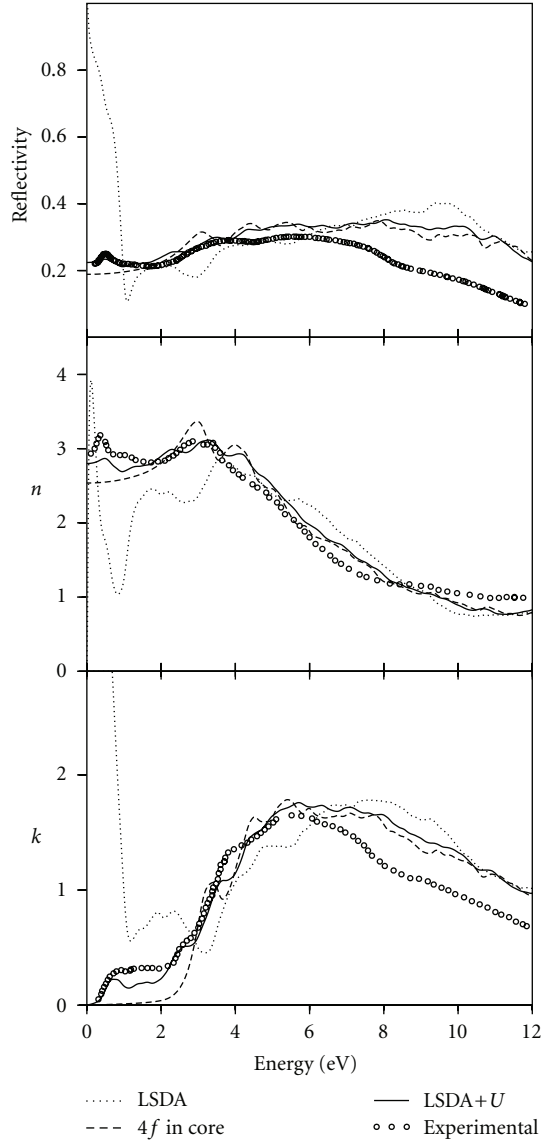


FIGURE 90: Calculated [455] optical reflectivity R , real refractive index n , and extinction coefficient k of Sm_3S_4 treating $4f$ states as (1) fully localized ($4f$ in core) (dashed line), (2) itinerant (dotted line), and (3) partly localized (LSDA+ U approximation) (solid line) compared with experimental data (open circles) [439].

evidence of charge-ordering at low temperature and show a charge-glass state due to the random distribution of Sm^{2+} and Sm^{3+} ions [445]. This glass transition of Sm_3X_4 is in strong contrast with the charge ordering of the isomorphous compound Eu_3S_4 . In the latter compound, a first-order charge-ordering transition occurs at about 188.5 K, below which the distribution of di- and trivalent cations is no longer random [450]. A microscopic description of the charge-ordering and the charge-glass states in rare-earth chalcogenides is completely lacking. Any detailed model calculations of these phenomena have to be based on the knowledge of their electronic and magnetic structures. In this section we compare Sm_3S_4 and Eu_3S_4 compounds in

TABLE 11: The calculated spin M_s , orbital M_l , and total M_t magnetic moments at the rare-earth site (in μ_B) of Sm_3S_4 and Eu_3S_4 (low-temperature charge-ordered $I\bar{4}2d$ phase) [455].

Ion	moment	Sm_3S_4	Eu_3S_4
R^{3+}	M_s	4.89	0.
	M_l	-4.39	0.
	M_t	0.50	0.
R^{2+}	M_s	0.	6.76
	M_l	0.	0.00
	M_t	0.	6.82

several aspects, namely, their band and magnetic structures, as well as the hybridization effects between the $4f$ and $3p$ electrons.

One should mention that the magnetism of the Eu^{2+} (configuration $4f^7$) and Eu^{3+} (configuration $4f^6$) ions is the reverse of that of the Sm^{2+} ($4f^6$) and Sm^{3+} ($4f^5$) ions; that is, the trivalent Eu ion has the same magnetic ground state of $J = 0$ as that of the divalent Sm ion. The magnetic ground state of the Eu^{2+} ions is $J = 7/2$, no orbital moment.

Table 11 lists the calculated spin M_s , orbital M_l , and total M_t magnetic moments (in μ_B) of Sm_3S_4 and Eu_3S_4 . The spin and orbital moments are almost equal in Sm_3S_4 and have opposite signs which gives a very small total magnetic moment of $0.5 \mu_B$ per ion. Due to its f^7 atomic configuration, Eu^{2+} has no orbital moment.

Figure 91 shows the expanded view of the band structures and total DOS's of Sm_3S_4 and Eu_3S_4 compounds. Both the compounds are semiconductors with an energy gap of 0.25 and 1.70 eV, respectively. The theoretically calculated energy gaps are in complete agreement with the optical measurements [439, 440]. The energy gap in Eu_3S_4 is formed by the $4f$ states at the $8d$ sublattice positioned between occupied Eu_{8d}^{2+} states which are strongly hybridized with $3p$ states and empty Eu_{8d}^{3+} states which cut the very bottom of Eu $5d$ band. The quite small energy gap in Sm_4S_3 also separates the $4f$ bands which belong to divalent and trivalent Sm ions, respectively. In both cases the gap depends on the position of the f states, and the choice of U can strongly affect its value; however, we should mention that in our calculations we did not consider the value of U as an adjustable parameter but calculated it using the constrained LSDA approach [34].

Goto and Lüthi [7] argue that the difference between the charge glass state in Sm_3X_4 ($X = \text{S}, \text{Se}, \text{or Te}$) and the charge ordering in Eu_3S_4 could be the different hybridization effect of the $4f$ electrons with $3p$ electrons of the chalcogenides.

From the comparison of band structures presented in Figure 91, we can conclude that the $4f$ - $3p$ hybridization effect is really quite different in Eu_3S_4 and Sm_3S_4 compounds. The $3p$ electrons hybridize with magnetic $\text{Eu}^{2+}4f$ electrons in Eu_3S_4 and nonmagnetic $\text{Sm}^{2+}4f$ electrons in Sm_3S_4 . Due to Zeeman splitting the magnetic $\text{Eu}^{2+}4f$ states occupy quite a large energy interval inside of the $3p$ band, strongly hybridized with $3p$ states. Nonmagnetic $\text{Sm}^{2+}4f$ states in Sm_3S_4 cross the very top of $3p$ band; therefore, the

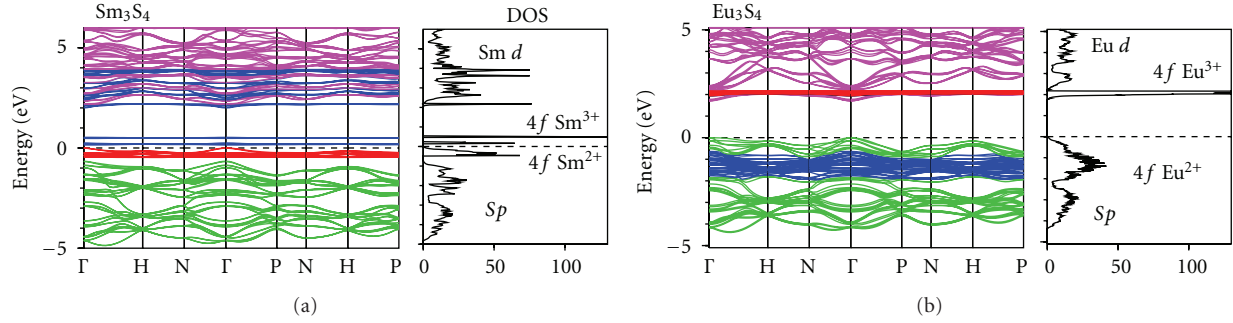


FIGURE 91: The energy band structure and total DOS (in states/(cell eV)) calculated for Sm_3S_4 and Eu_3S_4 calculated in the LSDA+ U approximation [455].

$4f-3p$ hybridization is expected to be smaller in comparison with the Eu_3S_4 compound.

On the other hand, in Sm_3Se_4 and Sm_3Te_4 , nonmagnetic $\text{Sm}^{2+}4f$ states are shifted downward from the top of chalcogen $3p$ band. Taking into account that the extension of chalcogen $3p$ valence wave function increases going from the top to the bottom of the band and also going from S to Te, one would expect that the $4f-3p$ hybridization is increased going from Sm_3S_4 to Sm_3Te_4 through the series. It manifests itself in a width of the $\text{Sm}^{2+}4f$ states in these compounds. In Sm_3S_4 $\text{Sm}^{2+}4f$ valence states are narrow with a high density of states. There is a hybridization energy gap of about 0.2 eV between $\text{Sm}^{2+}4f$ and S $3p$ states. In the case of Sm_3Se_4 and Sm_3Te_4 the $\text{Sm}^{2+}4f$ DOSs can hardly be distinguished from chalcogen $3p$ DOSs and the $4f-p$ hybridization in these compounds (not shown) is rather similar to the corresponding hybridization in Eu_3S_4 than in Sm_3S_4 . Nevertheless, Sm_3Se_4 as well as Sm_3Te_4 show no sign of a phase transition to charge ordering at low temperatures. In lowering the temperature the fluctuations of their $4f$ electrons freeze gradually into a charge glass state similar to Sm_3S_4 . Therefore, although the $4f-3p$ hybridization effect is quite different in Eu_3S_4 and Sm_3S_4 compounds, it is probably not a main reason for the difference in their ground states.

Seeking the answer to the question why Sm_3X_4 favors the charge glass state and does not exhibit charge ordering like Eu_3S_4 , it was performed two numerical experiments. In the first one, by reducing the number of the symmetry operations all the atoms in the unit cell were made to be nonequivalent and then interchange the places of di- and trivalent Sm and Eu ions. It was found that the interchanging of Sm ions with different valency in Sm_3S_4 costs smaller total energy than in the case of interchanging Eu ions in Eu_3S_4 . So Sm_3S_4 probably has a larger tendency to charge disorder in comparison with Eu_3S_4 .

In the second experiment we tried to check whether the local easy magnetization axes for two nonequivalent pairs of magnetic Sm^{3+} ions in Sm_3S_4 have the same orientation by calculating the total energy as a function of their magnetic moment direction. For simplicity $4f$ electrons of nonmagnetic Sm^{2+} ion were placed in the core. In order to minimize the contribution of the exchange interaction into the total energy Sm^{3+} ions in each pair antiferromagnetically was

arranged, thus making the exchange energy independent of the relative orientation of the magnetization of the pairs. It was found that the magnetic Sm^{3+} ions have different easy magnetization axes defined by the polar angles $\theta = 40^\circ$, $\phi = 90^\circ$ and $\theta = 40^\circ$, $\phi = 0^\circ$, for the first and the second Sm^{3+} pairs, respectively (θ and ϕ are defined with respect to the $[001]$ direction). In order to verify these results we calculated the dependence of the total energy on the magnetization direction for each Sm^{3+} pair independently. This was achieved by putting the spin-orbit interaction strength at another pair of Sm^{3+} ions to zero, which effectively decouples their magnetic moments from the lattice. The total energy minima were again found for different magnetization directions, close to those mentioned above. It should be pointed out that strong magnetocrystalline anisotropy in Sm_3S_4 prevents collinear magnetic order and may favor the charge glass state in this compound.

The chemical formula involving the information on the valence in Eu_3S_4 is given as $[\text{Eu}^{3+}]_{4a}[\text{Eu}^{2+}\text{Eu}^{3+}]_{8d}(\text{S}^{2-})_4$. There is only one type of magnetic Eu^{2+} ion in the unit cell of Eu_3S_4 and two types of nonmagnetic Eu^{3+} ions. Eu^{2+} has no orbital magnetic moment (Table 11), and Eu_3S_4 possesses a first-order nonmagnetic phase transition near $T_{\text{co}} = 188.5$ K [447, 450], as well as phase transition to a ferromagnetic state below $T_c = 3.8$ K [449]. However, a large difference between T_{co} and T_c indicates that the magnetic interactions probably play a minor role for the charge ordering in Eu_3S_4 .

The difference in the magnetic structures and the $4f-3p$ hybridization effects in Eu_3S_4 and Sm_3S_4 play an important role in determining their ground states properties. However, it is still not clear why Sm_3X_4 favors the charge glass state and does not exhibit charge ordering like Eu_3S_4 . This question needs additional theoretical investigation using more sophisticated many-body approaches.

9.6.1. Summary. For Sm_4Bi_3 , the LSDA+ U band structure calculations provide a two-band model of the electronic structure: (1) a wide, nearly fully occupied Bi p valence band and (2) a very narrow, marginally occupied Sm $4f$ band, weakly hybridized with the Bi p band in a small \mathbf{k} space region near the Γ point of the BZ. The mobility of heavy $4f$ electrons is assumed to be negligible in comparison with the mobility of pnictide p electrons. So the transport properties

of Sm_4Bi_3 are mostly determined by the number of pnictide p holes. Pressure, doping, and so forth, may slightly change the relative position of these two bands and hence strongly affect the low carrier density and the transport properties. But the $4f$ shell of the Sm^{3+} ions is little influenced as long as the charge order is maintained.

The most prominent difference in the electronic structure of the Sm_4Bi_3 compound in comparison with the other two samarium pnictides is in the position and occupation of the 6th hole $4f$ spin-up energy level. The pinning of a partly occupied 6th f spin-up level is different in these compounds. If one moves from Sm_4Bi_3 to Sm_4As_3 , the peak position of the 6th hole $4f$ spin-up level shifts toward higher energy from the Fermi level. The partial occupation of the 6th hole f level is thus decreasing going from Sm_4Bi_3 to Sm_4As_3 along with a decrease of the lattice constant.

As classical mixed-valence compounds Eu_3S_4 and Sm_3X_4 ($X = \text{S}, \text{Se}, \text{or Te}$) constitute very interesting systems exhibiting unusual behavior due to strong electronic correlations. A detailed comparison between Eu_3S_4 and Sm_3S_4 shows that these two compounds have quite different electronic and magnetic structures as well as different hybridization character of the $4f$ electrons with $3p$ electrons.

It was found that the $4f-3p$ hybridization in Sm_3S_4 is expected to be smaller in comparison with the Eu_3S_4 compound. On the other hand, the $4f-3p$ hybridization in Sm_3Se_4 and Sm_3Te_4 is closer rather to the corresponding hybridization in Eu_3S_4 than in Sm_3S_4 . Nevertheless, Sm_3Se_4 as well as Sm_3Te_4 shows no sign of a phase transition to a charge-ordered state at low temperatures. Therefore, the difference in the hybridization in Eu_3S_4 and Sm_3S_4 is probably not a main reason for the difference in their ground states.

Eu_3S_4 and Sm_3S_4 compounds have quite different magnetic structures. Eu^{2+} has no orbital moment. The orbital moment of magnetic Sm^{3+} ions in Sm_3S_4 is quite large and has the opposite direction to the spin moment. It was found that easy magnetization axes are different for two nonequivalent Sm^{3+} ions, and the strong local magnetocrystalline anisotropy in Sm_3S_4 might prevent the appearance of the collinear magnetic order in the compound.

In view of the distribution of valence ions, the low-temperature phase of Eu_3S_4 is similar to the room-temperature phase of magnetite. Di- and trivalent ions are randomly distributed in the B and $8d$ sublattices in Fe_3O_4 and Eu_3S_4 , respectively. However, Fe_3O_4 undergoes at $T_V = 120$ K a first-order phase transition (Verwey transition) [9]. This phase transition is accompanied by long-range charge ordering of Fe^{3+} and Fe^{2+} ions on $B1$ and $B2$ sites of the B sublattice. There are some indications that similar transitions with charge ordering of Eu^{2+} and Eu^{3+} on the $8d$ sublattice may occur also in Eu_3S_4 at low temperatures [450]. However, there are some serious technical difficulties in determining the crystal structure of Eu_3S_4 below $T = 3.8$ K [450].

10. YbMCu_4 ($M = \text{Cu}, \text{Ag}, \text{Au}, \text{Pd}, \text{and In}$)

The YbMCu_4 ($M = \text{Cu}, \text{Ag}, \text{Au}, \text{Pd}, \text{and In}$) compounds crystallize in the cubic AuBe_5 -type ($C15b$) structure and preserve the Yb ion in its trivalent state with total angular

momentum $J = 7/2$ [460, 461]. These systems have been investigated extensively because of their rich variety of phenomena at low temperature. In particular, YbAgCu_4 is known to show a typical dense Kondo behaviour [461, 462], in which localized moments of Yb^{3+} ($4f^{13}$) at high temperatures are gradually screened through the hybridization with the conduction electrons, resulting in the enhanced Pauli paramagnetic state down to very low temperatures. A moderately large electronic specific heat coefficient has also been reported as $\gamma = 245$ mJ/mol K^2 [463]. Recently prepared by a high-pressure technique YbCu_5 phase with $C15b$ structure also shows Kondo-lattice formation [464] with an even larger electronic specific heat coefficient $\gamma = 550$ mJ/mol K^2 . Furthermore, the temperature dependence of magnetic susceptibility [461] and magnetic part of specific heat [462] in these systems are well described by the Bethe-ansatz solution of the Coqulin-Schrieffer model [465]. No magnetic ordering was found in both compounds down to 2.0 K [464, 466]. On the other hand, the Kondo effect is not dominant in YbAuCu_4 and YbPdCu_4 , and long-range magnetic ordering is observed at 0.6 and 0.8 K, respectively [461]. Finally, YbInCu_4 has attracted much attention recently because it is the only known stoichiometric compound that undergoes a first-order isostructural valence transition at ambient pressure [460, 467–469]. At high temperature Yb appears to be essentially trivalent, displaying Curie-Weiss susceptibility with a paramagnetic moment near free ion value of $4.5 \mu_B$. At the first-order valence transition at $T_V = 42$ K, the Yb valence is reduced to approximately 2.8 (as estimated by X-ray-absorption and lattice constant measurements [467, 470]), with a consequent increase in lattice volume of 0.5% and a reduction in magnetic susceptibility and spin-disorder scattering [468]. High-resolution neutron powder-diffraction studies confirm that the first-order transition is an isostructural one, with YbInCu_4 retaining its $C15b$ structure at all temperatures [471, 472]. Such an “isomorphic” valence transition is fundamentally similar to the $\alpha \rightarrow \gamma$ transition in cerium [473], which rises the question whether both transitions have a common origin.

The optical properties of the YbMCu_4 ($M = \text{Ag}, \text{Au}, \text{Pd}, \text{and In}$) are investigated in [474]. In the case of YbInCu_4 relevant differences in the optical spectrum were observed between 0.1 and 2 eV, above and below the transition temperature [474].

10.1. YbInCu_4 . The LSDA fully relativistic spin-polarized energy band structure and partial density of states (DOSs) of LuInCu_4 are shown in Figure 92 [475]. The calculated energy band structure shows that LuInCu_4 is a compensated semimetal with small carrier density which agrees well with electrical resistivity and Hall effect measurements [476]. The Fermi surface consists of two sheets. The 32nd band has closed hole sheets h_{32} around W symmetry points, and the 33rd band has closed electron sheets e_{33} around X points. The bands in the lowest region of the occupied part of the band structure of LuInCu_4 between -9.5 and -7 eV have mostly In s character with some amount of Cu and Lu sp characters mixed in. The highest region can be characterized as a bonding combination of Cu d and In p states. Cu d bands

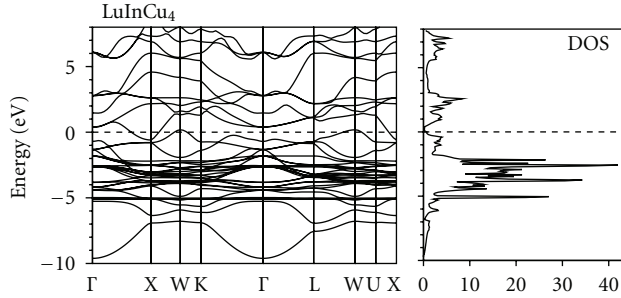


FIGURE 92: LSDA self-consistent fully relativistic, spin-polarized energy band structure and total DOS (in states/(unit cell eV)) of LuInCu₄ [475].

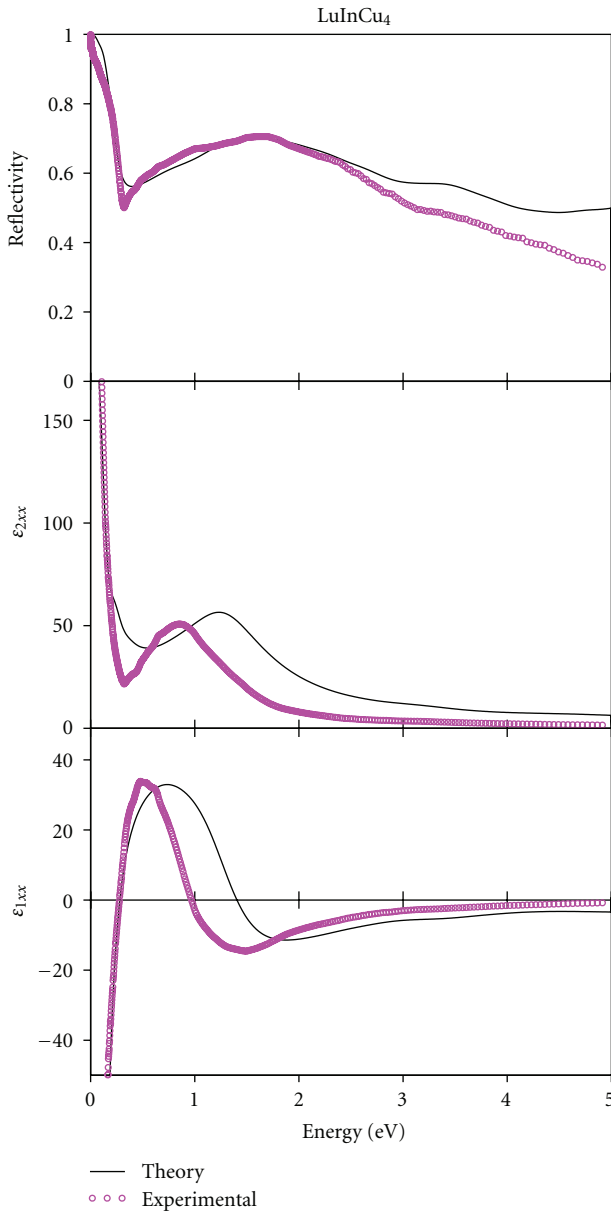


FIGURE 93: Comparison between the experimental (dots) and calculated optical reflectivity $R(\omega)$, real part $\epsilon_1(\omega)$ and imaginary part $\epsilon_2(\omega)$ of the dielectric function of LuInCu₄ calculated within LSDA (solid line) [475].

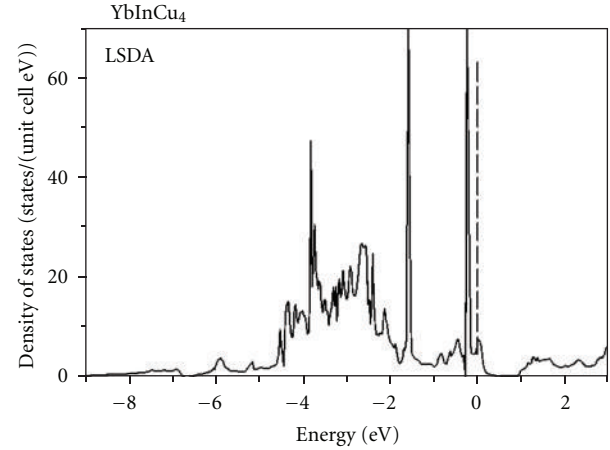


FIGURE 94: LSDA total DOS of YbInCu₄ in states/(unit cell eV) [475].

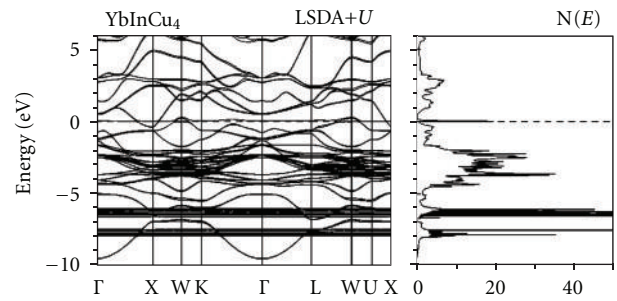


FIGURE 95: LSDA+ U self-consistent fully relativistic, spin-polarized energy band structure and total DOS (in states/(unit cell eV)) of YbInCu₄ ($U_{\text{eff}} = 6$ eV) [475].

are completely occupied and situated below the Fermi level at -4 to -1.5 eV. Lu d states are almost empty and situated above the Fermi level.

In Figure 93 we compare the calculated complex dielectric function $\epsilon(\omega)$ and the reflectivity $R(\omega)$ with experiment [475]. As can be seen, theory in LSDA and experiment agree very well. Above 3 eV theory gives a slightly larger reflectivity in comparison with experimental measurements. One of the possible reasons for this is a nonideal sample surface, its roughness could reduce the optical reflectivity above 3 eV.

The LSDA total DOS of YbInCu₄ is shown in Figure 94 [475]. The energy band structure of YbInCu₄ is very similar to the LuInCu₄ one. The bands in the lowest region have mostly In s character with some amount of Cu and Yb s characters mixed in. Cu d bands are completely occupied and situated below the Fermi level between -4 and -1.5 eV. The large narrow peak close to the Fermi energy is formed by Yb $4f$ states. Unoccupied $5d$ bands of Yb are separated from the $4f$ states by a quasigap, a characteristic and important feature of the YbInCu₄ compound. The position of the LSDA $4f$ states close to the Fermi energy is, on the other hand, in contradiction with the findings of XPS and BIS experiments [477].

The LSDA + U energy bands and partial density of states of YbInCu₄ for $U_{\text{eff}} = 6$ eV are shown in Figures 95 and 96

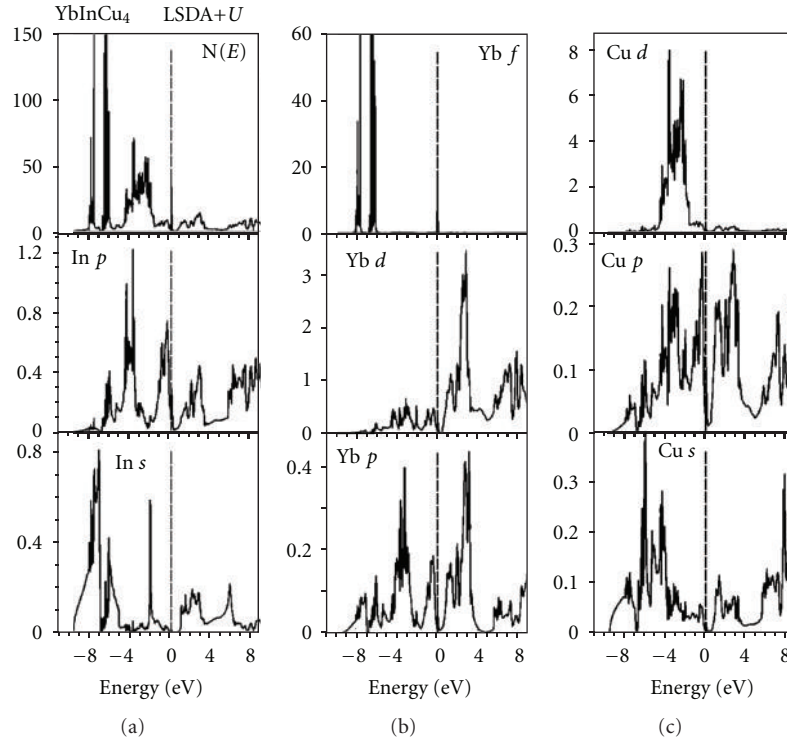


FIGURE 96: LSDA+ U total $N(E)$ (in states/(unit cell eV)) and partial DOS (in states/(atom eV)) of YbInCu_4 [475].

[475]. For the trivalent Yb ion, thirteen $4f$ electron bands are well below the Fermi level in the energy range between -6 and -8 eV (Figure 96). They are split due to spin-orbit coupling $\Delta\epsilon_{\text{so}} = 1.2$ eV and separated from a $4f$ hole state by the correlation energy U_{eff} . The unoccupied $4f^{14}$ level, which through the Coulomb interaction is initially placed above E_F , is pulled on E_F during the process of self-consistent relaxation. A fundamental aspect of this observation is that we find the pinning of the $4f^{14}$ state at E_F to be a genetic property of YbInCu_4 compound: it happens irrespective of the precise value of U_{eff} . The insensitiveness of this feature of the U_{eff} value, furthermore, can be understood as reflecting the large bandwidth of the In p band with a low DOS and existing of a quasigap just above the Fermi level. The $4f$ hole level should become partially occupied to achieve the required number of electrons within the Fermi sphere. Due to a small phase space for hybridization and small Yb $4f$ -In p orbital overlap, the DOS peak of the hole band is as narrow as 0.02 eV (Figure 97). It is now clear why the usual Kondo lattice scenario is inappropriate for this compound. For a Kondo resonance to develop both the occupied and empty $4f$ states must be sufficiently far away from the Fermi level. Quite opposite to this situation the (almost) empty level is pinned to the Fermi energy. Since the upper $4f$ level is only partly occupied, YbInCu_4 is calculated to be an intermediate valent compound in agreement with the experimental data [460, 467–469].

After the consideration of the above band structure properties we turn to the optical spectra. In Figure 98 we show the LSDA and LSDA+ U calculated and experimental

optical spectra of YbInCu_4 [475]. The best agreement between theory and the experiment was found to be when we used the LSDA+ U approximation. The most prominent discrepancy in the LSDA spectra is the shifting of the prominent peak in the optical conductivity and imaginary part of dielectric function $\epsilon_2(\omega)$ towards larger photon energies. This peak situated at ~ 1.2 eV in the experimentally measured optical spectra is mostly due to In $p \rightarrow$ Yb d interband transitions. These transitions take part between occupied and empty energy bands along L-W, X-W, and Γ -K symmetry directions and also in some inner parts of the Brillouin zone. Although $4f$ states do not participate in the optical interband transitions in the energy interval from 0 to 5 eV (due to a large binding energy of occupied $4f$ states and extremal narrowness of partly occupied hole $4f^{14}$ level), they affect the optical spectra indirectly through changing of the ionicity of the Yb ion. LSDA produces the energy band structure of YbInCu_4 with fully occupied $4f$ bands for divalent Yb ions (Figure 94). The Coulomb repulsion U_{eff} strongly influences the electronic structure of YbInCu_4 . Thirteen $4f$ occupied energy bands are well below the Fermi energy, and a hole $4f^{14}$ level is partly occupied and pinned at the Fermi level. Therefore, the ionicity of the Yb ion in the LSDA+ U calculations is close to $3+$. On the other hand, the $4f$ electron density is closer to the nucleus than that of the $4s$, p , and d electrons. Hence, the increasing of the Yb ionicity (decreasing the number of $4f$ electrons in the close vicinity of the nuclear) in the LSDA+ U calculations leads to narrowing of Yb d energy bands due to decreasing of nucleus screening. Therefore, empty Yb d states in the LSDA+ U

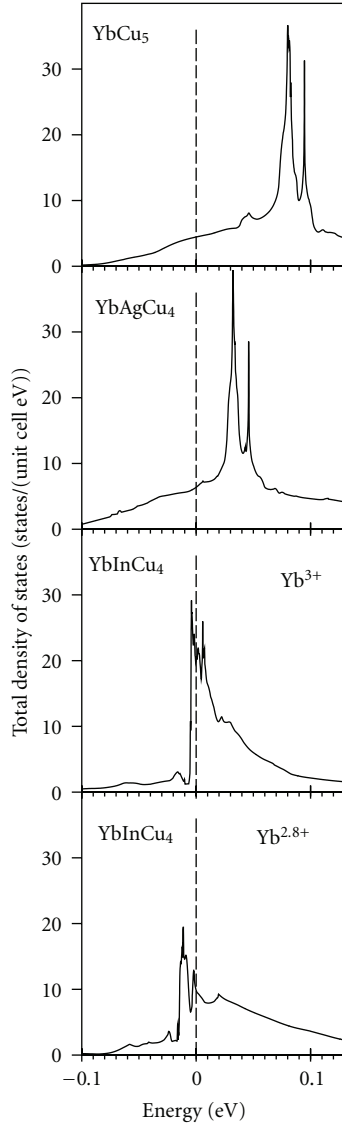


FIGURE 97: Expanded view of the total DOS $N(E)$ of YbCu_5 , YbAgCu_4 , and YbInCu_4 (for Yb^{3+} and $\text{Yb}^{2.8+}$ configurations) calculated in the LSDA+ U approximation [475].

calculations shift downwards decreasing the In $p \rightarrow$ Yb d interband energies and the prominent peak shifts to smaller energies in remarkable agreement with the experimental measurements (Figure 98).

The measurements of the optical spectra of YbInCu_4 in [474] show that its optical response abruptly changes at the phase transition temperature (Figure 99), whereas no distortion of the crystal structure occurs. The major effect of such a phenomenon is also due to the changing of the Yb ionicity. As estimated by X-ray absorption and lattice constant measurements [467, 470] at the first-order valence transition at $T_v = 42$ K, the Yb valence is reduced to approximately 2.8. In order to investigate the influence of the valence reduction of Yb ion, we performed the self-consistent LSDA+ U calculations of the energy band structure and optical spectra of YbInCu_4 using starting configuration of unoc-

cupied $4f^{14}$ level equal to 0.9 and 0.8. Such a virtual crystal approximation [478] leads to the energy band structure with wider Yb d energy bands due to increasing of the nuclear screening by $4f$ electrons. The optical spectra, therefore, are shifted towards higher photon energies with good agreement with the experimental measurements (Figure 99).

The LSDA+ U calculations show that the decreasing of Yb ionicity is accompanied by essential decreasing of the density of states at the Fermi level, which is equal to 17.0, 11.5, and 10.8 states/(unit cell eV) for Yb^{3+} , $\text{Yb}^{2.9+}$, and $\text{Yb}^{2.8+}$, respectively. This aspect reflects the fact that the ground state of YbInCu_4 has the Yb valence less than 3+. We should mention here that for the Yb^{3+} configuration we mean the starting configuration with zero occupation of $4f^{14}$ level. In the process of self-consistent relaxation initially empty hole $4f^{14}$ level becomes partly occupied due to pinning at the Fermi level with occupation number equal to 0.14 (valence $\nu = 2.86$). Using the $\text{Yb}^{2.9+}$ configuration as initial configuration we achieved after the self-consistent calculations an occupation number equal to 0.24. These results are in a good agreement with X-ray absorption measurements at the Yb L_{III} edge which gave $\nu(L_{\text{III}}) = 2.9$ and 2.8 above and below T_v , respectively [467].

The total DOS at the Fermi level, resulting essentially from the $4f$ hole states, yields for $U_{\text{eff}} = 6$ eV band structure contribution to the Sommerfeld constant of $\gamma = \pi^2 k_B^2 N_A N(\epsilon_F)/3 = 40, 27,$ and $25.4 \text{ mJ mol}^{-1} \text{ K}^{-2}$ for Yb^{3+} , $\text{Yb}^{2.9+}$, and $\text{Yb}^{2.8+}$, respectively in good agreement with specific heat measurements [467]. These measurements gave $\gamma = 22.3 \text{ mJ mol}^{-1} \text{ K}^{-2}$ at low temperatures below the phase transition. The specific heat is also abruptly increased at the phase transition temperature $T_v = 42$ K [467].

10.2. YbMCu_4 ($M = \text{Cu}, \text{Ag}, \text{Au},$ and Pd). As an example, we show the LSDA+ U energy bands of YbAgCu_4 and YbCu_5 for $U_{\text{eff}} = 6$ eV in Figures 100 and 101 [475]. The energy band structure of YbAgCu_4 as well as YbCu_5 compound is similar to YbInCu_4 one (Figure 95). For the trivalent Yb ion, thirteen $4f$ electron bands are well below the Fermi level in the energy range between -4.5 and -7 eV slightly shifted upwards in comparison with YbInCu_4 . They are split due to spin-orbit coupling $\Delta\epsilon_{\text{so}} = 1.5$ eV and separated from the $4f$ hole state by the correlation energy U_{eff} . The position of occupied $4f$ bands in YbAgCu_4 is in good agreement with X-ray photoemission measurements. According to the XPS measurements the multiplet structure of the $4f^{12}$ final states on Yb^{3+} sites is situated between -5 and -12 eV [477]. The most significant difference between the electronic structures of YbAgCu_4 and YbInCu_4 compounds is in the position of the hole $4f^{14}$ level. In the case of YbInCu_4 upper $4f$ level is partly occupied and pinned at the Fermi level due to the existence of a quasigap in the density of states just above the Fermi level (Figure 95). In the YbAgCu_4 occupied $4f$ states shifted upward, a similar quasigap situated at 1.5 eV above the Fermi energy (Figure 100); therefore, a hole level in YbAgCu_4 is completely empty and situated sufficiently far from the Fermi level (Figure 97). Such a situation is appropriate for the developing of the Kondo lattice scenario

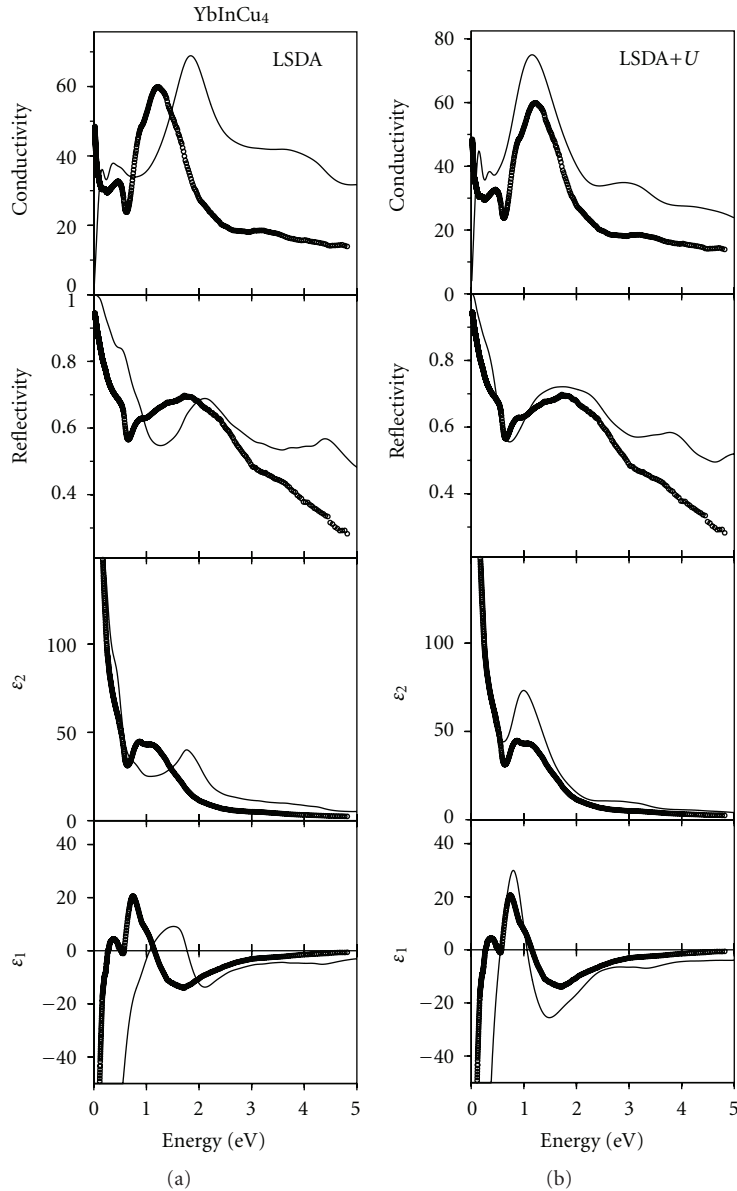


FIGURE 98: Comparison between the experimental (dots) optical conductivity $\sigma(\omega)$ (in 10^{14} s^{-1}), reflectivity R , real part $\epsilon_1(\omega)$ and imaginary part $\epsilon_2(\omega)$ of the dielectric function of YbInCu_4 calculated within LSDA and LSDA+ U approximations (solid line) [475].

in this compound. The hole level has a similar position in YbCu_5 (Figure 97), YbPdCu_4 and YbAuCu_4 compounds. YbCu_5 is really a typical dense Kondo system with an electronic specific heat coefficient $\Gamma = 550 \text{ mJ/mol K}^2$ [463], although, the Kondo effect is not dominant in YbAuCu_4 , and YbPdCu_4 , where a long-range magnetic ordering is observed at 0.6 and 0.8 K, respectively [461].

In Figures 102, 103 and 104 we show the LSDA+ U calculated and experimentally measured optical spectra of YbAgCu_4 , YbPdCu_4 and YbAuCu_4 [475]. The agreement between the theory and the experiment is very good.

10.2.1. Summary. The optical spectra of YbMCu_4 ($M = \text{Cu, Ag, Au, Pd, and In}$) are very sensitive tools for drawing

conclusions about the appropriate model description. On account of the calculated optical spectra we conclude that YbInCu_4 optical spectra are best described using the LSDA+ U approach. It was found that the main peak in the optical conductivity $\sigma(\omega)$ of YbMCu_4 at 1.2 eV results as $\text{In } p \rightarrow \text{Yb } d$ interband transitions between occupied and empty energy bands along L-W, X-W, and Γ -K symmetry directions and also in some inner parts of the Brillouin zone.

The measurements of the optical spectra of YbInCu_4 show that its optical spectra between 0.1 and 2 eV significantly change at phase transition temperature. The theoretical calculations show that the major effect is due to the changing of the Yb ionicity. At the first-order valence

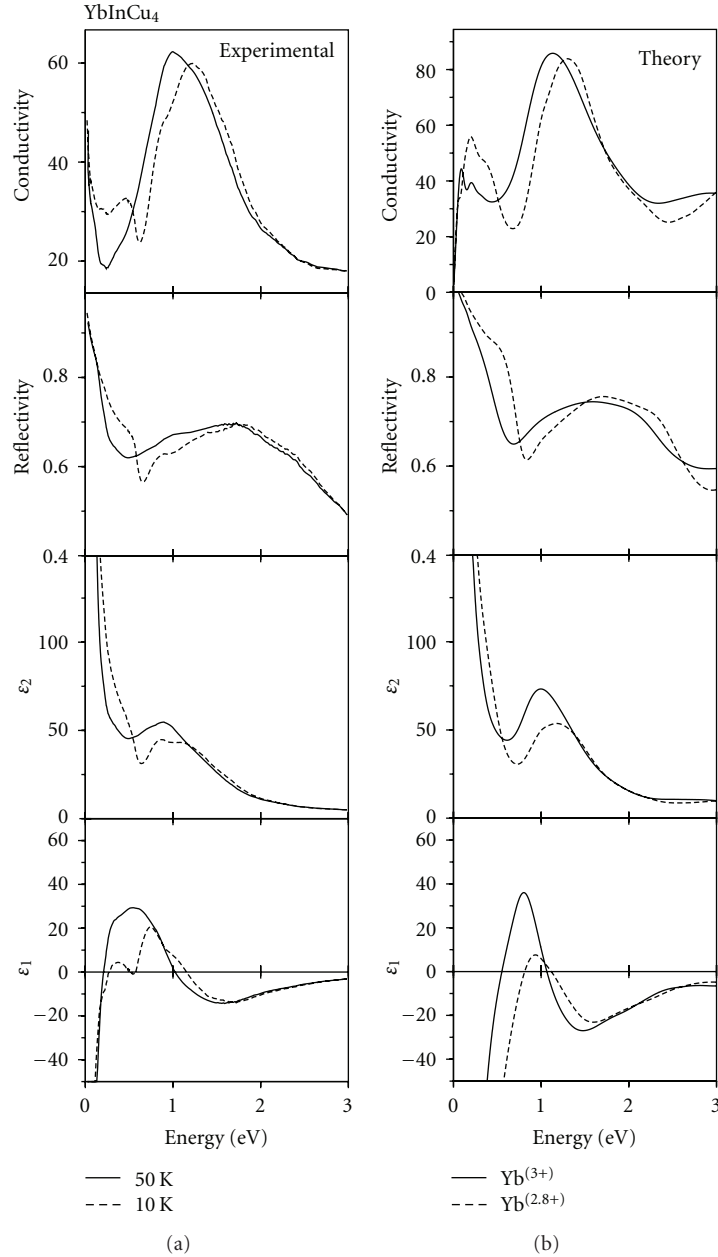


FIGURE 99: Comparison between the experimental optical spectra of YbInCu_4 measured below (10 K) and above (50 K) phase transition and calculated spectra for different occupation numbers of the hole $4f$ state in the LSDA+ U approximation [475].

transition at $T_v = 42$ K, the Yb valence is reduced from 2.9 to approximately 2.8. This leads to the increase of the nuclear screening by $4f$ electrons and increasing the In $p \rightarrow$ Yb d interband transition energies due to shifting of the empty Yb d band upwards.

In YbInCu_4 the upper hole $4f$ level is partly occupied and pinned at the Fermi energy; therefore, YbInCu_4 is calculated to be an intermediate valent compound in agreement with the experimental data. In the YbMCu_4 ($M = \text{Cu, Ag, Au, and Pd}$) a hole level is completely empty and situated sufficiently far from the Fermi level. Such a situation is appro-

priate for the developing of the Kondo lattice scenario. YbCu_5 and YbAgCu_4 are really typical dense Kondo systems, although the Kondo effect is not dominant in YbAuCu_4 , and YbPdCu_4 , where a long-range magnetic ordering is observed. The different ground states observed in YbMCu_4 ($M = \text{Cu, Ag, Au, and Pd}$) compounds result from the competition between three interactions: the crystal-field interaction, the magnetic intersite Ruderman-Kittel-Kasuya-Yosida interaction, and the intrasite Kondo effect. The evaluation of ground states of the compounds from first principles requires further investigation.

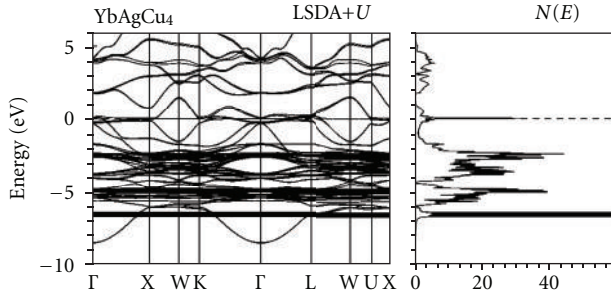


FIGURE 100: LSDA+ U self-consistent fully relativistic, spin-polarized energy band structure and total DOS (in states/(unit cell eV)) of YbAgCu_4 ($U_{\text{eff}} = 6$ eV) [475].

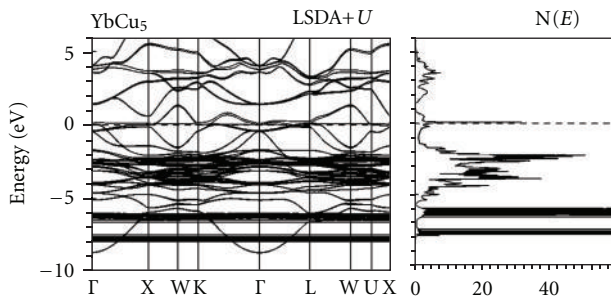


FIGURE 101: LSDA+ U self-consistent fully relativistic, spin-polarized energy band structure and total DOS (in states/(unit cell eV)) of YbCu_5 ($U_{\text{eff}} = 6$ eV) [475].

11. Conclusions

Almost localized electrons near the metal-insulator transitions are well described either by a simple itinerant picture in momentum space or by a localized picture in real space [2]. Theoretical and experimental efforts to make bridges between the itinerant and localized pictures have been made for years and have been fruitful [1]. However, this is still a challenging subject and many open questions have yet to be answered.

In this paper we present several examples of the first principle calculations of the electronic structure and various physical properties of transition metal oxides. The LSDA+ U study of the low-temperature phases of Fe_3O_4 and Fe_2O_3 as well as Ti_4O_7 show a charge- and orbitally ordered insulators below T_{co} . The theoretically calculated energy gaps are in good agreement with the experimental values. It was shown that, while the screening of the charge disproportion is so effective that the total $3d$ charge disproportion is rather small (0.23, 0.34, and 0.14 for the Fe_3O_4 , Fe_2O_3 , and Ti_4O_7 , resp.), the charge order is well pronounced with an order parameter defined as the difference of t_{2g} occupancies of Fe^{2+} and Fe^{3+} sites in the Fe_3O_4 and Fe_2O_3 and Ti^{3+} and Ti^{4+} cations in the Ti_4O_7 . This result demonstrates the utility of the LSDA+ U method as an aide to experimental studies of CO structures.

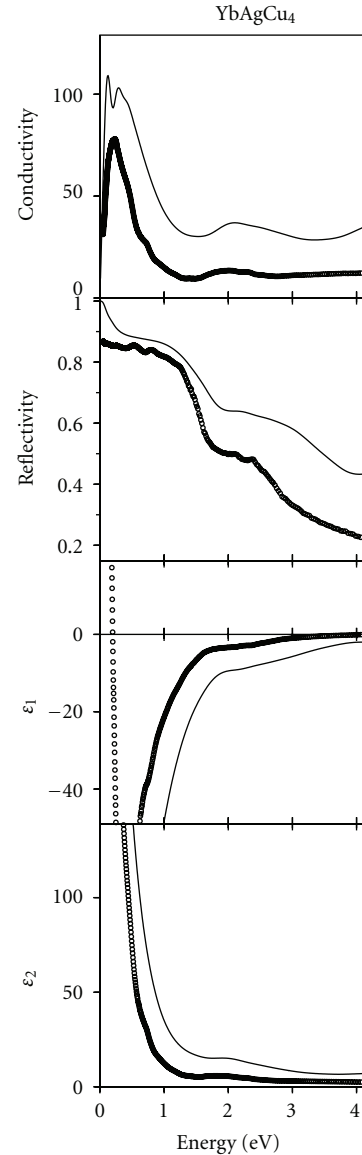


FIGURE 102: Comparison between the experimental (dots) and LSDA+ U calculated (solid line) optical spectra of YbAgCu_4 [475].

From the results of LDA+ U calculations performed for different models for the CO phase of α' - NaV_2O_5 , it was found that the energy of the CO model with zig-zag ordering of V^{4+} ions is lower than the energy of the in-line CO model. The calculated effective exchange constants between V^{4+} magnetic moments are in good agreement with the experimental values determined from the high-temperature susceptibility.

Many spectroscopic properties such as the optical conductivity, dielectric functions, Kerr angle and Kerr ellipticity, X-ray absorption, and X-ray magnetic circular dichroism calculated from the energy bands and the LMTO eigenvectors in the LSDA+ U approximation show an excellent agreement with derived from the experimental spectra in a wide energy range.

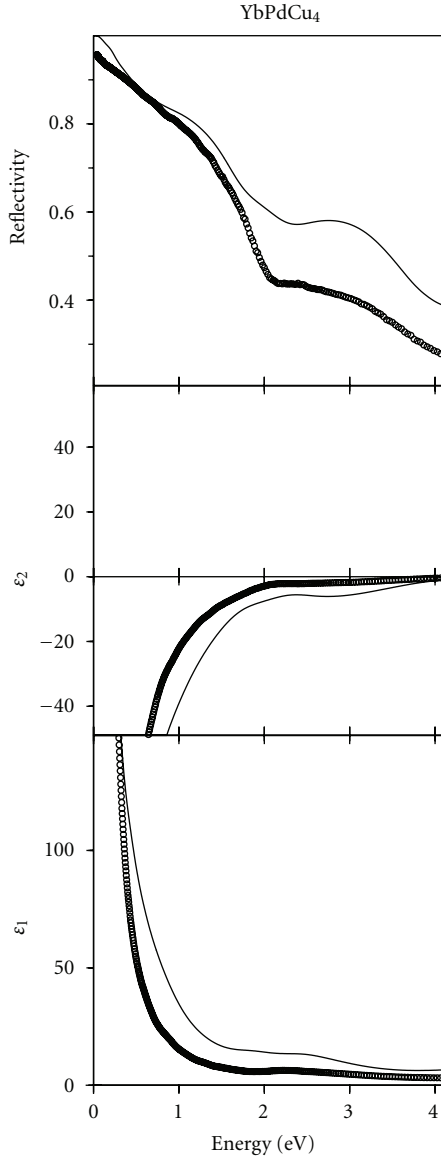


FIGURE 103: Comparison between the experimental (dots) and LSDA+ U calculated (solid line) optical spectra of YbPdCu₄ [475].

The global electronic structure of $3d$ transition metal compounds on the eV scale is now well understood from spectroscopic and first-principles studies. The electronic structure parameters such as the on-site Coulomb energy U , the charge-transfer energy, and exchange coupling constants have been deduced, and their systematic changes with chemical composition ranging from the Mott-Hubbard regime to the charge-transfer regime have been clarified [2]. The LSDA+ U method provides a practical way to incorporate electron-electron interactions into first-principles band structure calculations. However, in many cases, the U value has been determined not from first principles but empirically; that is, a true first-principles approach to strongly correlated systems is lacking so far. To understand the spectroscopic properties, effects of interactions that are not included in the standard models, namely, the long-range Coulomb

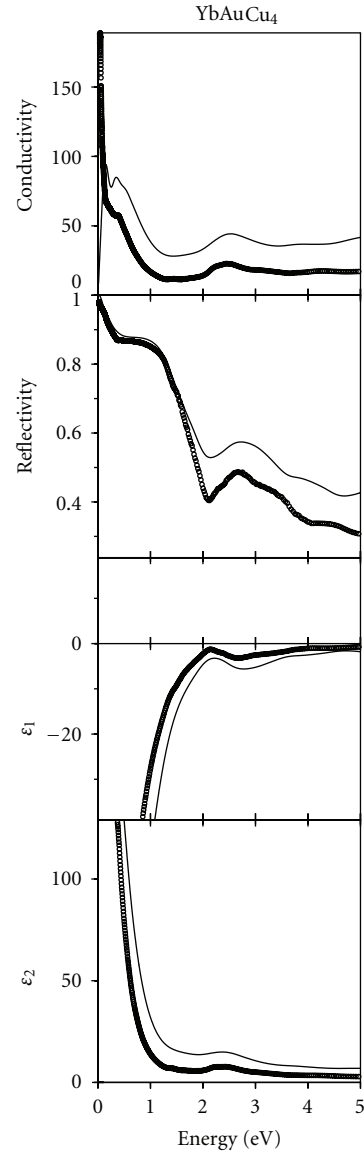


FIGURE 104: Comparison between the experimental (dots) and LSDA+ U calculated (solid line) optical spectra of YbAuCu₄ [475].

interaction, electron-phonon interaction, impurity potentials, and so forth, need to be studied further in the future.

Marginally retained metals near the metal-insulator transition have offered interesting and rich phenomena for decades and will continue to do so in the future, presenting fundamental problems in condensed matter physics as well as potential sources of applications.

The Ce $4f$ electrons in the CeFe₂ hybridize strongly with the Fe $3d$ electrons; therefore, calculations based on the density functional theory in the LSDA approach gave quite good description of the electronic structure and physical properties of CeFe₂. A large magnetic moment at the Fe site induces spin splitting of the itinerant Ce $5d$ and Ce $4f$ states through exchange and hybridization effect. From the LSDA calculations, it has been deduced that the total moment is the result of the antiparallel coupling between

Fe moment and cerium moment. This conclusion agrees well with the neutron diffraction, Compton scattering, and X-ray magnetic circular dichroism experiments. The XAS and XMCD spectra at the Ce $L_{2,3}$ edge reflect the energy distribution and the orbital character of the Ce $5d$ band-like states. The LSDA calculations are able to provide a good agreement in the shape of the X-ray absorption spectra at the Ce $L_{2,3}$ edges with the experimental measurements.

On the other hand, the LSDA produces the stable metallic solution for Sm monochalcogenides at ambient pressure in contradiction with the experimental measurements. In this case the LSDA+ U method gave correct insulator solution with energy gaps in good agreement with the experimental measurements. The Coulomb repulsion U_{eff} strongly influences the electronic structure of Sm monochalcogenides. For Sm^{2+} ions six $4f_{5/2}$ bands are fully occupied and situated in the gap between chalcogen $3p$ and Sm $5d$ states. The $4f_{7/2}$ hole levels are completely unoccupied and well above the Fermi level hybridized with Sm $5d$ states. LSDA+ U theory predicts that the samarium ion in these compounds is in an integer divalent state. It also shows a gradual decrease of the energy gap with reduction of the lattice constant. The LSDA+ U theoretical calculations describe well the optical spectra of Sm monochalcogenides.

When applying external pressure to SmS and, hence, decreasing its lattice constant, the widths of Sm $5d$ and $4f$ bands are increased and the crystal-field splitting of the $5d$ states $e_g - t_{2g}$ is also increased. At a given pressure the $5d$ band overlaps with the $4f_{5/2}$ states. This leads to a first-order valence $\text{Sm}^{2+} \rightarrow \text{Sm}^{3+}$ phase transition. The gap in SmS is closed at $a = 5.70 \text{ \AA}$ in good agreement with experimental measurements of SmS transport properties under pressure. For SmS with Sm^{3+} ions five $4f$ bands are fully occupied and hybridize with chalcogenide p states. The initially empty hole 6th $4f$ level in the process of self-consistent relaxation becomes partly occupied with the $4f$ DOS maximum situated in close vicinity of the Fermi level in the golden phase of SmS. The occupation number of the 6th $4f$ hole level is equal to 0.45 (valence 2.55+) in a good agreement with the experimental estimates from spectroscopic methods and susceptibility measurements.

As classical mixed-valence narrow gap semiconductors SmB_6 and YbB_{12} constitute very interesting systems exhibiting behavior due to strongly correlated electrons. The Coulomb repulsion U_{eff} strongly influences the electronic structure of SmB_6 . For Sm^{2+} ions eight $4f_{7/2}$ hole levels are completely unoccupied and well above the Fermi level hybridized with Sm $5d$ states. The $4f_{5/2}$ bands are situated in close vicinity of the Fermi level. One of the $4f_{5/2}$ levels is slightly unoccupied and extends just above the Fermi level around the X symmetry point, producing a noninteger Sm valency equal to 2.02+. There is a small hybridization gap at the Fermi level $\Delta E = 27 \text{ meV}$. The theoretically calculated energy gap is larger than the experimentally estimated one of around 3.6 to 5.2 meV determined from the activation energy and optical measurements. For Sm^{3+} five $4f$ bands are fully occupied and situated at around 6 eV below the Fermi level. A 6th $4f$ hole level is fully unoccupied and situated at about 0.34 eV above the Fermi level. The average positions of

the occupied $4f$ states in Sm^{2+} and Sm^{3+} calculations are in agreement with XPS measurements.

In the LSDA+ U energy band structure calculations of the electronic structure of YbB_{12} with divalent Yb ions, all 14 $4f$ bands are fully occupied and situated closely below the bottom of the Yb $5d$ band. They are split due to spin-orbit coupling by $\Delta\varepsilon_{\text{so}} = 1.4 \text{ eV}$. There is a small hybridization gap at the Fermi level. The theoretically calculated energy gap $\Delta E = 65 \text{ meV}$ between Yb $4f_{7/2}$ and Yb $5d$ states is somewhat larger than the gap estimated from the activation energy and optical measurements and smaller than observed in tunneling experiments. For the trivalent Yb ion, thirteen $4f$ electron bands are well below the Fermi level and hybridized with the B $2p$ states. They are separated from a $4f$ hole state by the correlation energy U_{eff} . The 14th $4f$ unoccupied hole level is well above the Fermi level at around 1.5 eV.

The optical spectra of YbB_{12} can be considered as a mixture of two spectra coming from di- and trivalent ytterbium ions. Good agreement between theory and high-temperature optical reflectivity spectrum can be reached if one uses the sum of the optical reflectivity spectrum consisting of 20% ytterbium divalent and 80% ytterbium trivalent spectra. Low-temperature measurements show that below 20 K there is a gap development in the optical conductivity and reflectivity spectra of YbB_{12} . The low-energy peak at 0.05 eV in the optical conductivity spectrum originates from the trivalent phase and can be explained as interband transitions between occupied and unoccupied Sm $5d$ states along Γ -X and X-W symmetry directions. The prominent peak in the $\sigma_{1xx}(\omega)$ spectrum at around 0.4 eV is mostly derived from interband transitions between occupied Yb $4f$ bands and empty Yb $5d$ bands of the divalent phase in the vicinity of the W symmetry point as well as along the X-W symmetry direction.

In contrast to LSDA, where the stable solution for TmTe is a metal, the LSDA+ U method gave an insulator with an indirect energy gap of 0.58 eV. LSDA+ U theory predicts that the thulium ion in TmTe is in an integer divalent state. It also shows a gradual decreasing of the energy gap with reduction of the lattice constant. The gap is closed at $a = 6.05 \text{ \AA}$ in a good agreement with experimental measurements of TmTe transport properties under pressure and the compositionally induced semiconductor—metal transition in the $\text{TmSe}_{1-x}\text{Te}_x$ system.

For the Tm^{3+} ions of TmS and TmSe twelve $4f$ bands are fully occupied and hybridize with chalcogenide p states. The 14th f hole level is completely unoccupied and well above the Fermi level. The hole 13th f level is partly occupied with $4f$ DOS maximum situated in close vicinity of the Fermi level in TmS and TmSe. The degree of occupation and position of the partly occupied 13th f level with respect to the Fermi level is different in TmS and TmSe. In TmS the hole level is almost empty and situated significantly far from the Fermi level. Such a situation is appropriate for achieving the Kondo lattice scenario. In TmSe the upper hole 13th f level is pinned at the Fermi level, therefore, TmSe is expected to be an intermediate valent compound in agreement with experimental data. The occupation number of the 13th f hole level is equal to 0.12 and 0.27 (valency 2.88+ and 2.73+) in TmS and TmSe, respectively, in a good agreement with the

experimental estimates from lattice constant and XPS and UPS measurements.

The LSDA+ U approach to band structure calculations of Yb_4As_3 produce a band gap between the As p band and the Yb $5d$ band. As a consequence, a very narrow marginally occupied $\text{Yb}^{3+}4f$ hole band is pinned close to the top of the As p valence band via the charge balance between Yb and As which is governed by the large (~ 30 eV) bare Coulomb integral of the Yb $4f$ state. The same charge balance pins the Fermi level close to the bottom of this $4f$ hole band which has a width of 0.007 eV (80 K). It leads to an extremely low carrier density in Yb_4As_3 . So for Yb_4As_3 , the LSDA+ U band structure calculations provide a two-band model of the electronic structure: (1) a wide, nearly fully occupied As $4p$ valence band and (2) a very narrow, marginally occupied Yb $4f$ band, very weakly hybridized with the As $4p$ band in a small k space region near the Γ point of the BZ. Pressure, doping and so forth, may slightly change the relative position of these two bands and hence strongly affected the low carrier density and the transport properties. But the $4f$ shell of the Yb^{3+} ions is little influenced as long as the charge order is maintained. Similar situation was found to be also in the Sm_4Bi_3 , where there is a wide, nearly fully occupied Bi p valence band and a very narrow, marginally occupied Sm $4f$ band, weakly hybridized with the Bi p band in a small k space region near the Γ point of the BZ.

As classical mixed-valence compounds Eu_3S_4 and Sm_3X_4 ($X = \text{S}, \text{Se}, \text{or Te}$) constitute very interesting systems exhibiting unusual behavior. A detailed comparison between Eu_3S_4 and Sm_3S_4 shows that these two compounds have quite different electronic and magnetic structures as well as different hybridization character of the $4f$ electrons with $3p$ electrons.

The $4f-3p$ hybridization in Sm_3S_4 is expected to be smaller in comparison with the Eu_3S_4 compound. On the other hand, the $4f-3p$ hybridization in Sm_3Se_4 and Sm_3Te_4 is closer rather to the corresponding hybridization in Eu_3S_4 than in Sm_3S_4 . Nevertheless, Sm_3Se_4 as well as Sm_3Te_4 shows no sign of a phase transition to a charge ordered state at low temperatures. Therefore, the difference in the hybridization in Eu_3S_4 and Sm_3S_4 is probably not a main reason for the difference in their ground states.

Eu_3S_4 and Sm_3S_4 compounds have quite different magnetic structures. Eu^{2+} has no orbital moment. The orbital moment of magnetic Sm^{3+} ions in Sm_3S_4 is quite large and has the opposite direction to the spin moment. It was found that easy magnetization axes are different for two nonequivalent Sm^{3+} ions, and the strong local magnetocrystalline anisotropy in Sm_3S_4 might prevent the appearance of the collinear magnetic order in the compound.

In the view of the distribution of valence ions, the low-temperature phase of Eu_3S_4 is similar to the room-temperature phase of magnetite. Di- and trivalent ions are randomly distributed in the B and $8d$ sublattices in Fe_3O_4 and Eu_3S_4 , respectively. However, Fe_3O_4 undergoes at $T_V = 120$ K a first-order phase transition (Verwey transition) accompanying by long-range charge ordering of Fe^{3+} and Fe^{2+} ions on different sublattices. There are some indications

that similar transitions with charge ordering of Eu^{2+} and Eu^{3+} on the $8d$ sublattice may occur also in Eu_3S_4 at low temperatures [450].

The optical spectra of YbMCu_4 ($M = \text{Cu}, \text{Ag}, \text{Au}, \text{Pd}, \text{and In}$) are very sensitive tools for drawing conclusions about the appropriate model description. On account of the calculated optical spectra, we conclude that YbInCu_4 optical spectra are best described using the LSDA+ U approach. It was found that the main peak in the optical conductivity $\sigma(\omega)$ of YbMCu_4 at 1.2 eV results as $\text{In } p \rightarrow \text{Yb } d$ interband transitions between occupied and empty energy bands along L-W, X-W, and Γ -K symmetry directions and also in some inner parts of the Brillouin zone. The measurements of the optical spectra of YbInCu_4 show that its optical spectra between 0.1 and 2 eV significantly change at phase transition temperature. The theoretical calculations show that the major effect is due to the changing of the Yb valency. At the first-order valence transition at $T_V = 42$ K the Yb valence is reduced from 2.9 to approximately 2.8. This leads to the increasing of the nuclear screening by $4f$ electrons and increasing the $\text{In } p \rightarrow \text{Yb } d$ interband transition energies due to shifting of the empty Yb d band upwards.

In YbInCu_4 the upper hole $4f$ level is partly occupied and pinned at the Fermi energy, therefore, YbInCu_4 is calculated to be an intermediate valent compound in agreement with the experimental data. In the YbMCu_4 ($M = \text{Cu}, \text{Ag}, \text{Au}, \text{and Pd}$) a hole level is completely empty and situated sufficiently far from the Fermi level. Such a situation is appropriate for the developing of the Kondo lattice scenario. YbCu_5 and YbAgCu_4 are really typical dense Kondo systems, although, the Kondo effect is not dominant in YbAuCu_4 and YbPdCu_4 , where a long-range magnetic ordering is observed. The different ground states observed in YbMCu_4 ($M = \text{Cu}, \text{Ag}, \text{Au}, \text{and Pd}$) compounds result from the competition between three interactions: the crystal field interaction, the magnetic intersite Ruderman-Kittel-Kasuya-Yosida interaction, and the intrasite Kondo effect. The evaluation of ground states of the compounds from first principles requires further investigation.

In conclusion we would like to point out that the LSDA+ U method which combines LSDA with a basically static, that is, Hartree-Fock-like, mean-field approximation for a multiband Anderson lattice model does not contain true many-body physics. However, this method can be considered as the first step towards a better description of strongly correlated electron systems. The LSDA+ U method provides a practical way to incorporate electron-electron interactions into first-principles band structure calculations. This method indeed makes better job in comparison with pure LSDA for most $4f$ compounds.

The LSDA+ U method gave a correct insulating ground state solution for Sm and Tm monochalcogenides, Sm and Yb borides as well as mixed-valent and charge-ordered Sm, Eu and Yb pnictides and chalcogenides R_4X_3 and R_3X_4 ($\text{R} = \text{Sm}, \text{Eu}, \text{Yb}; \text{X} = \text{As}, \text{Sb}, \text{Bi}$). This method is able to correctly describe many experimentally measured properties such as optical and magneto-optical spectroscopic measurements, X-ray photoemission and X-ray absorption,

and bremsstrahlung isochromat spectroscopy measurements as well as X-ray magnetic circular dichroism.

However, the formation of the MV state in SmB_6 and YbB_{12} clearly requires a treatment that goes beyond a static mean-field approximation and includes dynamical effects, for example, the frequency dependence of the self-energy. Similar is true also for the describing of the electronic structure of the charge glass state in Sm_3X_4 , which is characterized by the random distribution of Sm^{2+} and Sm^{3+} ions in space. It is still unclear how well it performs in describing the mixed-valence state in golden SmS in the pressure range from 6 to 20 kbar. On one hand, we found the pinning of a partly occupied 6th 4f level at the Fermi level, which is the typical situation for mixed-valence systems. On the other hand, LSDA+ U calculations always produce a nonzero magnetic moment in the high-pressure phase of SmS , although all attempts to find any sign of magnetic ordering in this system gave no positive results for the last 30 years. It is more likely that our LSDA+ U calculations describe well the situation in the metallic phase of SmS at pressure $P \geq 20$ kbar with trivalent samarium ions.

References

- [1] A. Georges, G. Kotliar, W. Krauth, and M. J. Rozenberg, "Dynamical mean-field theory of strongly correlated fermion systems and the limit of infinite dimensions," *Reviews of Modern Physics*, vol. 68, no. 1, pp. 13–125, 1996.
- [2] M. Imada, A. Fujimori, and Y. Tokura, "Metal-insulator transitions," *Reviews of Modern Physics*, vol. 70, no. 4, pp. 1039–1263, 1998.
- [3] C. M. Varma, "Mixed-valence compounds," *Reviews of Modern Physics*, vol. 48, no. 2, pp. 219–238, 1976.
- [4] J. M. Lawrence, P. S. Riseborough, and R. D. Parks, "Valence fluctuation phenomena," *Reports on Progress in Physics*, vol. 44, no. 1, pp. 1–84, 1981.
- [5] P. Wachter, "Intermediate valence and heavy fermions," in *Handbook of the Physics and Chemistry of Rare Earths*, K. A. Gschneidner, L. Eyring, and S. Hüfner, Eds., vol. 19, p. 177, North-Holland, Amsterdam, The Netherlands, 1994.
- [6] V. Antonov, B. Harmon, and A. Yaresko, *Electronic Structure and Magneto-Optical Properties of Solids*, Kluwer Academic Publishers, Dordrecht, The Netherlands, 2004.
- [7] T. Goto and B. Lüthi, "Charge ordering, charge fluctuations and lattice effects in strongly correlated electron systems," *Advances in Physics*, vol. 52, no. 2, pp. 67–118, 2003.
- [8] P. Fulde, "Crystallization of electrons confined to a lattice," *Annalen der Physik*, vol. 6, no. 3, pp. 178–186, 1997.
- [9] E. J. W. Verwey and P. W. Haayman, "Electronic conductivity and transition point of magnetite (Fe_3O_4)," *Physica*, vol. 8, no. 9, pp. 979–987, 1941.
- [10] V. N. Antonov, B. N. Harmon, V. P. Antropov, A. Y. Perlov, and A. N. Yaresko, "Electronic structure and magneto-optical Kerr effect of Fe_3O_4 and Mg^{2+} - or Al^{3+} -substituted Fe_3O_4 ," *Physical Review B*, vol. 64, no. 13, Article ID 134410, 12 pages, 2001.
- [11] I. Leonov, A. N. Yaresko, V. N. Antonov, M. A. Korotin, and V. I. Anisimov, "Charge and orbital order in Fe_3O_4 ," *Physical Review Letters*, vol. 93, no. 14, Article ID 146404, 2004.
- [12] J. P. Perdew and A. Zunger, "Self-interaction correction to density-functional approximations for many-electron systems," *Physical Review B*, vol. 23, no. 10, pp. 5048–5079, 1981.
- [13] V. I. Anisimov, J. Zaanen, and O. K. Andersen, "Band theory and Mott insulators: Hubbard U instead of Stoner I ," *Physical Review B*, vol. 44, no. 3, pp. 943–954, 1991.
- [14] L. Hedin, "New method for calculating the one-particle Green's function with application to the electron-gas problem," *Physical Review*, vol. 139, no. 3A, pp. A796–A823, 1965.
- [15] W. Metzner and D. Vollhardt, "Correlated lattice fermions in $d = \infty$ dimensions," *Physical Review Letters*, vol. 62, no. 3, pp. 324–327, 1989.
- [16] T. Pruschke, M. Jarrell, and J. K. Freericks, "Anomalous normal-state properties of high- T_c superconductors: intrinsic properties of strongly correlated electron systems?" *Advances in Physics*, vol. 44, no. 2, pp. 187–210, 1995.
- [17] V. I. Anisimov, F. Aryasetiawan, and A. I. Lichtenstein, "First-principles calculations of the electronic structure and spectra of strongly correlated systems: the LDA + U method," *Journal of Physics: Condensed Matter*, vol. 9, no. 4, pp. 767–808, 1997.
- [18] L. Hedin and B. I. Lundqvist, "Explicit local exchange-correlation potentials," *Journal of Physics C*, vol. 4, no. 14, pp. 2064–2083, 1971.
- [19] P. W. Anderson, "Localized magnetic states in metals," *Physical Review*, vol. 124, no. 1, pp. 41–53, 1961.
- [20] V. I. Anisimov, I. V. Solovyev, M. A. Korotin, M. T. Czyzyk, and G. A. Sawatzky, "Density-functional theory and NiO photoemission spectra," *Physical Review B*, vol. 48, no. 23, pp. 16929–16934, 1993.
- [21] I. V. Solovyev, A. I. Liechtenstein, and K. Terakura, "Is Hund's second rule responsible for the orbital magnetism in solids?" *Physical Review Letters*, vol. 80, no. 26, pp. 5758–5761, 1998.
- [22] A. N. Yaresko, V. N. Antonov, and P. Fulde, "Localized 5f electrons in UPd3 from LDA + U calculations," *Physical Review B*, vol. 67, no. 15, Article ID 155103, 10 pages, 2003.
- [23] H. Harima, "LDA+ U method applied for f-electron systems," *Journal of Magnetism and Magnetic Materials*, vol. 226–230, pp. 83–84, 2001.
- [24] C. Herring, "Exchange interactions among itinerant electrons," in *Magnetism*, G. T. Rado and H. Suhl, Eds., vol. 4, Academic Press, New York, NY, USA, 1966.
- [25] J. Hubbard, "Electron correlations in narrow energy bands," *Proceedings of the Royal Society A*, vol. 276, pp. 238–257, 1963.
- [26] J. Hubbard, "Electron correlations in narrow energy bands. II. The degenerate band case," *Proceedings of the Royal Society A*, vol. 277, pp. 237–259, 1964.
- [27] W. E. Pickett, S. C. Erwin, and E. C. Ethridge, "Reformulation of the LDA + U method for a local-orbital basis," *Physical Review B*, vol. 58, no. 3, pp. 1201–1209, 1998.
- [28] O. Bengone, M. Alouani, P. Blöchl, and J. Hugel, "Implementation of the projector augmented-wave LDA + U method: Application to the electronic structure of NiO," *Physical Review B*, vol. 62, no. 24, pp. 16392–16401, 2000.
- [29] M. Cococcioni and S. De Gironcoli, "Linear response approach to the calculation of the effective interaction parameters in the LDA+ U method," *Physical Review B*, vol. 71, no. 3, Article ID 035105, 16 pages, 2005.
- [30] P. E. Blöchl, "Projector augmented-wave method," *Physical Review B*, vol. 50, no. 24, pp. 17953–17979, 1994.
- [31] R. Car and M. Parrinello, "Unified approach for molecular dynamics and density-functional theory," *Physical Review Letters*, vol. 55, no. 22, pp. 2471–2474, 1985.
- [32] H. J. Kulik, M. Cococcioni, D. A. Scherlis, and N. Marzari, "Density functional theory in transition-metal chemistry: a self-consistent hubbard U approach," *Physical Review Letters*, vol. 97, no. 10, Article ID 103001, 2006.

- [33] D. A. Scherlis, M. Cococcioni, P. Sit, and N. Marzari, "Simulation of heme using DFT + U: a step toward accurate spin-state energetics," *Journal of Physical Chemistry B*, vol. 111, no. 25, pp. 7384–7391, 2007.
- [34] V. I. Anisimov and O. Gunnarsson, "Density-functional calculation of effective Coulomb interactions in metals," *Physical Review B*, vol. 43, no. 10, pp. 7570–7574, 1991.
- [35] P. H. Dederichs, S. Blügel, R. Zeller, and H. Akai, "Ground states of constrained systems: application to cerium impurities," *Physical Review Letters*, vol. 53, no. 26, pp. 2512–2515, 1984.
- [36] I. V. Solovyev, P. H. Dederichs, and V. I. Anisimov, "Corrected atomic limit in the local-density approximation and the electronic structure of d impurities in Rb," *Physical Review B*, vol. 50, no. 23, pp. 16861–16871, 1994.
- [37] J. F. Janak, "Proof that $\partial E/\partial n_i = \epsilon$ in density-functional theory," *Physical Review B*, vol. 18, no. 12, pp. 7165–7168, 1978.
- [38] J. F. Herbst and J. W. Wilkins, "Calculation of 4f excitation energies in the metals and relevance to mixed valence systems," in *Handbook of the Physics and Chemistry of Rare Earths*, K. A. Gschneidner, L. Eyring, and S. Hüfner, Eds., vol. 10, chapter 68, p. 321, North-Holland, Amsterdam, The Netherlands, 1987.
- [39] E. Antonides, E. C. Janse, and G. A. Sawatzky, "LMM Auger spectra of Cu, Zn, Ga, and Ge. I. Transition probabilities, term splittings, and effective Coulomb interaction," *Physical Review B*, vol. 15, no. 4, pp. 1669–1679, 1977.
- [40] D. van der Marel, G. A. Sawatzky, and F. U. Hillebrecht, "Direct observation of the exchange-split virtual bound state in dilute Mn alloys," *Physical Review Letters*, vol. 53, no. 2, pp. 206–209, 1984.
- [41] M. I. Friezer, "A survey of magneto-optic effects," *IEEE Transactions on Magnetics*, vol. 4, no. 2, pp. 152–161, 1968.
- [42] J. B. Kortright and S. K. Kim, "Resonant magneto-optical properties of Fe near its 2p levels: measurement and applications," *Physical Review B*, vol. 62, no. 18, pp. 12216–12228, 2000.
- [43] J. Schoenes, "Magneto-optical properties of metals, alloys and compounds," in *Electronic and Magnetic Properties of Metals and Ceramics*, R. W. Cahn, P. Haasen, and E. J. Kramer, Eds., vol. 3A of *Materials Science and Technology*, pp. 147–255, Verlag Chemie, Weinheim, Germany, 1992, volume editor: K. H. J. Buschow.
- [44] C. D. Mee and E. D. Daniel, *Magnetic Recording*, McGraw-Hill, New York, NY, USA, 1987.
- [45] K. H. J. Buschow, "Magneto-optical properties of alloys and intermetallic compounds," in *Handbook of Ferromagnetic Materials*, E. P. Wohlfarth and K. H. J. Buschow, Eds., vol. 4, pp. 493–588, North-Holland, Amsterdam, The Netherlands, 1988.
- [46] W. Reim and J. Schoenes, "Magneto-optical spectroscopy of f-electron systems," in *Ferromagnetic Materials*, E. P. Wohlfarth and K. H. J. Buschow, Eds., vol. 5, p. 133, North-Holland, Amsterdam, The Netherlands, 1990.
- [47] H. R. Hulme, "The Faraday effect in ferromagnetics," *Proceedings of the Royal Society A*, vol. 135, pp. 237–257, 1932.
- [48] C. Kittel, *Physical Review*, vol. 83, p. A208, 1951.
- [49] P. N. Argyres, "Theory of the Faraday and Kerr effects in ferromagnetics," *Physical Review*, vol. 97, no. 2, pp. 334–345, 1955.
- [50] B. R. Cooper, "Theory of the interband ferromagnetic kerr effect in nickel," *Physical Review*, vol. 139, no. 5A, pp. A1504–A1514, 1965.
- [51] R. Kubo, "Statistical-mechanical theory of irreversible processes. I. General theory and simple applications to magnetic and conduction problems," *Journal of the Physical Society of Japan*, vol. 12, pp. 570–586, 1957.
- [52] E. I. Kondorsky and A. V. Vediaev, "The electron-phonon scattering contribution to the anomalous magneto-optical effects in ferromagnetic metals," *Journal of Applied Physics*, vol. 39, no. 2, pp. 559–561, 1968.
- [53] C. S. Wang and J. Callaway, "Band structure of nickel: Spin-orbit coupling, the Fermi surface, and the optical conductivity," *Physical Review B*, vol. 9, no. 11, pp. 4897–4907, 1974.
- [54] H. Ebert, P. Strange, and B. L. Gyorffy, "Theory of circularly polarized X-ray absorption by ferromagnetic Fe," *Journal of Applied Physics*, vol. 63, no. 8, pp. 3055–3057, 1988.
- [55] F. Herman, J. Sticht, and M. van Schilfgaarde, "Spin-polarized band structure of magnetically coupled multilayers," *Journal of Applied Physics*, vol. 69, no. 8, pp. 4783–4785, 1991.
- [56] R. Wu, C. Li, and A. J. Freeman, "Structural, electronic and magnetic properties of Co/Pd(111) and Co/Pt(111)," *Journal of Magnetism and Magnetic Materials*, vol. 99, no. 1–3, pp. 71–80, 1991.
- [57] P. M. Oppeneer, T. Maurer, J. Sticht, and J. Kübler, "Ab initio calculated magneto-optical Kerr effect of ferromagnetic metals: Fe and Ni," *Physical Review B*, vol. 45, no. 19, pp. 10924–10933, 1992.
- [58] P. M. Oppeneer, J. Sticht, T. Maurer, and J. Kübler, "Ab initio investigation of microscopic enhancement factors in tuning the magneto-optical Kerr effect," *Zeitschrift für Physik B*, vol. 88, no. 3, pp. 309–315, 1992.
- [59] G. Y. Guo and H. Ebert, "Theoretical investigation of the orientation dependence of the magneto-optical Kerr effect in Co," *Physical Review B*, vol. 50, no. 14, pp. 10377–10380, 1994.
- [60] G. Y. Guo and H. Ebert, "Band-theoretical investigation of the magneto-optical Kerr effect in Fe and Co multilayers," *Physical Review B*, vol. 51, no. 18, pp. 12633–12643, 1995.
- [61] T. Kraft, P. M. Oppeneer, V. N. Antonov, and H. Eschrig, "Relativistic calculations of the magneto-optical Kerr spectra in (001) and (111) US, USE, and UTe," *Physical Review B*, vol. 52, no. 5, pp. 3561–3570, 1995.
- [62] A. N. Yaresko, P. M. Oppeneer, A. Y. Perlov, V. N. Antonov, T. Kraft, and H. Eschrig, "On the nature of the absolute maximal observable magneto-optical Kerr rotation of CeSb," *Europhysics Letters*, vol. 36, no. 7, pp. 551–556, 1996.
- [63] P. M. Oppeneer, M. S. S. Brooks, V. N. Antonov, T. Kraft, and H. Eschrig, "Band-theoretical description of the magneto-optical spectra of UAsSe," *Physical Review B*, vol. 53, no. 16, pp. R10437–R10440, 1996.
- [64] P. M. Oppeneer, V. N. Antonov, T. Kraft, H. Eschrig, A. N. Yaresko, and A. Y. Perlov, "Calculated magneto-optical Kerr spectra of XPt₃ compounds (X = V, Cr, Mn, Fe and Co)," *Journal of Physics: Condensed Matter*, vol. 8, no. 31, pp. 5769–5780, 1996.
- [65] P. M. Oppeneer, V. N. Antonov, T. Kraft, H. Eschrig, A. N. Yaresko, and A. Y. Perlov, "First-principles study of the giant magneto-optical Kerr effect in MnBi and related compounds," *Journal of Applied Physics*, vol. 80, no. 2, pp. 1099–1105, 1996.
- [66] V. N. Antonov, P. M. Oppeneer, A. N. Yaresko, A. Y. Perlov, and T. Kraft, "Computationally based explanation of the peculiar magneto-optical properties of PtMnSb and related ternary compounds," *Physical Review B*, vol. 56, no. 20, pp. 13012–13025, 1997.

- [67] P. M. Oppeneer, "Magneto-optical spectroscopy in the valence-band energy regime: relationship to the magnetocrystalline anisotropy," *Journal of Magnetism and Magnetic Materials*, vol. 188, no. 3, pp. 275–285, 1998.
- [68] V. N. Antonov, V. P. Antropov, B. N. Harmon, A. N. Yaresko, and A. Y. Perlov, "Fully relativistic spin-polarized LMTO calculations of the magneto-optical Kerr effect of d and f ferromagnetic materials. I. Chromium spinel chalcogenides," *Physical Review B*, vol. 59, no. 22, pp. 14552–14560, 1999.
- [69] V. N. Antonov, B. N. Harmon, A. Y. Perlov, and A. N. Yaresko, "Fully relativistic spin-polarized LMTO calculations of the magneto-optical Kerr effect of d and f ferromagnetic materials. II. Neodymium chalcogenides," *Physical Review B*, vol. 59, no. 22, pp. 14561–14570, 1999.
- [70] D. S. Wang, R. Wu, and A. J. Freeman, "State-tracking first-principles determination of magnetocrystalline anisotropy," *Physical Review Letters*, vol. 70, no. 6, pp. 869–872, 1993.
- [71] D. S. Wang, R. Wu, and A. J. Freeman, "Theoretical studies of the magneto-crystalline anisotropy: Monolayer Co," *Journal of Applied Physics*, vol. 73, no. 10, pp. 6745–6747, 1993.
- [72] R. Wu, D. Wang, and A. J. Freeman, "First principles investigation of the validity and range of applicability of the X-ray magnetic circular dichroism sum rule," *Physical Review Letters*, vol. 71, no. 21, pp. 3581–3584, 1993.
- [73] R. Wu, D. Wang, and A. J. Freeman, "Validity and the applicability of magnetic-circular-dichroism sum rules for transition metals (invited)," *Journal of Applied Physics*, vol. 75, no. 10, pp. 5802–5806, 1994.
- [74] R. Q. Wu and A. J. Freeman, "Limitation of the magnetic-circular-dichroism spin sum rule for transition metals and importance of the magnetic dipole term," *Physical Review Letters*, vol. 73, no. 14, pp. 1994–1997, 1994.
- [75] R. Wu and A. J. Freeman, "Magnetic circular dichroism at the K and L edges of Co and Cu in Co/Cu(001)," *Journal of Applied Physics*, vol. 79, no. 8, pp. 6500–6502, 1996.
- [76] V. I. Gavrilenko and R. Wu, "Magneto-optical properties of FeAu alloys and Fe/Au superlattices," *Journal of Applied Physics*, vol. 85, no. 8, pp. 5112–5114, 1999.
- [77] V. I. Gavrilenko and R. Wu, "Effect of magnetic ordering on optical and magneto-optical properties of Fe/Cr superlattices," *Journal of Magnetism and Magnetic Materials*, vol. 260, no. 3, pp. 330–335, 2003.
- [78] J. Hong and R. Q. Wu, "Magnetic ordering and X-ray magnetic circular dichroism of Co doped ZnO," *Journal of Applied Physics*, vol. 97, no. 6, pp. 1–5, 2005.
- [79] R. Wu and A. J. Freeman, "Spin-orbit induced magnetic phenomena in bulk metals and their surfaces and interfaces," *Journal of Magnetism and Magnetic Materials*, vol. 200, no. 1, pp. 498–514, 1999.
- [80] V. N. Antonov, B. N. Harmon, A. N. Yaresko, and A. Y. Perlov, "Fully relativistic spin-polarized LMTO calculations of the magneto-optical Kerr effect of d and f ferromagnetic materials. III. Uranium chalcogenides and pnictides," *Physical Review B*, vol. 59, no. 22, pp. 14571–14582, 1999.
- [81] P. Novák, J. Kuneš, and P. M. Oppeneer, "Electronic structure of magnetite," *Physica B*, vol. 312–313, pp. 785–786, 2002.
- [82] O. Horpynyuk, V. V. Nemoshkalenko, V. N. Antonov, B. N. Harmon, and A. N. Yaresko, "Electronic structure and magneto-optical Kerr effect in the compound UCuP₂," *Low Temperature Physics*, vol. 28, no. 7, pp. 745–751, 2002.
- [83] B. N. Harmon and V. N. Antonov, "Electronic structure, optical, and magneto-optical properties of Gd₅(Si₂Ge₂) compound," *Journal of Applied Physics*, vol. 91, no. 12, p. 9815, 2002.
- [84] V. N. Antonov, B. N. Harmon, O. Horpynyuk, and A. N. Yaresko, "Electronic structure and magneto-optical Kerr effect in UCuAs₂," *Low Temperature Physics*, vol. 29, no. 1, pp. 36–40, 2003.
- [85] V. N. Antonov, B. N. Harmon, and A. N. Yaresko, "Electronic structure and magneto-optical Kerr effect in UGa₂," *Journal of Applied Physics*, vol. 94, no. 11, pp. 7240–7245, 2003.
- [86] V. N. Antonov, B. N. Harmon, and A. N. Yaresko, "Electronic structure and magneto-optical Kerr effect in La monochalcogenides," *Physical Review B*, vol. 69, no. 9, Article ID 094404, 8 pages, 2004.
- [87] A. Stroppa, S. Picozzi, A. Continenza, M. Kim, and A. J. Freeman, "Magneto-optical properties of (Ga,Mn)As: an ab initio determination," *Physical Review B*, vol. 77, no. 3, Article ID 035208, 2008.
- [88] M. Amft, T. Burkert, B. Sanyal, and P. M. Oppeneer, "First-principles calculations of optical and magneto-optical properties of Ga_{1-x}Mn_xAs and MnAs," *Physica B*, vol. 404, no. 20, pp. 3782–3788, 2009.
- [89] V. N. Antonov, L. Uba, S. Uba, A. N. Yaresko, A. Y. Perlov, and V. V. Nemoshkalenko, "Magneto-optical spectroscopy of magnetic multilayers: theory and experiment," *Low Temperature Physics*, vol. 27, no. 6, pp. 425–462, 2001.
- [90] L. Uba, A. Polewko, S. Uba, R. Gontarz, A. N. Yaresko, and V. N. Antonov, "Determination of the interfacial magneto-optical properties in sputtered Fe/Au multilayer structures," *Physica Status Solidi A*, vol. 196, no. 1, pp. 145–148, 2003.
- [91] A. N. Yaresko, L. Uba, S. Uba, A. Y. Perlov, R. Gontarz, and V. N. Antonov, "Magneto-optical Kerr spectroscopy of palladium," *Physical Review B*, vol. 58, no. 12, pp. 7648–7653, 1998.
- [92] L. Uba, S. Uba, V. N. Antonov, A. N. Yaresko, and R. Gontarz, "Magneto-optical Kerr spectroscopy of platinum," *Physical Review B*, vol. 62, no. 24, pp. 16510–16521, 2000.
- [93] S. Uba, A. N. Yaresko, L. Uba et al., "Influence of alloy composition and local environment on the magneto-optical properties of Co_xPd_{1-x} alloys," *Physical Review B*, vol. 57, no. 3, pp. 1534–1538, 1998.
- [94] L. Uba, S. Uba, V. N. Antonov, A. N. Yaresko, and R. Gontarz, "Microscopic origin of the magneto-optical properties of CoPt alloys," *Physical Review B*, vol. 64, no. 12, Article ID 125105, 11 pages, 2001.
- [95] L. Uba, S. Uba, V. N. Antonov, A. N. Yaresko, T. Slezak, and J. Korecki, "Magneto-optical anisotropy study of Fe/Ni superlattices," *Physical Review B*, vol. 62, no. 20, pp. 13731–13747, 2000.
- [96] L. Uba, S. Uba, O. Horpynyuk, V. N. Antonov, and A. N. Yaresko, "Influence of the crystal structure and chemical order on the magnetic and magneto-optical properties of equiatomic CoPt alloy," *Journal of Applied Physics*, vol. 91, no. 2, pp. 775–779, 2002.
- [97] S. Uba, L. Uba, A. N. Yaresko, A. Y. Perlov, V. N. Antonov, and R. Gontarz, "The influence of interface structure on the magneto-optical properties of Co/Pd multilayers," *Journal of Physics: Condensed Matter*, vol. 10, no. 17, pp. 3769–3782, 1998.
- [98] S. Uba, L. Uba, R. Gontarz, V. N. Antonov, A. Y. Perlov, and A. N. Yaresko, "Experimental and theoretical study of the magneto-optical properties of Co Pt multilayers," *Journal of Magnetism and Magnetic Materials*, vol. 140–144, no. 1, pp. 575–576, 1995.
- [99] S. Uba, L. Uba, A. Y. Perlov, A. N. Yaresko, V. N. Antonov, and R. Gontarz, "Experimental and ab initia theoretical study of optical and magneto-optical properties of Co/Cu

- multilayers,” *Journal of Physics: Condensed Matter*, vol. 9, no. 2, pp. 447–460, 1997.
- [100] S. Uba, L. Uba, A. N. Yaresko, A. Y. Perlov, V. N. Antonov, and R. Gontarz, “Optical and magneto-optical properties of Co/Pt multilayers,” *Physical Review B*, vol. 53, no. 10, pp. 6526–6535, 1996.
- [101] A. J. Freeman, R. Wu, M. Kim, and V. I. Gavrilenko, “Magnetism, magneto-crystalline anisotropy, magnetostriction and MOKE at surfaces and interfaces,” *Journal of Magnetism and Magnetic Materials*, vol. 203, no. 1–3, pp. 1–5, 1999.
- [102] L. Uba, S. Uba, V. N. Antonov et al., “Giant magneto-optical anisotropy in Fe/Au monoatomic multilayer,” *Solid State Communications*, vol. 114, no. 8, pp. 441–445, 2000.
- [103] J. H. de Boer and E. J. W. Verwey, “Semi-conductors with partially and with completely filled 3d-lattice bands,” *Proceedings of the Physical Society*, vol. 49, p. 59, 1937.
- [104] N. F. Mott and R. Peierls, “Discussion of the paper by de Boer and Verwey,” *Proceedings of the Physical Society*, vol. 49, p. 72, 1937.
- [105] F. Bloch, “Bemerkung zur Elektronentheorie des Ferromagnetismus und der elektrischen Leitfähigkeit,” *Zeitschrift für Physik*, vol. 57, no. 7–8, pp. 545–555, 1929.
- [106] S. A. K. Wilson, “The narcolepsies,” *Brain*, vol. 51, no. 1, pp. 63–109, 1928.
- [107] A. H. Wilson, “The theory of electronic semi-conductors,” *Proceedings of the Royal Society A*, vol. 133, pp. 458–491, 1931.
- [108] A. H. Wilson, “The theory of electronic semi-conductors. II,” *Proceedings of the Royal Society A*, vol. 134, pp. 277–287, 1931.
- [109] E. J. W. Verwey, “Electronic conduction of magnetite (Fe_3O_4) and its transition point at low temperatures,” *Nature*, vol. 144, no. 3642, pp. 327–328, 1939.
- [110] E. J. Verwey, P. W. Haayman, and F. C. Romeijn, “Physical properties and cation arrangement of oxides with spinel structures II. Electronic conductivity,” *The Journal of Chemical Physics*, vol. 15, no. 4, pp. 181–187, 1947.
- [111] J. P. Wright, J. P. Attfield, and P. G. Radaelli, “Long range charge ordering in magnetite below the Verwey transition,” *Physical Review Letters*, vol. 87, no. 26, Article ID 266401, 4 pages, 2001.
- [112] G. Subías, J. García, J. Blasco, M. G. Proietti, H. Renevier, and M. C. Schez, “Magnetite, a model system for mixed-valence oxides, does not show charge ordering,” *Physical Review Letters*, vol. 93, no. 15, pp. 156408–1, 2004.
- [113] J. Smit and H. P. J. Wijn, *Ferrites*, Philips Technical Library, Eindhoven, The Netherlands, 1959.
- [114] V. A. M. Brabers, “Progress in spinel ferrite research,” in *Handbook of Magnetic Materials*, K. H. J. Buschow, Ed., vol. 8, p. 199, Elsevier Science, Amsterdam, The Netherlands, 1995.
- [115] N. Tsuda, K. Nasu, A. Yansen, and K. Siratory, *Electronic Conduction in Oxides*, vol. 94 of *Springer Series in Solid State Science*, Springer, Berlin, Germany, 1991.
- [116] N. F. Mott, *Metal-Insulator Transitions*, Taylor and Francis, London, UK, 1995.
- [117] J. Zaanen, G. A. Sawatzky, and J. W. Allen, “Band gaps and electronic structure of transition-metal compounds,” *Physical Review Letters*, vol. 55, no. 4, pp. 418–421, 1985.
- [118] H. Sawada and K. Terakura, “Orbital and magnetic orderings in localized t_{2g} systems, YTiO_3 and YVO_3 : comparison with a more itinerant eg system LaMnO_3 ,” *Physical Review B*, vol. 58, no. 11, pp. 6831–6836, 1998.
- [119] S. Kondo, D. C. Johnston, C. A. Swenson et al., “ LiV_2O_4 : a heavy fermion transition metal oxide,” *Physical Review Letters*, vol. 78, no. 19, pp. 3729–3732, 1997.
- [120] N. F. Mott, “Materials with mixed valency that show a verwey transition,” *Philosophical Magazine B*, vol. 42, no. 3, pp. 327–335, 1980.
- [121] B. A. Calhoun, “Magnetic and electric properties of magnetite at low temperatures,” *Physical Review*, vol. 94, no. 6, pp. 1577–1585, 1954.
- [122] P. A. Miles, W. B. Westphal, and A. von Hippel, “Dielectric spectroscopy of ferromagnetic semiconductors,” *Reviews of Modern Physics*, vol. 29, no. 3, pp. 279–307, 1957.
- [123] M. Matsui, S. Todo, and S. Chikazumi, “Specific heat and electrical conductivity of low temperature phase of magnetite,” *Journal of the Physical Society of Japan*, vol. 42, no. 5, pp. 1517–1524, 1977.
- [124] Y. Fujii, G. Shirane, and Y. Yamada, “Study of the 123-K phase transition of magnetite by critical neutron scattering,” *Physical Review B*, vol. 11, no. 5, pp. 2036–2041, 1975.
- [125] M. Iizumi and G. Shirane, “Crystal symmetry of the low temperature phase of magnetite,” *Solid State Communications*, vol. 17, no. 4, pp. 433–436, 1975.
- [126] S. Iida, K. Mizushima, M. Mizoguchi, S. Umemura, and J. Yoshida, “Electronic structure of magnetite at low temperature,” *Journal of Applied Physics*, vol. 49, no. 3, pp. 1455–1457, 1978.
- [127] C. Bonnelle, *Annals of Physics*, vol. 1, p. 439, 1966.
- [128] S. A. Mortimer, J. S. Johnson, and K. M. Weeks, “Quantitative analysis of RNA solvent accessibility by N-silylation of guanosine,” *Biochemistry*, vol. 48, no. 10, pp. 2109–2114, 2009.
- [129] S. G. Bishop and P. C. Kemeny, “Photoemission study of the electronic structure of magnetite,” *Solid State Communications*, vol. 15, no. 11–12, pp. 1877–1880, 1974.
- [130] A. J. M. Kuipers and V. A. M. Brabers, “Thermoelectric properties of magnetite at the verwey transition,” *Physical Review B*, vol. 14, no. 4, pp. 1401–1405, 1976.
- [131] A. J. M. Kuipers and V. A. M. Brabers, “Electrical transport in magnetite near the Verwey transition,” *Physical Review B*, vol. 20, no. 2, pp. 594–600, 1979.
- [132] A. Chainani, T. Yokoya, T. Morimoto, T. Takahashi, and S. Todo, “High-resolution photoemission spectroscopy of the Verwey transition in Fe_3O_4 ,” *Physical Review B*, vol. 51, no. 24, pp. 17976–17979, 1995.
- [133] S. F. Alvarado, W. Eib, F. Meier et al., “Observation of spin-polarized electron levels in ferrites,” *Physical Review Letters*, vol. 34, no. 6, pp. 319–322, 1975.
- [134] S. F. Alvarado, M. Erbudak, and P. Munz, “Final-state effects in the 3d photoelectron spectrum of Fe_3O_4 and comparison with Fe_xO ,” *Physical Review B*, vol. 14, no. 7, pp. 2740–2745, 1976.
- [135] K. Siratori, S. Suga, M. Taniguchi, K. Soda, S. Kimura, and A. Yanase, “Photoemission study of Fe_3O_4 ,” *Journal of the Physical Society of Japan*, vol. 55, no. 2, pp. 690–698, 1986.
- [136] T. Schedel-Niedrig, W. Weiss, and R. Schlögl, “Electronic structure of ultrathin ordered iron oxide films grown onto Pt(111),” *Physical Review B*, vol. 52, pp. 17449–17460, 1995.
- [137] M. Sancrotti, F. Ciccacci, M. Finazzi, E. Vescovo, and S. F. Alvarado, “Covalency in the electronic structure of Fe_3O_4 : an ultraviolet inverse photoemission investigation,” *Zeitschrift für Physik B*, vol. 84, no. 2, pp. 243–246, 1991.
- [138] Y. Q. Cai, M. Ritter, W. Weiss, and A. M. Bradshaw, “Valence-band structure of epitaxially grown Fe_3O_4 (111) films,” *Physical Review B*, vol. 58, p. 5042, 1998.
- [139] J. H. Park, L. H. Tjeng, J. W. Allen, P. Metcalf, and C. T. Chen, “Single-particle gap above the Verwey transition in Fe_3O_4 ,” *Physical Review B*, vol. 55, no. 19, pp. 12813–12817, 1997.

- [140] A. Schlegel, S. F. Alvarado, and P. Wachter, "Optical properties of magnetite (Fe_3O_4)," *Journal of Physics C*, vol. 12, no. 6, pp. 1157–1164, 1979.
- [141] S. K. Park, T. Ishikawa, and Y. Tokura, "Charge-gap formation upon the Verwey transition in Fe_3O_4 ," *Physical Review B*, vol. 58, no. 7, p. 3717, 1998.
- [142] X.-X. Zhang, J. Schoenes, W. Reim, and P. Wachter, "Evidence for $3d^n$ to $3d^{n-1}4s$ transitions in magnetite and in lithium and magnesium ferrites," *Journal of Physics C*, vol. 16, no. 31, pp. 6055–6072, 1983.
- [143] W. F. J. Fontijn, P. J. van der Zaag, M. A. C. Devillers, V. A. M. Brabers, and R. Metselaar, "Optical and magneto-optical polar Kerr spectra of Fe_3O_4 and Mg^{2+} - or Al^{3+} -substituted Fe_3O_4 ," *Physical Review B*, vol. 56, no. 9, pp. 5432–5442, 1997.
- [144] Z. Simsa, H. LeGall, and P. Siroky, "Polar Kerr effect of magnetite in the visible and near infrared spectral regions," *Physica Status Solidi B*, vol. 100, no. 2, pp. 665–670, 1980.
- [145] Z. Simsa, P. Siroky, P. J. Kolacek, and V. A. Brabers, "Optical and magneto-optical properties of magnetite and manganese ferrites," *Journal of Magnetism and Magnetic Materials*, vol. 15–18, part 2, pp. 775–776, 1980.
- [146] X. Zhang, J. Schoenes, and P. Wachter, "Kerr-effect and dielectric tensor elements of magnetite (Fe_3O_4) between 0.5 and 4.3 eV," *Solid State Communications*, vol. 39, no. 1, pp. 189–192, 1981.
- [147] S. Visnovsky, V. Prosser, R. Krishnan, V. Parizek, K. Nitsch, and L. Svobodova, "Magneto-optical Polar Kerr effect in ferrimagnetic garnets and spinels," *IEEE Transactions on Magnetics*, vol. 17, no. 6, pp. 3205–3210, 1981.
- [148] W. F. J. Fontijn, P. J. van der Zaag, and R. Metselaar, "On the origin of the magneto-optical effects in Li, Mg, Ni, and Co ferrite," *Journal of Applied Physics*, vol. 83, no. 11, pp. 6765–6767, 1998.
- [149] W. F. J. Fontijn, P. J. van der Zaag, L. F. Feiner, R. Metselaar, and M. A. C. Devillers, "A consistent interpretation of the magneto-optical spectra of spinel type ferrites (invited)," *Journal of Applied Physics*, vol. 85, no. 8, pp. 5100–5105, 1999.
- [150] P. Kuiper, B. G. Searle, L.-C. Duda, R. M. Wolf, and P. J. van der Zaag, "Fe $L_{2,3}$ linear and circular magnetic dichroism of Fe_3O_4 ," *Journal of Electron Spectroscopy and Related Phenomena*, vol. 86, no. 1–3, pp. 107–113, 1997.
- [151] T. Koide, T. Shidara, K. Ymaguchi et al., "Core-level magnetic circular dichroism in Fe_3O_4 and CoFe_2O_4 ," *Journal of Electron Spectroscopy and Related Phenomena*, vol. 78, pp. 275–278, 1996.
- [152] A. Yanase and K. Siratori, "Band structure in the high temperature phase of Fe_3O_4 ," *Journal of the Physical Society of Japan*, vol. 53, no. 1, pp. 312–317, 1984.
- [153] Z. Zhang and S. Satpathy, "Electron states, magnetism, and the Verwey transition in magnetite," *Physical Review B*, vol. 44, no. 24, pp. 13319–13331, 1991.
- [154] V. I. Anisimov, I. S. Elfimov, N. Hamada, and K. Terakura, "Charge-ordered insulating state of Fe_3O_4 from first-principles electronic structure calculations," *Physical Review B*, vol. 54, no. 7, pp. 4387–4390, 1996.
- [155] I. Leonov, A. N. Yaresko, V. N. Antonov, and V. I. Anisimov, "Electronic structure of charge-ordered Fe_3O_4 from calculated optical, magneto-optical Kerr effect, and O K-edge X-ray absorption spectra," *Physical Review B*, vol. 74, no. 16, Article ID 165117, 2006.
- [156] P. W. Anderson, "Ordering and antiferromagnetism in ferrites," *Physical Review*, vol. 102, no. 4, pp. 1008–1013, 1956.
- [157] R. Alben, "Nematic-smectic transitions in mixtures—a liquid crystal tricritical point," *Solid State Communications*, vol. 13, no. 11, pp. 1783–1785, 1973.
- [158] J. R. Cullen and E. Callen, "Band theory of multiple ordering and the metal-semiconductor transition in magnetite," *Physical Review Letters*, vol. 26, no. 5, pp. 236–238, 1971.
- [159] J. R. Cullen and E. R. Callen, "Multiple ordering in magnetite," *Physical Review B*, vol. 7, no. 1, pp. 397–402, 1973.
- [160] N. F. Mott, "The effect of electron interaction on variable-range hopping," *Philosophical Magazine*, vol. 34, no. 4, pp. 643–645, 1976.
- [161] N. F. Mott, "Electrons in disordered structures," *Advances in Physics*, vol. 16, no. 61, pp. 49–144, 1967.
- [162] N. F. Mott, "Hopping conduction and the Coulomb gap; applications to Fe_3O_4 , Ti_4O_7 and impurity conduction in Si:P," in *Festkörperprobleme*, vol. 19 of *Advances in Solid State Physics*, p. 331, Friedr. Vieweg & Sohn Verlagsgesellschaft mbH, 1979.
- [163] B. K. Chacraverty, "Verwey ordering on magnetite as a cooperative Jahn-Teller transition," *Solid State Communications*, vol. 15, pp. 1271–1275, 1974.
- [164] M. Mizoguchi, "NMR study of the low temperature phase of Fe_3O_4 . I. Experiments," *Journal of the Physical Society of Japan*, vol. 44, no. 5, pp. 1501–1511, 1978.
- [165] M. Mizoguchi, "NMR study of the low temperature phase of Fe_3O_4 . II. Electron ordering analysis," *Journal of the Physical Society of Japan*, vol. 44, no. 5, pp. 1512–1520, 1978.
- [166] N. C. Tombs and H. P. Rooksby, "Structure transition and antiferromagnetism in magnetite," *Acta Crystallographica*, vol. 4, pp. 474–475, 1951.
- [167] H. P. Rooksby and B. T. M. Willis, "The low-temperature crystal structure of magnetite," *Acta Crystallographica*, vol. 6, pp. 565–566, 1953.
- [168] E. J. Samuelsen, E. J. Bleeker, L. Dobrzynski, and T. Riste, "Neutron scattering from magnetite below 119°K," *Journal of Applied Physics*, vol. 39, no. 2, pp. 1114–1115, 1968.
- [169] T. Yamada, K. Suzuki, and S. Chikazumi, "Electron microscopy of orthorhombic phase in magnetite," *Applied Physics Letters*, vol. 13, no. 5, pp. 172–174, 1968.
- [170] J. Yoshida and S. Iida, "X-ray study of the phase transition in magnetite," *Journal of the Physical Society of Japan*, vol. 47, no. 5, pp. 1627–1633, 1979.
- [171] Y. Miyamoto and M. Shindo, "Magnetolectric measurement of magnetite (Fe_3O_4) at low temperatures and direct evidence for nonexistence of ac mirror plane," *Journal of the Physical Society of Japan*, vol. 62, no. 5, pp. 1423–1426, 1993.
- [172] Several reviews of research on the Verwey transition up to 1980 are contained in the special issue of *Philos. Mag. B* 42, (1980).
- [173] J. M. Zuo, J. C. H. Spence, and W. Petuskey, "Charge ordering in magnetite at low temperatures," *Physical Review B*, vol. 42, no. 13, pp. 8451–8464, 1990.
- [174] N. F. Mott, "Materials with mixed valency that show a Verwey transition," *Philosophical Magazine B*, vol. 42, pp. 327–335, 1980.
- [175] Y. Yamada, "Molecular polarons and valence fluctuations in Fe_3O_4 ," *Philosophical Magazine B*, vol. 42, pp. 377–385, 1980.
- [176] D. Ihle and B. Lorenz, "Small-polaron conduction and short-range order in Fe_3O_4 ," *Journal of Physics C*, vol. 19, p. 5239, 1986.
- [177] H. Seo, M. Ogata, and H. Fukuyama, "Aspects of the Verwey transition in magnetite," *Physical Review B*, vol. 65, Article ID 085107, 9 pages, 2002.

- [178] N. E. Brese and M. O’Keeffe, “Bond-valence parameters for solids,” *Acta Crystallographica Section B*, vol. 47, pp. 192–197, 1991.
- [179] J. P. Wright, J. P. Attfield, and P. G. Radaelli, “Charge ordered structure of magnetite Fe_3O_4 below the Verwey transition,” *Physical Review B*, vol. 66, no. 21, Article ID 214422, 15 pages, 2002.
- [180] J. Garcia, G. Subias, J. Blasco, and M. G. Proietti, “Comment on “Long range ordering in magnetite below the Verwey transition”,” <http://arxiv.org/abs/cond-mat/0211407>.
- [181] I. Leonov, A. N. Yaresko, V. N. Antonov, M. A. Korotin, and V. I. Anisimov, “Charge and orbital order in Fe_3O_4 ,” *Physical Review Letters*, vol. 93, no. 14, Article ID 146404, 4 pages, 2004.
- [182] H. T. Jeng, G. Y. Guo, and D. J. Huang, “Charge-orbital ordering and verwey transition in magnetite,” *Physical Review Letters*, vol. 93, no. 15, Article ID 156403, 4 pages, 2004.
- [183] I. Leonov, A. N. Yaresko, V. N. Antonov, J. P. Attfield, and V. I. Anisimov, “Charge order in Fe_2OBO_3 : an LSDA+U study,” *Physical Review B*, vol. 72, no. 1, Article ID 014407, 7 pages, 2005.
- [184] I. Leonov, A. N. Yaresko, V. N. Antonov, U. Schwingenschlogl, V. Eyert, and V. I. Anisimov, “Charge order and spin-singlet pairs formation in Ti_4O_7 ,” *Journal of Physics: Condensed Matter*, vol. 18, no. 48, p. 10955, 2006.
- [185] A. Yaresko, I. Leonov, and P. Fulde, “Electronic structure and exchange couplings in AlV_2O_4 ,” *Physica B*, vol. 378–380, pp. 1054–1055, 2006.
- [186] I. Leonov, *Charge order in transition metal oxides*, Ph.D. thesis, Universität Augsburg, Augsburg, Germany, 2006.
- [187] I. Leonov, A. N. Yaresko, V. N. Antonov, U. Schwingenschlogl, V. Eyert, and V. I. Anisimov, “Charge order and spin-singlet pair formation in Ti_4O_7 ,” *Journal of Physics: Condensed Matter*, vol. 18, no. 48, pp. 10955–10964, 2006.
- [188] L. Neel, “Magnetic properties of ferrites: ferromagnetism and antiferromagnetism,” *Annals of Physics*, vol. 3, pp. 137–198, 1948.
- [189] C. G. Shull, E. O. Wollan, and W. C. Koehler, “Neutron scattering and polarization by ferromagnetic materials,” *Physical Review*, vol. 84, no. 5, pp. 912–921, 1951.
- [190] V. C. Rakhecha and N. S. Murthy, “Spin-transfer due to covalency for the tetrahedral-site Fe^{3+} ions in Fe_3O_4 ,” *Journal of Physics C*, vol. 11, no. 21, pp. 4389–4404, 1978.
- [191] V. N. Antonov, B. N. Harmon, and A. N. Yaresko, “Electronic structure and X-ray magnetic circular dichroism in Fe_3O_4 and Mn-, Co-, or Ni-substituted Fe_3O_4 ,” *Physical Review B*, vol. 67, no. 2, Article ID 024417, 14 pages, 2003.
- [192] G. Van Der Laan, C. M. B. Henderson, R. A. D. Patrick et al., “Orbital polarization in NiFe_2O_4 measured by Ni-2p X-ray magnetic circular dichroism,” *Physical Review B*, vol. 59, no. 6, pp. 4314–4321, 1999.
- [193] W. F. Pong, Y. K. Chang, M. H. Su et al., “Magnetic orientation of Ni in Zn-Ni ferrites studied by soft-X-ray magnetic circular dichroism,” *Physical Review B*, vol. 55, no. 17, pp. 11409–11413, 1997.
- [194] S. Suga and S. Imada, “Magnetic dichroism in core absorption and photoemission,” *Journal of Electron Spectroscopy and Related Phenomena*, vol. 92, no. 1–3, pp. 1–9, 1998.
- [195] H. Ebert, “Magneto-optical effects in transition metal systems,” *Reports on Progress in Physics*, vol. 59, no. 12, pp. 1665–1735, 1996.
- [196] M. Iizumi, T. F. Koetzle, G. Shirane, S. Chikazumi, M. Matsui, and S. Todo, “Structure of magnetite (Fe_3O_4) below the Verwey transition temperature,” *Acta Crystallographica Section B*, vol. 38, no. 8, pp. 2121–2133, 1982.
- [197] J. Chen, D. J. Huang, A. Tanaka et al., “Magnetic circular dichroism in Fe 2p resonant photoemission of magnetite,” *Physical Review B*, vol. 69, no. 8, Article ID 085107, 8 pages, 2004.
- [198] A. Yanase and N. Hamada, “Electronic structure in high temperature phase of Fe_3O_4 ,” *Journal of the Physical Society of Japan*, vol. 68, no. 5, pp. 1607–1613, 1999.
- [199] K. I. Kugel and D. I. Khomskii, *Soviet Physics. Solid State*, vol. 17, p. 285, 1975.
- [200] K. I. Kugel and D. I. Khomskii, “The Jahn-Teller effect and magnetism: transition metal compounds,” *Soviet Physics-Uspokhi*, vol. 25, p. 231, 1982.
- [201] H. Häffner, *Untersuchung des Verwey-übergangs in Magnetit unter uniaxialem Druck*, Diplomarbeit, Universität Augsburg, Augsburg, Germany, 2003.
- [202] I. Loa, X. Wang, K. Syassen et al., “Pressure-driven orbital reorientation and change in Mott-Hubbard gap in YTiO_3 ,” <http://arxiv.org/abs/cond-mat/0504383>.
- [203] D. J. Huang, C. F. Chang, H. T. Jeng et al., “Spin and orbital magnetic moments of Fe_3O_4 ,” *Physical Review Letters*, vol. 93, no. 7, Article ID 077204, 2004.
- [204] E. Goering, S. Gold, M. Lafkioti, and G. Schutz, “Vanishing Fe 3d orbital moments in single-crystalline magnetite,” *Europhysics Letters*, vol. 73, no. 1, pp. 97–103, 2006.
- [205] A. I. Liechtenstein, V. I. Anisimov, and J. Zaanen, “Density-functional theory and strong interactions: orbital ordering in Mott-Hubbard insulators,” *Physical Review B*, vol. 52, no. 8, pp. R5467–R5470, 1995.
- [206] J. Loos and P. Novák, “Double exchange and superexchange in a ferrimagnetic half-metal,” *Physical Review B*, vol. 66, no. 13, Article ID 132403, 4 pages, 2002.
- [207] C. M. Srivastava, G. Srinivasan, and N. G. Nanadikar, “Exchange constants in spinel ferrites,” *Physical Review B*, vol. 19, no. 1, pp. 499–508, 1979.
- [208] J. P. Attfield, A. M. T. Bell, L. M. Rodriguez-Martinez et al., “Synthesis, structure and properties of a semivalent iron oxoborate, Fe_2OBO_3 ,” *Journal of Materials Chemistry*, vol. 9, no. 1, pp. 205–209, 1999.
- [209] R. J. Goff, A. J. Williams, and J. P. Attfield, “Spin, charge, and orbital order in Mn_2OBO_3 ,” *Physical Review B*, vol. 70, no. 1, Article ID 014426, 5 pages, 2004.
- [210] N. Suda, K. Kohn, and S. Nakamura, “Dielectric and magnetic properties of a mixed valence oxide Fe_2BO_4 ,” *Ferroelectrics*, vol. 286, pp. 155–165, 2003.
- [211] I. Leonov, A. N. Yaresko, V. N. Antonov, J. P. Attfield, and V. I. Anisimov, “Charge order in Fe_2OBO_3 : an LSDA+U study,” *Physical Review B*, vol. 72, no. 1, Article ID 014407, 7 pages, 2005.
- [212] A. P. Douvalis, V. Papaefthymiou, A. Moukarika, T. Bakas, and G. Kallias, “Mössbauer and magnetization studies of Fe_2BO_4 ,” *Journal of Physics: Condensed Matter*, vol. 12, no. 2, pp. 177–188, 2000.
- [213] G. K. Rozenberg, G. R. Hearne, M. P. Pasternak, P. A. Metcalf, and J. M. Honig, “Nature of the Verwey transition in magnetite (Fe_3O_4) to pressures of 16 GPa,” *Physical Review B*, vol. 53, no. 10, pp. 6482–6487, 1996.
- [214] U. Schwingenschlogl, V. Eyert, and U. Eckern, “From VO_2 to V_2O_3 : the metal-insulator transition of the Magnéli phase V_6O_{11} ,” *Europhysics Letters*, vol. 61, no. 3, p. 361, 2003.
- [215] R. M. Wentzcovitch, W. W. Schulz, and P. B. Allen, “ VO_2 : Peierls or Mott-Hubbard? A view from band theory,” *Physical Review Letters*, vol. 72, no. 21, pp. 3389–3392, 1994.

- [216] M. A. Korotin, N. A. Skorikov, and V. I. Anisimov, "Variation of orbital symmetry of the localized $3d^1$ electron of the V^{4+} ion upon the metal-insulator transition in VO_2 ," *Physics of Metals and Metallography*, vol. 94, no. 1, pp. 17–23, 2002.
- [217] V. Eyert, "The metal-insulator transition of NbO_2 : an embedded Peierls instability," *Europhysics Letters*, vol. 58, no. 6, pp. 851–856, 2002.
- [218] S. Biermann, A. Poteryaev, A. I. Lichtenstein, and A. Georges, "Dynamical singlets and correlation-assisted peierls transition in VO_2 ," *Physical Review Letters*, vol. 94, no. 2, Article ID 026404, 2005.
- [219] S. Lakkis, C. Schlenker, B. K. Chakraverty, R. Buder, and M. Marezio, "Metal-insulator transitions in Ti_4O_7 single crystals: crystal characterization, specific heat, and electron paramagnetic resonance," *Physical Review B*, vol. 14, no. 4, pp. 1429–1440, 1976.
- [220] Y. Le Page and M. Marezio, "Structural chemistry of magnéli phases Ti_nO_{2n-1} ($4 \leq n \leq 9$). IV. Superstructure in Ti_4O_7 at 140 K," *Journal of Solid State Chemistry*, vol. 53, no. 1, pp. 13–21, 1984.
- [221] V. Eyert, U. Schwingenschlöggl, and U. Eckern, "Charge order, orbital order, and electron localization in the Magnéli phase Ti_4O_7 ," *Chemical Physics Letters*, vol. 390, no. 1–3, pp. 151–156, 2004.
- [222] V. I. Anisimov, D. E. Kondakov, A. V. Kozhevnikov et al., "Full orbital calculation scheme for materials with strongly correlated electrons," *Physical Review B*, vol. 71, no. 12, Article ID 125119, 16 pages, 2005.
- [223] M. Isobe and Y. Ueda, "Magnetic susceptibility of quasi-one-dimensional compound α' - NaV_2O_5 possible spin-Peierls compound with high critical temperature of 34 K," *Journal of the Physical Society of Japan*, vol. 65, no. 5, pp. 1178–1181, 1996.
- [224] M. Hase, I. Terasaki, and K. Uchinokura, "Observation of the spin-peierls transition in linear Cu^{2+} (spin-1/2) chains in an inorganic compound $CuGeO_3$," *Physical Review Letters*, vol. 70, no. 23, pp. 3651–3654, 1993.
- [225] A. Carpy and J. Galy, "Affinement de la structure cristalline du bronze $NaV_2O_5\alpha'$," *Acta Crystallographica Section B*, vol. 31, pp. 1481–1482, 1975.
- [226] H. von Schnering, Y. Grin, M. Knaupp et al., "Different structures for two very similar 2-benzoylpyridine azacyclothiosemicarbazones," *Zeitschrift für Kristallographie*, vol. 213, no. 4, pp. 246–248, 1998.
- [227] H. Smolinski, C. Gros, W. Weber et al., " NaV_2O_5 as a quarter-filled ladder compound," *Physical Review Letters*, vol. 80, no. 23, pp. 5164–5167, 1998.
- [228] T. Ohama, M. Isobe, H. Yasuoka, and Y. Ueda, " ^{23}Na NMR study of spin-Peierls transition in NaV_2O_5 ," *Journal of the Physical Society of Japan*, vol. 66, p. 545, 1977.
- [229] T. Ohama, H. Yasuoka, M. Isobe, and Y. Ueda, "Mixed valency and charge ordering in α' - NaV_2O_5 ," *Physical Review B*, vol. 59, no. 5, pp. 3299–3302, 1999.
- [230] M. Köppen, D. Pankert, R. Hauptmann et al., "Interference of a first-order transition with the formation of a spin-Peierls state in α' - NaV_2O_5 ," *Physical Review B*, vol. 57, no. 14, pp. 8466–8471, 1998.
- [231] P. Thalmeier and P. Fulde, "Charge ordering and spin-Peierls transition in α' - NaV_2O_5 ," *Europhysics Letters*, vol. 44, no. 2, pp. 242–248, 1998.
- [232] T. Chatterji, K. D. Liß, G. J. McIntyre, M. Weiden, R. Hauptmann, and C. Geibel, "The ground state of NaV_2O_5 ," *Solid State Communications*, vol. 108, no. 1, pp. 23–26, 1998.
- [233] H. Seo and H. Fukuyama, "Charge ordering and spin gap in NaV_2O_5 ," *Journal of the Physical Society of Japan*, vol. 67, no. 8, pp. 2602–2605, 1998.
- [234] J. Lüdecke, A. Jobst, S. van Smaalen, E. Morré, C. Geibel, and H.-G. Krane, "Acentric low-temperature superstructure of NaV_2O_5 ," *Physical Review Letters*, vol. 82, no. 18, pp. 3633–3636, 1999.
- [235] T. T. Yoshida, M. Nishi, K. Nakajima et al., "Spin dynamics in NaV_2O_5 —inelastic neutron scattering," *Journal of the Physical Society of Japan*, vol. 67, pp. 744–747, 1998.
- [236] C. Gros and R. Valenti, "Magnon splitting induced by charge ordering in NaV_2O_5 ," *Physical Review Letters*, vol. 82, pp. 976–979, 1999.
- [237] S. A. Golubchik, M. Isobe, A. N. Ivlev et al., "Raman, infrared and optical spectra of spin-peierls compound NaV_2O_5 ," *Journal of the Physical Society of Japan*, vol. 68, p. 318, 1999.
- [238] A. Damascelli, D. van der Marel, M. Grüninger et al., "Direct two-magnon optical absorption in α' - NaV_2O_5 : "Charged" magnons," *Physical Review Letters*, vol. 81, no. 4, pp. 918–921, 1998.
- [239] V. C. Long, Z. Zhu, J. L. Musfeldt et al., "Polarized optical reflectance and electronic band structure of α' - NaV_2O_5 ," *Physical Review B*, vol. 60, no. 23, pp. 15721–15727, 1999.
- [240] Z. S. Popović and F. R. Vukajlović, "Coulomb-correlated band structure of one-dimensional spin-Peierls α' - NaV_2O_5 ," *Physical Review B*, vol. 59, pp. 5333–5340, 1999.
- [241] H. Wu and Q.-Q. Zheng, "Electronic structure of the spin-Peierls system NaV_2O_5 ," *Physical Review B*, vol. 59, no. 23, pp. 15027–15032, 1999.
- [242] N. Katoh, T. Miyazaki, and T. Ohno, "First-principles study on the insulating state of α' - NaV_2O_5 ," *Physical Review B*, vol. 59, no. 20, pp. R12723–R12727, 1999.
- [243] P. Horsch and F. Mack, "A new view of the electronic structure of the spin-Peierls compound α' - NaV_2O_5 ," *The European Physical Journal B*, vol. 5, pp. 367–370, 1998.
- [244] A. Carpy, A. Casalot, M. Pouchard, J. Galy, and P. Hagenmüller, "Propriétés électriques et magnétiques des bronzes oxyfluorés de vanadium de formule α' - $NaV_2O_{5-x}F_x$ ($0 \leq x \leq 1$)," *Journal of Solid State Chemistry*, vol. 5, no. 2, pp. 229–238, 1972.
- [245] A. N. Yaresko, V. N. Antonov, H. Eschrig, P. Thalmeier, and P. Fulde, "Electronic structure and exchange coupling in α' - NaV_2O_5 ," *Physical Review B*, vol. 62, no. 23, pp. 15538–15546, 2000.
- [246] I. Solovyev, N. Hamada, and K. Terakura, " t_{2g} versus all $3d$ localization in $LaMO_3$ perovskites ($M = Ti-Cu$): first-principles study," *Physical Review B*, vol. 53, no. 11, pp. 7158–7170, 1996.
- [247] A. I. Smirnov, M. N. Popova, A. B. Sushkov et al., "High-frequency dielectric and magnetic anomaly at the phase transition in NaV_2O_5 ," *Physical Review B*, vol. 59, no. 22, pp. 14546–14551, 1999.
- [248] M. Poirier, P. Fertey, J. Jegoudez, and A. Revcolevschi, "Dielectric behavior and charge ordering in NaV_2O_5 ," *Physical Review B*, vol. 60, no. 10, pp. 7341–7345, 1999.
- [249] S. Atzkern, M. Knupfer, M. S. Golden et al., "One-dimensional dynamics of the d electrons in α' - NaV_2O_5 ," *Physical Review B*, vol. 63, Article ID 165113, 16 pages, 2001.
- [250] R. Pittini, J. Schoenes, and P. Wachter, "MO Kerr study of the $4f_1$ state," *Physica B*, vol. 230–232, pp. 538–543, 1997.
- [251] K. Hiraoka, R. Pittini, and P. Wachter, "Hall effect in Cemonochalcogenides CeX ($X = S, Se, Te$)," *Physica B*, vol. 230–232, pp. 136–138, 1997.

- [252] N. Takeda, Y. S. Kwon, Y. Haga, N. Sato, T. Suzuki, and T. Komatsubara, "Fermi surface and cyclotron mass of extremely low carrier system CeAs," *Physica B*, vol. 186–188, pp. 153–155, 1993.
- [253] J. Schoenes and F. Hulliger, "Transport properties of cerium monochalcogenides," *Journal of Magnetism and Magnetic Materials*, vol. 63–64, pp. 43–45, 1987.
- [254] P. Schobinger-Papamantellos, A. Niggli, P. Fischer, E. Kaldis, and V. Hildebrandt, "Magnetic ordering of rare earth monochalcogenides. I. Neutron diffraction investigation of CeS, NdS, NdSe, NdTe and TbSe," *Journal of Physics C*, vol. 7, no. 11, pp. 2023–2038, 1974.
- [255] W. Reim, "Magneto-optical Kerr-effect of uranium compounds: a study of the electronic structure," *Journal of Magnetism and Magnetic Materials*, vol. 58, pp. 1–47, 1986.
- [256] R. Pittini, J. Schoenes, and P. Wachter, "Optical and magneto-optical properties of the cerium monochalcogenides," *Physica B*, vol. 206–207, pp. 92–94, 1995.
- [257] R. Pittini, J. Schoenes, and P. Wachter, "Giant magneto-optical Kerr rotation observed in CeS single crystals," *Physical Review B*, vol. 55, no. 12, pp. 7524–7532, 1997.
- [258] S. P. Lim, D. L. Price, and B. R. Cooper, "Giant magneto-optic rotations: the role of orbital polarization and explicit correlation effects," *IEEE Transactions on Magnetics*, vol. 27, no. 4, pp. 3648–3654, 1991.
- [259] B. R. Cooper, S. P. Lim, I. Avgin, Q. G. sheng, and D. L. Price, "Trade-off between increased size and increased broadening of magneto-optic effects in cerium and uranium systems," *Journal of Physics and Chemistry of Solids*, vol. 56, no. 11, pp. 1509–1516, 1995.
- [260] D. L. Price, B. R. Cooper, S. P. Lim, and I. Avgin, "Variation of the LDA + U method appropriate to f -state localization: application to magneto-optical properties," *Physical Review B*, vol. 61, pp. 9867–9870, 2000.
- [261] V. N. Antonov, B. N. Harmon, and A. N. Yaresko, unpublished results, 1999.
- [262] R. Pittini, J. Schoenes, O. Vogt, and P. Wachter, "Discovery of 90 degree magneto-optical polar Kerr rotation in CeSb," *Physical Review Letters*, vol. 77, no. 5, pp. 944–947, 1996.
- [263] J. Schoenes and W. Reim, "The $f \rightarrow d$ oscillator strength in rare earth compounds as indicator of 4f delocalization," *Journal of The Less-Common Metals*, vol. 112, no. 1–2, pp. 19–25, 1985.
- [264] W. Reim, J. Schoenes, F. Hulliger, and O. Vogt, "Giant Kerr rotation and electronic structure of $\text{CeSb}_x\text{Te}_{1-x}$," *Journal of Magnetism and Magnetic Materials*, vol. 54–57, no. 3, pp. 1401–1402, 1986.
- [265] Y.-S. Kwon, T. Suzuki, and T. Kasuya, *Japanese Journal of Applied Physics*, vol. 8, p. 104, 1993.
- [266] F. Salghetti-Drioli, K. Mattenberger, P. Wachter, and L. Degiorgi, "The puzzle of the 90° Kerr rotation in CeSb," *Solid State Communications*, vol. 109, no. 11, pp. 687–691, 1999.
- [267] Y. A. Uspenskii, V. P. Antropov, and B. N. Harmon, "90° magneto-optical Kerr rotation: criteria of existence and features," *Physical Review B*, vol. 56, no. 18, pp. R11396–R11398, 1997.
- [268] U. Pustogowa, W. Hubner, and K. H. Bennemann, "The origin of the 90 degree magneto-optical Kerr rotation in CeSb," *Solid State Communications*, vol. 106, pp. 769–774, 1998.
- [269] A. I. Liechtenstein, V. P. Antropov, and B. N. Harmon, "Electronic structure and magneto-optical effects in CeSb," *Physical Review B*, vol. 49, no. 15, pp. 10770–10773, 1994.
- [270] V. N. Antonov, B. N. Harmon, and A. N. Yaresko, unpublished results, 2000.
- [271] Y. Baer, R. Hauger, C. Zürcher, M. Campagna, and G. K. Wertheim, "X-ray photoemission study of Ce-pnictides," *Physical Review B*, vol. 18, no. 8, pp. 4433–4439, 1978.
- [272] A. Franciosi, J. H. Weaver, N. Mårtensson, and M. Croft, "Evidence of 4f photoemission satellites in cerium compounds," *Physical Review B*, vol. 24, no. 6, pp. 3651–3654, 1981.
- [273] W. Gudat, M. Iwan, R. Pinchauh, and F. Hulliger, "Electronic structure of Ce pnictides and chalcogenides by photoelectron spectroscopy with synchrotron radiation," in *Valence Instabilities*, P. Wachter and H. Boppert, Eds., p. 249, North-Holland, Amsterdam, The Netherlands, 1982.
- [274] P. Fischer, G. Meier, B. Lebeck, B. D. Rainford, and O. Vogt, "Magnetic phase transitions of CeSb. I. Zero applied magnetic field," *Journal of Physics C*, vol. 11, no. 2, pp. 345–364, 1978.
- [275] G. Meier, P. Fischer, W. Halg, B. Lebeck, B. D. Rainford, and O. Vogt, "Magnetic phase transitions of CeSb. II. Effects of applied magnetic fields," *Journal of Physics C*, vol. 11, no. 6, pp. 1173–1186, 1978.
- [276] P. M. Oppeneer, A. Y. Perlov, V. N. Antonov, A. N. Yaresko, T. Kraft, and M. S. S. Brooks, "Optical and magneto-optical spectroscopy of uranium and plutonium compounds: recent theoretical progress," *Journal of Alloys and Compounds*, vol. 271–273, pp. 831–836, 1998.
- [277] M. S. S. Brooks and B. Johansson, "Ferromagnetic materials," in *Handbook of Magnetic Materials*, K. H. J. Buschow, Ed., vol. 7, p. 139, North-Holland, Amsterdam, The Netherlands, 1993.
- [278] J. Déportes, D. Givord, and K. R. A. Ziebeck, "Evidence of short range magnetic order at four times T_c in a metallic compound containing Fe: susceptibility and paramagnetic scattering in CeFe_2 ," *Journal of Applied Physics*, vol. 52, no. 3, pp. 2074–2076, 1981.
- [279] C. Giorgetti, S. Pizzini, E. Dartyge et al., "Magnetic circular X-ray dichroism in Ce intermetallic compounds," *Physical Review B*, vol. 48, no. 17, pp. 12732–12742, 1993.
- [280] L. Paolasini, P. Dervenagas, P. Vulliet et al., "Magnetic response function of the itinerant ferromagnet CeFe_2 ," *Physical Review B*, vol. 58, no. 18, pp. 12117–12124, 1998.
- [281] L. Paolasini, B. Ouladdiaf, N. Bernhoeft et al., "Magnetic ground state of pure and doped CeFe_2 ," *Physical Review Letters*, vol. 90, no. 5, Article ID 057201, 4 pages, 2003.
- [282] H. Fukuda, H. Fujii, H. Kamura, A. Uchida, M. Kosaka, and Y. Uwatoko, "Near the collapse of ferromagnetism in CeFe_2 under high pressures," *Journal of Magnetism and Magnetic Materials*, vol. 226–230, pp. 1200–1202, 2001.
- [283] T. Fujiwara, H. Fujii, Y. Ishii et al., "Evidence of the anisotropically developed antiferromagnetic spin fluctuation in CeFe_2 under high pressures," *Physica B*, vol. 312–313, pp. 336–338, 2002.
- [284] O. Eriksson, L. Nordström, M. S. S. Brooks, and B. Johansson, "4f-band magnetism in CeFe_2 ," *Physical Review Letters*, vol. 60, no. 24, pp. 2523–2526, 1988.
- [285] P. K. Khowash, "Anomalous magnetic behavior in pseudobinary compounds of CeFe_2 ," *Physical Review B*, vol. 43, no. 7, pp. 6170–6173, 1991.
- [286] J. Trygg, J. M. Wills, B. Johansson, and O. Eriksson, "First-principles study of the magnetization density in CeFe_2 ," *Physical Review B*, vol. 50, no. 6, pp. 4200–4203, 1994.
- [287] T. Konishi, K. Morikawa, K. Kobayashi et al., "Electronic structure of the strongly hybridized ferromagnet CeFe_2 ," *Physical Review B*, vol. 62, no. 21, pp. 14304–14312, 2000.

- [288] V. N. Antonov, D. A. Kukusta, and A. N. Yaresko, "X-ray magnetic circular dichroism in CeFe_2 : first-principles calculations," *Physical Review B*, vol. 78, no. 9, Article ID 094401, 2008.
- [289] V. N. Antonov, A. P. Shpak, and A. N. Yaresko, "X-ray magnetic circular dichroism in d and f ferromagnetic materials: recent theoretical progress. Part I," *Low Temperature Physics*, vol. 34, p. 1, 2008.
- [290] V. N. Antonov, A. P. Shpak, and A. N. Yaresko, "X-ray magnetic circular dichroism in d and f ferromagnetic materials: recent theoretical progress. Part II," *Low Temperature Physics*, vol. 34, p. 79, 2008.
- [291] J. P. Schillé, F. Bertran, M. Finazzi, C. Brouder, J. P. Kappler, and G. Krill, "4f orbital and spin magnetism in cerium intermetallic compounds studied by magnetic circular X-ray dichroism," *Physical Review B*, vol. 50, no. 5, pp. 2985–2989, 1994.
- [292] A. Delobbe, A. M. Dias, M. Finazzi, L. Stichauer, J. P. Kappler, and G. Krill, "X-ray magnetic circular dichroism study on CeFe_2 ," *Europhysics Letters*, vol. 43, no. 3, pp. 320–325, 1998.
- [293] M. Mizumaki, K. Yoshii, Y. Watanabe, and S. Nanao, "X-ray magnetic circular dichroism studies in $\text{Ce}(\text{Fe}_{1-x}\text{Co}_x)_2$," *Journal of Alloys and Compounds*, vol. 408–412, pp. 737–740, 2006.
- [294] F. Klose, O. Schulte, F. Rose et al., "Interfaces of Ce/Fe and La/Fe multilayers probed by magnetic circular X-ray dichroism," *Physical Review B*, vol. 50, no. 9, pp. 6174–6183, 1994.
- [295] O. Gunnarsson and K. Schönhammer, "Photoemission from Ce compounds: exact model calculation in the limit of large degeneracy," *Physical Review Letters*, vol. 50, no. 8, pp. 604–607, 1983.
- [296] J. W. Allen, S. J. Oh, O. Gunnarsson et al., "Electronic structure of cerium and light rare-earth intermetallics," *Advances in Physics*, vol. 35, no. 3, pp. 275–316, 1986.
- [297] H. Matsuyama, I. Harada, and A. Kotani, "Roles of 4 f-5 d exchange interactions in magnetic circular X-ray dichroism at the rare-earth $L_{2,3}$ edges," *Journal of the Physical Society of Japan*, vol. 66, no. 2, pp. 337–340, 1997.
- [298] K. Fukui, H. Matsuyama, I. Harada, J. C. Parlebas, and A. Kotani, "Phenomenological interpretation of MCXD in $L_{2,3}$ XAS of trivalent cerium compound," *Journal of Electron Spectroscopy and Related Phenomena*, vol. 104, pp. 67–72, 1999.
- [299] K. Asakura, K. Fukui, H. Ogasawara, I. Harada, J. C. Parlebas, and A. Kotani, "Theory of magnetic circular dichroism of the Ce $L_{2,3}$ X-ray absorption spectra in mixed valence compound CeFe_2 ," *Journal of the Physical Society of Japan*, vol. 73, p. 2008, 2004.
- [300] J. C. Parlebas and A. Kotani, "Electron correlation and surface/bulk effects in various spectra of Ce compounds," *Journal of Electron Spectroscopy and Related Phenomena*, vol. 136, pp. 3–14, 2004.
- [301] K. Asakura, A. Kotani, and I. Harada, "Theory of magnetic circular dichroism in resonant X-ray emission spectra at L_3 edge of mixed valence compound CeFe_2 ," *Journal of the Physical Society of Japan*, vol. 74, no. 4, pp. 1328–1333, 2005.
- [302] J. C. Parlebas, K. Asakura, A. Fujiwara, I. Harada, and A. Kotani, "X-ray magnetic circular dichroism at rare-earth $L_{2,3}$ absorption edges in various compounds and alloys," *Physics Reports*, vol. 431, no. 1, pp. 1–38, 2006.
- [303] S. D. Brown, P. Strange, L. Bouchenoire et al., "Dipolar excitations at the LIII X-ray absorption edges of the heavy rare-earth metals," *Physical Review Letters*, vol. 99, no. 24, Article ID 247401, 2007.
- [304] B. N. Harmon and V. N. Antonov, "Electronic structure and X-ray magnetic circular dichroism in $\text{Gd}_5(\text{Si}_2\text{Ge}_2)$," *Journal of Applied Physics*, vol. 93, no. 8, pp. 4678–4685, 2003.
- [305] J. W. Kim, Y. Lee, D. Wermeille et al., "Systematics of X-ray resonant scattering amplitudes in RNi_2Ge_2 ($R = \text{Gd, Tb, Dy, Ho, Er, Tm}$): The origin of the branching ratio at the L edges of the heavy rare earths," *Physical Review B*, vol. 72, no. 6, Article ID 064403, 6 pages, 2005.
- [306] Y. Lee, B. N. Harmon, A. I. Goldman, and J. C. Lang, "Temperature dependent X-ray magnetic circular dichroism in $\text{Er}_2\text{Fe}_{17}$," *Journal of Applied Physics*, vol. 101, no. 9, Article ID 09G525, 2007.
- [307] V. N. Antonov, B. N. Harmon, A. N. Yaresko, and A. P. Shpak, "X-ray magnetic circular dichroism in GdN: first-principles calculations," *Physical Review B*, vol. 75, no. 18, Article ID 184422, 2007.
- [308] S. Abdelouahed and M. Alouani, "Calculated electronic properties and structural phase transitions of GdN pnictide under hydrostatic pressure," *Physical Review B*, vol. 74, Article ID 214409, 7 pages, 2006.
- [309] M. Forsthuber, F. Lehner, G. Wiesinger et al., "Unstable magnetic ordering in $\text{Ce}(\text{Fe}_{1-x}\text{X}_x)_2$, $X = \text{Al, Ga, Si, Ru, Co}$," *Journal of Magnetism and Magnetic Materials*, vol. 90, pp. 471–473, 1990.
- [310] S. J. Kennedy and B. R. Coles, "The magnetic phases of pseudobinary $\text{Ce}(\text{Fe}_{1-x}\text{M}_x)_2$ intermetallic compounds; $M = \text{Al, Co, Ru}$," *Journal of Physics: Condensed Matter*, vol. 2, no. 5, pp. 1213–1222, 1990.
- [311] S. J. Kennedy, P. J. Brown, and B. R. Coles, "A polarized neutron study of the magnetic form factors in CeFe_2 ," *Journal of Physics: Condensed Matter*, vol. 5, no. 29, pp. 5169–5178, 1993.
- [312] M. J. Cooper, P. K. Lawson, M. A. G. Dixon et al., "Compton scattering study of 4f magnetism in CeFe_2 ," *Physical Review B*, vol. 54, no. 6, pp. 4068–4074, 1996.
- [313] V. N. Antonov, B. N. Harmon, and A. N. Yaresko, "Electronic structure of mixed-valence semiconductors in the LSDA + U approximation. I. Sm monochalcogenides," *Physical Review B*, vol. 66, Article ID 165208, 10 pages, 2002.
- [314] M. Campagna, E. Bucher, G. K. Wertheim, and L. D. Longinotti, "Valence mixing and semiconductor-metal transition in the Sm monochalcogenides," *Physical Review Letters*, vol. 33, no. 3, pp. 165–168, 1974.
- [315] B. Batlogg, E. Kaldis, A. Schlegel, and P. Wachter, "Electronic structure of Sm monochalcogenides," *Physical Review B*, vol. 14, no. 12, pp. 5503–5514, 1976.
- [316] A. Jayaraman, V. Narayanamurti, E. Bucher, and R. G. Maines, "Pressure-induced metal-semiconductor transition and 4f electron delocalization in Sm Te," *Physical Review Letters*, vol. 25, no. 6, pp. 368–370, 1970.
- [317] E. Bucher, V. Narayanamurti, and A. Jayaraman, "Magnetism, metal-insulator transition, and optical properties in Sm- and some other divalent rare-earth monochalcogenides," *Journal of Applied Physics*, vol. 42, no. 4, pp. 1741–1745, 1971.
- [318] A. F. Sovestnov, V. A. Shaburov, L. A. Markova, and E. M. Savitski, *Fizika Tverdogo Tela*, vol. 23, p. 2827, 1981, translated in *Soviet Physics. Solid State*, vol. 23, p. 1652, 1981.
- [319] J. M. D. Coey, S. K. Ghatak, M. Avignon, and F. Holtzberg, "Electronic configuration of samarium sulphide and related compounds: Mössbauer-effect measurements and a model," *Physical Review B*, vol. 14, no. 9, pp. 3744–3752, 1976.
- [320] M. B. Maple and D. Wohleben, *Physical Review Letters*, vol. 14, p. 3744, 1976.

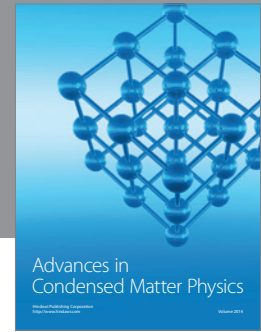
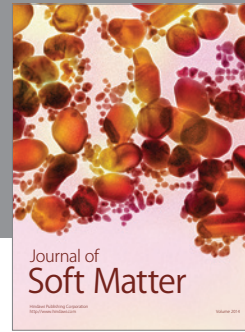
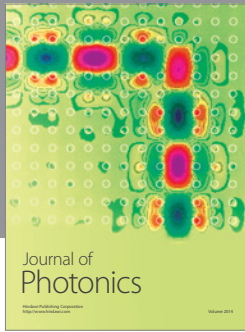
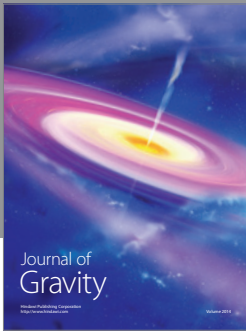
- [321] G. Travaglini and P. Wachter, "Low-energy electronic structure of intermediate-valence "golden" SmS," *Physical Review B*, vol. 30, no. 10, pp. 5877–5883, 1984.
- [322] S. D. Bader, N. E. Phillips, and D. B. McWhan, "Heat capacity and resistivity of metallic smS at high pressure," *Physical Review B*, vol. 7, no. 10, pp. 4686–4688, 1973.
- [323] E. E. Vanstein, S. M. Blokhin, and Y. B. Paderno, *Soviet Physics. Solid State*, vol. 6, p. 281, 1965.
- [324] P. S. Riseborough, "Heavy fermion semiconductors," *Advances in Physics*, vol. 49, no. 3, pp. 257–320, 2000.
- [325] L. Degiorgi, "The electrodynamic response of heavy-electron compounds," *Reviews of Modern Physics*, vol. 71, pp. 687–734, 1999.
- [326] Z. Fisk, J. L. Sarrao, S. L. Cooper et al., "Kondo insulators," *Physica B*, vol. 223–224, no. 1–4, pp. 409–412, 1996.
- [327] S. von Molnar, T. Theis, A. Benoit et al., "Study of the energy gap in single crystal SmB₆," in *Valence Instabilities*, P. Wachter and H. Boppert, Eds., pp. 389–395, North-Holland, Amsterdam, The Netherlands, 1982.
- [328] T. Nanba, H. Ohta, M. Motokawa, S. Kimura, S. Kunii, and T. Kasuya, "Gap state of SmB₆," *Physica B*, vol. 186–188, pp. 440–443, 1993.
- [329] P. A. Alekseev, V. A. Lazukov, R. Osborn et al., *Europhysics Letters*, vol. 23, p. 347, 1993.
- [330] J. M. Mignot, P. A. Alekseev, J. Rossat-Mignod, V. N. Lazukov, and I. P. Sadikov, "Local singlet bound state and magnetic excitations in mixed-valence SmB₆," *Physica B*, vol. 199–200, pp. 430–432, 1994.
- [331] P. A. Alekseev, J. M. Mignot, J. Rossat-Mignod et al., "Magnetic excitation spectrum of mixed-valence SmB₆ studied by neutron scattering on a single crystal," *Journal of Physics: Condensed Matter*, vol. 7, no. 2, pp. 289–305, 1995.
- [332] J. M. Mignot and P. A. Alekseev, "Neutron scattering studies of mixed-valence semiconductors," *Physica B*, vol. 215, no. 1, pp. 99–109, 1995.
- [333] G. Travaglini and P. Wachter, "Intermediate-valent SmB₆ and the hybridization model: an optical study," *Physical Review B*, vol. 29, no. 2, pp. 893–898, 1984.
- [334] B. Battlog, P. H. Schmidt, and J. M. Rowwel, in *Valence Fluctuations in Solids*, L. M. Falikov and W. Hunke, Eds., p. 357, North-Holland, Amsterdam, The Netherlands, 1981.
- [335] A. Menth, E. Buehler, and T. H. Geballe, "Magnetic and semiconducting properties of SmB₆," *Physical Review Letters*, vol. 22, no. 7, pp. 295–297, 1969.
- [336] J. C. Nickerson, R. M. White, K. N. Lee, R. Bachmann, T. H. Geballe, and G. W. Hull, "Physical properties of SmB₆," *Physical Review B*, vol. 3, no. 6, pp. 2030–2042, 1971.
- [337] J. W. Allen, B. Battlogg, and P. Wachter, "Large low-temperature Hall effect and resistivity in mixed-valent SmB₆," *Physical Review B*, vol. 20, no. 12, pp. 4807–4813, 1979.
- [338] J. C. Cooley, M. C. Aronson, Z. Fisk, and P. C. Canfield, "SmB₆: Kondo insulator or exotic metal?" *Physical Review Letters*, vol. 74, no. 9, pp. 1629–1632, 1995.
- [339] T. Kasuya, K. Takegahara, T. Fujita, T. Tanaka, and E. Bannai, "Valence fluctuating state in SmB₆," *Journal de Physique Colloques*, vol. 40, pp. C5-308–C5-313, 1979.
- [340] J. Morillo, G. Bordier, C. H. de Novion, J. P. Senateur, and J. Jun, "Radiation damage in SmS, SmS_{1-x}P_x and SmB₆," *Journal of Magnetism and Magnetic Materials*, vol. 47–48, pp. 465–468, 1985.
- [341] T. H. Geballe, A. Menth, E. Buehler, and G. W. Hull, "Properties of SmB₆ doped with Eu and Gd," *Journal of Applied Physics*, vol. 41, no. 3, pp. 904–905, 1970.
- [342] S. Kunii, "Point-contact spectroscopy of mutual REB₆ (RE = La, Y, Sm, Ce) by automatic in situ cleaning," *Journal of Magnetism and Magnetic Materials*, vol. 63–64, pp. 673–676, 1987.
- [343] B. Gorshunov, N. Sluchanko, A. Volkov et al., "Low-energy electrostatics of SmB₆," *Physical Review B*, vol. 59, pp. 1808–1814, 1999.
- [344] J. M. Taraskon, Y. Isikawa, B. Chevalier, J. Etourneau, P. Hagenmuller, and M. Kasuya, "Temperature dependence of the samarium oxidation state in SmB₆ and Sm_{1-x}La_xB₆," *Journal de Physique*, vol. 41, p. 1141, 1980.
- [345] T. Kasuya, M. Kasaya, K. Takegahara et al., "Mechanisms for anomalous properties in SmB₆," *Journal of Magnetism and Magnetic Materials*, vol. 31–34, no. 1, pp. 447–450, 1983.
- [346] M. Campagna, G. K. Wertheim, and E. Bucher, *Structure and Bonding*, vol. 30, Springer, Berlin, Germany, 1976.
- [347] R. L. Cohen, M. Eibschütz, K. W. West, and E. Buehler, "Electronic configuration of SmB₆," *Journal of Applied Physics*, vol. 41, p. 898, 1970.
- [348] A. Yanase and H. Harima, "Band calculations on YbB₁₂, SmB₆ and CeNiSn," *Progress of Theoretical Physics. Supplement*, vol. 108, p. 19, 1992.
- [349] V. N. Antonov, B. N. Harmon, and A. N. Yaresko, "Electronic structure of mixed-valence semiconductors in the LSDA + U approximation. I. Sm monochalcogenides," *Physical Review B*, vol. 66, Article ID 165209, 10 pages, 2002.
- [350] E. Kierzek-Pecold, "Plasma reflection edge in crystalline MB₆ compounds," *Physica Status Solidi*, vol. 33, no. 2, pp. 523–531, 1969.
- [351] S. I. Kimura, T. Nanba, S. Kunii, and T. Kasuya, "Interband optical spectra of rare-earth hexaborides," *Journal of the Physical Society of Japan*, vol. 59, no. 9, pp. 3388–3392, 1990.
- [352] S. Kimura, T. Nanba, M. Tomikawa, S. Kunii, and T. Kasuya, "Electronic structure of rare-earth hexaborides," *Physical Review B*, vol. 46, no. 19, pp. 12196–12204, 1992.
- [353] S. I. Kimura, T. Nanba, S. Kunii, and T. Kasuya, "Low-energy optical excitation in rare-earth hexaborides," *Physical Review B*, vol. 50, no. 3, pp. 1406–1414, 1994.
- [354] T. Susaki, Y. Takeda, M. Arita et al., "Temperature-dependent high-resolution photoemission study of the Kondo insulator YbB₁₂," *Physical Review Letters*, vol. 82, no. 5, pp. 992–995, 1999.
- [355] M. Kasaya, F. Iga, K. Negishi, S. Nakai, and T. Kasuya, "A new and typical valence fluctuating system, YbB₁₂," *Journal of Magnetism and Magnetic Materials*, vol. 31–34, no. 1, pp. 437–438, 1983.
- [356] M. Kasaya, F. Iga, M. Takigawa, and T. Kasuya, "Mixed valence properties of YbB₁₂," *Journal of Magnetism and Magnetic Materials*, vol. 47–48, pp. 429–435, 1985.
- [357] F. Iga, N. Shimizu, and T. Takabatake, "Single crystal growth and physical properties of Kondo insulator YbB₁₂," *Journal of Magnetism and Magnetic Materials*, vol. 177–181, no. 1, pp. 337–338, 1998.
- [358] H. Okamura, S. Kimura, H. Shinozaki et al., "Optical conductivity of the Kondo insulator YbB₁₂: gap formation and low-energy excitations," *Physical Review B*, vol. 58, no. 12, pp. R7496–R7499, 1998.
- [359] T. Ekino, H. Umeda, F. Iga, N. Shimizu, T. Takabatake, and H. Fujii, "Tunneling spectroscopy of the Kondo-semiconducting gap in YbB₁₂," *Physica B*, vol. 259–261, pp. 315–316, 1999.
- [360] T. Susaki, A. Sekijama, K. Kobayaashi et al., "Low-energy electronic structure of the Kondo insulator YbB₁₂," *Physical Review Letters*, vol. 77, pp. 4269–4272, 1996.

- [361] F. Gerken, "Calculated photoemission spectra of the 4f states in the rare-earth metals," *Journal of Physics F*, vol. 13, no. 3, p. 703, 1983.
- [362] H. S. Bennett and E. A. Stern, "Faraday effect in solids," *Physical Review*, vol. 137, no. 2A, pp. A448–A461, 1965.
- [363] P. A. Alekseev, E. V. Nefedova, U. Staub et al., "Low-energy magnetic response and Yb valence in the Kondo insulator YbB₁₂," *Physical Review B*, vol. 63, no. 6, Article ID 064411, 6 pages, 2001.
- [364] E. Bucher, K. Andres, F. J. Di Salvo et al., "Magnetic and some thermal properties of chalcogenides of Pr and Tm and a few other rare earths," *Physical Review B*, vol. 11, no. 1, pp. 500–513, 1975.
- [365] R. Suryanarayanan, G. Güntherodt, J. L. Freeout, and F. Holtzberg, "Optical and photoemission studies of TmTe," *Physical Review B*, vol. 12, pp. 4215–4222, 1975.
- [366] Y. Lassailly, C. Vettier, F. Holtzberg, J. Flouquet, C. M. E. Zeyen, and F. Lapierre, "Modulated magnetic structure of the Kondo compound TmS," *Physical Review B*, vol. 28, no. 5, pp. 2880–2882, 1983.
- [367] A. Berger, E. Bucher, P. Haen et al., in *Valence Instabilities and Related Narrow Band Phenomena*, R. D. Parks, Ed., p. 491, Plenum, New York, NY, USA, 1977.
- [368] P. Haen, H. Bioud, F. Lapierre, and F. Holtzberg, in *Theoretical and Experimental Aspects of Valence Fluctuations, Proceedings of the 5th International Conference on Valence Fluctuations, Bangalore*, L. C. Gupta and S. K. Malik, Eds., p. 445, Plenum, New York, NY, USA, 1987.
- [369] F. Lapierre, P. Haen, B. Coqblin, M. Ribault, and F. Holtzberg, "Pressure effects on the resistivity of TmS," *Physica B*, vol. 108B, no. 1–3, pp. 1351–1352, 1981.
- [370] M. Campagna, E. Bucher, G. K. Wertheim, D. N. E. Buchanan, and L. D. Longinotti, "Spontaneous interconfiguration fluctuations in the Tm monochalcogenides," *Physical Review Letters*, vol. 32, no. 16, pp. 885–889, 1974.
- [371] G. Kaindl, C. Laubschat, B. Reihl et al., "Surface effects on core-level binding energies and valence in thulium chalcogenides," *Physical Review B*, vol. 26, pp. 1713–1727, 1982.
- [372] G. K. Wertheim, W. Eib, E. Kaldis, and M. Campagna, "Mixed valency of TmSe," *Physical Review B*, vol. 22, no. 12, pp. 6240–6246, 1980.
- [373] Y. Ufuktepe, S. I. Kimura, T. Kinoshita et al., "Resonant photoemission studies of thulium monochalcogenides around the Tm 4d threshold," *Journal of the Physical Society of Japan*, vol. 67, no. 6, pp. 2018–2026, 1998.
- [374] B. Batlogg, H. R. Ott, E. Kaldis, W. Thöni, and P. Wachter, "Magnetic mixed valent TmSe," *Physical Review B*, vol. 19, no. 1, pp. 247–259, 1979.
- [375] P. Haen, F. Lapierre, J. M. Mignot, R. Tournier, and F. Holtzberg, "Divergence of the very-low-temperature residual resistivity of Tm_xSe as $x \rightarrow 1$," *Physical Review Letters*, vol. 43, no. 4, pp. 304–307, 1979.
- [376] M. Ribault, J. Flouquet, P. Haen, F. Lapierre, J. M. Mignot, and F. Holtzberg, "Pressure study of the metal-insulator transition in TmSe," *Physical Review Letters*, vol. 45, no. 15, pp. 1295–1298, 1980.
- [377] K. Andres, W. M. Walsh, S. Darack, L. W. Rupp, and L. D. Longinotti, "On the resistivity of the magnetically ordered ground state of the intermediate valence compound TmSe," *Solid State Communications*, vol. 27, no. 9, pp. 825–828, 1978.
- [378] A. Berton, J. Chaussy, B. Cornut et al., "Specific-heat measurements of TmSe," *Physical Review B*, vol. 23, no. 7, pp. 3504–3513, 1981.
- [379] F. Holtzberg, T. Penney, and R. Tournier, "Valence instabilities of Tm in its compounds and solid solutions," *Journal de Physique*, vol. 40, pp. 314–320, 1979.
- [380] E. Kaldis and B. Frizler, *Progress in Solid State Chemistry*, vol. 14, pp. 95–139, 1982.
- [381] P. Hayen, F. Holtzberg, F. Lapierre, T. Penney, and R. Tournier, "Negative magnetoresistance, Hall effect and field induced transition in the Kondo systems TmSe and TmS," in *Valence Instabilities and Related Narrow Band Phenomena*, R. D. Parks, Ed., p. 495, Plenum, New York, NY, USA, 1977.
- [382] Y. Lassailly, C. Vettier, F. Holtzberg, A. Benoit, and J. Flouquet, "Magnetic ordering in TmTe," *Solid State Communications*, vol. 52, pp. 717–719, 1984.
- [383] E. Clementyev, R. Kohler, M. Braden et al., "Neutron scattering study of crystal-field excitations in TmTe," *Physica B*, vol. 230–232, pp. 735–737, 1977.
- [384] V. N. Antonov, B. N. Harmon, and A. N. Yaresko, "Electronic structure and magneto-optical Kerr effect of Tm monochalcogenides," *Physical Review B*, vol. 63, no. 20, Article ID 205112, 17 pages, 2001.
- [385] J. J. Yeh and I. Lindau, "Atomic subshell photoionization cross sections and asymmetry parameters: $1 \leq Z \leq 103$," *Atomic Data and Nuclear Data Tables*, vol. 32, no. 1, pp. 1–155, 1985.
- [386] P. Wachter, S. Kamba, and M. Grioni, "Empty 4f states in TmS," *Physica B*, vol. 252, no. 3, pp. 178–185, 1998.
- [387] P. A. Cox, *Structure and Bonding*, vol. 24, Springer, New York, NY, USA, 1975.
- [388] G. Racah, "Theory of complex spectra. IV," *Physical Review*, vol. 76, no. 9, pp. 1352–1365, 1949.
- [389] B. Batlogg, "Dielectric response of mixed-valent TmSe," *Physical Review B*, vol. 23, no. 4, pp. 1827–1838, 1981.
- [390] W. Reim, J. Schoenes, and O. Vogt, "Magneto-optical investigation of the electronic and magnetic structure of UAs₂Se_{1-x}," *Physical Review B*, vol. 29, no. 6, pp. 3252–3258, 1984.
- [391] H. Feil and C. Haas, "Magneto-optical Kerr effect, enhanced by the plasma resonance of charge carriers," *Physical Review Letters*, vol. 58, pp. 65–68, 1987.
- [392] T. Matsumura, T. Kosaka, J. Tang et al., "Pressure induced semiconductor to metal transition in TmTe," *Physical Review Letters*, vol. 78, no. 6, pp. 1138–1141, 1997.
- [393] L. L. Hirst, "Theory of magnetic impurities in metals," *Zeitschrift für Physik B*, vol. 11, no. 3, pp. 255–278, 1970.
- [394] F. Marabelli and P. Wachter, in *Theoretical and Experimental Aspects of Valence Fluctuations and Heavy Fermions*, L. C. Gupta and S. K. Malik, Eds., p. 269, Plenum Press, New York, NY, USA, 1987.
- [395] P. Wachter, "TmSe and its alloys," *Journal of Magnetism and Magnetic Materials*, vol. 31–34, no. 1, pp. 439–442, 1983.
- [396] A. Amato and J. Sierro, "Magneto-thermopower of TmS and TmSe," *Journal of Magnetism and Magnetic Materials*, vol. 47–48, pp. 475–477, 1985.
- [397] B. Batlogg, A. Schlegel, and P. Wachter, "Optical study of valence fluctuation of metallic SmS and TmSe," *Physica B*, vol. 86–88, no. 1, pp. 229–230, 1977.
- [398] A. I. Lichtenstein and M. I. Katsnelson, "Ab initio calculations of quasiparticle band structure in correlated systems: LDA++ approach," *Physical Review B*, vol. 57, no. 12, pp. 6884–6895, 1998.
- [399] A. Ochiai, T. Suzuki, and T. Kasuya, "Heavy fermion behavior in extremely low carrier concentration system Yb₄As₃," *Journal of the Physical Society of Japan*, vol. 59, no. 11, pp. 4129–4141, 1990.

- [400] A. Ochiai, H. Aoki, T. Suzuki, R. Helfrich, and F. Steglich, "Strongly correlated electron system without free carrier $\text{Yb}_4(\text{As}_{1-x}\text{Px})_3$," *Physica B*, vol. 230–232, pp. 708–710, 1997.
- [401] P. Bonville, A. Ochiai, T. Suzuki, and E. Vincent, "Heterogeneous Yb^{3+} - Yb^{2+} mixed valency and unusual Kondo ground state in Yb_4As_3 ," *Journal de Physique I*, vol. 4, pp. 595–603, 1994.
- [402] P. H. P. Reinders, U. Ahlheim, K. Fraas, F. Steglich, and T. Suzuki, "Specific heat measurements of Yb_4As_3 . A heavy fermion system with low carrier concentration?" *Physica B*, vol. 186–188, pp. 434–436, 1993.
- [403] T. Suzuki, "Heavy fermion state in low carrier concentration systems for rare earth pnictides and chalcogenides," *Physica B*, vol. 186–188, pp. 347–354, 1993.
- [404] T. Suzuki, *Japanese Journal of Applied Physics*, vol. 8, p. 267, 1993.
- [405] A. Ochiai, D. X. Li, Y. Haga, O. Nakamura, and T. Suzuki, "Charge-ordering in Sm_4Bi_3 and Yb_4As_3 with the anti- Th_3P_4 structure," *Physica B*, vol. 186–188, pp. 437–439, 1993.
- [406] T. Kasuya, "Physical mechanism of anomalous heavy fermion in Yb_4As_3 ," *Journal of the Physical Society of Japan*, vol. 63, no. 7, pp. 2481–2484, 1994.
- [407] T. Suzuki, *Japanese Journal of Applied Physics*, vol. 8, p. 44, 1993.
- [408] M. O'Keeffe and S. Andersson, "Rod packings and crystal chemistry," *Acta Crystallographica Section A*, vol. 33, pp. 914–923, 1977.
- [409] M. Kohgi, K. Iwasa, A. Ochiai et al., "Charge order and one-dimensional properties of Yb_4As_3 ," *Physica B*, vol. 230–232, pp. 638–640, 1997.
- [410] T. Goto, Y. Nemoto, S. Nakamura, A. Ochiai, and T. Suzuki, "Elastic anomalies of charge ordering in Yb_4As_3 ," *Physica B*, vol. 230–232, pp. 702–704, 1997.
- [411] T. Suzuki, Y. Haga, D. X. Li et al., "Anomalous physical properties of the low carrier concentration state in f-electron systems," *Physica B*, vol. 206–207, pp. 771–779, 1995.
- [412] Y. Okunuki, N. Mōri, A. Ochiai, Y. Haga, and T. Suzuki, "Pressure effects on transport properties of Yb_4As_3 ," *Journal of the Physical Society of Japan*, vol. 64, no. 2, pp. 533–539, 1995.
- [413] N. Mōri, H. Takahashi, Y. Sekine et al., "Anomalous transport and electronic properties of Yb_4As_3 under high pressure," *Physica B*, vol. 230–232, pp. 630–634, 1997.
- [414] S. Suga, S. Ogawa, H. Namatame et al., "XPS and UPS studies of valence fluctuation and surface states of Yb_4As_3 , Yb_4Sb_3 and Yb_4Bi_3 ," *Journal of the Physical Society of Japan*, vol. 58, no. 12, pp. 4534–4543, 1989.
- [415] Y. Saitoh, S. Suga, H. Matsubara et al., "BIS and XPS study of YbP , YbAs and Yb_4As_3 ," *Journal of the Physical Society of Japan*, vol. 60, no. 12, pp. 4005–4008, 1991.
- [416] S. I. Kimura, M. Ikezawa, A. Ochiai, and T. Suzuki, "Optical study on heavy fermion and mixed valence in Yb_4As_3 ," *Journal of the Physical Society of Japan*, vol. 65, no. 11, pp. 3591–3598, 1996.
- [417] S. I. Kimura, A. Ochiai, and T. Suzuki, "Low energy excitation of Yb_4As_3 ," *Physica B*, vol. 230–232, pp. 705–707, 1997.
- [418] Y. S. Kwon, A. Ochiai, H. Kitazawa et al., "Kondo states of Yb_4Sb_3 and Yb_4As_3 ," *Journal of Magnetism and Magnetic Materials*, vol. 70, no. 1–3, pp. 397–399, 1987.
- [419] T. Kasuya, "Magnetic polaron in Yb monopnictides," *Journal of the Physical Society of Japan*, vol. 63, pp. 843–846, 1994.
- [420] P. Fulde, B. Schmidt, and P. Thalmeier, "Theoretical model for the semimetal Yb_4As_3 ," *Europhysics Letters*, vol. 31, p. 323, 1995.
- [421] B. Schmidt, P. Thalmeier, and P. Fulde, "Charge ordering and heavy fermions in the semimetal Yb_4As_3 ," *Physica B*, vol. 223–224, no. 1–4, pp. 373–375, 1996.
- [422] Y. M. Li, N. D'Ambrumenil, and P. Fulde, "Properties of a band Jahn-Teller system with strong electron correlations: Application to Yb_4As_3 ," *Physical Review Letters*, vol. 78, no. 17, pp. 3386–3389, 1997.
- [423] V. N. Antonov, A. N. Yaresko, A. Y. Perlov et al., "Electronic structure of low-carrier Yb_4As_3 and related compounds," *Physical Review B*, vol. 58, no. 15, pp. 9752–9762, 1998.
- [424] P. Fulde, *Electron Correlations in Molecules and Solids*, Springer, Berlin, Germany, 1995.
- [425] Y. Kagan, K. A. Kikion, and N. V. Prokof'ev, "Heavy fermions in the Kondo lattice as neutral quasiparticles," *Physica B*, vol. 182, no. 3, pp. 201–208, 1992.
- [426] K. Neumaier, K. Andres, and H. R. Ott, "On the valence transformation and the ground state of mixed valent Sm_4Bi_3 ," *Physica B*, vol. 108, no. 1–3, pp. 1343–1344, 1981.
- [427] A. Ochiai, T. Suzuki, and T. Kasuya, "Kondo state in Sm_4X_3 ($\text{X} = \text{Bi}, \text{Sb}$ and As)," *Journal of Magnetism and Magnetic Materials*, vol. 52, no. 1–4, pp. 13–17, 1985.
- [428] J. X. Boucherle, F. Givord, J. Schweizer et al., "Polarized neutron investigation of charge-ordering in mixed-valence Sm_4Bi_3 ," *Physica B*, vol. 267–268, pp. 47–50, 1999.
- [429] A. Ochiai, Y. Shima, and M. Shirakawa, "Charge ordering and ferromagnetic transition in single-crystal Eu_4As_3 ," *Journal of the Physical Society of Japan*, vol. 72, no. 12, pp. 3174–3181, 2003.
- [430] A. Jayaraman, R. G. Maines, and E. Bucher, "Pressure-induced valence instability in Sm_4Bi_3 ," *Solid State Communications*, vol. 27, no. 7, pp. 709–711, 1978.
- [431] H. Aoki, A. Ochiai, and T. Suzuki, "Charge and magnetic ordering in mixed valence system $\text{Sm}_4(\text{Bi}_{1-x}\text{Sb}_x)_3$," *Physica B*, vol. 259–261, pp. 349–350, 1999.
- [432] S. Suga, "Ultraviolet photoemission studies of highly correlated electron systems in Sm, Yb and U pnictides," *Physica Scripta*, vol. 17, pp. 228–239, 1978.
- [433] S. Suga, A. Sekiyama, S. Imada, T. Suzuki, H. Aoki, and A. Ochiai, "Electronic states of Sm_4As_3 and Sm_4Bi_3 studied with photoemission spectroscopy," *Physica B*, vol. 281–282, pp. 158–160, 2000.
- [434] F. Hulliger, *Materials Research Bulletin*, vol. 14, p. 33, 1979.
- [435] G. Wortmann, E. V. Sampathkumaran, and G. Kaindl, "Verwey transition in Eu_4As_3 ," *Journal of Magnetism and Magnetic Materials*, vol. 54–57, part 1, pp. 338–340, 1986.
- [436] F. L. Carter, "Vacancy and charge ordering in the Th_3P_4 related structures," *Journal of Solid State Chemistry*, vol. 5, no. 2, pp. 300–313, 1972.
- [437] M. Picon, L. Domange, J. Flahaut, M. Guittard, and M. Patrie, *Bulletin de la Société Chimique de France*, vol. 2, p. 221, 1960.
- [438] A. Tamaki, T. Goto, M. Sugita, T. Suzuki, T. Fujimura, and T. Kasuya, "Transport properties in valence fluctuation compound Sm_3Se_4 ," *Journal of Magnetism and Magnetic Materials*, vol. 31–34, part 1, pp. 383–384, 1983.
- [439] B. Batlogg, E. Kaldis, A. Schlegel, G. von Schulthess, and P. Wachter, "Optical and electrical properties of the mixed valence compound Sm_3S_4 ," *Solid State Communications*, vol. 19, no. 7, pp. 673–676, 1976.
- [440] N. F. Mott, "Physics of Eu_3S_4 and Sm_3S_4 ," *Philosophical Magazine Part B*, vol. 42, no. 3, pp. 497–498, 1980.
- [441] H. Goto, K. Baba, T. Goto et al., "Dielectric dispersion of valence fluctuation compound Sm_3Se_4 ," *Journal of the Physical Society of Japan*, vol. 62, pp. 1365–1371, 1993.

- [442] J. M. D. Coey, B. Cornut, F. Holtzberg, and S. Von Molnar, "Magnetic and thermal properties of the mixed valence compounds Sm_2S_3 , Sm_3S_4 , and Sm_3Se_4 ," *Journal of Applied Physics*, vol. 50, no. 3, pp. 1923–1925, 1979.
- [443] P. A. Alekseev, J.-M. Mignot, R. Kahn et al., "Neutron scattering study of the magnetic excitation spectra in mixed-valence $^{154}\text{Sm}_3\text{Te}_4$," *Journal of Physics: Condensed Matter*, vol. 12, p. 2725, 2000.
- [444] S. Takagi, H. Suzuki, A. Ochiai, and T. Suzuki, "First NMR observation of valence fluctuation in rare-earth compounds ^{77}Se NMR studies of temperature-activated valence fluctuation in Sm_3Se_4 ," *Journal of the Physical Society of Japan*, vol. 62, no. 8, pp. 2861–2868, 1993.
- [445] A. Tamaki, T. Goto, S. Kunii, T. Suzuki, T. Fujimura, and T. Kasuya, "Valence fluctuation of Sm_3Se_4 ," *Journal of Physics C*, vol. 18, no. 31, p. 5849, 1985.
- [446] T. Tayama, K. Tenya, H. Amitsuka, T. Sakakibara, A. Ochiai, and T. Suzuki, "Magnetization study of the valence fluctuation compound Sm_3Te_4 at very low temperatures," *Journal of the Physical Society of Japan*, vol. 65, no. 11, pp. 3467–3470, 1996.
- [447] R. Pott, G. Güntherodt, W. Wichelhaus, M. Ohl, and H. Bach, "Thermal properties of Eu_3S_4 : order-disorder transition," *Physical Review B*, vol. 27, no. 1, pp. 359–363, 1983.
- [448] F. Holtzberg, "The verwey transition," *Philosophical Magazine B*, vol. 42, no. 3, p. 325, 1980.
- [449] E. Gorlich, H. U. Hryniewicz, R. Kmiec, K. Latka, and K. Tomala, "The Mössbauer effect in Eu_3S_4 at low temperatures," *Physica Status Solidi B*, vol. 64, p. 147, 1974.
- [450] H. Ohara, S. Sasaki, Y. Konoike, T. Toyoda, K. Yamawaki, and M. Tanaka, "Charge ordering in Eu_3S_4 determined by the valence-difference contrast of synchrotron X-ray diffraction," *Physica B*, vol. 350, no. 1–3, pp. 353–365, 2004.
- [451] M. Sugita, S. Kunii, K. Takegahara et al., "Electronic structure and crystal field in Sm_3Se_4 and Sm_3Te_4 ," in *Crystalline Electric Field Effects in f-Electron Magnetism*, R. P. Guertin, W. Suski, and Z. Zolnierak, Eds., p. 479, Plenum, New York, NY, USA, 1982.
- [452] S. Takagi, T. Suzuki, A. Amato, F. N. Gyax, A. Schenck, and A. Ochiai, " μSR studies of the low-temperature magnetism in a valence-fluctuation compound Sm_3Se_4 ," *Hyperfine Interactions*, vol. 104, no. 1–4, pp. 151–156, 1997.
- [453] U. Ahlheim, K. Fraas, P. H. P. Reinders et al., "Antiferromagnetism and heavy-fermion effects in a semiconductor: Sm_3Te_4 ," *Journal of Magnetism and Magnetic Materials*, vol. 108, pp. 213–214, 1992.
- [454] P. Villars and L. D. Calvert, *Pearson's Handbook of Crystallographic Data for Intermetallic Phases*, ASM International, Materials Park, Ohio, USA, 1991.
- [455] V. N. Antonov, B. N. Harmon, and A. N. Yaresko, "Electronic structure of mixed-valence and charge-ordered Sm and Eu pnictides and chalcogenides," *Physical Review B*, vol. 72, no. 8, Article ID 085119, 13 pages, 2005.
- [456] B. Schmidt, H. Aoki, T. Cichorek et al., "Low-energy excitations of the semimetallic one-dimensional $S = 1/2$ antiferromagnet Yb_4As_3 ," *Physica B*, vol. 300, pp. 121–138, 2001.
- [457] R. D. Shannon and C. T. Prewitt, "Effective ionic radii in oxides and fluorides," *Acta Crystallographica Section B*, vol. 25, pp. 925–954, 1969.
- [458] O. Berkooz, M. Malamud, and S. Shtrikman, "Observation of electron hopping in $^{151}\text{Eu}_3\text{S}_4$ by Mössbauer spectroscopy," *Solid State Communications*, vol. 6, no. 3, pp. 185–188, 1968.
- [459] T. Toyoda, S. Sasaki, and M. Tanaka, "X-ray diffuse scattering study of magnetite by the valence-difference contrast method," *Japanese Journal of Applied Physics*, vol. 36, no. 4, pp. 2247–2252, 1997.
- [460] K. Kojima, H. Hayashi, A. Minami, Y. Kasamatsu, and T. Hihara, "Crystal phases and Yb valence transition in $\text{Yb}_{x>}\text{In}_{1-x}<}\text{Cu}_2$," *Journal of Magnetism and Magnetic Materials*, vol. 81, no. 3, pp. 267–272, 1989.
- [461] C. Rossel, K. N. Yang, M. B. Maple, Z. Fisk, E. Zirngiebl, and J. D. Thomson, "Strong electronic correlations in a new class of Yb-based compounds: YbXCu_4 ($X = \text{Ag, Au, Pd}$)," *Physical Review B*, vol. 35, pp. 1914–1918, 1987.
- [462] M. J. Besnus, P. Haen, N. Hamdaoui, A. Herr, and A. Meyer, "Kondo behavior of YbAgCu_4 ," *Physica B*, vol. 163, no. 1–3, pp. 571–573, 1990.
- [463] N. Tsujii, J. He, K. Yoshimura et al., "Heavy-fermion behavior in $\text{YbCu}_{5-x}\text{Ag}_x\text{s}$," *Physical Review B*, vol. 55, no. 2, pp. 1032–1039, 1997.
- [464] N. Tsujii, J. He, F. Amita et al., "Kondo-lattice formation in cubic-phase YbCu_5 ," *Physical Review B*, vol. 56, no. 13, pp. 8103–8108, 1997.
- [465] V. T. Rajan, "Magnetic susceptibility and specific heat of the coqblin-schrieffer model," *Physical Review Letters*, vol. 51, no. 4, pp. 308–311, 1983.
- [466] A. Severing, A. P. Murani, J. D. Thompson, Z. Fisk, and C. K. Loong, "Neutron scattering experiments on YbXCu_4 and ErXCu_4 ($X = \text{Au, Pd, and Ag}$)," *Physical Review B*, vol. 41, no. 4, pp. 1739–1749, 1990.
- [467] I. Felner, I. Nowik, D. Vaknin et al., "Ytterbium valence phase transition in $\text{Yb}_x\text{In}_{1-x}\text{Cu}_2$," *Physical Review B*, vol. 35, pp. 6956–6963, 1987.
- [468] J. L. Sarrao, C. D. Immer, C. L. Benton et al., "Evolution from first-order valence transition to heavy-fermion behavior in $\text{YbIn}_{1-x}\text{Ag}_x\text{Cu}_4$," *Physical Review B*, vol. 54, no. 17, pp. 12207–12211, 1996.
- [469] B. Kindler, D. Finsterbusch, R. Graft, F. Ritter, W. Assmus, and B. Luthi, "Mixed-valence transition in YbInCu_4 ," *Physical Review B*, vol. 50, pp. 704–707, 1994.
- [470] A. L. Cornelius, J. M. Lawrence, J. L. Sarrao et al., "Experimental studies of the phase transition in $\text{YbIn}_{1-x}\text{Ag}_x\text{Cu}_4$," *Physical Review B*, vol. 56, no. 13, pp. 7993–8000, 1997.
- [471] J. M. Lawrence, G. H. Kwei, J. L. Sarrao, Z. Fisk, D. Mandrus, and J. D. Thompson, "Structure and disorder in YbInCu_4 ," *Physical Review B*, vol. 54, pp. 6011–6014, 1996.
- [472] K. Kojima, Y. Nakai, T. Suzuki et al., "Neutron and X-ray diffraction studies of a valence fluctuating compound YbInCu_4 ," *Journal of the Physical Society of Japan*, vol. 59, no. 3, pp. 792–795, 1990.
- [473] J. W. Allen and L. Z. Liu, " α - γ transition in Ce. II. A detailed analysis of the Kondo volume-collapse model," *Physical Review B*, vol. 46, pp. 5047–5054, 1992.
- [474] M. Galli, F. Marabelli, and E. Bauer, "The electronic structure of YbCu_4In as observed through optical measurements," *Physica B*, vol. 230–232, pp. 304–306, 1997.
- [475] V. N. Antonov, M. Galli, F. Marabelli, A. N. Yaresko, A. Y. Perlov, and E. Bauer, "Electronic structure and optical spectra of LuInCu_4 and YbMCu_4 ($M = \text{Cu, Ag, Au, Pd, and In}$)," *Physical Review B*, vol. 62, no. 3, pp. 1742–1752, 2000.
- [476] E. Bauer, "Anomalous properties of Ce-Cu- and Yb-Cu-based compounds," *Advances in Physics*, vol. 40, pp. 417–534, 1991.

- [477] J. S. Kang, J. W. Allen, C. Rossel, C. L. Seaman, and M. B. Maple, "Electron-spectroscopy study of YbXCu_4 ($X = \text{Ag, Au, Pd}$)," *Physical Review B*, vol. 41, no. 7, pp. 4078–4082, 1990.
- [478] J. M. Ziman, *Models of Disorder: The Theoretical Physics of Homogeneously Disordered System*, Cambridge University Press, Cambridge, UK, 1979.



Hindawi

Submit your manuscripts at
<http://www.hindawi.com>

